Greenhouse gas exchange in the Amazon:

Carbon dioxide and methane insights from the
Amazon Tall Tower Observatory

Santiago Botía Bocanegra

Greenhouse gas exchange in the Amazon region

Carbon dioxide and methane insights from the Amazon Tall Tower Observatory (ATTO)

Santiago Botía Bocanegra

Thesis committee

Promotor
Prof. Dr W. Peters
Professor of Meteorology and Air Quality
Wageningen University & Research

Co-promotors
Dr C. Gerbig
Group Leader
Max Planck Institute for Biogeochemistry, Jena, Germany

Other members
Prof. Dr L. Poorter, Wageningen University & Research
Prof. Dr I. Levin, Heidelberg University
Dr A. Bastos, Max Planck for Biogeochemistry, Jena, Germany
Prof. Dr S. Houweling, University of Amsterdam

Greenhouse gas exchange
in the Amazon region

**Carbon dioxide and methane insights from the
Amazon Tall Tower Observatory (ATTO)**

Santiago Botía Bocanegra

Acknowledgements

Summary

The Amazon region is crucial for the Earth system, it stores large amounts of carbon in soils and biomass, has the largest freshwater basin in the world and it is a biodiversity hotspot. In this vast expanse of forest, massive amounts of carbon, water and energy circulate between the biosphere and the atmosphere, providing ecosystem services that are vital for humanity. The carbon stored has a global importance from a climate change perspective, the water cycle is crucial for Andean and lowland amazonian communities, and biodiversity sustains life and healthy forests. Humans have been part of the Amazon system for several thousands years, but only during the last decades, our activities have led to unprecedented changes in this system with consequences yet to be known. These consequences have a complex nature, yet they are prone to be studied as they manifest leaving measurable signals in different compartments of the Amazon system. The atmosphere is one of these compartments, in which the changes in abundance of some constituents, like carbon dioxide (CO_2) and methane (CH_4), can be linked to different natural or anthropogenic processes. In the Amazon, CO_2 is mainly controlled by the vegetation, and CH_4 by decomposition processes in the absence of oxygen in the sediments of aquatic habitats. Therefore, by measuring the atmospheric changes of CO_2 and CH_4 one can learn something about the sources and sinks of these two greenhouse gases (GHG), which are highly relevant for global warming. As such, the central objective of this thesis is to use atmospheric data to better understand the spatial and temporal patterns of sinks and sources of CO_2 and CH_4.

In the first chapter a general introduction is provided. There, I describe the Global and the Amazon carbon cycle (mainly from a CO_2 perspective), highlighting the role of CH_4 at both scales. The Amazon Tall Tower Observatory (ATTO), the research station where data was collected, is introduced giving a historical view on how the site started and what is the actual state in terms of greenhouse gas instrumentation. After that, the research objectives of the thesis are given together with a conceptual framework for each chapter.

In Chapter 2, the CH_4 time series is analyzed for the period between June 2013 and November 2018. We investigated a specific nighttime event in which CH_4 levels are significantly higher at the top of the tower than the lowest measurement height. For this analysis, an approach based on observational data was applied and we found that the events have a seasonal pattern, being more frequent during the dry season. Furthermore, a hypothesis is proposed suggesting a potential source for this methane. The most likely source location is the Uatumã River, possibly influenced by dead stands of flooded forest trees that may be enhancing CH_4 emissions from those areas.

Using biosphere models and an atmospheric transport model, six years of the the CO_2 time series is analyzed in Chapter 3. With this approach, it was possible to study the seasonal and inter-annual patterns of the continental CO_2 signal. When comparing it to local fluxes, we found differences that are interpreted as an indication of how local and non-local drivers are coupled or decoupled in the atmospheric CO_2 signal. An example of this is the effect of the 2015/2016 El Niño-induced drought, in which the effect of the drought was observed first in the atmospheric CO_2 and later in the local fluxes. In addition, we found that simulating CO_2 mole fractions at ATTO can be improved when including river fluxes. However, the overall performance of the simulations was found to be hampered mainly because biosphere models do not represent the vegetation dynamics properly.

Of particular interest in Chapter 4, is the role of the Amazon region as a sink or source of carbon to the atmosphere. To study this question, we use a regional inversion system to estimate net CO_2 fluxes using atmospheric data. The set of data used, is the ATTO CO_2 observations and also a network of airborne measurements of CO_2 vertical profiles. We found an amazon vegetation sink of -0.35 $\pm$ 0.3 PgC year^{-1} for the period between 2010-2018, which as we discussed in Chapter 4, is consistent with other inversions. Furthermore, our set up allowed us to infer spatial patterns for the Amazon region and also other neighboring ecosystems like the semi-arid Caatinga and Cerrado in the northeast of Brazil. We found an emerging sink-source gradient between the Amazon region (sink) and the Cerrado and Caatinga together (source). Finally, we highlight the main limitations of our study, giving priority to the regions that are less constrained and where more observations are needed.

In the last chapter, the fundamental aspects of this work are discussed. A reflection on the role of atmospheric transport and seasonal drivers of CO_2 and CH_4 is provided, with a strong focus on the main limitations of this thesis and thinking about future lines of research. Furthermore, contextualizing the findings of Chapter 4, the importance of studying other biomes for regional carbon budgets is highlighted. In the Outlook we provide several concrete ideas for follow-up work, some of which are under current development.

Resumen

El Amazonas es crucial para el sistema terrestre. Almacena grandes cantidades de carbono en los suelos y la biomasa aérea, tiene la mayor cuenca de agua dulce del mundo y cuenta con una biodiversidad extraordinaria. En esta vasta extensión de bosque circulan enormes cantidades de carbono, agua y energía entre la biosfera y la atmósfera, proporcionando servicios ecosistémicos vitales para la humanidad. El carbono almacenado tiene una importancia global asociada al cambio climático, el ciclo del agua es crucial para las comunidades andinas y amazónicas, y la biodiversidad sostiene la vida y la salud de los bosques. Los seres humanos forman parte del sistema amazónico desde hace varios miles de años, pero sólo en las últimas décadas nuestras actividades han provocado cambios sin precedentes en este sistema con consecuencias aún desconocidas. Estas consecuencias tienen una naturaleza compleja, pero ya que se manifiestan dejando señales medibles en diferentes compartimentos del sistema amazónico, las podemos estudiar. La atmósfera es uno de estos compartimentos, en el que los cambios en la abundancia de algunos constituyentes, como el dióxido de carbono (CO_2) y el metano (CH_4), pueden asociarse a diferentes procesos naturales o antropogénicos. En la Amazonia, el CO_2 está controlado principalmente por la vegetación y el CH_4 por los procesos de descomposición en ausencia de oxígeno en los sedimentos de los hábitats acuáticos. Por lo tanto, los cambios en la concentración atmosférica de CO_2 y CH_4 contienen información sobre las fuentes y los sumideros de estos dos gases de efecto invernadero (GEI), relevantes para el calentamiento global. Por lo tanto, el objetivo central de esta tésis es utilizar datos atmosféricos para comprender mejor los patrones espaciales y temporales de los sumideros y las fuentes de CO_2 y CH_4.

En el primer capítulo se hace una introducción general y se describen el ciclo del carbono global y el de la región amazónica. Adicionalmente, con una perspectiva histórica se introduce el Observatorio de la Torre Alta del Amazonas (ATTO); la estación de investigación donde se recolectaron los datos. Finalmente en este capítulo, se describen los objetivos de investigación y el marco conceptual de cada capítulo. En el capítulo 2, se analiza la serie temporal de CH_4 para el periodo entre junio de 2013 y noviembre de 2018. Se investigó un evento específico en el que los niveles de CH_4 en la noche son significativamente más altos en la parte superior de la torre que en la parte de medición más baja. Se hizo un análisis observacional (puramente basado en datos y no modelos) y encontramos que los

eventos nocturnos tienen un patrón estacional, siendo más frecuentes durante la estación seca. Además, se propone una hipótesis que sugiere una fuente para este metano. La ubicación más probable de esta fuente es el río Uatumã, posiblemente influenciada por los árboles muertos en los bosques inundables, que pueden estar aumentando las emisiones de CH_4 de esas áreas.

Utilizando modelos de vegetación y un modelo de transporte atmosférico, en el capítulo 3 se analizan seis años de la serie temporal de CO_2. Allí se investigaron los patrones estacionales e interanuales de la señal regional de CO_2 atmosférico (en unidades de ppm). La señal regional de CO_2 equivale a la concentración atmosférica de CO_2 después de restar la concentración con la cual las masas de aire entran al continente. Dicha señal regional se comparó con los flujos de CO_2 locales (en unidades de umol m^{-2} s^{-1}), los cuales contienen información a una escala local. La diferencia en fase a escala estacional e interanual, se interpretó como un indicador de acople o desacople entre los factores locales y regionales que controlan la señal regional de CO_2 observada. La sequía inducida por El Niño 2015/2016 es un claro ejemplo de desacople, ya que los efectos de la sequía se observaron primero en el CO_2 atmosférico y después en los flujos locales. Además, comprobamos que la simulación de la concentración de CO_2 en ATTO puede mejorarse al incluir los flujos de CO_2 provenientes de los ríos. Sin embargo, las simulaciones atmosféricas no reproducen las mediciones de CO_2 y concluimos que la razón principal es porque los modelos de vegetación utilizados no representan adecuadamente la dinámica de la estacional de la absorción neta de CO_2.

En el capítulo 4, se estudió el papel de la región amazónica como sumidero o fuente de carbono a la atmósfera. Para estudiar este tema, utilizamos un sistema de inversión atmosférica regional para estimar los flujos netos de CO_2 utilizando datos atmosféricos. El conjunto de datos utilizados son las observaciones de CO_2 de ATTO y también una red de mediciones aéreas de perfiles verticales de CO_2. Encontramos un sumidero de vegetación amazónica de -0.35 ± 0.3 PgC $año^{-1}$ para el periodo entre 2010-2018, que es consistente con otras estimaciones. Además, el método utilizado nos permitió inferir patrones espaciales para la región amazónica y también para otros ecosistemas vecinos como la Caatinga y el Cerrado en el noreste de Brasil. Encontramos un gradiente emergente entre la región amazónica (sumidero) y el Cerrado y la Caatinga juntos (fuente). Por último, destacamos las principales limitaciones de nuestro estudio, dando prioridad a las regiones que están menos restringidas y en las que se necesitan más observaciones. En el capítulo 5, se discuten los aspectos fundamentales de este trabajo. Se hace una reflexión sobre el papel del transporte atmosférico y los controles estacionales de CO_2 y CH_4, con un enfoque en las principales limitaciones de esta tesis y proponiendo futuras líneas de investigación. Además, se destaca la importancia de estudiar otros biomas para la cuantificación del balance regional de carbono. Finalmente, se proponen varias ideas concretas para darle continuidad al trabajo de esta tésis, algunas de las cuales se están desarrollando actualmente.

Contents

Chapter 1

Introduction

1.1 Global carbon cycle

Back in 1856, the scientist Eunice Foote first described that carbon dioxide (CO_2) and water vapor absorb heat from solar radiation. She also made a direct link between past climate change and atmospheric changes of these two gases (Jackson, 2020). Some years later, in 1859, John Tyndall made similar experiments but only using longwave infrared radiation (i.e. emitted by the Earth itself), which led to the physical basis of the greenhouse effect (Jackson, 2020). One of the first predictions of how a rise in atmospheric CO_2 could lead to an increase in global temperature was done in 1897 by Svante Arrhenius (Arrhenius & Holden, 1897). Decades later, by measuring atmospheric CO_2 mole fractions in Mauna Loa, Hawaii, Charles Keeling documented for the first time a steep increase of CO_2 in the atmosphere (Keeling et al., 1976). These early studies laid the foundations of the atmospheric perspective of the global carbon cycle.

Like CO_2, methane (CH_4) can absorb longwave radiation and contribute to global warming with a larger global warming potential (Myhre et al., 2013). Today these two gases, CO_2 and CH_4, constitute less than 1% of the atmosphere, and yet they have a massive impact on Earth's temperature by absorbing heat (Myhre et al., 2013). The CO_2 mole fraction in 1750 was 277 parts per million (ppm) (Joos & Spahni, 2008) while in 2020 it reached 412 ± 0.1 ppm (Dlugokencky, 2020). For CH_4 in a similar time period (from 1750 to 2018) the atmospheric mole fraction has increased by a factor of 2.6, reaching 1857 parts per billion (ppb) in 2018 (Saunois et al., 2020). Although both species are part of the global carbon cycle, CO_2 is more abundant and has a longer lifetime in the atmosphere. Because of different sources and sinks these species are studied separately (Saunois et al., 2020; Friedlingstein et al., 2022). Therefore, here we introduce the global carbon cycle from a CO_2 perspective briefly highlighting the role of CH_4, and in the next Section the main sources and sinks of CH_4 are described.

The natural carbon cycle can be separated into four main components, the atmosphere, the ocean, the terrestrial biosphere and geologic reservoirs (Ciais et al., 2013). Carbon circulates between these reservoirs on different timescales ranging from hours to thousands of years or even more for the geologic reservoirs (Archer et al., 2009). According to the last report of the Global Carbon Project (Friedlingstein et al., 2022) (see Figure 1.1), in the last decade (2011-2020) anthropogenic emissions were on average 10.6 ± 0.7 PgC year^{-1}, after adding fossil fuel and land use change emissions. From this, 3.1 ± 0.6 PgC year^{-1} is captured by the terrestrial biosphere, 2.8 ± 0.4 PgC year^{-1} by the ocean and 5.1 ± 0.02 PgC year^{-1} accumulates in the atmosphere. Anthropogenic emissions are thus embedded in a carbon cycle in which the exchange between reservoirs lead to changes in carbon stocks (see Figure 1.1) over different temporal scales. The anthropogenic perturbation leads to a fast (at decadal timescales) increase of CO_2 levels in the atmosphere. The main driver of such increase before 1950 was anthropogenic emissions not associated with burning fossil fuels, like deforestation and other land use change activities (Canadell et al., 2021).

After 1950, emissions from fossil fuels turned into the dominant driver of the atmospheric increase of CO_2 (Canadell et al., 2021).
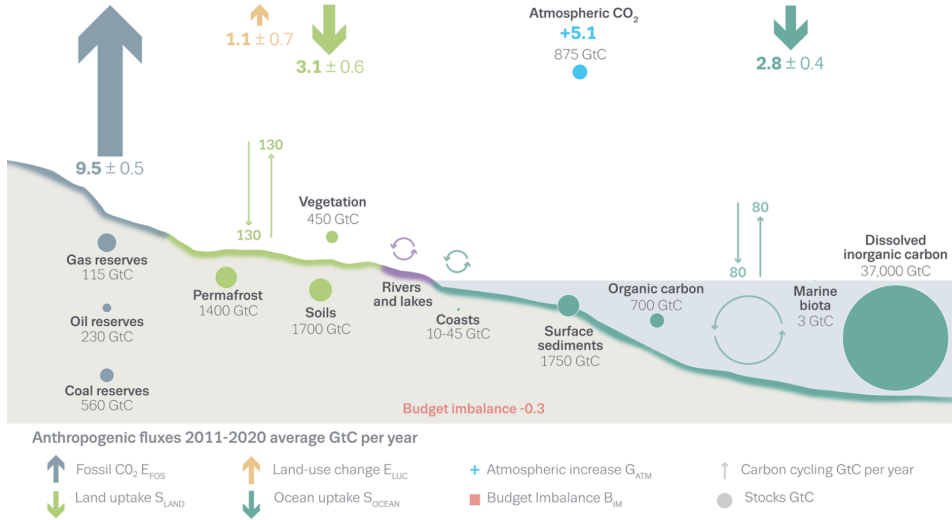
Figure 1.1: The global carbon cycle. Taken from Friedlingstein et al. (2022). The GtC unit is equivalent to PgC (10^{15} grams). The uncertainty of the atmospheric growth rate is ± 0.02 PgC year^{-1} and not shown in the Figure as described in Friedlingstein et al. (2022).

In reality, the sources (E) should balance the sinks (S) of carbon plus what accumulates in the atmosphere (Friedlingstein et al., 2022). Emissions from fossil fuel combustion (E_{FOS}) and land use change (E_{LUC}) are distributed in what is taken up by the ocean (S_{OCEAN}), the terrestrial biosphere (S_{LAND}), and the atmospheric growth rate (G_{ATM}). However, in practice when adding up the estimated sources and sinks, there is an imbalance (B_{IM}, see equation 1.1) which reflects a mismatch between emissions and the partitioning into G_{ATM}, S_{OCEAN}, S_{LAND}. Each component of equation 1.1 is estimated using different methods, containing uncertainties associated with an incomplete understanding of processes, analytical errors or processes that are not included (Friedlingstein et al., 2022).

$$B_{IM} = E_{FOS} + E_{LUC} - (G_{ATM} + S_{Ocean} + S_{LAND}) \qquad (1.1)$$

One of the processes not included in E_{FOS}, albeit small in magnitude but contributing to G_{ATM} and adding to B_{IM} is the production of atmospheric CO_2 by the oxidation of CH_4 (Friedlingstein et al., 2022). Amongst the several sources of CH_4 the most important contributing to G_{ATM} is fossil fuel emissions of CH_4 and in particular fugitive emissions

of coal, oil and gas (Friedlingstein et al., 2022). Despite the short atmospheric lifetime of CH_4 (approximately 9 years, Prather et al. (2012)) and its relatively small magnitude of anthropogenic emissions (~ 570 $TgCH_4$, 1 Tg is 10^{12}g Saunois et al. (2020)), its global warming potential is 28 times stronger than CO_2 over a 100 year horizon (Myhre et al., 2013). Consequently, the increasing atmospheric CH_4 have contributed with 23% of the additional energy input since 1750 (Etminan et al., 2016) leading to global warming. The natural and anthropogenic sources of methane at the global scale are described in the next Section.

1.1.1 Global sources and sinks of CH_4

The main anthropogenic sources (see Figure 1.2) of CH_4 are fossil fuel production and use, and agricultural activities and waste disposal. Based on top-down estimates reported by Saunois et al. (2020), 'agriculture and waste disposal' is the largest source of CH_4 with an average emission of 217 (207-240, min-max range) $TgCH_4$ year^{-1} over 2008-2017. Fossil fuel production is about half with 111 (81-131) $TgCH_4$ year^{-1}. Natural sources like wetlands amount to 181 (159-200) $TgCH_4$ year^{-1} being the most prominent natural source and larger than fossil fuel. Other natural sources (termites, wild animals, permafrost, inland waters and oceans) are smaller, 37 (21-50) $TgCH_4$ year^{-1}. CH_4 emissions from biomass burning, which is categorized by Saunois et al. (2020) as both an anthropogenic and a natural source, is of the same order of magnitude with 30 (22-36) $TgCH_4$ year^{-1}. In total, methane emissions sum up to 576 (550-594) $TgCH_4$ year^{-1}. Unlike CO_2, methane has a more complex chemistry which represents important atmospheric sinks. The main atmospheric sink of CH_4 is the oxidation by OH, which occurs in the Troposphere (approximately the first 10 km of the atmosphere) and produces CO_2. Over the same decade (2008-2017), the averaged CH_4 removal by such a sink was 518 (474-532) $TgCH_4$ year^{-1}, while consumption in unsaturated soils by methanotrophic bacteria was 38 (27-45) $TgCH_4$ year^{-1} (Saunois et al., 2020).
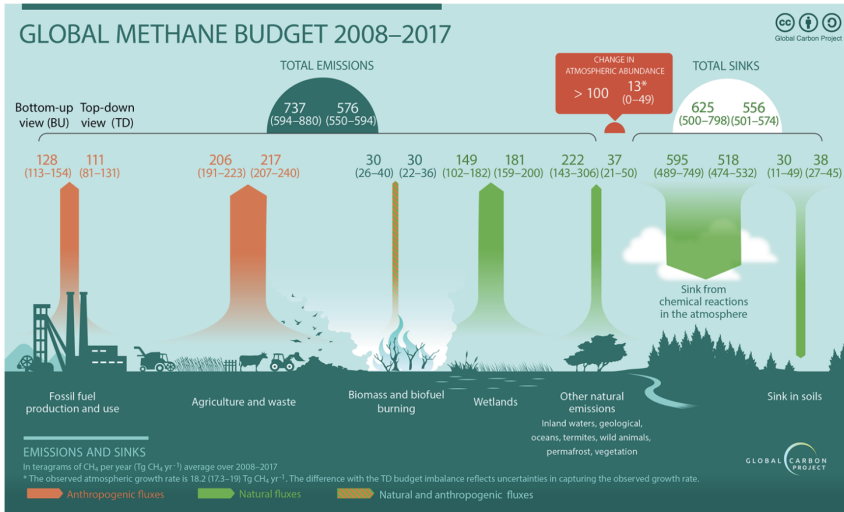
Figure 1.2: Global methane budget for the 2008–2017. Figure taken from Saunois et al. (2020). Even though, both bottom-up (left) and top-down (right) estimates (Tg CH4 year^{-1}) are provided, in the main text we only refer to the top-down estimates.

During 1999 and 2006 the atmospheric growth rate of CH_4 was stable (Dlugokencky E. et al., 2011), followed by a renewed growth, steeper than that of the years before 1999 (Nisbet et al., 2016). These contrasting dynamics have led to large interest in understanding what caused the stagnation and what is causing the actual steep growth. There are several hypotheses (Nisbet et al., 2016; Schaefer et al., 2016; Turner et al., 2017; Rigby et al., 2017; Jackson et al., 2020), from which the contribution from fossil fuels and microbial sources is the more likely explanation (Saunois et al., 2017), yet the debate is still ongoing (Saunois et al., 2020). What remains clear is that to constrain the global CH_4 budget, natural emissions from wetlands need to be better quantified, as this is the single largest source of uncertainty in the global budget (Kirschke et al., 2013; Saunois et al., 2016). It is worth noting that more than 60% of global CH_4 emissions come from tropical regions (Jackson et al., 2020). In South America, wetlands are the dominant source (Jackson et al., 2020) with a large contribution from the Amazon basin (Pangala et al., 2017; Basso et al., 2021). In the next Section, after describing the Amazon carbon cycle, a glimpse into the methane dynamics in the Amazon region is provided.

1.2   The Amazon carbon cycle

The Amazon is a crucial component of the global carbon cycle and the Earth system, storing 150-200 PgC, including carbon in soils and above- and belowground biomass (Saatchi et al., 2007; Malhi et al., 2009; Marques et al., 2017). These stocks result from an active exchange of carbon between the vegetation and the atmosphere. Beer et al. (2010) estimated that the photosynthetic uptake in the Amazon accounts for 16% of the global gross CO_2 uptake by terrestrial vegetation. The net carbon balance in the Amazon will be addressed in Chapter 4, but here we highlight the main processes with some estimates of their flux magnitude (see Figure 1.3) based on the SPA (2021) and references therein.

The net carbon balance of the vegetation in the Amazon results from the uptake of atmospheric CO_2 by vegetation, known as Gross Primary productivity (GPP) and the release of CO_2 due to metabolic and decomposition processes, known as Terrestrial Ecosystem Respiration (TER). The magnitude of GPP is ($\sim$14 PgC year^{-1}), very similar to that of TER with $\sim$13.6 PgC year^{-1}. TER is composed of plant respiration ($\sim$8.5 PgC year^{-1}), decomposition of litter and roots ($\sim$3.8 PgC year^{-1}), and decomposition of dead biomass ($\sim$1.3 PgC year^{-1}). The difference between GPP and what is respired by living plants is the Net Primary Productivity (NPP), which represents the net production of biomass (i.e. woody tissue, leafs, fine roots, flowers and fruits) (Malhi et al., 2015). According to Malhi et al. (2015) part of this biomass serves short-term roles for reproduction or metabolism (e.g. fruits, flower, fine roots), after which they are decomposed releasing CO_2 black to the atmosphere, but the remaining carbon adds up to the woody biomass storage in stems and roots. A fraction of this carbon is released by tree mortality and decomposition over longer timescales. The remaining carbon ($\sim$0.4 PgC year^{-1}) can be interpreted as a carbon sink, representing approximately 13% of the terrestrial carbon sink (3.1 ± 0.6 PgC year^{-1}, see Figure 1.1). Recent evidence (Brienen et al., 2015; Hubau et al., 2020), suggested that over the last three decades the Amazon carbon sink has been decreasing, mainly driven by an increasing tree mortality. The seasonal and inter-annual variability of this sink is largely dependent on plant phenology (Saleska et al., 2003; Albert et al., 2018), climate (Malhi et al., 2015) and geological history (Quesada et al., 2012). In Chapter 4, a detailed analysis on the Amazon carbon sink and our own estimate is provided.

When studying the Amazon region as a whole one needs to take into account other carbon sources that can offset the vegetation sink. These carbon sources are driven by natural or anthropogenic disturbances (Davidson et al., 2012) that can influence the storage and cycling of carbon with long-term effects (Wigneron et al., 2020). Human-driven deforestation is linked to fire-CO_2 emissions (van der Werf et al., 2010), but deforestation can also result in CO_2 emissions from forest degradation (Assis et al., 2020). In addition, forest CO_2 uptake can be reduced by limited water supply during droughts (Phillips et al., 2009;

Gatti et al., 2014; van der Laan-Luijkx et al., 2015; Koren et al., 2018), leading to stomatal closure (Garcia et al., 2021) and/or leaf shedding (Doughty et al., 2015). Climate driven events such as El Niño Southern Oscillation (ENSO) can amplify droughts, causing tree mortality in species not well-adapted to such stress (Esquivel-Muelbert et al., 2020). Further disturbances are associated with the intensification of the hydrological cycle (Gloor et al., 2015), which can be further amplified by climate change (Barichivich et al., 2018; Gouveia et al., 2019) and lead to tree mortality due to flooding (Aleixo et al., 2019). In June 2021 one of the largest flooding events was recorded in Manaus, with water levels above the critical threshold for more than three months (Espinoza et al., 2022). In early studies (Richey et al., 2002, 2009) aquatic CO_2 emissions in the Amazon were seen as a large source of CO_2 to the atmosphere (Richey et al., 2002, 2009). However, recent estimates suggest that when integrated over the entire basin, aquatic habitats are in balance (yet with a large a uncertainty) due to the offset resulting from carbon uptake by aquatic vegetation and algae (SPA, 2021). Therefore, the Amazon carbon cycle is constantly changing and the interaction of human activities, natural forest dynamics, aquatic systems, climate and other species like CH_4, presents a system of high complexity difficult to understand.
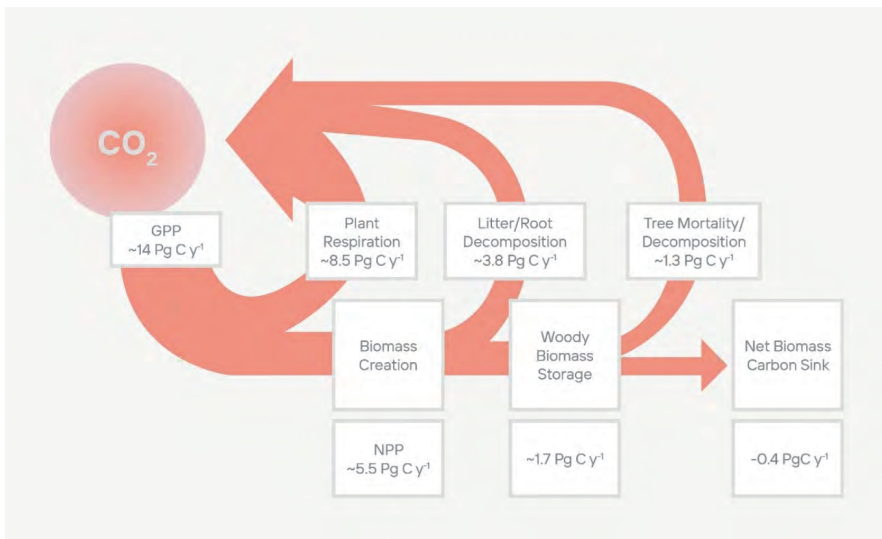
Figure 1.3: Terrestrial carbon cycling in the Amazon. Figure taken from SPA (2021). The data on the Figure was taken from Malhi et al. (2015) and Brienen et al. (2015) and extrapolated to the Amazon.

1.2.1 Methane in the Amazon carbon cycle

Methane research in the Amazon has mainly focused on aquatic emissions, but there are several other sources and sinks that are worth highlighting before describing the aquatic sources. In the upland forest, well-drained soils have been described as a small sink of CH_4 (Davidson & Artaxo, 2004; Dutaur & Verchot, 2007), yet microsites with absence of oxygen can be found in places with poor drainage and particular soil properties, leading to small sources of CH_4 (Verchot et al., 2000).

Upland tree stems and leaf surfaces were suggested as potential sinks (Covey & Megonigal, 2019), yet there are no direct observations of such mechanism. Within the canopy, bromeliads (Martinson et al., 2010) and mounds of soil feeding termites (van Asperen et al., 2021) were found to be large site-specific CH_4 hotspots. The large heterogeneity of the latter sources makes it difficult to upscale them and a potential underestimation of these sources at the ecosystem scale seems likely (SPA, 2021). The contribution from fires to the methane sources in the Amazon varies regionally (Basso et al., 2021), and it represents approximately 16% of the total CH_4 sources (Basso et al., 2021).

Aquatic habitats are the most important source of CH_4 in the Amazon. These habitats are: rivers, lakes, streams, wetlands and flooded forests, hydroelectric reservoirs and other inland waters. The processes (see Figure 1.4) by which methane is emitted in these habitats are: 1. diffusion, 2. ebullition (bubbling) and 3. plant mediated transport (bubbling through plants) (Bridgham et al., 2013; Pangala et al., 2017). It is important to note that CH_4 emitted via these pathways is produced in the wetland soils under anaerobic conditions. In the case of plant mediated transport, this should not be mistaken for emissions of CH_4 produced by plants. Floodplain trees and aquatic vegetation (i.e. macrophytes) mediate CH_4 emission from the soil to the atmosphere via large lenticels and hollow conduits (Pangala et al., 2014). These vegetative adaptations are common in floodplain vegetation as they permit the entrance of oxygen from the atmosphere to the roots.
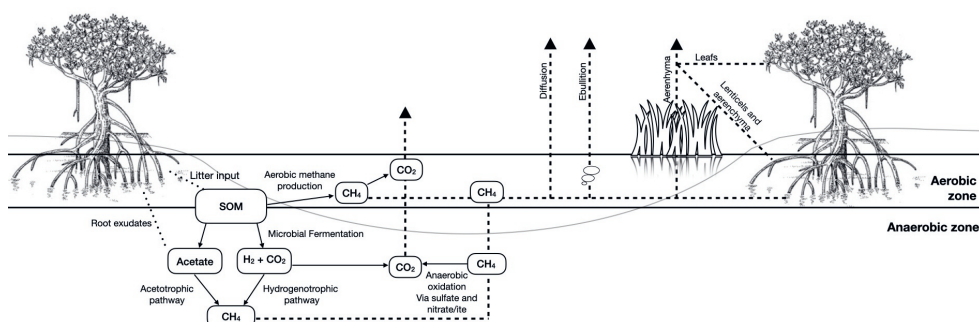
Figure 1.4: Methane production pathways in wetlands. The boxes indicate carbon pools in different chemical forms (e.g. acetate: $C_2H_3O_2$). The dotted lines are carbon inputs from vegetation as either litter or exudates. The solid arrows indicate the transformation of a carbon pool by the process outlined. The dashed lines are gaseous products of the indicated process, mainly as CO_2 and CH_4, which eventually are emitted to the atmosphere. The processes were adapted from Bridgham et al. (2013).

Flooded forest and wetlands are the largest source of CH_4 in the Amazon, thus here an overview of previous studies estimating this source is given. The study of Melack et al. (2004) was one of the first approaches to provide a bottom-up estimate of wetland methane emissions in the Amazon region by combining in-situ flux measurements done in the 1990s (Devol et al., 1990) and remote sensing data on the wetland extend. More recent studies (Melack & Hess, 2010; Hess et al., 2015) provide unprecedented advances in wetland extent, distribution and vegetation mapping in the Amazon region. Melack & Hess (2010) provide the extent and distribution of wetlands in the Amazon, while Hess et al. (2015) generated an inundation extent map combining low water and high water extent at 100 m resolution. The latter was used by Pangala et al. (2017) to upscale fluxes to the entire Amazon lowland (< 500 m) region, resulting in new valuable insights. Pangala et al. (2017) found that plant mediated CH_4 emission by floodplain trees is the dominant pathway for methane production in the Amazon. This finding suggested that previous disagreement between top-down and bottom-up estimates of CH_4 emissions was due to the omission of the tree mediated source in bottom-up estimates. As Pangala et al. (2017) indicate, previous studies (Bartlett et al., 1988; Devol et al., 1990) have focused primarily on macrophyte mediated transport and CH_4 fluxes at water surfaces. Therefore, when upscaling those measured fluxes, tree mediated transport emissions were not included.

Table 1.1: Bottom-up and top-down estimates of annual CH$_4$ emissions for the Amazon. Adapted form Pangala et al. (2017) with some additions:the WETCHIMP results (Melton et al., 2013), the study of Basso et al. (2021) and the synthesis from SPA (2021). Note that the areas for integrating fluxes in models and inversions, and for upscaling fluxes might differ. We therefore, refer the reader to the reference for the exact areas.

Approach	Method/Model	Source estimated	Annual CH$_4$ emissions (TgCH$_4$ year^{-1})	Reference
Top-down	Column technique	all	42.7 ±5.6	Pangala et al. (2017)
Top-down	Inversion	all	40.2 to 52	Bergamaschi et al. (2009)
Top-down	Inversion	all	37 ±5.9	Wilson et al. (2016)
Top-down	Inversion	all	38.2 ± 5.3–45.6 ± 5.2	Wilson et al. (2021)
Top-down	Inversion ensemble	all	47.3–78.2	Saunois et al. (2020)
Top-down	Column technique	all	46.2 ± 10.3	Basso et al. (2021)
	WETCHIMP Models			Melton et al. (2013)
Bottom-up	Bern-LPJ	Wetlands	8.2	Melton et al. (2013)
Bottom-up	DLEM	Wetlands	8.8	Melton et al. (2013)
Bottom-up	SDGVM	Wetlands	59.8	Melton et al. (2013)
Bottom-up	WSL	Wetlands	20.5	Melton et al. (2013)
Bottom-up	ORCHIDEE	Wetlands	59	Melton et al. (2013)
Bottom-up	CLM4Me	Wetlands	55.1	Melton et al. (2013)
	Other models			
Bottom-up	LPX-Bern	Wetlands	44 ± 4.8	Ringeval et al. (2014) Reported by Basso et al. (2021)
Bottom-up	WetCHARTs	Wetlands	39.4 ± 10.3	using Bloom et al. (2017)
Bottom up	DMCM	Wetlands	26.2 ±9.8	Bloom et al. (2012)
Bottom-up	Flux upscale	Wetlands with trees	35.6 ±5.6 to 41.7 ± 5.9	Pangala et al. (2017)
Bottom-up	Flux upscale	Wetlands	29.4	Melack et al. (2004)
Bottom-up	Flux upscale	All aquatic sources with trees and dams	51	SPA (2021)

A summary of the bottom-up and top-down estimates of annual CH$_4$ emissions is given in Table 1.1. Note that the top-down estimates include fire emissions, while bottom-up do no include this source. Thus, the bottom-up estimates like some of the WETCHIMP models with more than 50 TgCH$_4$ year^{-1} are likely overestimating wetland emissions. Top-down methods range from 37 to 78 TgCH$_4$ year^{-1}, for the annual CH$_4$ emissions in the Amazon including all sources (Bergamaschi et al., 2009; Ringeval et al., 2014; Pangala et al., 2017; Basso et al., 2021; Saunois et al., 2020; Basso et al., 2021). The mean of this range is 57.5 TgCH$_4$ year^{-1} for all the sources in the region. A recent estimate by Basso et al. (2021) reported 46 TgCH$_4$ year^{-1} using airborne profiles of CH$_4$ in different locations across the Amazon and including fires. The upscaled estimate of Pangala et al. (2017) ranges from 35 to 41 TgCH$_4$ year^{-1} for only wetlands. While upscaled bottom-up and top-down approaches seem to converge somewhere around 40-50 TgCH$_4$ year^{-1} for wetland emissions, process-based modeling efforts show a large spread in their estimates for the Amazon (Melton et al., 2013). One of the main limitations that models face is the correct mapping of wetland extent and flooding dynamics (Melton et al., 2013). The latter also influences the bottom-up estimates, as fluxes need wetland extent maps to be upscaled. More challenges to upscale CH$_4$ emissions in the Amazon region are discussed in the review by Melack et al. (2022), in which atmospheric observations are highlighted as one of the aspects needed to overcome some of these challenges. The ATTO site plays an important role in this regard, thus in the next Section a we describe the ATTO site.

1.3   The Amazon Tall Tower Observatory (ATTO): a new data stream

The Amazon region has received wide scientific attention in the last decades. In the 1980s, an influential study defined the Amazon rainforest as a system in equilibrium (Salati & Vose, 1984). From that perspective of equilibrium, a decade ago it became clear that rapid changes in the eastern parts of the Amazon were signs of a disturbance-dominated regime in state of transition (Davidson et al., 2012). The transition of a system in equilibrium to what is likely a tipping point (Lovejoy & Nobre, 2018) is at least conceivable for the eastern part of the Amazon, where deforestation and climate change have had a massive impact leading to a net source of carbon in the last decade (Gatti et al., 2021). The purpose of the Amazon Tall Tower Observatory is to provide continuous, long-term measurements to support studies that can document such transition taking place and thus shed light on how the Amazon system is changing. Hence, ATTO's development builds upon three to four decades of large experiments in the Amazon. The Amazon Boundary Layer Experiment (ABLE, Harriss et al. (1988, 1990)), the Anglo-Brazilian Climate Observation Study (ABRACOS, Gash et al. (1996)) and the Large-Scale Biosphere-Atmosphere Experiment in Amazonia (LBA, Keller et al. (2004b); de Gonçalves et al. (2013)). Different from the eddy-flux-oriented perspective of LBA, the ATTO project has additionally a strong focus on high-precision atmospheric measurements. The general overview of the ATTO research plan and pilot measurements is given by Andreae et al. (2015), where the specific research objective associated with greenhouse gases is stated as:

1. to obtain regionally representative measurements of carbon gas concentrations (CO_2, CH_4, CO, and VOC), in order to improve our understanding of the carbon budget of the Amazonian rain forest under changing climate, land use, and other anthropogenic influences in the fetch region of ATTO.

Profile measurements within the boundary layer from a tall tower permits studying local and regional processes (Bakwin et al., 1998; Andrews et al., 2014) depending on the height of the measurement inlet. Furthermore, at the upper levels the concentration footprint can reach scales close to 1000 km (Gloor et al., 2001). Because of these advantages and the sparseness of data, Gloor et al. (2000) highlighted the need for tall tower measurements in particular for South America, Africa and Eurasia. Years later the Zotino Tall Tower Observatory (ZOTTO) was built in Siberia as part of a Russian-German collaboration and measurements started in 2006. During that time, the idea of a tall tower in the Amazon was conceived and in 2008 the project began as a Brazilian-German partnership which led to the first measurements in 2012. The conditions for site selection according to Andreae et al. (2015) were: (1) large fetch with minimal current human perturbation, but with potential future land use change at a large scale, (2) relatively flat topography

with no large wetlands in the fetch region, (3) stable and protected land ownership and controlled access, and (4) the possibility to reach the site in a reasonable time to facilitate research and educational activities. The site is located in the central part of the Amazon, almost 200 km northeast of Manaus and can be accessed in about five hours from the city. The site is -to our knowledge- the only continuous profile measurement system in the region, which complements airborne profiles (twice per month) and weekly flasks that are collected at continental and marine sites (Figure 1.5).
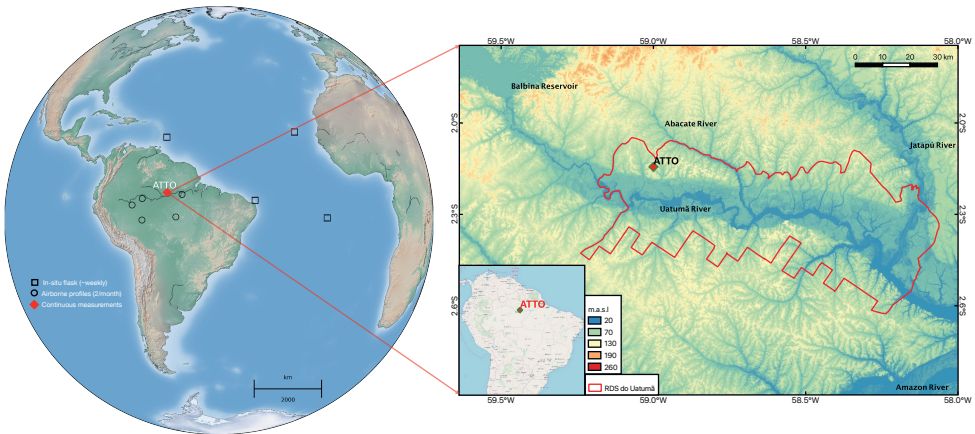
Figure 1.5: Left panel: ATTO Location with respect to other measurement sites in the continent and in remote sites outside South America. Right panel: The surroundings of the ATTO site located within the 'Reserva de Desenvolvimento Sustentável do Uatumã'.

The greenhouse gas (GHG) profile system is an adaptation from that designed for ZOTTO (Winderlich et al., 2010). It was installed in 2012 on an initial 80-m tower consisting of five inlet heights at 79, 53, 38, 24, and 4 m above ground. The canopy height is close to 35 m, so there are two inlets within the canopy, two above it and one in the transition canopy-atmosphere. From 2012 to 2021 two cavity ring-down-based analyzers (Picarro Inc.), a G1301 and a G1302 measuring CH_4 / CO_2 and CO_2 / CO were used. For more on precision and technical aspects of this first generation of ATTO measurements, we refer the reader to Chapter 2 and 3. In May 2021 both analyzers broke and were replaced in March 2022 by the other two cavity ring-down-based analyzers (Picarro Inc.), models G2401 (CO_2, CH_4 and CO) and G2201-i (^{13}C-CO_2/CH_4 and CO_2 and CH_4), installed at the same heights. Additional greenhouse gas measurements were recently installed (February/March 2022) at the Tall Tower (325 m) using two different systems. A Fourier Transform Infrared (FTIR) sprectrometer (Spectronous, Ecotech) (Griffith et al., 2012)

was installed, sampling air from 6 heights (2, 42, 81, 150, 271 and 321 m) and measuring atmospheric mole fractions of CO_2, CH_4, CO, N_2O and $\delta^{13}CO_2$. In September 2021 a weekly 3L flask sampler was installed following the design of the ICOS flask sampler system in Europe (Levin et al., 2020). All these provide a comprehensive suite of GHG measurements with great potential to study processes at different temporal and spatial scales. To give the reader an impression of the ATTO site, some photos were gathered to show the Tall Tower from different perspectives (Figure 1.6A,B,C,D), the canopy seen from above (Figure 1.6E), fog formation in the lower levels close to the canopy (Figure 1.6F), how the inlet lines are set up from the filter to the analyzer inside the container at the surface (Figure 1.6G,H,I,J,K), and an impression of the scale of the vegetation in the surroundings (Figure 1.6L).
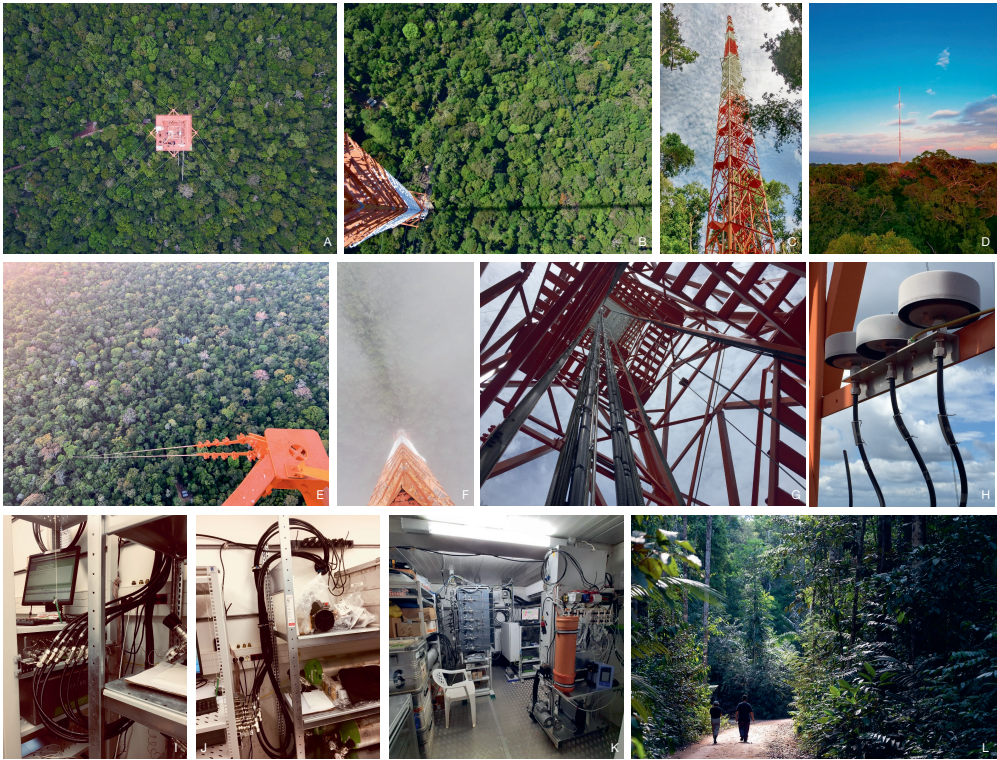
Figure 1.6: Photos from the ATTO site. The photos A, C, D, F, L were taken from https://www.attoproject.org/media/gallery/, photos B, E, G, H, I, J were taken by Santiago Botía and photo K by Hella van Asperen.

1.4 Conceptual framework and research objectives

The ATTO site was built with the general objective of better understanding the complexity of the Amazon system as described in the previous sections. At the beginning of this PhD project in January 2018, the ATTO site had already been running continuously since 2013. With five years worth of data and building upon the first reports from Andreae et al. (2015), the objectives of this project were primarily centered on studying and interpreting the first years of data for both CO_2 and CH_4. Following this line of research, the project set to answer the following overarching question which encompasses and orients the specific research objectives:

To what extent the long-term and continuous ATTO record serves to understand local and regional processes leading to sources and sinks of CO_2 and CH_4?

To address this question it was needed to explore different spatial and temporal scales that influenced the observational record. These scales and their connection to each one of the core chapters of this thesis are shown on Figure 1.7. We went from a local scale studying nighttime methane signals to CO_2 flux estimation at continental scale. In the first local study, we used an observational approach to investigate seasonal and diurnal patterns of CH_4. In the second one, the focus shifted to the use of models to simulate atmospheric transport of CO_2 at seasonal and inter-annual scales with a regional view. Finally, CO_2 flux estimation at continental scale was attempted, by integrating the ATTO time series with a regional network of aircraft CO_2 profiles and a bayesian inversion system. The conceptual and theoretical details of each chapter are provided next.

1.4.1 Local CH_4 signals and nighttime transport (Chapter 2)

From the overview given by Andreae et al. (2015) an interesting nighttime signal at the top of the 80-m tower was evident in the mean diurnal cycle. However, it was unknown what where the atmospheric characteristics of this signal, where it was coming from and what were the potential sources. Therefore, the first question addressed was:

What is the nocturnal source of methane and what are the atmospheric transport mechanisms responsible for it at the Amazon Tall Tower Observatory?

In Chapter 2, this question is addressed and in doing so the complex mechanisms by which gases are transported in the atmosphere had to be studied. Here a brief introduction of the main concepts is given. The planetary boundary layer (PBL) is the lowest portion of the atmosphere where trace gases (e.g. CO_2 and CH_4), momentum and energy are exchanged between the surface and the air above it (Stull, 1988; Fisch et al., 2004).
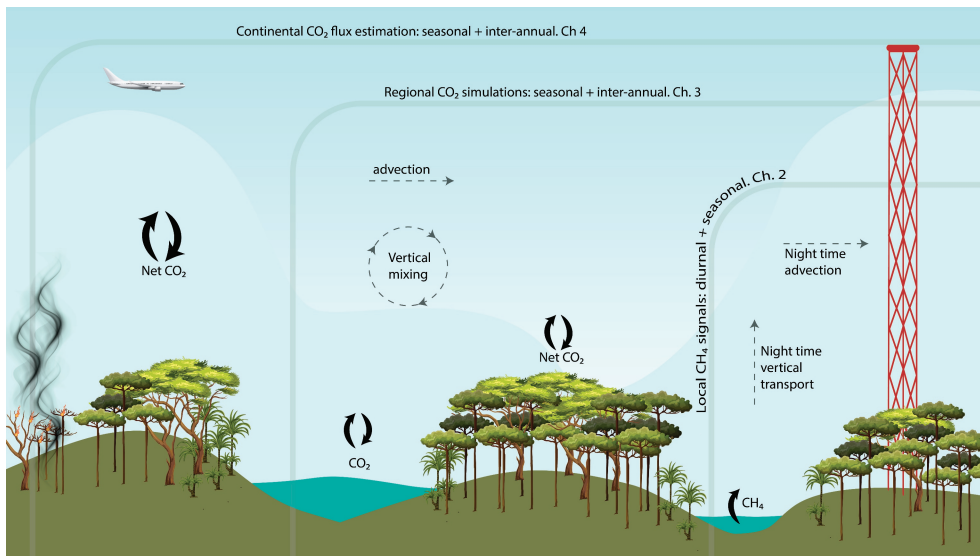
Figure 1.7: Graphical representation of the topics addressed in each core chapter of this thesis. Each chapter tackles different spatial and temporal scales. Illustration made by María Camila Botía.

This exchange flux is subjected to atmospheric transport in the PBL, hence understanding and being able to simulate transport within the PBL is crucial to interpreting measurements taken at the ATTO site. Transport in the PBL of the Amazon can be separated into daytime and nighttime regimes, due to a strong diurnal cycle associated with heating and cooling of the surface (Stull, 1988) or the canopy, in the case of ATTO. During daytime, buoyancy generated turbulence is the main driving motion in the PBL, related to unstable conditions and causing convective transport (Fisch et al., 2004). During the first hours of the day, entrainment at the top of the PBL brings air with low-CO_2 mole fractions which is comparable to the surface uptake by vegetation. As the day progresses, scalars are well-mixed vertically and the height of the PBL reaches it maximum (Stull, 1988; Fisch et al., 2004; Carneiro, 2018) and the air within the canopy and above it are strongly coupled (Andreae et al., 2015). In contrast, during the nighttime in the absence of heat input stable conditions result in less turbulence activity, with a decoupling (in some cases) of the canopy and the air above it (Andreae et al., 2015) and the lowest PBL height (Stull, 1988).

In the Amazon and in particular for ATTO, in the absence of strong vertical motions during the night, scalar fluxes converge into shallow layers and can accumulate considerably in short time periods (Andreae et al., 2015). In such conditions alternative physical processes, such as drainage flow (Araújo et al., 2008), intermittent turbulence (Mahrt, 1999), and gravity waves (Zeri & Sá, 2011; Andreae et al., 2015) amongst others (Steen-

eveld et al., 2008) are responsible for horizontal and vertical transport inside the canopy and above it. Drainage flow has been characterized in the Amazon to explain nighttime advection of CO_2 following a height gradient from plateaus to valleys (Araújo et al., 2008), which translates into a "loss" of mass during the stable nights that makes eddy covariance measurements challenging. Intermittent turbulence events at the canopy level were linked to wind shear above the canopy and observed during decoupled nights (Andreae et al., 2015). Such intermittent events break down nocturnal stability and connect the canopy with the PBL, permitting vertical transport of CO_2 and other scalars to layers aloft (Andreae et al., 2015). However, Andreae et al. (2015) state that it is not clear what triggers such intermittent events. In Chapter 2, we study the influence of these nighttime transport mechanisms on the nighttime CH_4 signals at ATTO.

1.4.2   Seasonal and inter-annual CO_2 patterns (Chapter 3)

The next step in the project was to study the CO_2 signals with a regional perspective using an atmospheric transport model. Motivated by the study of Restrepo-Coupe et al. (2017), where they showed that dynamic global vegetation models did not simulate correctly the seasonality of GPP in the Amazon region. GPP is a component of the net ecosystem exchange (NEE = Respiration - GPP), so we designed the following study. Several estimates of NEE were used, together with a Lagrangian atmospheric transport model and evaluated at ATTO using the CO_2 measurements. With this, we could study how well the NEE estimates could reproduce CO_2 after transported into the atmosphere and thus answer the following question:

What are the main drivers of seasonal and inter-annual variability for CO_2 at ATTO?

Atmospheric transport models (ATM) help to understand the influence of surface fluxes upwind of the measurement site. In Chapter 3, we use a Lagrangian ATM and here provide the conceptual basis of how the model is formulated and the main governing equations. In general the ATMs can adopt two formulations: Lagrangian and Eulerian models. In the Lagrangian formulation of ATM the motion of the air parcels is resolved along a trajectory. Eulerian models resolve the mass and momentum equations as a function of space and time, which can be more computationally expensive, yet provides a solution for a 3-dimensional grid. As Lin et al. (2003) pointed out, both formulations face two main challenges to simulate concentrations in the PBL: 1. resolving the "near-field" variability in observed concentrations that are linked to heterogeneity of the surface fluxes and 2. poor representation of mixing and advection within PBL. The term near-field in this context can be described as the surface that had contact with the air transported to the measurement location before a specific time point (Lin et al., 2003). The advantages of using Lagrangian particle dispersion models to overcome these challenges are the following based on Lin et al. (2003):

   1. The distribution of particle locations are not restricted to grid cells, which enables

capturing fine structures resulting from heterogeneity in surface fluxes.

2. Advection and dispersion in the PBL are simulated by explicitly using turbulent velocity statistics in the trajectories of the particles (Stohl, 1998), different from assuming conserved air parcels like the traditional mean wind trajectory models (Stohl & Wotawa, 1995).

A "particle" can be interpreted as the representation of a gas or air parcel that is transported by the wind. In Chapter 3, we used the Stochastic Time Inverted Lagrangian Transport (STILT) model Lin et al. (2003). It simulates the transport in the near-field by releasing an ensemble of particles (generally 100) and following their time-evolution in space, backward in time. The STILT model was based on the source code of the Hybrid Single-Particle Lagrangian Integrated Trajectory (HYSPLIT) (Draxler & Hess, 1998), using a different turbulent module but the same mean advection scheme. The main feature developed in STILT is the direct connection between surface fluxes and concentration changes at a measurement site or receptor, this is known as surface influence or footprint. The receptor can be a fixed tower, satellite columns or sequenced (vertically or horizontally distributed) airborne measurements. The following provides a brief mathematical description of the STILT model based on Lin et al. (2003).

The influence function $I(\boldsymbol{x}_r, t_r | \boldsymbol{x}, t)$ calculates the fraction of a particle at location (x_r) and time (t_r), given that it was previously at x and t. In other words, this function connects spatially and temporally resolved surface sources and sinks for a number of particles (N_{tot}), released from a specific location $\boldsymbol{x}_r$ and time t_r, with density of $\rho(\boldsymbol{x}_r, t_r | \boldsymbol{x}, t)$ at $(\boldsymbol{x}, t)$, and is given by:

$$I(\boldsymbol{x}_r, t_r | \boldsymbol{x}, t) = \frac{\rho(\boldsymbol{x}_r, t_r | \boldsymbol{x}, t)}{N_{tot}} \tag{1.2}$$

Here $I(\boldsymbol{x}_r, t_r | \boldsymbol{x}, t)$ has units of (1 volume^{-1}) and $\boldsymbol{x}$ is a vector containing the location of the particle ensemble or receptor locations. Now, by diluting the surface fluxes $F(x, y, t)$ (units of moles time^{-1}) into a column of air with height h in which turbulent mixing is assumed to be strong enough to mix the surface fluxes, we can establish a connection to a volume source/sink $S(x, t)$ with (units of mixing ratio time^{-1}). The condition is then:

$$S(\boldsymbol{x}, t) = \begin{cases} \frac{F(x,y,t) m_{air}}{h \bar{\rho}(x,y,t)}, & \text{for } z \leq h \\ 0, & \text{for } z > h \end{cases} \tag{1.3}$$

In STILT h is taken as half of the mixing height, $\bar{\rho}$ denotes the average density below h and m_{air} is the molar mass of air. The mole fraction changes (in ppm) at the receptor $\Delta C_{m,i,j}(\boldsymbol{x}_r, t_r)$ takes the following form:

$$\Delta C_{m,i,j}(\boldsymbol{x}_r, t_r) = f(\boldsymbol{x}_r, t_r | x_j, y_j, t_m) F(x_i, y_j, t_m) \tag{1.4}$$

Where the footprint elements $f(\boldsymbol{x}_r, t_r | x_j, y_j, t_m)$ link the discretized surface fluxes $F(x_i, y_j, t_m)$ at location (x_i, y_j) and time (t_m) to $\Delta C_{m,i,j}(\boldsymbol{x}_r, t_r)$. The surface fluxes are in units of $\mu mol\ m^{-2}s^{-1}$ and $f(\boldsymbol{x}_r, t_r | x_j, y_j, t_m)$ in (ppm per $\mu mol\ m^{-2}s-1$). Equation 1.5 describes the integrated footprint $f(\boldsymbol{x}_r, t_r | x_j, y_j, t_m)$ derived from particle locations, which quantifies the total amount of time each particle (p) remains in the volume element i, j, k.:

$$f(\boldsymbol{x}_r, t_r | x_j, y_j, t_m) = \frac{m_{air}}{h \times \bar{\rho}(x_i, y_j, t_m)} \frac{1}{N_{tot}} \sum_{p=1}^{N_{tot}} \Delta t_{p,i,j,k} \tag{1.5}$$

1.4.3   Net CO$_2$ flux estimates using the ATTO CO$_2$ record (Chapter 4)

After analyzing the main drivers of seasonal and inter-annual variability of CO$_2$ at ATTO, the follow up study was aimed at estimating surface fluxes of CO$_2$ using a regional atmospheric inversion system. As part of the data constraint we not only used the ATTO CO$_2$ time series, but also a network of aircraft measurements providing vertical profiles of CO$_2$ mole fractions at five different locations in the Amazon region. With this set up, in Chapter 4 we addressed the following questions:

What is the added value of the ATTO site for flux estimation using inverse modeling?

What is magnitude of the Amazon carbon sink as inferred from inverse modeling?

A brief perspective on inverse modeling is given here, but we refer the reader to Chapter 4 and the references cited here for more information. The technique to solve inverse problems reverses the normal direction of causality (Enting, 2002), explaining the use of the term "inversion". A common application in atmospheric sciences is the retrieval of surface fluxes by using atmospheric observations. Commonly known as a top-down approach, atmospheric inversions have been widely applied using CO$_2$ observations to retrieve net carbon fluxes globally (Gurney et al., 2002; Rödenbeck et al., 2003; Michalak, 2004; Peylin et al., 2013; van der Laan-Luijkx et al., 2017) and/or regionally (Gerbig et al., 2003; Peters et al., 2007; Schuh et al., 2010; Kountouris et al., 2018a; Koren, 2020). This method requires well-calibrated measurements and depends to a large extent in the spatial density and representativeness of the observational network (Gerbig et al., 2009). Given the spatio-temporal variability of the observations, the atmospheric inversion can estimate probable surface flux patterns in both space and time. In the linear Bayesian inverse estimation, prior information of the target variable is often associated with the vegetation net carbon flux. The mathematical expression of the problem is defined by the cost function $J(x)$ in equation 1.6.

$$J(x) = (y - Hx)^T \boldsymbol{Q}_m^{-1}(y - Hx) + (x - x_p)^T \boldsymbol{Q}_p^{-1}(x - x_p) \qquad (1.6)$$

Where, x_p contains the prior fluxes, y the observations, Hx represents the simulated CO_2 mole fractions, which uses the observation operator H, and x is the state vector containing the unknowns of the target variable, which will be adjusted by minimizing $J(x)$. The observation operator (H) can be interpreted as the connection between surface fluxes and observed mole fractions. In the atmospheric inversion context, atmospheric transport models are used as observation operator. In the particular case of Chapter 4, we use the transport model STILT (Lin et al., 2003) as observation operator for a regional inversion. The matrices Q_m and Q_p contain the error covariances for the observations (model-data mismatch) and for prior fluxes, respectively. The underlying mathematical concept for the CarboScope global system has been extensively described in Rödenbeck et al. (2003), and the iterative algorithm to find the cost function minimum is explained in Rödenbeck (2005). The development of the CarboScope regional inversion system is described in Rödenbeck et al. (2009) and Trusilova et al. (2010), and recent applications were carried out by Kountouris et al. (2018b), Kountouris et al. (2018a) and Munassar et al. (2021). Note that this work represents -to date- the first regional application of the Carboscope regional system for flux retrievals using CO_2 observations in South America.

1.5 Thesis outline

Each core chapter of this thesis contains introduction, methods, results, discussion and conclusion sections. In Chapter 2, we look into a nighttime CH_4 enhancement at the uppermost inlet (80 m) of particular interest, due to its unexpected nature: very large (50 ppb) enhancements during several hours in the night and sometimes with no connection with the canopy surface. To investigate this phenomenon an extensive observational analysis is performed describing the atmospheric characteristics in which the CH_4 enhancements occur, suggesting potential sources and discarding the potential influence of a CH_4-fire signal.

In Chapter 3 the CO_2 record is investigated. In this chapter there is a strong focus on seasonal and inter-annual scales. We also assess the contribution of different spatial scales to the measured CO_2. The spatial scales range from local (eddy covariance scale), mesoscale (~ 100 km) to synoptic scale (~ 1000 km). For this we subtract the background CO_2 mole fraction from our measurements and compare that regional signal with local eddy covariance and environmental variables. Furthermore, to provide a larger spatial scale perspective we couple a STILT with different flux components that contribute to the integrated CO_2 signal in the atmosphere. A broad selection of net CO_2 vegetation fluxes amongst other components like fires, rivers and fossil fuels are used. Particular emphasis is put on the riverine component, which emerged as an important signal to

better interpret the measurements at ATTO.

In Chapter 4 we use the CO_2 record at ATTO and additional CO_2 mole fraction datasets in the region, to estimate surface fluxes using atmospheric inverse modeling. We use the CarboScope Regional (CSR) inversion system (Rödenbeck et al., 2009) to obtain net biome exchange (NBE) for tropical South America and the Amazon region. In the Chapter more detailed information on the inversion system and the particular set-up is provided. Of particular importance is the information added by the ATTO measurements, but we also discuss the main limitations of the observational constraint for specific regions within the domain analyzed. Spatial and temporal patterns over 9 years are analyzed and emerging spatial gradients are described. Furthermore, we provide estimates with associated uncertainty on the Amazon carbon sink and place those results in context.

Finally, in Chapter 5 we reflect on the main insights of this work. The topics discussed connect all the core chapters of the thesis. The relevance of atmospheric transport to interpret measurements, the main seasonal drivers of GHG variability, and the importance of other biomes, different from the Amazon, for the regional carbon budget are the topics addressed. With this some of the remaining challenges and conclusions are given. In the Outlook, we provide ideas for future lines of research arising from the insights of the present work.

Chapter 2

Understanding nighttime methane signals at ATTO

Abstract

Methane (CH_4) atmospheric mixing ratio measurements are analyzed for the period between June 2013 and November 2018 at the Amazon Tall Tower Observatory (ATTO). We describe the seasonal and diurnal patterns of nighttime events in which CH_4 mixing ratios at the uppermost (79 m a.g.l) inlet are significantly higher than the lowermost inlet (4 m a.g.l) by 8 ppb or more. These nighttime events were found to be associated with a wind direction originating from the southeast and wind speeds between 2 and 5 m s^{-1}. We found that these events happen under specific nighttime atmospheric conditions when compared to other nights, exhibiting less variable sensible heat flux, low net radiation and a strong thermal stratification above the canopy were found. Our analysis indicates that even at wind speeds of 5.8 m s^{-1} the turbulence intensity, given by the standard deviation of the vertical velocity, is suppressed to values lower than 0.3 m s^{-1}. Given these findings, we suggest that these nighttime CH_4 enhancements are advected from their source location by horizontal non-turbulent motions. The most likely source location is the Uatumã River, possibly influenced by dead stands of flooded forest trees that may be enhancing CH_4 emissions from those areas. Finally, biomass burning and the Amazon River were discarded as potential CH_4 sources.

2.1   Introduction

In the last decades atmospheric CH_4 has followed contrasting trends. Following decades of growth, during the period between 1999 to 2006, atmospheric CH_4 mixing ratios were stable (Dlugokencky E. et al., 2011), whereas during the last decade a steep growth has been reported (Nisbet et al., 2016). Currently the reasons for these trends are not clear and several explanations have been proposed (Nisbet et al., 2016; Schaefer et al., 2016; Turner et al., 2017; Rigby et al., 2017; Howarth, 2019). What is evident in the current debate is that CH_4 emissions from tropical wetlands are the single largest source of uncertainty to the global CH_4 budget (Kirschke et al., 2013; Saunois et al., 2016). Recent estimates suggest that Amazon CH_4 emissions could contribute about a third of the global wetland CH_4 emissions (Pangala et al., 2017). Therefore, better knowledge of the seasonal and diurnal dynamics of these emissions will provide valuable insights for developing process-based models that more accurately represent CH_4 emission and uptake (Turner et al., 2019). Our long term measurements of CH_4 mixing ratios at the Amazon Tall Tower Observatory (ATTO) provide an opportunity for better understanding such seasonal and diurnal dynamics, which are necessarily linked to atmospheric transport (Gloor et al., 2001).

CH_4 is transported from surface sources, which in the Amazon are dominated by wetland ecosystems (Saunois et al., 2016; Wilson et al., 2016), to the upper levels of the troposphere. Therefore, the vertical profile of CH_4 mixing ratios in the troposphere generally decreases with height, showing higher mixing ratios in the boundary layer (Miller et al., 2007; Beck et al., 2012; Webb et al., 2016). The profiles discussed in previous studies have been based on airborne measurements taken at daytime under well-mixed conditions during specific campaigns (e.g., Beck et al., 2012) or during regular sampling programs with aircraft flights at least twice per month (e.g., Gatti et al., 2014; Webb et al., 2016). These studies provide valuable insights about regional atmospheric transport (Miller et al., 2007), spatial distribution of dominant CH_4 sources (Wilson et al., 2016) and the seasonal cycle across the Amazon region (Webb et al., 2016).

Closer to the surface, the proximity to the canopy and to the CH_4 sources becomes more important, dominating the variability of CH_4 mixing ratios at diurnal time scales. This strong variability is driven by a heterogeneous spatial distribution of sources (Gloor et al., 2001) and the complexity of atmospheric transport mechanisms in the first meters of the boundary layer (Stull, 1988). Despite these complexities, mixing ratio measurements close to the surface are the most feasible way to perform long-term measurements at high temporal resolution that can provide insights at diurnal and seasonal time scales. However, such type of measurements are sparse in this region, particularly for CH_4.

There are two studies that provide an idea of the diurnal variability of CH_4 mixing ratios in the Amazon region (Carmo et al., 2006; Querino et al., 2011). Both of these studies were conducted in upland forest sites, similar to the present study. Carmo et al. (2006) performed CH_4 mixing ratios measurements during the dry and wet season at three different sites in the Amazon. At all sites they focused their profile measurements on the canopy layer, which included one sampling inlet not more than 10 m above the canopy top. This study found that mixing ratios were generally higher at nighttime than during the day at all sites. As Carmo et al. (2006) focused on identifying local sources and calculating a local budget, the authors do not specify the amplitude of the diurnal cycle for the dry and wet seasons. Querino et al. (2011) provide one of the few records showing the diurnal variability of CH_4 above the canopy (53 m), as well as mixing ratio profiles within the canopy. CH_4 mixing ratios above the forest were higher during the night than during the day. The amplitude of the diurnal cycle was particularly large in July ($>$ 30 ppb), whereas in November there was no diurnal variability (Querino et al., 2011). Vertical CH_4 mixing ratios inside the canopy were found to decrease with height, during both day and night, but more strongly during nighttime measurements, agreeing with Carmo et al. (2006). Both Querino et al. (2011) and Carmo et al. (2006) attributed this feature to a source located in the soil, and they both concluded that the upland forest is a source of CH_4. The observed high nighttime CH_4 mixing ratios were explained by referring to a shallower nocturnal boundary layer that led to accumulation of CH_4 above the canopy (at 53 m) in Querino et al. (2011) and throughout the canopy layer in Carmo et al. (2006).

In the present study we describe similar nighttime CH_4 mixing ratio patterns using the unprecedented long-term measurements at ATTO. This unique data set allows us to better describe the seasonal and diurnal variability of nighttime CH_4 signals at the 80 m tower. Furthermore, we provide a detailed analysis of the dominant atmospheric conditions under which high CH_4 mixing ratios are measured during the night at the top of the tower. Finally, we suggest possible sources of this nighttime CH_4 together with a description of the transport mechanisms that could be responsible for the vertical and horizontal transport of CH_4 in the nocturnal boundary layer.

2.2   Data and Methods

2.2.1   Site description

The Amazon Tall Tower Observatory (ATTO) research station was described in detail by
Andreae et al. (2015), here we will only highlight aspects relevant to the current study.
The ATTO site is located in the Uatumã Sustainable Development Reserve (USDR),
which is ∼150 km northeast of the city of Manaus, in Central Amazonia. The site was
built on a plateau (130 m-a.s.l) surrounded by a large drainage network composed of
depressions or valleys at lower elevation, which together with the plateaus form a small-
scale heterogeneous topography with maximum height gradients of about 100 m (see
Figure 2.1).
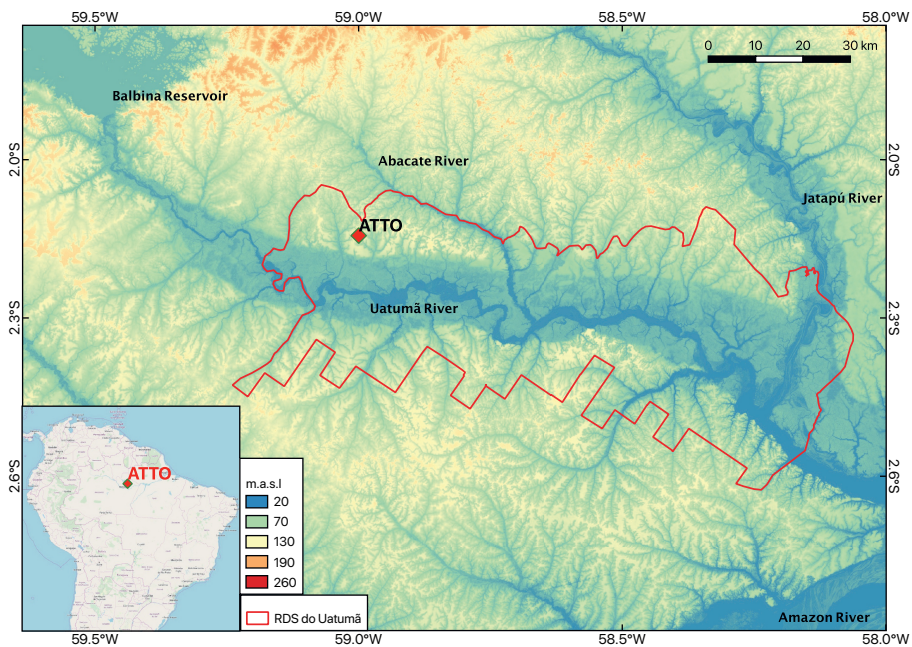
Figure 2.1: Location of ATTO relative to the continent. The topography, in the background,
is based on the elevation model from the Shuttle Radar Topography Mission (NASA-JPL,
2013). The boundaries of the Uatumã Sustainable Development Reserve (USDR) are high-
lighted in the red polygon and the major rivers are labeled. Background layer of the inset
map: ©OpenStreetMap contributors 2020. Distributed under a Creative Commons BY-SA
License

The site is located in the interfluve between the Uatumã River and its tributary, the Abacate River. Both of these rivers flow in a NW to SE direction, merging their waters further southeast of the site. The flow of the Uatumã River is controlled by the Balbina reservoir, a hydroelectric dam located 55-60 km to the northwest of ATTO. The natural flood pulse of the Uatumã River was disturbed by the Balbina reservoir, causing large tree mortality along the riverside (Assahira et al., 2017; Resende et al., 2019). It is worth noting that the Abacate River has not suffered hydrological disturbances, still presenting a natural flooding seasonality.

The vegetation of the USDR is composed of different ecosystems. Upland dense forest (*terra firme*) is the characteristic vegetation on the plateaus and slopes, with the highest canopy when compared to the surrounding valleys (Andreae et al., 2015). The canopy height at ATTO is around 37 m, but the mean canopy height over the plateau is 20.7 ± 0.4 m (Andreae et al., 2015). In between the permanent flowing river channels and the *terra firme* forest, a savanna-type ecosystem on white-sand soil (*campina*) and forest on white-sand soil (*campinarana*) are found. In the *campina* there are smaller shrubs and trees with a vegetation height of 13.1 ± 2 m. The *campinarana* has a canopy with emergent trees up until 17 m (Klein & Piedade, 2019). Along the Uatumã and the Abacate rivers, seasonally flooded black-water forest (*igapó*) is the dominant type of vegetation (Andreae et al., 2015).

The regional atmospheric circulation has a seasonal pattern driven by the annual north-south shift of the Inter-tropical Convergence Zone (ITCZ) over the Atlantic Ocean (Andreae et al., 2012, 2015; Pöhlker et al., 2019). During the dry season, which we define here from July to October, ATTO is located south of the ITCZ. During the wet season, defined here from February to May, ATTO is located north of the ITCZ. This seasonal shift influences the origin of the air masses entering the continent and arriving at ATTO. During the dry season the prevailing wind direction is from the east, whereas the wind direction during the wet season is predominantly from the northeast (Andreae et al., 2015). Easterly winds during the dry season transport air masses containing signals from biomass burning, occurring mainly in the eastern part of the arc of deforestation in Brazil. The northeasterly winds during the wet season are transported over a large fetch of continuous rainforest, yet containing high background mixing ratios of greenhouse gases due to the influence of the northern hemisphere (Andreae et al., 2012, 2015). The dry and wet seasons were defined using precipitation data collected at the site with 30-minute resolution covering a period from January 2013 to December 2018. The highest precipitation values are recorded from February to May, with a maximum of 300 mm month^{-1} during March, while the lowest values, at below 100 mm month^{-1}, are found for the months between July and October (Figure 2.2).
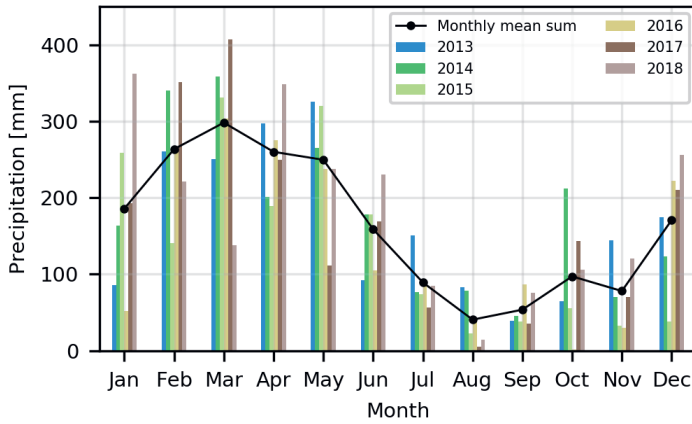
Figure 2.2: Monthly sums of precipitation for the period between 2013-2018 at ATTO.

2.2.2 CH_4 mixing ratio sampling system

Our continuous measurements system was installed in March 2012 in the 80-m-tall tower. This tower was built during the pilot phase of an ongoing measurement program. There are five air inlets located at 79, 53, 38, 24 and 4 m above ground. At these heights, we measure atmospheric mixing ratios of CH_4, carbon dioxide (CO_2) and carbon monoxide (CO) using two Picarro Analyzers, the G1301 for CH_4 and CO_2 and the G1302 for CO_2 and CO. The G1301 analyzer (Serial CFADS-109) provides data with a standard deviation of the raw data below 0.05 ppm for CO_2 and 0.5 ppb for CH_4. For the G1302 (Serial CKADS-018), the standard deviation of the raw data is 0.04 ppm for CO_2 and 7 ppb for CO. For more details on precision and long-term drift see Andreae et al. (2015). Similar to Winderlich et al. (2010), downstream of each sampling line 8 l stainless steel spheres act as buffer volumes. This buffer system provides ideal air mixing characteristics to have continuous near-concurrent measurements at all heights (Winderlich et al., 2010). In Winderlich et al. (2010) the buffers integrate the air signal from every inlet with an e-folding time of approximately 37 min, with a flow of 150 standard cubic centimeter per minute (sccm), at 700 mbar. As we have two analyzers our time resolution is higher with an e-folding time of approximately 18 min (8 l/(150x2) sccm at 700 mbar). Therefore, we assume that the 15 min averages used in Section. 2.3.3.iii correspond to independent samples. The standard data available at *http://attodata.org* are at 30-minute resolution.

2.2.3   Meteorological instrumentation

For this study we use wind direction, wind speed, air temperature, net radiation, precipitation and soil moisture. Sonic anemometers are fixed at 14, 22, 41, 55 and 81 m (above ground level; a.g.l.), but in this study we mainly use wind speed and direction at 81 m (Windmaster, Gill Instruments Limited). In Section 2.3.1 we show wind speed profiles for specific nights, using additional data from the sonic anemometers (model CSAT3, Campbell Scientific, Inc.) at 14, 41 and 55 m which perform fast response wind (u, v, and w) measurements. At 81 m molar densities of CO_2 and H_2O are measured with an IRGA (LI-7500A, LI-COR Inc., USA). Air temperature is measured at 10 heights: 81, 73, 55, 40, 36, 26, 12, 4, 1.5 and 0.4 m (a.g.l) with a Termohygrometer (C215, Rotronic Measurement Solutions, UK.). Net radiation is measured with a Net radiometer (NR-Lite2, Kipp and Zonen, Netherlands) at 75 m (a.g.l). For precipitation data, a rain gauge (TB4, Hydrological Services Pty. Ltd., Australia) is installed at 81 m, and for soil moisture a water content reflectometer (CS615, Campbell Scientific Inc., USA) provides data for the depths: 0.1, 0.2, 0.3 0.4, 0.6 and 1 m.

2.2.4   Time period of data used

In the present study we have used CH_4 mixing ratio and meteorological data at different time resolutions. When mentioning meteorological data, we refer to the variables described in 2.2.3. To provide more clarity we specify what type of data were used in each section. In Section 2.3.2, 2.3.3.i and 2.3.3.ii we used CH_4 mixing ratios and meteorological variables at 30-minute resolution. The CH_4 mixing ratio record covers the period from June 2013 to November 2018, which enabled us to study the diurnal and seasonal variability within this period. In Section 2.3.3.iii, we used high-frequency (10 Hz) meteorological data, in particular all wind components (u, v and w), in order to associate turbulence regimes with CH_4 mixing ratios at 15-minute resolution. More on the assumptions to link high-frequency wind data with 15-minute mixing ratios is given below. In Section 2.3.4, we use 30-minute averages of CH_4, CO and Black Carbon (BC) equivalent mass concentrations to assess the influence of biomass burning emissions in our CH_4 signals. The raw BC mass concentrations at 1-minute time resolution were obtained using a Multi-angle Absorption Photometer (MAAP, model 5012, Thermo Fisher Scientific, Waltham, USA), as described in Saturno et al. (2018). The instrument measures the absorption coefficient of aerosol particles deposited on a filter, which is converted to BC mass concentration by assuming a mass absorption cross section of 6.6 m^2 g^{-1}. In Table 2.1, we provide a list of the data used in each section, specifying the time resolution and the period of time used.

Table 2.1: Observational data used in each of the sections. We specify the time resolution and the period of time used.

Sections	Data used	Time resolution	Period of time
2.3.2, 2.3.3.i/ii	CH_4 mixing ratios	30 min	2013-06 to 2018-11
	Meteorological data	30 min	2013-06 to 2018-11
2.3.3.iii	CH_4 mixing ratios	15 min	2014: Mar-May, July-Sep
	Meteorological data	10 Hz (avg. to 1 min)	2014: Mar-May, July-Sep
2.3.4	CH_4 mixing ratios	30 min	2013-06 to 2018-11
	CO mixing ratios in CH_4:CO	30 min	2013-06 to 2018-11
	CO mixing ratios in BC:CO	30 min	2013-06 to 2018-05
	Black Carbon	30 min	2013-06 to 2018-05

2.2.5 CH_4 gradient definition

A CH_4 gradient is defined as $CH_{4_{grad}} = CH_{4_{79m}}$ - $CH_{4_{4m}}$. We indicate that the units of the $CH_{4_{grad}}$ and the comparisons here are in parts per billion (ppb). We refer to a positive gradient when $CH_{4_{grad}} > 0$ ppb, or to a negative gradient when $CH_{4_{grad}} < 0$ ppb. Note that positive gradients are related to higher CH_4 mixing ratios at 79 m than at 4 m, while negative gradients to higher mixing ratios at 4 m. Throughout this paper we also use a 8 ppb threshold for classifying positive gradients and negative gradients. In Section 2.3.2 we use three classes. The first one refers to very strong positive gradients ($CH_{4_{grad}} >$ 8 ppb or above-8-ppb class); the second one to gradients in between -8 ppb and 8 ppb ($-8 < CH_{4_{grad}} < 8$ ppb); the third one to very strong negative gradients ($CH_{4_{grad}} < -8$ ppb). In Section 2.3.3, we have limited our analysis to two classes, $CH_{4_{grad}} > 8$ ppb, and $CH_{4_{grad}} < 8$ ppb (below-8-ppb class). The motivation to use 8 ppb as the threshold value is to leave out small mixing ratio variations and select very strong events. The $\pm$ 8 ppb threshold is conservative and filters for strong gradients, if we consider that the annual global increase in atmospheric CH_4 during the last three years was 7.06, 6.95 and 10.77 ppb year^{-1} for 2016, 2017 and 2018 respectively (Dlugokencky, 2019). It is always stated in the text which of these classes is being considered.

2.2.6   Analysis of 30-minute averages

In Section 2.3.2, the 30-min averages of CH_4 mixing ratios were grouped into daytime and nighttime and further classified into the three classes as described in Section 2.2.5. In Section 2.3.3.i strong CH_4 positive gradients were associated with wind direction by using the Openair package in R developed by Carslaw & Ropkins (2012). This R package provides useful predetermined functions to interpret air pollution characteristics based on wind speed, wind direction and other variables. Micro-meteorological data were used together with collocated CH_4 mixing ratio data at ATTO (Section 2.3.3.ii).

The heights of the highest sonic anemometer and the highest air inlet for CH_4 mixing ratio measurements differ by two meters, with the former at 81 m and the latter at 79 m. We assume that the effect of the two meters can be neglected and thus interpret all the 81 m data as valid for 79 m. In order to maintain consistency, we used the same 8 ppb threshold as in Section 2.3.2, but this time we clustered the other two classes ($CH_{4_{grad}} <$ -8 ppb and $-8 < CH_{4_{grad}} < 8$ ppb) into only one: below-8-ppb. The latter provides more clarity in the interpretation, as we are strictly interested in the above-8-ppb class.

2.2.7   Analysis of 1-minute averages

In Section 2.3.3.iii we analyze the CH_4 positive gradients for the stable boundary layer taking into account the turbulence regimes defined by Sun et al. (2012). For this analysis, we use high-frequency data (10 Hz) for micro-meteorological variables but we averaged to 1-minute in order to be consistent with recent practice in nocturnal boundary layer studies (Marht et al., 2013; Acevedo et al., 2016, 2019) and to more strictly filter out low-frequency submeso fluctuations (i.e. non-turbulent motions at scales smaller than those at the mesoscale) (Mahrt, 2009) in all wind components. We focus on 6 months of 2014 (March, April, May, July, August and September). We have selected these months to target wet and dry seasons, and discarded June because it is considered a transition month based on precipitation. These turbulence regimes are classified into two classes: above-8-ppb and below-8-ppb. This classification is performed using the highest temporal resolution of CH_4 mixing ratio data, which is 15 minutes. We assume that the gradient is constant for each 15-minute interval. For example, if the CH_4 gradient is 5 ppb at 21:00 LT (local time), we use the same value for every minute until 21:14 LT.

2.3   Results

2.3.1   Example of CH_4 gradient events

In Figure 2.3a we show a night in which a very strong positive gradient occurred. After 00:00 and before 01:00, there is a sudden and abrupt divergence of CH_4 mixing ratios measured at 79 m. This increase in CH_4 is not seen at the first three measurement levels, while at 53 m is observed with some delay and with less intensity. The divergence at 79 m reaches a CH_4 peak of 1960 ppb at around 04:00, at which point the lowest three inlets show CH_4 mixing ratios lower than 1880 ppb. At this time there is a strong thermal inversion for the air above the canopy and the wind speed at 81 m decreases to almost 1 m s^{-1}. The duration of this positive gradient, considering the time in which the 79 m inlet had mixing ratios higher than 1880 ppb, was about 5 hours. These positive gradient events are very common in our time series and they vary mainly in duration and magnitude. For the case shown in Figure 2.3a, we can see that the decoupling between the air above and within the canopy was very strong up until 53 m. At the 53 m level

the signal, first measured at 79 m, arrived about 30 minutes later when the CH_4 mixing ratio began to increase, but at the lower levels the behavior is completely independent. Decoupled conditions can be explained by a very strong thermal inversion that obstructs vertical mixing, which could be triggered by wind shear under stable conditions (Mahrt, 2009).
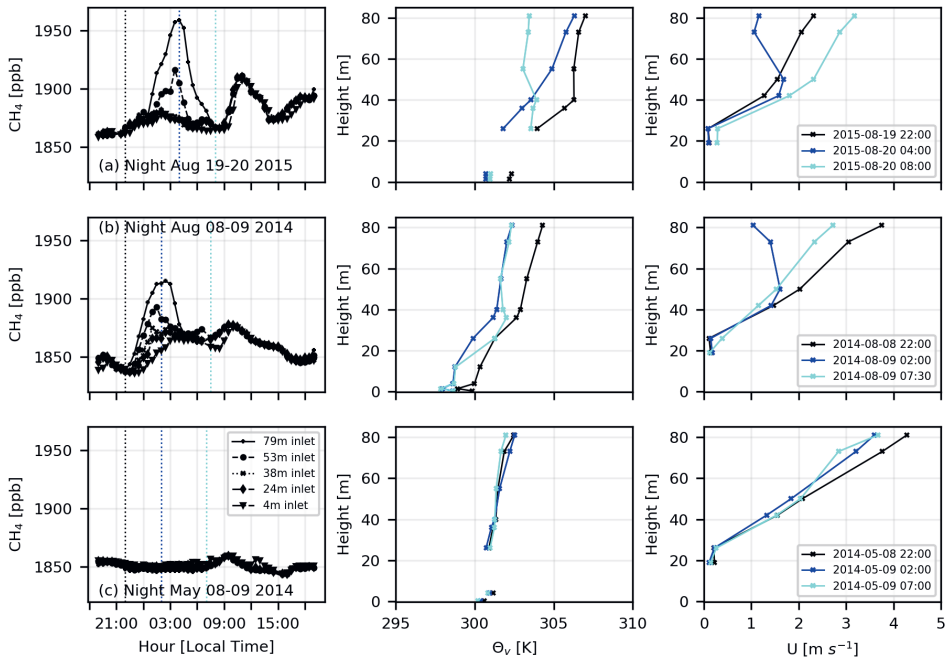
Figure 2.3: CH_4 time series for three selected nights (first column) showing a 24-hour interval, virtual potential temperature (second column) and mean wind profiles (third column) for three selected periods of the CH_4 time series. The times at which the profiles are plotted are highlighted on the CH_4 time series with the same colors. The canopy height is approximately 35 m. Note that due to instrument malfunctioning the Θ_v profiles are lacking data at 12 m. The wind speed profiles cover from 19 m to 81 m.

For other cases in which we observed positive gradient events during nighttime, the signals measured at 79 m are then measured at the lowest inlet (4 m) after some time, varying from 30 minutes to 1.5 hours (see Fig. 2.3b). For these situations, when the coherent response at the lowest levels is within the next half an hour, it could be explained by the sequential sampling (top-bottom) and the buffer volume in our measurement system. However, in the case of such a subsequent top-down signal we also find that the decoupling between the air above and within the canopy is weaker or non-existent.

The virtual potential temperature (Θ_v) profiles above the canopy at 22:00 and 02:00 show a very similar gradient with a weak thermal inversion. Interestingly, at 02:00 when the CH_4 mixing ratio at 79 m reached the maximum, the wind speed at 81 m decreased to 1 m s^{-1} and for the same time the Θ_v profile showed a mild gradient of about 1.2 K. This mild temperature increase with height above 41 m indicates that the decoupling of the air above the forest is less strong, explaining why the CH_4 is measured subsequently at lower heights. Note that vertical transport for these situations is triggered by mechanical turbulence (generated by wind shear instabilities) or intermittent turbulence that, in the absence of a very strong thermal inversion, can transport CH_4 to the lower inlets and inside the canopy (Oliveira et al., 2018). During this night, the gradient was less pronounced and it lasted for less time than in the night shown in Figure 2.3a.

In Figure 2.3c a night in which no gradient was measured is shown. An almost constant Θ_v profile indicates the coupling of the air above the canopy for the three selected times of the night. The thermal gradient for the layer above the canopy is about 1.5 K. The CH_4 mixing ratios are very similar at all inlet heights for the full 24-hour period. During this night the wind speed has both the largest values and the lowest variability during the course of the night. From these three cases, one can see that positive gradient events are associated with atmospheric stability and wind speed. However, as we show in the next Section 2.3.3.i, the wind speed is not necessarily always weak for positive gradients.

2.3.2   Seasonal and diurnal patterns of CH_4 gradients at ATTO

In Figure 2.4 we show that for all years except 2016, monthly mean positive CH_4 gradients (hereafter simply referred to as positive gradients) occur mainly during the dry season, whereas the mean gradient is close to zero during the wet season. The monthly mean gradient is significantly different from zero during the dry months, with p-values (two sided t-test) lower than 0.01. This positive gradient at ATTO is more pronounced during the month of August, when the lowest precipitation values are less than 50 mm (Figure 2.2). A different behavior is observed for 2016, in which a strong negative gradient during June and July suggests a possible CH_4 source within the canopy measured at 4 m. The reason for this is unclear, yet we provide some ideas discussed later in this section. The dry season peak is also seen at the other measurement heights (not shown here), but at 79 m the measured CH_4 mixing ratios are the highest, indicating that non-local sources are

predominant during this period of time. It is interesting to note that in the dry season also the largest variability in the gradient was observed, as opposed to the reduced variability during the wet season and transition months such as December and January.
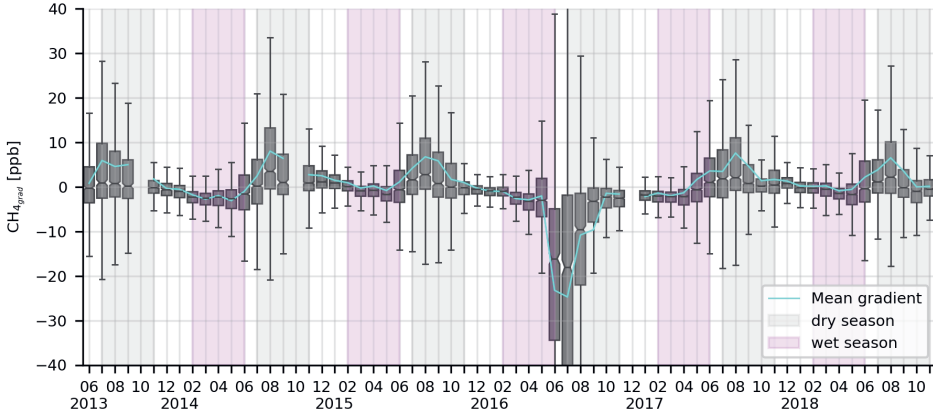
Figure 2.4: Monthly box-and-whisker plot of CH_4 gradient between the 79 m and 4 m levels. The box denotes the inter-quartile range (IQR), showing the median with a notched line. The whiskers range from Q1-1.5*IQR to Q3+1.5*IQR, with Q1 and Q3 being the 25th and 75th percentiles. The cyan line is the monthly mean gradient. The monthly statistics are calculated from half-hourly measurements at ATTO.

The positive gradients observed during the dry season are associated with nighttime CH_4 mixing ratio peaks at 79 m. Figure 2.5 depicts the fraction of time for daytime and nighttime measurements for each of the classes described in Section 2.2.6. For all months, daytime measurements (Figure 2.5a) are within the -8 to 8 ppb range over 60% of the time. Gradients lower than -8 ppb or higher than 8 ppb are more frequent and increase their contribution to the total time during May, June, July, August and September. For these months negative gradients are measured 8.7%, 18.6%, 22.3%, and 17.6% and 7.8% of the total daytime hours, while positive gradients are found 3.6%, 6.2%, 10%, 12.2% and 8.4%.

Nighttime measurements, in general, show a larger contribution of positive gradients to the total time (Figure 2.5b). Nighttime positive gradients occur in all months of the year, from 4.1% of the time in January to 43.3% of the time in August. The highest percentages are recorded during the dry season months of July (30.2%), August (43.3%) and September (30.2%). Unsurprisingly, these months also have the highest mean nighttime gradients, with 2.6 ± 23 ppb, 9.7 ± 21 ppb and 6.2 ± 23 ppb for July, August and September, respectively. The maximum nighttime positive gradients were observed between 03:00 and 06:00 am LT (not shown), with values larger than 130 ppb. During daytime, the

maximum positive gradients occur between 07:00 and 08:00 LT, with values over 150 ppb. Note that these gradients are generated during nighttime and can persist for a couple of hours until the erosion of the nocturnal boundary layer and subsequent growth of the convective boundary layer, which occurs between 08:00 and 09:00 am LT (Fisch et al., 2004; Carneiro, 2018).
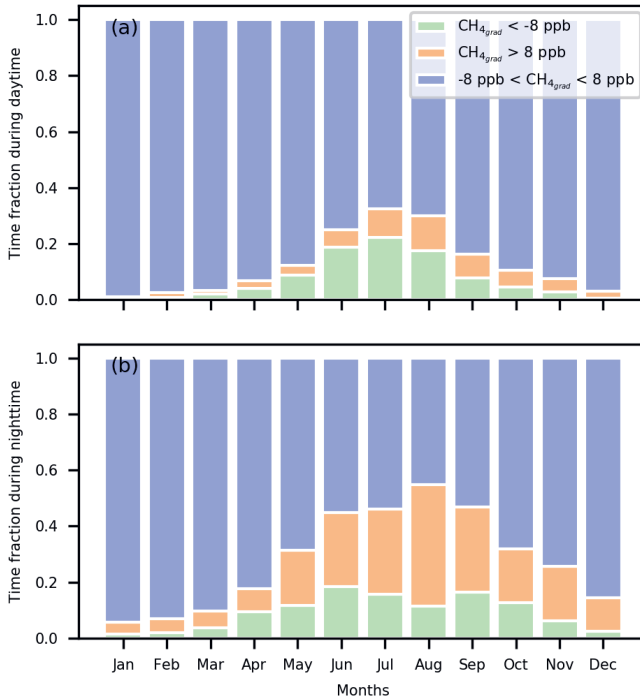
Figure 2.5: Time fractions for daytime (a) and nighttime (b) measurements in which $CH_{4_{grad}}$ > 8 ppb, -8 < $CH_{4_{grad}}$ < 8 ppb and $CH_{4_{grad}}$ < -8 ppb. Nighttime is defined as between 20:00 and 06:00 LT and daytime as between 07:00 and 18:00 LT.

The mean diurnal cycles of the CH_4 gradient for dry and wet seasons provide interesting insights (Figure 2.6). The amplitude of the mean diurnal cycle gradient during the dry season (12.1 ppb) is 4 times larger than that of the wet season (2.7 ppb). This substantial difference can be attributed to two main reasons. First, due to strong nighttime positive gradients during the dry season, the maximum mean (7.1 ppb) is much larger than the maximum mean of the wet season (0.5 ppb). Interestingly, both of these mean maxima occur at night, indicating that nighttime positive gradients are pulling up the mean in

both seasons. Second, during the dry season the daytime planetary boundary layer is higher by a few hundred meters as a result of a larger sensible heat flux caused by the higher incoming shortwave radiation during this season (Fisch et al., 2004; Carneiro, 2018). Under this case with higher mixing ratios close to the surface and lower free tropospheric mixing ratios (as shown for dry and wet seasons by Beck et al. (2012)), a deeper boundary layer directly affects daytime CH_4 mixing ratios because CH_4 enhancements near the surface will be diluted in a larger volume. This dilution effect does not happen at the 4 m inlet, because the within-canopy air volume remains the same throughout the seasons. This boundary layer effect together with higher CH_4 mixing ratios at 4 m compared to 79 m during the dry season yield a lower dry season daytime mean minimum of -5.0 ppb, whereas the mean minimum during the wet season is -2.2 ppb.
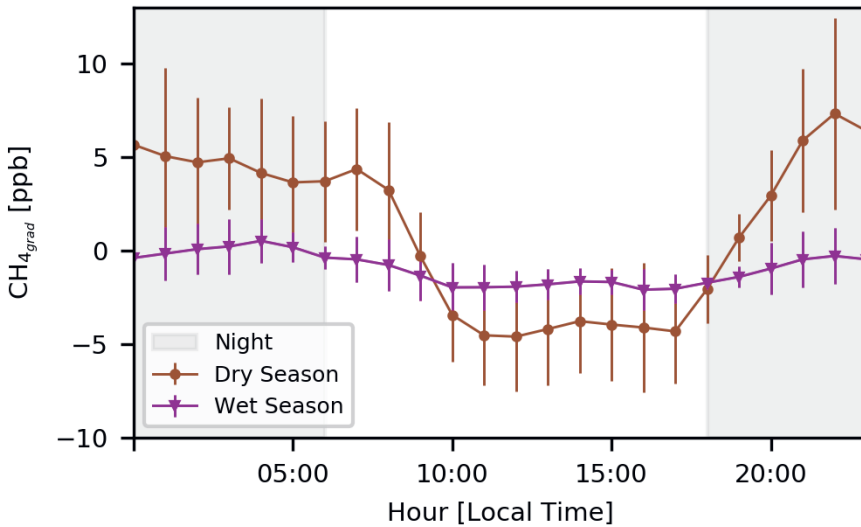
Figure 2.6: Mean diurnal cycle of the CH_4 gradient between the 79 and 4 m levels. The period between June 2013 and November 2018 was used and separated by dry and wet seasons. The error bars show the standard deviations.

Another possibility that might contribute to this seasonal difference is local production of CH_4 during the wet season. Though we lack long-term CH_4 flux measurements at the site, we can infer a potential local source during the wet season considering that the mean monthly gradient during daytime hours of the wet season is always negative (not shown), meaning that the CH_4 mixing ratio at 4 m is higher than at 79 m. Although outside of the scope of this study, strong negative gradients are more common during daytime, reaching differences as large as -455 ppb, measured in May of 2014.

The 4 m inlet is too high above the soil to directly associate this signal with the soil below, but is well within the canopy indicating that the source must be local possibly within a horizontal distance of few hundred meters. The event in May 2014, coincided with a strong signal measured for carbon monoxide (CO) with the same timing, but not for carbon dioxide (CO_2), which suggests a source not related to combustion.

The mechanism producing this strong CH_4 signal within the canopy is currently under investigation, yet here we discuss what the potential sources could be. Our first thought is that the soil on the plateau is producing CH_4 episodically. Given some additional parameters, we can calculate the water-filled pore space (WFPS) for the depth (60 cm) of maximum soil moisture content, at which we believe CH_4 could be produced. To be conservative we take the mean soil moisture value for the entire record at 60 cm, 0.35 m^3 m^{-3}. According to Andreae et al. (2015) $\sim$85% of the soil in the plateau is clay, thus we use a soil particle density of 2.86 g cm^{-3} (Schjønning et al., 2017). Also from Andreae et al. (2015), we use a bulk density of 1.1 g cm^{-3}. This results in a WFPS of 57%, which is likely to enhance the abundance of anaerobic micro-sites where methanogenic bacteria can be activated. At values above 60% Verchot et al. (2000) found positive CH_4 fluxes, at the ATTO site values above 60% are often seen during the wet season. Upland *terra-firme* soils are generally considered as CH_4 sinks (Dörr et al., 1993; Dutaur & Verchot, 2007; Saunois et al., 2016), but at local scales the soil can become a source depending on the balance between CH_4 production and oxidation (Verchot et al., 2000). Moreover, tree stems were found to play an important role as conduits for soil-generated CH_4 in upland *terra-firme* tropical forest (Welch et al., 2019). These findings, together with our data, suggest that the upland *terra-firme* CH_4 sink at ATTO needs to be further studied.

A second option is related to daytime anabatic flows within the canopy transported from the depressions to the plateau (Tóta et al., 2012). These anabatic flows could transport CH_4 produced in saturated soils of these low-lying areas. Recent (May 2019) unpublished CH_4 mixing ratio measurements suggest a possible source at the lowest point of one depression close to the ATTO site. A further possibility, not likely explaining the complete signal at 4 m, but probably contributing to it, might be termite production within the canopy. Termite CH_4 production is common in tropical ecosystems (Sanderson, 1996), however flux measurements from this source have not been performed at the site. The 2016 episode mentioned earlier provides evidence that CH_4 mixing ratios at 4 m could be strongly enhanced by unidentified processes that need further research. The natural variability of upland *terra-firme* CH_4 sources or sinks could have been altered by the El Niño event that began in 2015 and lasted until early 2016, as shown by Pfannerstill et al. (2018) for OH at the ATTO site. For these episodes, which occurred during June and July (see Fig. 2.4), the enhancement at 4 m lasted for more than 5 hours presenting the onset at nighttime and maintained during daytime. Furthermore, the air within the 4 m layer above the ground seemed to be strongly decoupled from the layers above as none of the upper inlets measured the signal observed at 4 m (not shown). Therefore, the 4

m episodes described here are very likely a combination of an enhanced source and the stability conditions of the air within the canopy for those specific dates.

2.3.3   Atmospheric characteristics of positive CH$_4$ gradients

i. CH$_4$ positive gradients and wind direction for 2013-2018

For hourly time scales, we find that for nighttime hours and when the mean CH$_{4_{grad}}$ is above 8 ppb the wind direction is within the range of 90 and 180 degrees, hereafter southeasterly (Figure 2.7, left panel). Note that the wind directions ranging between 180-270 degrees, hereafter southwesterly, also show positive mean CH$_{4_{grad}}$ during nighttime hours but these are lower than those seen when the wind comes from the southeast. For lower or negative mean CH$_4$ gradients and other times of the day, mainly daytime, the wind direction does not show a dominant pattern.
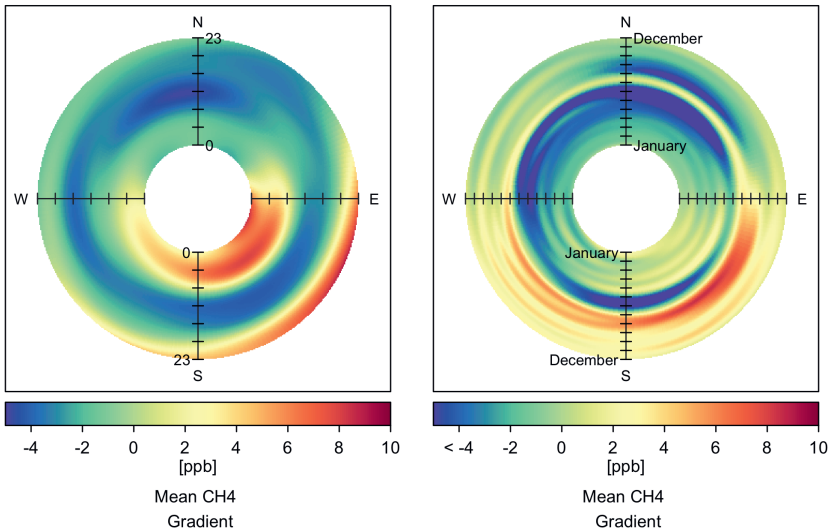

Figure 2.7: Mean CH$_4$ gradient for each bin of wind direction and time of day (left panel) or month of the year (right panel). Wind direction measured at 81 m and CH$_4$ mixing ratios at 79 m. Plot produced in R with the Openair package (Carslaw et al., 2010)

At monthly time scales we observed similar behavior, with a dominant southeasterly wind direction for mean $CH_{4_{grad}}$ above 8 ppb and the dry season months of August and September. During August and September, the southwesterly direction shows mean $CH_{4_{grad}}$ above 4 ppb, suggesting that this wind direction plays an important role in the positive $CH_{4_{grad}}$ events. Yet, it is very clear that large positive $CH_{4_{grad}}$ are mainly driven by southeasterly winds. During dry season months the wind is more frequently coming from the east whereas during the wet season there is a shift to northeasterly winds. *In-situ* measurements of wind direction confirm this pattern. The monthly mean wind roses (see Figure 2.A1) show that the wind is more frequently coming from the east and it is more likely to bring air masses from southeastern areas of ATTO during June, July, August and September. These months have wind direction frequencies close to 20% with wind speeds ranging from 1 to 7 $m\ s^{-1}$. The mean wind rose plots for each hour of the diurnal cycle (see Figure 2.A2) indicate that after 15:00 local time, wind directions in the 90-180 degrees quadrant become more important than in previous hours of the day, with frequencies of about 15%. After 18:00, the frequency increases at this wind direction until 23:00. These wind direction patterns together with the prevailing wind direction for the positive $CH_{4_{grad}}$ suggest that nighttime positive gradient are more frequent in the dry season due to the prevailing wind direction, being more likely to bring air masses from the potential source region located to the southeast of ATTO.

The probability of measuring gradients above the 88th percentile (8 ppb) together with wind direction and wind speed at 81 m is shown in Figure 2.8. The highest probability (50%) of having a gradient above 8 ppb is associated with a particular wind speed range, mainly from 4 to 5 m s^{-1}. This wind speed range is seen for different wind directions, with the two southern quadrants (from 90 to 270 degrees) having a very similar probability of 40 to 50%, with a slightly higher conditional probability in the southeastern quadrant than the southwestern quadrant. For the northwest quadrant (270 to 360 degrees) the probability observed is lower than 40% but interestingly the wind speed range holds. Therefore, the gradients above 8 ppb are associated not only with a range of wind directions but also with a particular wind speed range. We showed previously that southeasterly winds are clearly bringing CH_4-enriched air masses, but there is also a 40% probability of having these enhancements (above 8 ppb) when the wind direction shifts to the southwesterly direction and also when it comes from the northwest with approximately 25% probability at wind speeds of 5 m s^{-1}. It is relevant to note that 68% of the positive $CH_{4_{grad}}$ occur at wind speeds between 2 and 5 m s^{-1} (not shown), which in the southern quadrants still have a higher probability of occurrence.

Considering these results, we can infer that dominant large scale circulation patterns explain why large positive CH_4 gradients are more common during the dry season months. Thus, the wind arriving at ATTO is more likely to come from the source areas to the south of the site.

CPF (8 to 195)
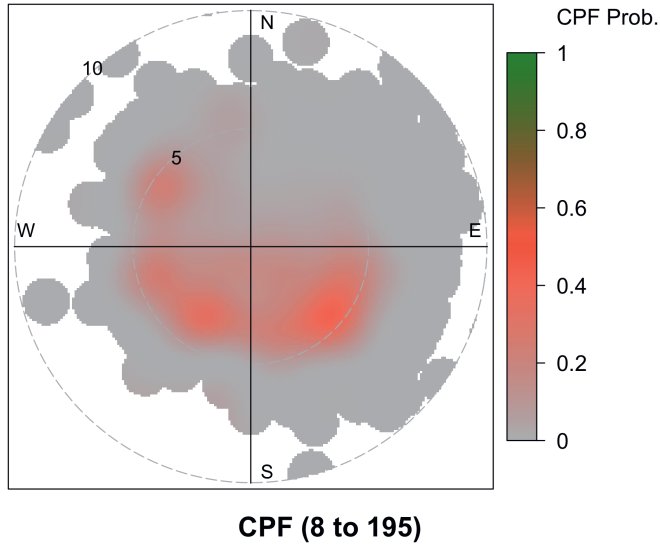
Figure 2.8: Polar plot showing the conditional probability function (CPF) of the gradients above 8 ppb (88th to 100th percentiles, shown in the bottom of the graph as 8 to 195 ppb). The radial axis shows wind speed intervals and the colors the probability of having gradient above 88th percentile. This is shown for each bin composed by wind direction and wind speed at 81 m. Plot produced in R with the openair package (Carslaw et al., 2010).

Moreover, this also explains why large positive CH_4 gradients are more strongly associated with the southeasterly direction; wind direction frequency is larger for these months than for other months of the year. Large positive CH_4 gradients can also come from other wind directions, but they are less frequent. Therefore, we identify a potential source of the nighttime signals with a probability of 40% to 50% to the south of the ATTO site (see Figure 2.8). Here it is important to recall that these percentages are based on the conservative threshold of 8 ppb, analyses not shown here using a lower threshold yield higher probabilities. The nighttime average wind direction is more frequently coming from the southeast, explaining why positive $CH_{4_{grad}}$ are more strongly associated with these wind directions at this timescale.

ii. Net radiation, sensible heat flux, friction velocity and thermal stratification for CH_4 positive gradients 2013-2018

Net radiation for the above-8-ppb class is more negative, indicating a stronger radiative cooling at ATTO (see Figure 2.9a) when these episodes occur. Net radiation is less variable for positive gradients with lower mean and median values for all night hours. This can be explained because positive gradients are more frequent during the dry season and in particular in August, when there is less cloud cover, as can be inferred by our precipitation record (Fig. 2.2), and as reported in Andreae et al. (2015). Clear skies contribute with a more effective radiative cooling at the canopy top, leading to a stronger thermal inversion in the NBL.
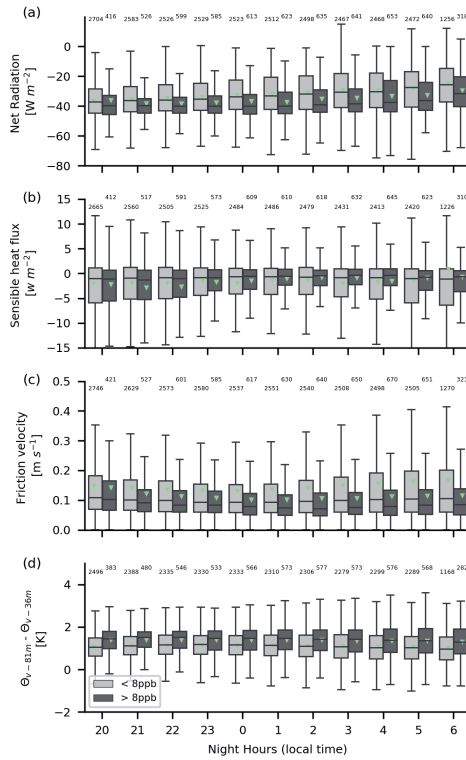
Figure 2.9: Box-and-whisker plots of net radiation (a), sensible heat flux (b), friction velocity (c), and virtual potential temperature difference (d) for nighttime hours. At each hour the gray colors indicate data points that correspond to either a gradient above 8 ppb or below 8 ppb. The means are indicated by the green triangles and the number of data points for each box-and-whisker plot is shown on the top of each panel. Note that the sensible heat flux and the friction velocity were measured at 81 m and net radiation at 75 m. Note that the air inlet for CH_4 mole ratios is at 79 m.

Net radiation estimates at ATTO provide indirect evidence that suggest a shallower NBL height during the dry season. Values above the canopy are more negative during the dry season than during the wet season (see Figure 2.A3), suggesting a strong thermal inversion driven by large nighttime radiative cooling at the top of the canopy. For stable nights at the ATTO site, Oliveira et al. (2018) found that at 81 m the turbulent fluxes were clearly less variable than at lower heights, indicating a very shallow NBL height.

The above-8-ppb class is associated with a less variable H (see Figure 2.9b), tending to values close to zero. For this class, the mean and median values of H at the beginning of the night hours, mainly from 20:00 to 23:00 LT, are slightly more negative than for the other class. After midnight these values tend to be closer to zero for the above-8-ppb class, suggesting that the nocturnal boundary layer is more stable for positive gradient events. The variability of both classes between 20:00 and 23:00 LT is not as different as for the rest of the hours, but still is slightly lower for the above-8-ppb class. Considering the height at which the H is zero a proxy to infer the NBL height, one could say that positive CH_4 gradient events are associated with a very shallow nocturnal boundary layer, close to 81 m. The seasonal difference in NBL height was studied by Carneiro (2018) during the GoAmazon campaign (Martin et al., 2016), using a ceilometer, a lidar and a SODAR, among other instruments. Carneiro (2018) found that the time to erode (total erosion is considered to be when sensible heat flux and net radiation become positive) the nocturnal boundary layer is larger during the wet season, suggesting a deeper NBL height as one of the reasons to explain this. It is worth noting that the ceilometer sensitivity differs between instruments and it can also be affected by changes in the background radiation (Wiegner & Geiß, 2012). The ceilometer used by Carneiro (2018) is a CL31 (Vaisala Inc., Finland) and the one at ATTO is a Jenoptik CHM15kx, used recently by Dias-Júnior et al. (2019) to determine the mixing layer depth using only daytime backscatter profiles. In another study with the Jenoptik CHM15kx, Wiegner & Geiß (2012) found that the lowest detectable mixing height is around 150 m, therefore nights with a NBL height lower than this might not be well captured. Furthermore, the study was conducted over pasture which has different roughness and radiative characteristics compared to old-growth forest, and as such the results cannot be extrapolated to ATTO. Nonetheless the study provides valuable information about seasonal differences of the NBL height.

Positive gradients are also associated with low friction velocity (u_*) variability as well as low mean and median values for all nighttime hours (see Figure 2.9c). As a measure of mechanical turbulence, low u_* values suggest that positive gradients occur mainly at low turbulence intensity. This finding is not surprising as strong stability and the absence of turbulence can lead to accumulation of trace gases in the NBL (Stull, 1988; Fitzjarrald & Moore, 1990) due to reduced vertical mixing.

However, under this common assumption and considering that the NBL above the canopy can attain shallow depths, one would expect to measure the accumulation of trace gases at least at the other inlet heights above the canopy or at inlet heights closer to the canopy, where the possible source could be located, but for many of these events this is not the case. The CH_4 signal that arrives at the uppermost inlet (79 m), driving a positive gradient, is often not seen at lower inlets. This is very often the case for the inlet at 38 m but less so for that at 53 m, indicating that the CH_4 rich air is advected within a layer that includes the 79 m inlet and sometimes the 53 m inlet, but not those below 53 m. Having low friction velocity values and considering that the dominant wind speeds at which positive gradients have more probability of occurrence are between 2 to 5 m s^{-1} (see Figure 2.8), suggest that CH_4 signals are transported mainly by horizontal non-turbulent motions, which are probably formed by inactive turbulence mainly seen at the upper layers. Such inactive turbulence contributes very little to the generation of turbulence as was indicated by Högström (1990).

The difference of θ_v between 81 and 36 m is slightly higher for the above-8-ppb class than for the below-8-ppb class (see Figure 2.9d). The difference between the median values of the two classes is approximately 0.5 K for all night hours, hinting at relatively faster radiative cooling at the top of the canopy for the above-8-ppb class. The variability of this difference is very similar between both classes, although the above-8-ppb class is more skewed towards positive values. The difference between mean and median values for both classes is small, but the fact that we see a systematic difference at all night hours, strengthens the argument that thermal stratification is stronger when positive gradients occur than for the other class.

iii. Association of positive CH$_4$ gradients and NBL turbulence regimes

We have defined the NBL turbulence regimes following the work of Sun et al. (2012), which was further applied by Dias-Junior et al. (2017) at another site within the Amazon forest. In regime 1, turbulence is produced by local shear at low wind speed and low σ_w. In regime 2, σ_w increases with wind speed and bulk shear in the NBL triggers turbulence (Sun et al., 2012). In Figure 2.10a the standard deviation of the vertical velocity (σ_w) is plotted as a function of mean horizontal wind speed (U) for all the data available in 2014 without differentiating between gradient classes. Here, one can see that the regime transition (between regime 1 and 2) occurs at the wind speed bin of 5.8 m s^{-1}, which comprises the range between 5.6 and 6.0 m s^{-1}. At this threshold the uppermost quartile of σ_w exceeds 0.5 m s^{-1} and the slope defined by median values changes notably. Therefore, we define this bin as the wind speed threshold that marks the transition from regime 1 to regime 2. Subdividing this further into the gradient classes above and below 8 ppb (Figure 2.10b), we observe that the variability of σ_w close to the wind speed threshold (bins 5.8 and 6.5 m s^{-1}) is reduced for the above-8-ppb class. The upper quartile of σ_w for the above-8-ppb class exceeds 0.5 m s^{-1} only up to 6.5 m s^{-1}.

The median σ_w for both classes display a similar range of variability at 7.5 m s^{-1}. The above-8-ppb class has a different distribution in the same wind speed bins close to the wind speed threshold, having lower median values of σ_w. This finding implies that vertical motions are even more suppressed at 81 m for the above-8-ppb class, regardless of the wind speed exceeding the threshold value.

Given these facts, we can associate positive gradients with the more stable regime 1: low σ_w even at wind speeds exceeding the threshold value, identified without separating into gradient classes. In other words, the wind speed threshold under positive gradient events is shifted to a higher wind speed, maintaining low σ_w values. To account for wind speed variations that could affect our assumption of constant CH$_4$ mixing ratios for every 15-minute window, we have filtered out the 15-minute time periods in which the difference between the maximum and minimum wind speed is larger than 0.5 m s^{-1} (Fig. 2.10c). After filtering, the dependence of σ_w on wind speed shows a similar pattern for each of the classes. In general, σ_w is less variable for positive gradients events. However, the difference in wind speed threshold is even more evident at the wind speed bins of 5.9 and 6.1 m s^{-1}. According to Sun et al. (2012), turbulence in regime 1 is weak and is controlled by vertical temperature gradients, in line with our finding of a stronger thermal stratification for positive gradients shown before. In regime 1 eddies generated at the observation height triggered by local shear do not come into contact with the ground (Sun et al., 2012). This is because, as stated by Sun et al. (2012), the length scale of the local shear is smaller than the observation height.

More evidence about the dominant regime of the NBL when the positive gradients occur is given by the potential temperature gradient ($\frac{d\theta}{dz}$) between 81 m and 36 m. We found that 99.95% of the positive gradients occur with positive values of $\frac{d\theta}{dz}$. As a result, one can infer the absence of vertical motions at the tower location. We can only attribute this lack of vertical mixing above the canopy to the tower location. Therefore, we have to separate the NBL conditions at the tower and at the potential source location. Unfortunately, we only have measurements at the tower and it is not realistic to measure at all possible source locations. Thus, the transport mechanisms can be divided into 1. those responsible for vertical transport of CH$_4$ at the source location and 2. those responsible for the horizontal advection bringing the CH$_4$ signals to the tower. More on the vertical and horizontal transport mechanisms is discussed in Section 2.4.2.
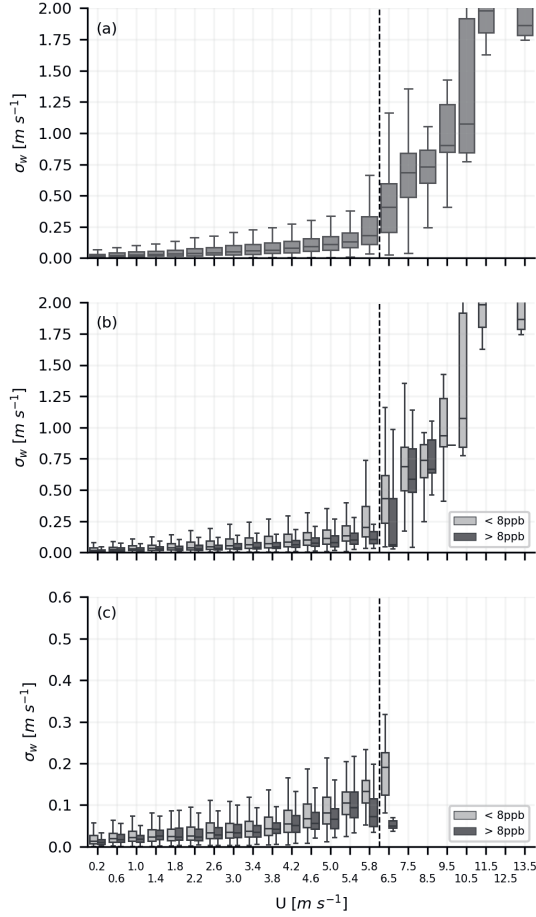
Figure 2.10: Standard deviation (σ_w) of the vertical velocity, plotted against the mean wind speed, for 1-minute averaging time. On the top panel (a), the variability of σ_w for each wind speed bin is shown for all data points, with no classification based on CH_4 gradients. On (b), the same as (a) is shown, but separating between measurements with gradients above and below 8 ppb. Note that our CH_4 mixing ratio measurements are at 15-minute resolution, therefore we assume the same value every 15-minute window so we can associate the 1-minute σ_w and U with CH_4 mixing ratios. On the bottom panel (c), we excluded the 15-minute time periods where the wind speed varied by more than 0.5 $m\ s^{-1}$. Note the difference in y-axis for (c). The wind speed bins are shown every 0.4 $m\ s^{-1}$ until 5.8 $m\ s^{-1}$, after the spacing is 1 $m\ s^{-1}$. This gradually increase to coarser wind speed bins is done due to less amount of data at higher wind speeds. High-frequency measurements cover six months of 2014: March, April, May, July, August and September.

2.3.4 Rejecting biomass burning and the Amazon river as potential sources

The timing of the biomass burning season coincides with the dry season in the Amazon region (Gatti et al., 2014; van der Laan-Luijkx et al., 2015; Aragão et al., 2018), thus one could think that CH_4 from combustion is responsible for the positive gradients presented here. During incomplete combustion, CH_4 is co-emitted together with carbon monoxide (CO) (Akagi et al., 2011; Kirschke et al., 2013; Andreae, 2019), thus CO is considered a good proxy for biomass burning and it can be used as a reference to get an idea of enhancement ratios due to fire emissions.

In Figure 2.11 large CO mixing ratios (>200 ppb) are observed, suggesting that for these measurements we could have sampled air with biomass burning signals. However, these data points represent only 10% of the data shown. Moreover, biomass burning typically produces CH_4 in a certain emission ratio to CO, dependent on the fuel type (Andreae & Merlet, 2001; Andreae, 2019). These reference ratios are shown as lines in Figure 2.11 and it can be seen that very few points fall on the reference lines and the CH_4 mixing ratios are substantially enhanced compared to those of CO, indicating an additional source of CH_4 seen for all wind directions. The mean CO mixing ratio during nighttime in the dry season at 79 m (140 ± 1.6 ppb) is on average 33 ppb higher than during the wet season (107 ± 1.25 ppb), suggesting that during the dry season we observe a "background enhancement" of CO mixing ratios at ATTO. Therefore, we can conclude that CH_4 measurements at ATTO during the dry season will always have a contribution of biomass burning, but as Figure 2.11 shows this "background enhancement" of CO can not completely explain the additional CH_4 of the positive gradients. Note that most of the data points are grouped below 200 ppb for CO, suggesting that positive gradients occur with CO mixing ratios close to the mean dry season mixing ratio. Given these facts, we believe that positive gradients have a minor contribution of CH_4 from biomass burning, but the magnitude of the CH_4 enhancement relative to the CO mixing ratios needs to have an additional source.

Therefore, the challenge constraining to what extent fire emissions affect our CH_4 relies on identifying a clear and distinctive fire plume that provides information on not only the CH_4:CO but also the ratio relative to other species. Considering that black carbon (BC) particles are emitted in smoldering and flaming fires (Andreae & Merlet, 2001) together with CO and CH_4, we use BC measurements to gain more insights about the influence of fire emissions on the full CH_4 signal at ATTO. Following the same approach as in Figure 2.11, the BC:CO ratios in Figure 2.12 indicate a more clear fire signal for the ESE and SSE wind directions. Note that the time period used in this plot is five months shorter than in Figure 2.11 and contains fewer data points, yet some of those points fall on the reference slopes of Andreae (2019).

Figure 2.11: Methane (CH_4) as a function of carbon monoxide (CO) together with the slopes of the expected emission ratios (ER) for different types of fires based on the updated assessment of Andreae (2019) and classified into the dominant wind direction clusters for positive gradients (southern quadrants: from 90 to 270 degrees). The data points were filtered to select only nighttime measurements, and the CO data were further filtered to select the same times for which the above-8-ppb class was seen for our CH_4 mixing ratio measurements. The data cover the time period between June 2013 and November 2018. All measurements were performed at 79 m.

In general terms, even though fire signals are measured at ATTO during nighttime for positive CH_4 gradients as suggested by Figure 2.12, the nighttime CH_4 enhancements at 79 m are not fully explained by combustion. Most of the data points in the ESE wind direction match the reference slope for biofuel and tropical forest burning. Both linked to human activity and according to the comprehensive study of Pöhlker et al. (2019), in the ESE direction there is substantial fire activity, the rainforest has suffered more fragmentation and degradation and there are more settlements. It is worth recalling that here we are focusing on nighttime data when stable atmospheric conditions prevail, therefore the BC associated with biofuel burning might come from nearby settlements. For other directions the fire signal is not so evident and for some data points the CO mixing ratio is very high. This can be seen for all wind directions, and we believe that this can be explained by a possible weakening of the BC:CO due to deposition of BC (Saturno et al., 2018). Last but not least, even though biomass burning takes place throughout the entire dry season, its influence at the ATTO site is more relevant during October and November, as shown by Saturno et al. (2018) and our carbon monoxide time series. Despite being able to detect a clear fire signature, CH_4 enhancements are too high relative to CO suggesting that an additional source is needed to explain the positive CH_4 gradients enhancement during nighttime.
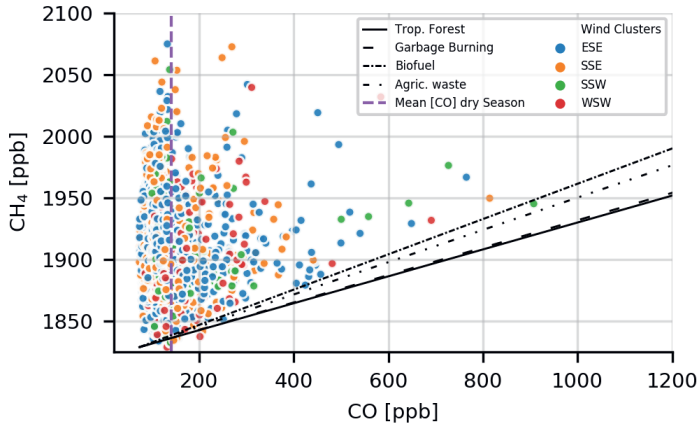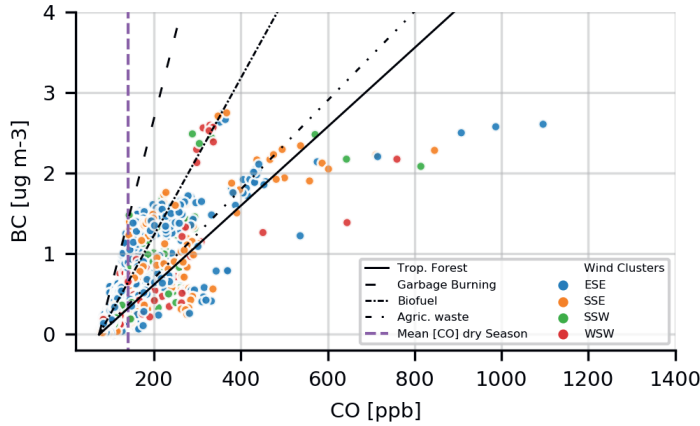
Figure 2.12: Black Carbon (BC) as a function of carbon monoxide (CO) together with the slopes of the expected emission ratios (ER) for different types of fires based on the updated assessment of Andreae (2019) and classified into the dominant wind direction clusters for positive gradients (southern quadrants: from 90 to 270 degrees). The data points were filtered to select only nighttime measurements, and the BC data were further filtered to select the same periods at which the above-8-ppb class was seen for our CH_4 mixing ratio measurements. Note that the BC data set spans from June 2013 to May 2018. The heights of CO and BC measurements are 79 and 60 m a.g.l., respectively.

The Amazon River was discarded as a potential source even though it coincides with the wind direction found for the positive gradients. The Amazon River is 120 km southeast of ATTO, which means that a strong CH_4 emission into the nocturnal boundary layer will have to be advected at a wind speed of 6 m s^{-1} to reach ATTO in five hours. This might be possible on some occasions, but as we saw before (Figure 2.8) positive gradients are associated with wind speeds between 2 and 5 m s^{-1}. Moreover, 80% of the wind speed for nighttime positive gradients is below 4 m s^{-1}. In addition, we calculated the distance to the CH_4 source by time-integrating the wind speed at 81 m from 20:00 (beginning of the night) until the first occurrence of a positive gradient (> 8 ppb). The distribution of these distances is shown in Figure 2.13. The distances with more counts are below 50 km, 90% of the data points fall below 100 km, and 80% of the data points are below 72 km. Given these facts, the Amazon River is not considered as a potential source for the nighttime CH_4 positive gradients.
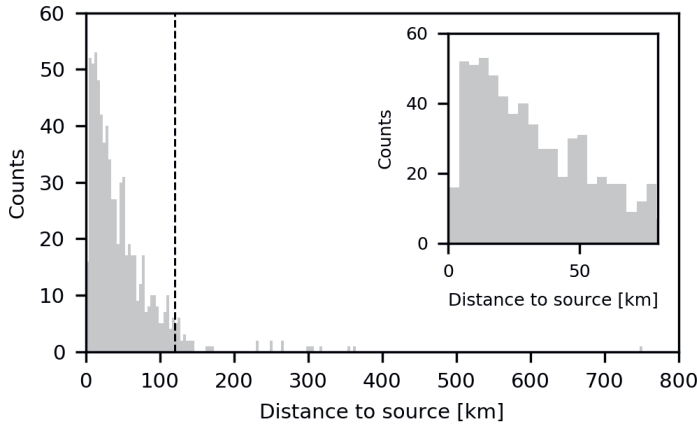
Figure 2.13: Distribution of the cumulative distance the wind at 81 m travelled from the potential source. The distance was calculated by time-integrating the wind speed at 81 m from 20:00 (beginning of the night) until the first occurrence of a positive gradient (> 8 ppb). The vertical dashed line shows the distance to the Amazon River in the southeast direction. The inset on the top right is a zoomed in view showing the x-axis until 80 km.

2.4 Discussion

2.4.1 Constraining potential nighttime CH_4 sources

Based on the predominant wind direction of the positive gradients, we propose a potential source of the nighttime CH_4 signals at the 79 m level. First in importance and most dominant is the southeastern quadrant, second in line is the southwestern quadrant (see Figures 2.7 and 2.8). In these directions lies the Uatumã River, which we believe is the most likely main source (but not unique) of the positive gradients seen at ATTO. In addition to the natural CH_4 production by this river, there are two additional sources that could enhance CH_4 degassing from this water body. The first one is related to an enhanced CH_4 concentration downstream of the Balbina reservoir. As it was shown by Kemenes et al. (2007), the Balbina reservoir not only leaks methane at the turbine intake due to depressurization but it also enhances CH_4 concentrations downstream along the Uatumã river. Kemenes et al. (2007) found that CH_4 concentrations in the Uatumã River decreased gradually until 30 km below the Balbina reservoir and remained constant for the next 70 km. It is worth noting that the CH_4 concentrations in the river were on average 24 μM (Kemenes et al., 2007), three orders of magnitude higher than the average background value (0.05 μM) for Amazonian rivers (Richey et al., 1988; Kemenes et al., 2007). The second additional source is very likely decomposition of dead flooded forest stands downstream the Balbina reservoir along the Uatumã River.

The dead stands are a consequence of the Balbina damming, which has changed the natural flooding pulse along the river, causing massive mortality of flooded forest trees along a 80 km stretch downstream of the dam (Resende et al., 2019). These dead stands were mapped recently by Resende et al. (2019), and their spatial distribution coincides with the wind directions associated with the positive gradient events (see Figure 2.A4). Rivers also emit carbon dioxide (CO_2), but the CH_4 enhancements described here do not coincide with an increase of CO_2. This is mainly because nighttime respiration is very strong and any non-local enhancement at 79 m is masked by local CO_2 signals at lower levels.

In addition, CH_4 could also be produced in the topographic depressions or valleys that form the drainage network surrounding ATTO. We have mentioned earlier that unpublished measurements of atmospheric CH_4 mixing ratios performed recently in one of these valleys indicate a nighttime increase of CH_4 within the canopy. Based on Junk et al. (2011), these depressions can be classified as *wetlands subjected to unpredictable, polymodal flood pulses fed by rainwater*, with low nutrient availability compared to the plateaus. The flooding dynamics are driven by flash flood pulses after precipitation events, which can flush out a large amount of the organic material available for decomposition (Wittmann F., 2019, personal communication). Therefore, these depressions were assumed to have low potential of producing CH_4. Nevertheless, the accumulation seen for CH_4 mixing ratio measurements performed during May and June in 2019 indicate that either CH_4 is transported to the lowest part of the valley and accumulates during the night, or that CH_4 is produced at the valley and accumulated *in-situ*.

The question that arises here is, why do we see a seasonal pattern in the positive gradients, being more frequent and predominant during the dry season? Considering the Uatumã River as the main source, we can explain this seasonality based on the effectiveness with which methane is degassed from the river to the atmosphere and the prevailing atmospheric conditions that drive atmospheric transport from the river to ATTO. During the dry season, when the river levels are low, degassing is more effective due to lower hydrostatic pressure, rendering the ebullitive pathway more efficient due to a shorter water column, which also reduces the probability of oxidation (Sawakuchi et al., 2014).

Therefore, during the dry season the CH_4 produced in the river sediment plus that added by the Balbina reservoir could be more effectively emitted to the atmosphere. It is important to note here that the suggested source coming from the anaerobic decomposition of the dead stands of flooded forests or *igapós*, could also be affected by the shorter water column during the dry season. However, in terms of enabling anaerobic conditions in the sediments, we have to make a distinction between floodplain and riverine environments, as these could have different responses to flooding.

Anaerobic conditions in floodplains soils seem to follow the established idea that with a higher water level there should be higher methane emissions (Kaplan, 2002; Bloom et al., 2012; Melton et al., 2013; Ringeval et al., 2014; Bloom et al., 2017), which are either diffused or transported by ebullition or trees (Pangala et al., 2017) to the atmosphere. In contrast, sediment in rivers could always be anaerobic with the potential to produce methane regardless of the season. What is really affected by a deeper water column in a river is the time for CH_4 to be oxidized and the increased hydrostatic pressure that can inhibit the ebullitive pathway (Sawakuchi et al., 2014).

Given the aforementioned, we can now link these potential sources along the Uatumã river and its seasonal pattern with the dominant atmospheric conditions during the dry season months. During these months and in particular in August the frequency with which the wind brings air from the southeast to ATTO is higher than during the wet season months, when the prevailing wind direction is from the northeast (see Figure 2.A1). Therefore, the probability of advecting methane-rich air emitted in the Uatumã River area and potentially the valleys along that same direction is also higher during the dry season.

2.4.2 Atmospheric transport mechanisms from the source

Nocturnal vertical exchange, can be driven by intermittent turbulence (Acevedo et al., 2006; Oliveira et al., 2018), gravity waves (Zeri & Sá, 2011), katabatic or drainage flows (Goulden et al., 2006; Tóta et al., 2008; Araújo et al., 2008; Tóta et al., 2012) and nocturnal land-river breezes (De Oliveira & Fitzjarrald, 1994; Sun et al., 1998). Intermittent turbulence mainly occurs as top-down bursts (Sun et al., 2012) that can connect the upper layers of the NBL with the canopy and even penetrate the upper part of it, as was shown to be important for ozone and CO_2 fluxes at the ATTO site by Oliveira et al. (2018). However, as intermittent turbulence (or regime 3 events as defined by Sun et al. (2012)) are mainly observed as top-down intrusions, we discard it as a vertical transport mechanism at the source locations given that the source of CH_4 has to be at the surface. Gravity waves were shown to be responsible for transporting mass out of the sub-canopy layer during strong stability conditions and clear nights (Fitzjarrald & Moore, 1990), yet Cava et al. (2004) suggested that wave motions do not play an important role in scalar transport over a pine forest, based on the fact that one wave period had zero mean flux. Furthermore, Zeri & Sá (2011) for a study in the Amazon, found that the wave passage was not directly associated with vertical fluxes of CO_2. Therefore, it is difficult to firmly associate gravity waves with a vertical transport of CH_4 at the valleys or at the Uatumã River.

Having discarded these mechanisms, we believe that land breezes and drainage flows are the most probable inducing vertical transport at the Uatumã River and the valleys close to ATTO.

During the night, due to differential radiative cooling over land and water, the river is warmer than the forest, leading to slightly warmer air over the water. This leads to a breeze from the land to the water that can transport trace gases from the forest to the river. Such breeze (from land to water) was observed over the Balbina reservoir by Vale et al. (2018), finding a nocturnal accumulation of CO_2 over the water. Measurements during the ABLE experiment showed that the Amazon River could be 6 degrees warmer than the forest (De Oliveira & Fitzjarrald, 1994). Considering that black water rivers, such as the Uatumã are warmer than white water rivers, like the Amazon River, it is very likely that the Uatumã River is warmer than the surrounding forest. The temperature difference produces a pressure gradient as warm and less dense air moves vertically over the river. These air parcels can vertically transport CH_4 to upper parts of the NBL. This mechanism was described as a "chimney effect" in the study of Sun et al. (1998), in which they found that water vapor, ozone and CO_2 can be vertically transported by these events over a lake. The width of the lake in their study was about 10 km, and the width of the largest open water flooded areas along the Uatumã River southeast of ATTO, the Lago Cumateúba and Lago Araçatuba, are 3.5 km and 1.8 km.

The vertical transport mechanism at the valleys could be slightly different from that over the river. We believe that updrafts driven by air convergence forced by drainage flows can lead to vertical transport. Drainage flows in the Amazon were inferred by Goulden et al. (2006) using *in-situ* measurements and remote sensing imagery and although vertical transport mechanisms at the lower topographic areas were not addressed, they suggest that the air at the center could be well-mixed. Later, Araújo et al. (2008) showed that nocturnal katabatic flow from the plateau to the valley not only affects the horizontal distribution of CO_2 mixing ratios along a topographic gradient but also the vertical profile of CO_2 mixing ratios over the valley. They had tower measurements on the plateau, on the slope and at the valley floor. With this setup they could confirm the occurrence of a shallow convergence zone over the valley that breaks down the thermal inversion and transports air vertically from the valley floor to the layers above. Araújo et al. (2008) suggest that the air might sink over the slope to maintain the local circulation, but the katabatic or drainage flow at ATTO could be more pronounced due to steeper slopes compared to those in Araújo et al. (2008). On a different study (Tóta et al., 2012), drainage flows were found to occur above the canopy, moving from the plateau to the valley as in Araújo et al. (2008), but in the sub-canopy layer they observed upward (anabatic) flow during nighttime. If this process occurs at the ATTO site despite its steeper topographic gradients, it would not explain the observed positive CH_4 gradients. Such a mechanism would instead result in negative CH_4 gradients as the CH_4 signal would arrive first to the 4 m inlet.

For the horizontal transport of CH_4 towards the tower from the source location, we have discarded a nocturnal low-level jet since these events are commonly associated with high wind speed, high friction velocities and weak to unstable conditions (Karipot et al., 2008), whereas positive gradients coincide with low u_* and a broad range of wind speeds between 2 and 5 m s^{-1}, and they are not specifically associated with large wind speed. Therefore, we believe that horizontal transport of CH_4 from the source location to the tower is driven by horizontal advection of the prevailing wind, bringing methane-rich air when the wind direction coincides with those shown in Figure 2.7.

2.5 Conclusions

We showed that during the dry season, CH_4 mixing ratios are on average higher at the top of the 80 m tower than at the lower inlet heights. We have defined these events as positive CH_4 gradients based on the condition: $CH_{4_{79m}}$ - $CH_{4_{44m}} > 8$ ppb, which was applied to 6 years of continuous measurements at 30-minute resolution to classify our measurements. The CH_4 positive gradients of the dry season are associated with very strong CH_4 signals measured at 79 m, that occur more frequently during nighttime. Nighttime positive gradients ($CH_{4_{79m}} > CH_{4_{44m}}$) are more frequent during July, August and September. The amplitude of the mean diurnal cycle of the CH_4 gradient during the dry season is four times larger than that of the wet season due to the strong nighttime positive gradients. The dominant wind direction for these nighttime episodes, at monthly and diurnal time scales, is southeast of ATTO. In addition, this direction has the highest probability, 50%, of bringing air that will cause a positive gradient (> 8 ppb). This probability was also found to be linked to a wind speed range between 4 and 5 m s^{-1}. Despite these moderate wind speeds, these CH_4 enhancements showed lower net radiation (it is more negative by -2 to -3 W m^{-2}, see Figure 2.9), less variable sensible heat flux, low friction velocity (< 0.3 m s^{-1}) and a strong thermal inversion above the canopy. Further analysis of high-frequency micro-meteorological data suggests that positive gradients are associated with regime 1 of the nocturnal boundary layer, in which turbulence is weak, controlled by temperature gradients and generated by wind shear (Sun et al., 2012).

Based on CH_4:CO enhancement ratios, we excluded biomass burning as the main driver of the positive gradients, and have shown that the Uatumã River is very likely the most important source, due to the coincidence with the dominant wind direction. In addition, we suggest that two additional CH_4 sources might enhance the natural emissions from the river area. The first one is a Balbina-reservoir-driven increase in CH_4 concentrations in the river (Kemenes et al., 2007), and the second possible source of CH_4 is due to anaerobic decomposition of dead stands of flooded forest along the Uatumã River downstream of the reservoir (i.e. the areas mapped by Resende et al. (2019)).

The atmospheric transport mechanisms were divided into those responsible for horizontal advection of CH_4 from the source locations to the ATTO site, and those that transport air vertically from the source location to the upper layers of the nocturnal boundary layer. We suggest that vertical transport over the Uatumã River results from differential radiative cooling of the forest and the water, producing a horizontal pressure difference that causes an upward displacement of air parcels over the river and transporting CH_4 aloft. These air parcels are then advected by the prevailing horizontal wind towards the ATTO site and subsequently measured at the 79 m level.

In the near future the 325 m tower will be fully equipped, providing valuable information in terms of CH_4 mixing ratios and meteorological variables which will enable us to study if the positive gradient extends to upper layers of the nocturnal boundary layer. We will be able to assess the influence of the residual layer and the height of the nocturnal boundary layer in our CH_4 measurements. To better understand local circulation and its effect on vertical CH_4 transport, we strongly recommend performing profile measurements at the river and in nearby valleys with emerging measurement techniques, such as unmanned aerial vehicles. High resolution atmospheric transport models, such as the Weather Research Forecast for greenhouse gases (WRF-GHG), could also help to understand and either reject or confirm the mechanisms mentioned here. Furthermore, an upcoming campaign at ATTO specifically aims to determine the isotopic signature of the CH_4 mixing ratio during a positive gradient event, providing more accurate information about the CH_4 source.

Appendix
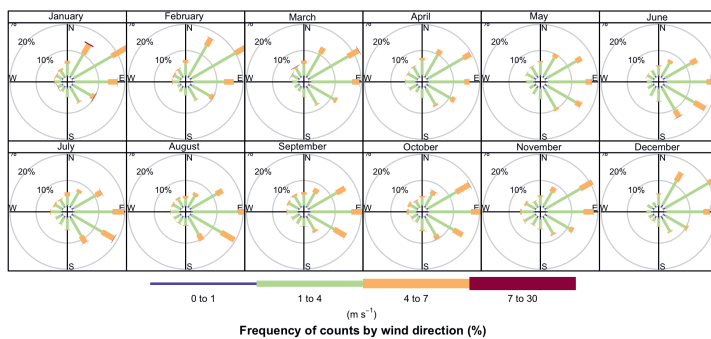
Figure 2.A1: Monthly averaged wind rose plots at 81 m.
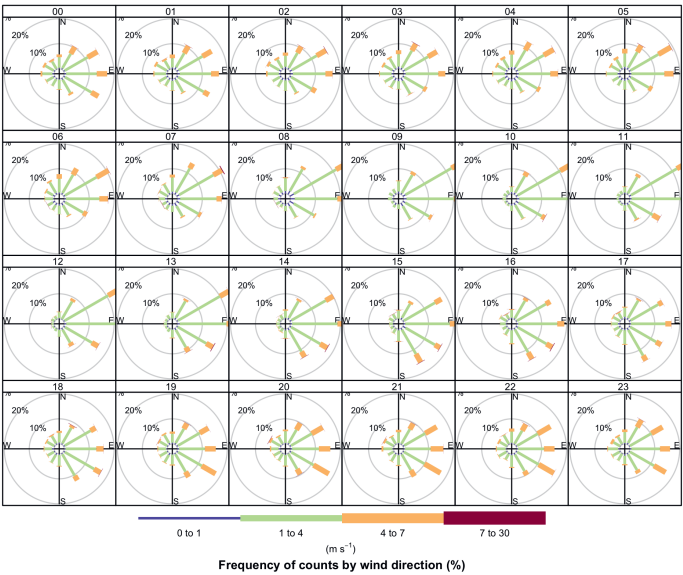
Figure 2.A2: Hourly mean wind rose plots for each hour of the day. Averaged over all measurement period at 81m.
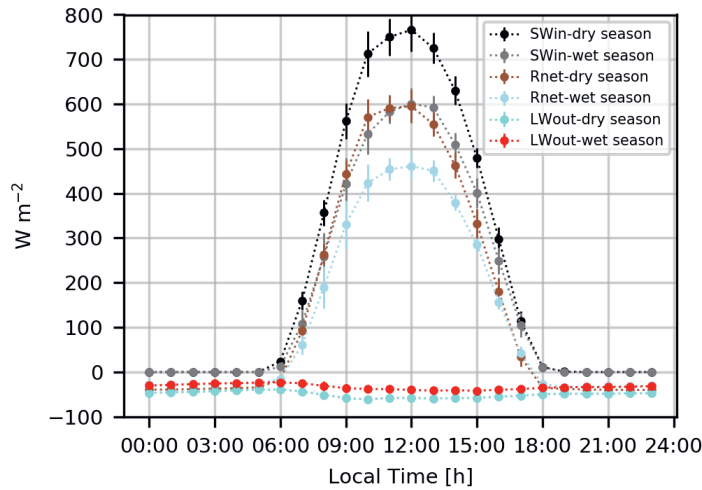
Figure 2.A3: Net, short wave incoming, and long wave outgoing radiation for dry and wet seasons at ATTO.
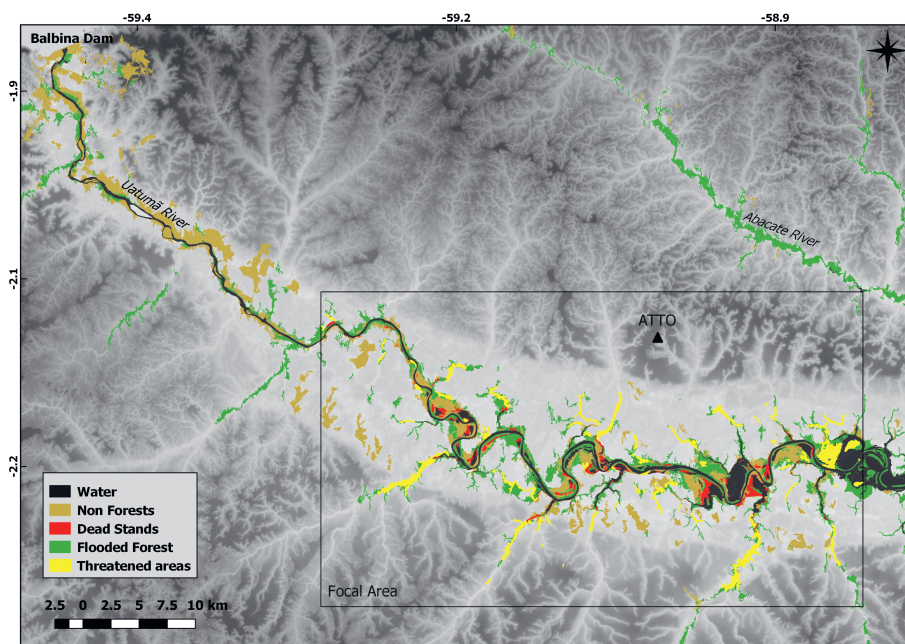
Figure 2.A4: Map showing the dead stands and potentially threatened areas due to the tree mortality caused by the Balbina Dam. This map was modified from Science of The Total Environment, Vol 659, Authors: Angélica Faria de Resende, Jochen Schöngart, Annia Susin Streher, Jefferson Ferreira-Ferreira, Maria Teresa Fernandez Piedade, and Thiago Sanna Freire Silva, Massive tree mortality from flood pulse disturbances in Amazonian floodplain forests: The collateral effects of hydropower production, Pages 587-598, Copyright (2019), with permission from Elsevier.

Chapter 3

The CO$_2$ record at the Amazon Tall Tower Observatory: a new opportunity to study processes on seasonal and inter-annual scales

Abstract

High quality atmospheric CO$_2$ measurements are sparse in Amazonia, but can provide critical insights into the spatial and temporal variability of sources and sinks of CO$_2$. In this study we present the first six years (2014-2019) of continuous, high-precision measurements of atmospheric CO$_2$ at the Amazon Tall Tower Observatory (ATTO, 2.1° S, 58.9° W). After subtracting the simulated background concentrations from our observational record, we define a CO$_2$ regional signal ($\Delta CO_{2_{obs}}$) that has a marked seasonal cycle with an amplitude of about 4 ppm. At both seasonal and inter-annual scales we find differences in phase between $\Delta CO_{2_{obs}}$ and the local eddy covariance net ecosystem exchange (EC-NEE), which is interpreted as an indicator of a decoupling between local and non-local drivers of $\Delta CO_{2_{obs}}$. In addition, we present how the 2015/2016 El Niño-induced drought was captured by our atmospheric record as a positive 2σ anomaly in both the wet and dry season of 2016. Furthermore, we analyzed the observed seasonal cycle and inter-annual variability of $\Delta CO_{2_{obs}}$ together with net ecosystem exchange (NEE) using a suite of modeled flux products representing biospheric and aquatic CO$_2$ exchange. We use both non-optimized and optimized (i.e., resulting from atmospheric inverse modeling) NEE fluxes as input in an atmospheric transport model (STILT). The observed shape and amplitude of the seasonal cycle was captured neither by the simulations using the optimized fluxes nor by those using the diagnostic Vegetation and Photosynthesis Respiration Model (VPRM). We show that including the contribution of CO$_2$ from river evasion improves the simulated shape (not the magnitude) of the seasonal cycle when using a data-driven non-optimized NEE product (FLUXCOM). The simulated contribution from river evasion was found to be 25% of the seasonal cycle amplitude. Our study demonstrates the importance of the ATTO record to better understand the Amazon carbon cycle at various spatial and temporal scales.

3.1 Introduction

Amazonia covers approximately one third of South America, and 70-80% of its area is rain forest (Goulding et al., 2003). This vast expanse of forest stores approximately 85-130 Pg of carbon in above- and below-ground biomass, making it one of the largest carbon pools on the globe (Malhi et al., 2006; Saatchi et al., 2007; Feldpausch et al., 2012; Baccini et al., 2012). Hence, Amazonia plays a fundamental role in the global carbon cycle not only by storing massive amounts of carbon, but also by acting as an immense "biogeochemical reactor" (Andreae, 2001). The exchange between the biosphere and the atmosphere occurs mainly through CO_2 exchange (Friedlingstein et al., 2020). Therefore, atmospheric mole fraction measurements of CO_2 can provide information about this exchange, as they integrate signals from the underlying ecosystem over large scales. Atmospheric CO_2 can thus be used to study the spatial and temporal variability of the dominant sources and sinks of carbon, which in the central part of Amazonia are mainly photosynthesis and respiration (Malhi et al., 2015).

The principal threats to Amazonia are forest degradation and deforestation, agricultural expansion and climate variability (Davidson et al., 2012; Mitchard, 2018). Deforestation was recently shown to cause disturbed rainfall patterns upwind and downwind of the cleared areas during the dry season in Amazonia (Khanna et al., 2017). In addition, deforestation and agricultural expansion are directly associated with biomass burning (van der Werf et al., 2010; Barlow et al., 2020), which in turn can be intensified by severe drought (Gatti et al., 2014; van der Laan-Luijkx et al., 2015; Marengo & Espinoza, 2016; Aragão et al., 2018). Extremes in the hydrological cycle include both droughts and flooding, which can be enhanced by large-scale events, such as those occuring during the extreme phases of the El Niño Southern Oscillation (ENSO) cycle (Marengo & Espinoza, 2016; van Schaik et al., 2018; Malhi et al., 2018). Variability in the hydrological cycle in the Amazon has increased over the last two decades (Gloor et al., 2015), with more frequent extreme events. At the same time, a significant increase in the length of the dry season in southern Amazonia has been reported by Fu et al. (2013). Gloor et al. (2012) suggest that even though biospheric carbon uptake currently compensates for deforestation and fossil fuel emissions in South America, the continent could become a net source of carbon over the next decades, as projected by up-scaled plot level studies (Brienen et al., 2015; Hubau et al., 2020). Therefore, observational ground sites (such as ATTO) that can provide ground truth data for evaluating predictions are critical to improve our understanding of the carbon cycle in Amazonia.

The ecosystem net carbon exchange can be estimated using either a top-down or a bottom-up approach. Atmospheric inversions (i.e., the top-down approach) use measurements of atmospheric CO$_2$ mole fractions to optimize a prior estimate of net ecosystem exchange (NEE) fluxes at global (Gurney et al., 2002; Rödenbeck et al., 2003; van der Laan-Luijkx et al., 2017) and continental scales (Gerbig et al., 2003; Peters et al., 2007; Schuh et al., 2010; Shiga et al., 2018; Kountouris et al., 2018a; Hu et al., 2019). This method is highly dependent on well-calibrated accurate measurements, their spatial density and representativeness (Gerbig et al., 2009). Typically, fluxes in regions with few measurements will be estimated with high uncertainties that will lead to limited understanding of spatial and temporal patterns (Gurney et al., 2002; Peylin et al., 2013; van der Laan-Luijkx et al., 2015; Thompson et al., 2016). Global inverse models have been found to be under-constrained (Gurney et al., 2002; Gaubert et al., 2019) and to a large extent hampered by model uncertainties and insufficient measurements in the Amazon region (Molina et al., 2015). Moreover, the density of remotely-sensed satellite columns over the region, characterized by deep convection, is highly reduced due to persistent cloud cover (Liu et al., 2017; Basu et al., 2018). The combination of these factors makes it difficult to constrain the seasonal and inter-annual variability of carbon exchange in Amazonia (Molina et al., 2015). The aircraft network of CO$_2$ profiles (Gatti et al., 2014) at several sites across Amazonia represents an important advance in the regional effort to improve the observational constraint for inverse modeling studies (van der Laan-Luijkx et al., 2015; Alden et al., 2016), yet identifying the relevant processes responsible for inter-annual and seasonal changes remains challenging.

Process-based biosphere models (representing the bottom-up approach) provide an alternative to constrain carbon exchange accross a wide range of ecosystems (Sitch et al., 2015). However, the inability to reproduce the cycle of gross primary productivity (GPP), which influences the amplitude and phase of NEE at equatorial sites in Amazonia is one of the important limitations of biosphere models (Restrepo-Coupe et al., 2017). Others include e.g. CO$_2$ fertilization effect (Fleischer et al., 2019) and ecosystem respiration (Carvalhais et al., 2014). While process-based model simulations show a decline in dry-season GPP at equatorial sites, presumably based on an incorrect assumption of water-limitation, observations typically suggest that GPP increases during the dry season (Huete et al., 2006; Myneni et al., 2007; Brando et al., 2010; Restrepo-Coupe et al., 2013; Borchert et al., 2015; Wu et al., 2016; Green et al., 2020). This discrepancy may be explained by the lack of leaf phenology in model formulations (Gonçalves et al., 2020). Chen et al. (2020) recently corroborated this by implementing this mechanism in the biosphere model ORCHIDEE, yet it is still missing in other biosphere models.

The evaluation of model-based biosphere-atmosphere flux estimates is generally performed by comparing simulated fluxes with in-situ flux measurements. Eddy-flux and plot-level studies serve such purposes and are valuable for understanding processes and underlying drivers of carbon exchange (Verbeeck et al., 2011; von Randow et al., 2013; Restrepo-Coupe et al., 2017). An alternative approach to evaluate both biosphere models and inverse modeling results is to use surface fluxes as an input in atmospheric transport models, and compare simulated and observed mole fractions at independent measurement sites. This method has the advantage of attributing the observed CO_2 regional signal to a larger spatial area, as compared to local eddy-flux spatial coverage, especially when atmospheric CO_2 is measured at a tall tower (Gloor et al., 2001). However, atmospheric transport errors can add additional biases that should be considered when interpreting patterns at different temporal scales (Gerbig et al., 2008). This leads to different models presenting widely varying perspectives on the processes influencing Amazonia's carbon budget, with most of them being poorly constrained by actual observations.

All things considered, accurate atmospheric CO_2 measurements at high temporal resolution can provide valuable information about the spatial and temporal variability of sources and sinks of CO_2. In this work, we present six years of observations from the Amazon Tall Tower Observatory (ATTO) in central Amazonia, and demonstrate how they can be used to increase our process understanding by identifying the main sources of variability at seasonal and inter-annual scales. Furthermore, we use the CO_2 measurements to evaluate state-of-the-art top-down as well as bottom-up NEE products using an atmospheric transport model. A highlight of this study is that we use three different estimates of NEE fluxes generated using CarbonTracker South America (an inverse modeling system) (van der Laan-Luijkx et al., 2015), the Vegetation Photosynthesis and Respiration diagnostic model (VPRM) (Mahadevan et al., 2008), and a statistically upscaled NEE product (Bodesheim et al., 2018) (FLUXCOM). With such a diverse dataset of NEE fluxes, we cover the inherent variability of different model formulations. We also evaluate the capability of an inversion system, using different data streams for optimization, to constrain the variability of atmospheric CO_2 at ATTO. Thus, we provide valuable insights that will serve not only to better understand the processes that control atmospheric CO_2 at ATTO, but also to evaluate biosphere flux models from an atmospheric perspective.

3.2   Data and Methods

3.2.1   Site description

The Amazon Tall Tower Observatory (ATTO) site (2.14°S, 58.99°W, see Figure 3.1) has been described extensively in Andreae et al. (2015). In this paper, we present aspects considered important for our study. ATTO is located in the Uatumã Sustainable Development Reserve (USDR) in central Amazonia, 150 km northeast of the closest large city, Manaus. The main infrastructure and research facilities were built in the dense upland forest (terra fime, at 130 m a.s.l.), where the highest vegetation is found. The canopy height at the tower location is around 37 m, however the average tree height on the terra firme forest plateau is 20.7 ± 0.4 m (Andreae et al., 2015).

The local precipitation regime shows a distinct seasonality (see Figure 3.A1, left panel), and agrees very well (r=0.8, p-value<0.01) with the Multi-Satellite Precipitation Analysis from the Tropical Rainfall Measuring Mission (TRMM 3B42-daily at a resolution of 0.25 deg, obtained from: `https://disc.gsfc.nasa.gov/datasets/TRMM\_3B42\_Daily\_7 /summary`) (Huffman et al., 2016) sampled at the grid cell closest to ATTO (2.12° S, 58.87° W). However the local measurements show a lower mean annual precipitation (MAP) than the climatological average obtained using the TRMM dataset (1934.1 mm yr^{-1} vs 2382.2 mm yr^{-1}). The monthly and annual mean biases of the TRMM estimate with respect to the local measurements is +40 mm and +489 mm, respectively. The local time series is based on an 8-year record (2012-2019), and thus the seasonal average is highly affected by the 2015/2016 El Niño drought. Therefore, we consider the longer TRMM dataset (ATTO-TRMM 1998-2019 in Table 3.1) to be more reliable as a climatology. Thus, we use the ATTO-TRMM (1998-2019) record as a reference; the dry season length (DSL) is 3 months with a mean dry season precipitation of 63.3 mm month^{-1}. The annual minimum average precipitation (MiAP) is 45.1 mm month^{-1}. A comparison of these values between the local record and the TRMM dataset is shown in Table 3.1. For this study we have defined the climatological dry season as the months whose seasonal median is lower than 100 mm (July to October). For the wet season we selected the months whose 25th percentile was clearly above 200 mm (February to June), see Figure 3.A1 right panel for details.

3.2.2   Atmospheric mole fraction measurements

The continuous measurement system was installed in March 2012 at the 81 m walk-up tower at ATTO and has been described in Andreae et al. (2015) and Botía et al. (2020). Here we highlight the features relevant for this study. The atmospheric mixing ratio data presented here were collected with two cavity ring-down-based analyzers (Picarro Inc., USA), a G1301 and a G1302 measuring CH$_4$/CO$_2$ and CO$_2$/CO, respectively. Both analyzers provide CO$_2$ data at a 15-minute resolution calibrated on the World Meteorological

Table 3.1: Mean annual precipitation (MAP), mean dry season precipitation (DSP), mean dry season length (DSL) and annual minimum average precipitation (MiAP) at ATTO using the local precipitation measurements (2012-2019) and data from the tropical rainfall measuring mission (TRMM) from 1998-2019 (Huffman et al., 2016). For comparison we show the same values reported by Restrepo-Coupe et al. (2017) for the research station (K34) for the period 1998-2014.

Site	Lat (°)	Lon(°)	MAP (mm year^{-1})	DSP (mm month^{-1})	DSL (months)	MiAP (mm month^{-1})
ATTO-Local (2012-2019)	-2.14	-58.99	1934.1	53.2	3.8	25.3
ATTO-TRMM (2012-2019)	-2.12	-58.87	2422.6	63.3	2.8	42.2
ATTO-TRMM (1998-2019)	-2.12	-58.87	2382.2	63.3	3	45.1
k34-TRMM (1998-2014)	-2.61	-60.21	2672.6	99.7	1-2	99.7

Organization (WMO) CO_2 X2007 scale. These data were subsequently averaged to half-hourly data. The overall accuracy of both analyzers, including the uncertainties of the water vapor correction, are estimated to be 0.09 ppm CO_2 (1 ppm = 1 μmol mol^{-1} of dry air).

The analyzers measure the air from five lines connected to inlets located at 79, 53, 38, 24 and 4 m above ground. Downstream of each sampling line, a stainless steel sphere (8 liters volume) acts as a buffer volume. By mixing the sampled air, these buffers integrate the atmospheric signal, allowing a continuous, near-concurrent measurement from all heights (Winderlich et al., 2010). The time series presented here is based on only daytime dry air mole fractions (i.e., 13:00 to 17:00 local time (LT)), representative of well-mixed convective conditions. In order to maximize the data coverage, we use observations from both instruments whenever they are available, with the mean calculated for the periods when both were operational simultaneously. The mean bias between the datasets at half-hourly resolution was estimated to be 0.02 ppm CO_2. The data presented here are available upon request at https://attodata.org (last access: 25 January 2021).

3.2.3   Phenology measurements and leaf area index age classes

Upper canopy leaf phenology is monitored with a RGB Stardot Netcam model XL 3MP (2048×2536 pixels) mounted on the top of the 81 m tower. For an in-depth description of the camera set-up, radiometric calibration and detection of phenostages, we refer the reader to Lopes et al. (2016). We used only pictures obtained in the morning (i.e., no backlit crowns), under cloudy sky or under the shadow of a cloud, providing a spatially even and temporally consistent illumination of the irregular canopy surface. For each crown (n=194), we were able to detect abrupt increase in greenness (i.e., leaf flush) or abrupt green-down (i.e., leaf abscission). By counting the number of individual trees per month for each category (flush or abscission), we built a monthly time series for the period between July 2013 and November 2018. From the trees that the camera sees, 69% (n=134) have clear flushing and abscission patterns, and from these the time series was built.

Using the number of days after each individual flushing event, we determined leaf age classes and attributed a fraction of the upper canopy crowns to an age class at monthly intervals. As in Wu et al. (2016), we defined the following leaf age classes: i) young leaves (0-2 months), ii) mature leaves (2-6 months), and iii) old leaves (>6 months). Next, we partitioned the age classes into classes of leaf area index (LAI) (i.e., young, mature, and old LAI) by normalizing each leaf age class with the total LAI measured at ATTO. We used a constant LAI of 5.32 m^2 m^{-2} for all months, as the variability of this number throughout the year was not statistically significant (unpublished results). For the normalization we took into account the total number of trees in the camera frame (n=194), assuming that the 30% that does not have clear flushing patterns are part of the old age class. For more details on the methods and assumptions for the separation of LAI into leaf age classes, see Wu et al. (2016). LAI was measured using two LAI-2200 PCA sensors (LI-COR Inc., Lincoln, NE, USA) recording simultaneous readings above and within the canopy. The sensor above the canopy (the reference) was installed on the 80 m tower (approximately 50 meters above top canopy). All measurements were performed under diffuse light conditions. The within-canopy measurements were carried out using 40 cm supports (sampling points) on the ground. The spatial sampling design was a square grid with 42 sampling points (21x2 and 80m between points). We carried out monthly campaigns from March 2016 to March 2019. The flushing and abscission data (`http://doi.org/10.17871/atto.223.7.840`) together with the raw LAI age classes (`http://doi.org/10.17871/atto.230.4.842`) are available upon request request at `https://attodata.org`.

3.2.4 Eddy covariance measurements

In this study, we use eddy covariance (EC) measurements from 2014 to 2019. They were done using a 3-D sonic anemometer (CSAT3, Campbell Scientific Inc., Logan, USA) and an open-path infrared gas analyser (LI7500, Li-COR Inc., Lincoln, USA), both installed at the top of the 81 m tower, approximately 40 m above the local canopy top. Half-hourly EC-sensible heat (EC-H), EC-latent heat (EC-LE), and EC-CO$_2$ fluxes were calculated by using EddyPro software (Li-COR Inc., Lincoln, USA). Raw time series data were de-spiked and screened according to Vickers & Mahrt (1997), and data quality control on half-hourly EC-H/LE/CO$_2$ fluxes was carried out following the method of Mauder & Foken (2004). EC flux data meeting the highest quality criteria (flags 0 and 1) for H, LE and CO$_2$ and from the EC-favourable wind direction ([-90° : +90°] sector) were selected for further analysis. The raw eddy-flux data are available upon request at https://attodata.org (last access: 25 January 2021).

Net ecosystem exchange (EC-NEE) was calculated as the sum of the half-hourly EC-CO$_2$ flux and storage CO$_2$ flux. The storage flux was obtained using the 5-inlet CO$_2$ mole fraction profile measurements at the 81 m tower following the calculation procedure of Winderlich et al. (2014).

When the profiles were missing measurements from one or two heights, the storage flux was obtained from 3 or 4 inlets that included both the 4 m and 79 m heights, this occurred only 2.42% of the time over the six years. In cases where only half-hourly EC-CO_2 flux data were available, missing CO_2 storage fluxes were gap-filled with mean diurnal variations over $\pm$ 14-day periods as performed by the REddyProc package (Wutzler et al., 2018). In addition, negative EC-NEE data during nighttime periods (defined as 18:00 to 6:00 with global radiation (R_g) < 20 W m^{-2}) were removed. In cases where nighttime R_g data were not available, we discarded negative EC-NEE data between 19:00 and 5:00.

A distribution of friction velocity (u*) thresholds (5th, 50th and 95th percentiles) in each year was estimated according to Papale et al. (2006) using REddyProc. For this study, we used the yearly median (50th percentile) u* values as representative for our site (see Table 3.A1). Our u* values are lower than those from previous studies due to the higher measurement height (81 m), we refer the reader to Table 3.A2 for a comparison of u* values in other sites in Amazonia. After the u* filtering, 20.4 % of EC-NEE data remained. The effect of having more or less data due to a larger or lower u* threshold does not affect the seasonal cycle of neither EC-NEE, GPP nor R_{eco}, this is shown in Figure 3.A2. The gap-filling of the EC-NEE data was performed using REddyProc and then negative gap-filled nighttime EC-NEE data were screened out. The missing nighttime EC-NEE data were gap-filled by a linear interpolation for less than two missing hours or a mean NEE value over one nighttime period. Nighttime EC-NEE was assigned as nighttime ecosystem respiration (R_{eco}), and daytime R_{eco} was derived from averaging R_{eco} over two adjacent nighttime periods, similar to Restrepo-Coupe et al. (2013). Then, gross primary productivity (GPP) was obtained by subtracting EC-NEE from R_{eco}. We adopted the above NEE partitioning method because nighttime R_{eco} did not correlate well with nighttime air temperature, which is needed for commonly used methods (e.g., the nighttime method (Reichstein et al., 2005), the daytime method (Lasslop et al., 2010) and modified daytime methods (Keenan et al., 2019)). In this study, we interpret EC-GPP (hereafter GPP) as gross ecosystem productivity (GEP).

3.2.5 STILT simulations

STILT model description

The Stochastic Time Inverted Lagrangian Transport (STILT) model (Lin et al., 2003) is useful for diagnosing the impact of surface emissions at a specific measurement location or receptor by resolving transport in the near-field (i.e., the surface with which the planetary boundary layer air has had contact with). STILT simulates the transport in the near-field by following the time evolution of an ensemble of particles (to be interpreted as an air parcel) and by interpolating meteorological fields to the sub-grid location of each particle. Turbulent motions in the planetary boundary layer (PBL) are modelled as a Markov chain

process using turbulent velocity statistics (Lin et al., 2003). Moist convection in STILT uses vertical profiles of convective mass fluxes within updrafts and downdrafts, as well as entrainment and detrainment fluxes into and out of the up- and downdrafts (for details, see Nehrkorn et al., 2010). Vertical profiles of in-cloud mass fluxes are derived from the driving meteorological fields using the Tiedtke scheme (Tiedtke, 1989).

The time-inverted feature of the model refers to the capability of resolving the near-field transport of the particle ensemble prior to its arrival at the receptor location. In this study, the model was run at hourly resolution for the six-year period from 2014 to 2019. Every hour a 100-particle ensemble was released at the receptor height of 80 m above ground, and the back trajectories were calculated for the preceding 10 days to ensure most backward trajectories have left the continent, such that the footprints represent the full influence of surface fluxes on measurements at ATTO. The difference between the modelled receptor height and the air inlet is only 1 meter, which we assume can be neglected.

The model was driven by 3-hourly meteorological fields from ECMWF short-term forecasts (following the contemporary IFS cycle development; for more info see `https://www.ec mwf.int/en/publications/ifs-documentation`). The original meteorological fields were preprocessed and interpolated to a spatial resolution of 0.25° by 0.25°, covering South America between 20°S–15°N latitude and 85°W–35°W longitude bands. The original vertical structure was maintained, however only the 89 lowest of the 137 total levels were used, limiting the top model level to an altitude of about 21 km.

Seasonally-averaged footprint calculation

To better interpret our measurements and attribute signals to particular regions, spatially explicit surface influence maps or footprints were calculated using the STILT model. From the back trajectory particle ensembles we derived hourly-gridded footprints. The footprints are derived at higher spatial resolution (1/12° by 1/8°) than the driving meteorological data, and they can be defined as the flux sensitivity of mole fractions measured at the receptor location, with units of ppm per μmol m^{-2} s^{-1}. To obtain the seasonally-averaged footprints, we first filtered for daytime (i.e., 13:00-17:00 LT at the receptor) values to ensure well-mixed convective conditions at the measurement location. These individual hourly footprints were aggregated to a climatological monthly mean. From these monthly means we averaged over: November, December, January (NDJ), February, March, April (FMA), May, June, July (MJJ) and August, September and October (ASO). The averaging periods were chosen in this way to allow a good distinction between wet and dry seasons (FMA and ASO), as well as the transition periods in between (NDJ and MJJ). The monthly climatology of concentration footprints generated for this study is available at `http://doi.org/10.17871/atto.208.8.811`.

The regional extent of the seasonally-averaged footprints is shown in Figure 3.1 to provide an idea of the dominant vegetation types within the areas of influence. The 50th percentile footprint during NDJ and FMA covers an area of mainly intact forest, whereas in MJJ and ASO the footprints cover areas characterized by a larger presence of disturbed forest, located on the southern bank of the Amazon River. The area of the 50th percentile footprint increases from 208,058 km^2 in NDJ to 236,969 km^2 in FMA and decreases from 244,482 km^2 in MJJ to 207,812 km^2 in ASO. Note that the Cerrado and Caatinga biomes (semiarid ecosystems), are within the 75th percentile footprint in MJJ and ASO, although their relative influence on the signals measured at ATTO is estimated to be low.
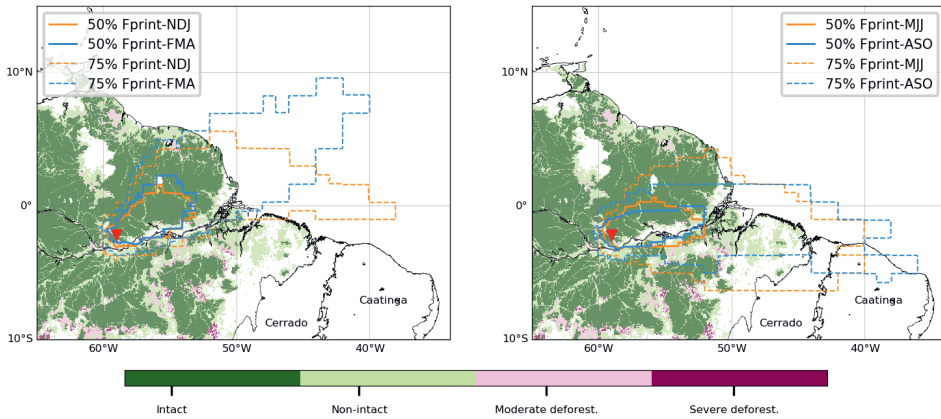
Figure 3.1: The 50th and 75th percentiles for the seasonally averaged footprint for NDJ and FMA (left panel) and MJJ and ASO (right panel) overlain with the distribution of intact forest (dark green), non-intact forest (pale green), moderately deforested (pink) and severely deforested (magenta). Cerrado and Caatinga biomes are labeled but not coloured. The ATTO site is indicated with a red triangle. The distribution of vegetation state is taken from Baker & Spracklen (2019).

STILT tracer simulations

Lateral Boundary Conditions (LBC). As we are dealing with an atmospheric transport model within a limited domain, we have to consider the influence of the air masses entering it at its borders (LBC, Lateral Boundary Conditions) to compare the simulated mole fractions to in situ observations. This additional signal, hereafter also referred to as "background", is added in STILT to the CO_2 mole fractions related to fluxes from within the domain. In the case of ATTO, it is almost exclusively advected from the northeastern or eastern border of our domain (see Figure 3.1). The LBC include the global information that influences our domain of interest, such as the increasing trend due to fossil fuel burning and variations on seasonal and synoptic scales.

In this study, we have used the Jena Carboscope (s04ocv4.3) as our LBC. We refer the reader to Rödenbeck et al. (2003) and to `http://www.bgc-jena.mpg.de/CarboScope/` to get more details on the data assimilated in this system.

The validity of the LBC is a fundamental aspect in our tracer simulations. To assess this validity and potential biases, we evaluated the 3D fields of CO$_2$ used as LBC at three background stations located at the east and northeast of our regional domain: Ragged Point Barbados (RPB, 13.16°N, 59.43°W), Ascension Island (ASC, 7.94°S, 14.35°W) and Cape Verde (CVR, 15.12°N, 23.60°W). We sampled the original global fields at the location of each station and calculated the difference between the simulated and observed mole fractions (see Figure 3.A3). Since the data from the above stations were assimilated in the Jena CarboScope inversion system, they have small Mean Bias Errors (MBE) (-0.09 ± 0.26 ppm at RPB, -0.036 ± 0.28 ppm at ASC and -0.176 ± 0.8 ppm at CVR). Even though these small MBE indicate a strong constraint on the LBC, we have bias corrected the LBC used to calculate the observed regional signal. The magnitude of the bias-correction will be shown in the Results section. We define an observed regional signal ($\Delta CO_{2_{obs}}$, which is bias-corrected) and a simulated regional signal ($\Delta CO_{2_{sim}}$). The first is calculated by subtracting the LBC from the measured CO$_2$ mole fractions, and the second by leaving the LBC tracer out of equations 3.1 and 3.2.

Input fluxes. To obtain simulated mole fractions at the tower location, we coupled the footprints with the surface fluxes at hourly resolution. By adding all the tracer components and the LBC, we can obtain multiple realizations of simulated CO$_2$ mole fractions at the ATTO site that can be compared to observations, and assess how the underlying fluxes affect the simulated signal. To account for all the sources and sinks of CO$_2$ and their uncertainties in Amazonia, we use a wide range of available data sets, including both optimized (i.e., resulting from atmospheric inverse modeling) and non-optimized NEE flux fields (see Table 3.2).

Equations 3.1 and 3.2 show the main tracer components that were added to obtain the integrated CO$_2$ mole fractions at ATTO. The subscripts represent the flux categories associated with different processes and the * indicates we use multiple NEE sources for each equation as we explain below. The complete overview of input flux fields used for each tracer is given in Table 3.2.

$$CO_{2_{TopDown}}[ppm] = \sum CO_{2_k}, \quad k = LBC, NEE^*_{TopDown}, ocean, fires, fossil fuel \quad (3.1)$$

$$CO_{2_{BotUp}}[ppm] = \sum CO_{2_k}, \quad k = LBC, NEE^*_{BotUp}, ocean, fires, rivers, fossil fuel \quad (3.2)$$

As vegetation dominates the CO$_2$ exchange within our domain, we used five Net Ecosystem Exchange (NEE) data sets, three of which are optimized using an atmospheric inversion system.

The atmospheric inversion system (Peters et al., 2005) utilizes available in situ and remote sensing measurements for the assimilation process; it should be noted, however, that observations from ATTO were not assimilated in any of the products discussed here. In equations 3.1 and 3.2, NEE is replaced according to the list in Table 3.2 and thus we obtain five STILT-model results for simulated CO_2 mole fractions at ATTO.

The optimized NEE flux fields (i.e. Top-down) were produced using different settings but the same CarbonTracker Data Assimilation System (CTDAS, van der Laan-Luijkx et al. (2017)). All inversions use the transport model TM5 (Krol et al., 2005), where the default run (CTE2020) uses a global transport resolution of 3° x 2° with 1° x 1° zoom regions over Europe and North America, and two South-America-specific setups of the system (CT-SAM, van der Laan-Luijkx et al. (2015); Koren (2020): CT-SAM-OCO2 and CT-SAM-Flask) use a global resolution of 6° x 4° with a nested zoom over South America of 3° x 2° and 1° x 1°. The three inversions also use different sets of atmospheric CO_2 data for the assimilation: surface flask measurements from ObsPack GLOBALVIEWplus 5.0 (available here: `https://doi.org/10.25925/20190812`) (CTE2020), the same GLOBALVIEWplus 5.0 but with additional aircraft profiles (Gatti et al., 2014) from different locations in Amazonia (CT-SAM-Flask), or OCO2 satellite column retrievals (CT-SAM-OCO2). For the CT-SAM-OCO2 the NASA retrieval v9r was used (`https://docserver.gesdisc.eosdis.nasa.gov/public/project/OCO/OCO2\_DUG.V9.pdf`). The column observations were aggregated to 10-second super observations (following the method described in (Crowell et al., 2019)) and retrievals above water were excluded. CT-SAM optimizes NEE on a gridded state vector of 1° x 1° over South America, whereas CTE2020 optimizes NEE in the region using larger "ecoregions" following the plant-functional types in the prior biosphere model (SiBCASA, Schaefer et al. (2008)). Note that the driving meteorology in CTE2020 uses ERA5 (C3S, 2017) instead of ERA-interim, as in CT-SAM-Flask and CT-SAM-OCO2.

Table 3.2: Input fluxes and lateral boundary condition data sets used in STILT. Column "Input type" indicates whether the fluxes are based on atmospheric inversions (prefix "Opt").

Tracer	Product Name	Input type	Time coverage	Notes	Reference
LBC	Jena CarboScope (s04ocv4.3)	mole fractions	2014-2019	LBC - lateral boundary condition	Rödenbeck et al. (2003)
Ocean	CTE2020	Opt flux	2014-2019	Top-down (TD) and Opt. atm. inversion	van der Laan-Luijkx et al. (2017)
NEE	CTE2020	Opt flux	2014-2019	TD and Opt.	van der Laan-Luijkx et al. (2017)
NEE	FLUXCOM	Flux	2014-2019	Bottom-up (BU)	Bodesheim et al. (2018)
NEE	VPRM	Flux, online	2014-2019	BU	Mahadevan et al. (2008)
NEE	CT-SAM-OCO2	Opt flux	2015-2017	TD, not used for other years (Opt)	Koren (2020)
NEE	CT-SAM-Flask	Opt flux	2014-2017	TD, 2018 and 2019, 2008-2017 average (Opt)	Koren (2020)
Rivers	ORCHILEAK	Flux	2014-2019	1980-2010 - Climatology	Hastie et al. (2019)
Biomass burning	GFAS	Emissions	2014-2019		Kaiser et al. (2012)
Fossil Fuels	EDGAR 4.3.2	Emissions	Annual mean	All sectors, aggregated	Janssens-Maenhout et al. (2017)

The non-optimized NEE fluxes (VPRM and FLUXCOM, i.e. bottom-up) use different approaches. The Vegetation Photosynthesis and Respiration model (VPRM) estimates NEE using a simple diagnostic light-use-efficiency model driven by the Enhanced Vegetation Index (EVI) and Land Surface Water Index (LSWI), derived from surface reflectance measured by the Moderate Resolution Imaging Spectroradiometer (MODIS), together with

2-m air temperature and shortwave radiation at the surface provided from the meteorological model (Mahadevan et al., 2008), in this case STILT. Two parameters per vegetation type (Jung et al., 2006) are optimized based on eddy covariance measurements from 9 sites between 2001 and 2010, obtained from the LBA-ECO repository (`https://daac.ornl.gov/daacdata/lba/carbon\_dynamics/CD32\_Brazil\_Flux\_Network/data/`, last access: 19 October 2020). The FLUXCOM product is derived from up-scaling site-level data (FLUXNET, `http://fluxnet.fluxdata.org/` (last access: 29 September 2020)) to global scales by using a set of predictors which are fed to a random forest regression (Bodesheim et al., 2018). The reader is referred to Bodesheim et al. (2018) and Jung et al. (2020) for more information on the predictors and the up-scaling methods.

We use river CO$_2$ fluxes from the updated version (Hastie et al., 2019) of the ORCHILEAK model (Lauerwald et al., 2017), which uses a high spatial resolution (100 m) wetland distribution map (Hess et al., 2015). We only add the river flux component to the bottom-up simulations, as for the top-down simulations the river signal should be captured by the assimilated observations (Kondo et al., 2020). In order to avoid double counting of fluxes from floodplains, which could be captured by VPRM and FLUXCOM during a low water stage, we only used the river CO$_2$ evasion component from the ORCHILEAK model. The tracers that are not varied in equations 3.1 and 3.2 (i.e., ocean, fires, fossil fuel) are always added to the simulated mole fraction of each STILT-model realization.

We also simulated the anthropogenic signal component using the annual mean emissions from EDGAR v4.3.2 (Janssens-Maenhout et al., 2017) reported for 2012; original gridded emissions (0.1° x 0.1° spatial resolution) from all fossil fuel sectors were aggregated into an emission field of a single tracer. Since anthropogenic emissions are of minor importance in our domain we assumed constant annual emissions in our simulations. For the contribution of biomass burning or fires we use daily emissions from the Global Fire Assimilation System (GFAS) at 0.1° x 0.1° spatial resolution (Kaiser et al., 2012). Last but not least, we use optimized oceanic CO$_2$ fluxes from CTE2020. It is worth mentioning that in CTE2020, different from previous releases, the ocean prior flux is taken from the Jena Carboscope system.

Input flux adjustments for STILT simulations

The input fluxes have been converted for use in STILT into units of μmol m^{-2} s^{-1}. Furthermore, we have adjusted the weekly mean posterior NEE fluxes of CTE2020, CT-SAM-OCO2 and CT-SAM-Flask to represent the original diurnal variability of its prior biosphere model (SiBCASA) before using them as input in STILT. Equation 3.3 describes this adjustment, which projects the original 3-hourly deviations from the monthly average diurnal cycle back onto the weekly mean posterior flux. For CTE2020, equation 3.3 was used for each week (k) that fluxes are available, in which the deviation of the 3-hourly (j=1,..8) flux from the corresponding monthly (i) mean is added to the weekly posterior.

For the CT-SAM-OCO2 and CT-SAM-Flask the prior and diurnal mean NEE in equation 3.3 (1st and 2nd term on the right-hand side) were replaced by its climatology for each month (i=1-12), as their multi-annual record was smaller and included an ENSO extreme event. This adjustment was performed in order to convert monthly optimized NEE fluxes (CTE2020, CT-SAM-OCO2 and CT-SAM-Flask) to hourly resolution and thus couple them with the hourly footprints. This is important because the diurnal variability in atmospheric transport has to be considered for more accurate simulations. We consider that the adjustment is precise enough because the simulated diurnal cycle of CO2 at the tower resembles that of the other simulations which are originally provided as hourly fluxes. This is shown in Figure 3.A4.

$$NEE_{post_{3h_{k,j}}} \quad = \quad (NEE_{prior_{3h_{k,j}}} - DiurnalMeanNEE_{prior_{3h_{i,j}}}) + NEE_{post_{Weekly_k}} \qquad (3.3)$$

3.3 Results

3.3.1 ATTO atmospheric CO_2 time series

The observed CO_2 trend (Figure 3.2a) at ATTO for the 6-year record is 2.38 ppm year^{-1} (2.18-2.60 95% CI), which is very similar to the mean global CO_2 growth rate of 2.49 $\pm$ 0.08 ppm year^{-1} reported by Dlugokencky & Tans (2021) for the same time period. From the monthly record, we can highlight the wet seasons of 2016 and 2019 as two distinctive events of important inter-annual variability in which the footprint of the tower was likely a source of CO_2 to the atmosphere. In the transition from wet to dry seasons, our measurements reach a peak that is followed by a consistent decline throughout the dry season. On average, this decline has an onset in July and August. We also note that the monthly variability is lower in the dry season than in the wet season, strengthening the consistency of the dry season decline.

The simulated background mole fractions (LBC-CScope) have a marked seasonality, reaching the highest values during the wet season, indicating that the air masses coming into our domain are enriched with CO_2. This is in accordance with Figure 3.1, in which we showed that the surface influence during the wet season is oriented to the northeast, bringing air from the northern hemisphere. When subtracting the simulated background mole fractions from our measurements, we can diagnose specifically the regional signal of CO_2, defined as $\Delta CO_{2_{obs}}$ in Section 3.2.5. The seasonal cycle of $\Delta CO_{2_{obs}}$ (Figure 3.2b) has an amplitude of 4.14 ppm (default) and 4.11 ppm (bias-corrected) and two distinct periods in which the signal at ATTO is below the LBC tracer (< 0 ppm). It is worth mentioning that $\Delta CO_{2_{obs}}$ contains information about the real fluxes in our domain, but it also has an atmospheric transport component, making it difficult to interpret it solely as a source (> 0 ppm) or an uptake (< 0 ppm) of CO_2.
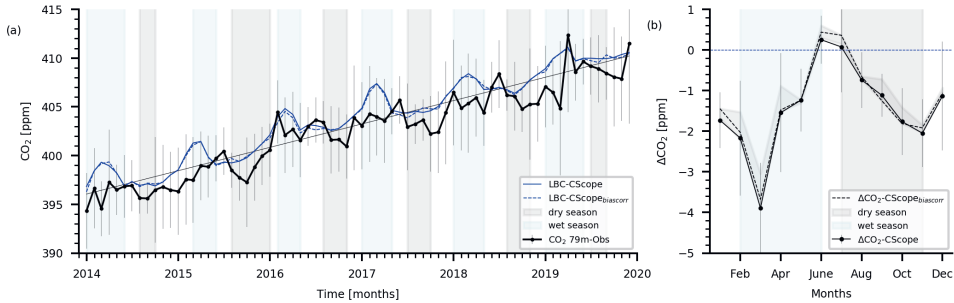
Figure 3.2: Monthly time series of the ATTO CO$_2$ measurements together with the simulated background concentrations without bias correction (continuous blue line) and with bias correction (dashed blue line) (a). The observed mole fractions at ATTO (measurement height 79 m) are shown in a thicker black line in (a) and the error bar represents $\pm 1\,\sigma$. The thin black line represents the linear trend fitted using the Theil-Sen slope. In (b) the seasonal cycle of the regional signal ($\Delta CO_{2_{obs}}$) is shown. The grey shading represents the min-max range given by the spread of the independent $\Delta CO_{2_{obs}}$, calculated using the interpolation between ASC and RPB, and the bias corrected $\Delta CO_{2_{obs}}$. To aggregate to monthly averages we selected only daytime values (i.e. 13:00-17:00 LT) to ensure well-mixed conditions in the PBL. The dry and wet seasons in (b) are the climatological seasons calculated with the TRMM dataset described in Section 3.2.1.

As $\Delta CO_{2_{obs}}$ is the object of study in this paper, we have assessed its uncertainty by obtaining a range between an independent LBC estimate and a bias corrected version of the LBC-CScope. The first, was calculated by taking the measurements at the background stations ASC and RPB and interpolating a new LBC based on the latitude of the STILT-particles once they exit our domain. To account for the minor biases of the LBC-CScope at the background stations, we have bias corrected the LBC-CScope, the magnitude of this correction is shown in Figure 3.2a by the dashed blue line. The min-max range of these two $\Delta CO_{2_{obs}}$ estimates is lower than the inter-annual monthly standard deviation of the $\Delta CO_{2_{obs}}$, which strengthens the robustness of this quantity. For the rest of this study we will use the bias-corrected $\Delta CO_{2_{obs}}$.

Drivers of seasonal variability

$\Delta CO_{2_{obs}}$ is affected by local (eddy covariance scale) and non-local scales (concentration footprint scale). At the local scale, we confront the $\Delta CO_{2_{obs-bio}}$ with the EC-NEE in Figure 3.3a. The $\Delta CO_{2_{obs-bio}}$ was calculated using the bias-corrected $\Delta CO_{2_{obs}}$ and subtracting the simulated contribution of rivers, fires, fossil fuel and ocean. The phase of the seasonality of $\Delta CO_{2_{obs-bio}}$ differs from that of EC-NEE, mainly in January, February and March and in October, November and December.
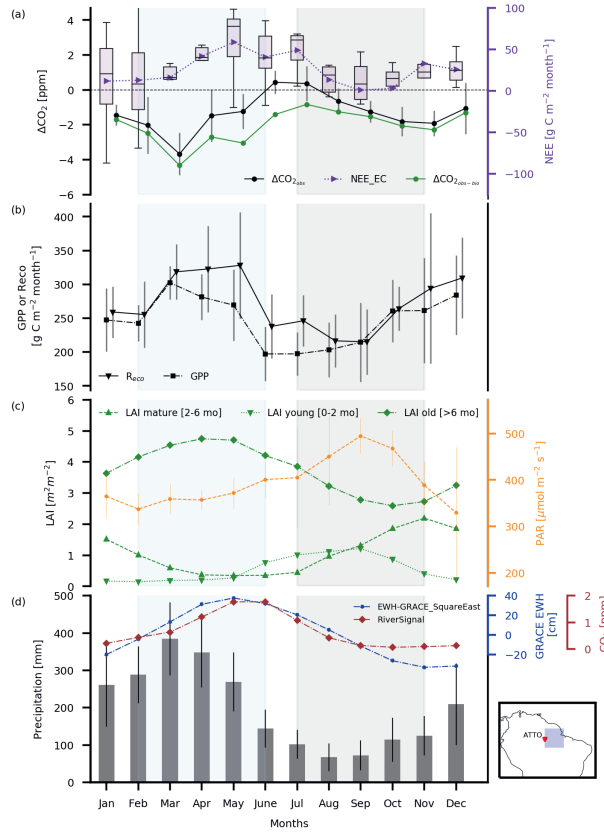
Figure 3.3: Mean seasonal cycle of the observed CO_2 regional signal $\Delta CO_{2_{obs}}$ and $\Delta CO_{2_{obs-bio}}$, together with monthly box-and-whisker plots of the eddy-covariance-derived NEE (EC-NEE) flux are shown in (a). Note that the EC-NEE includes the storage flux and the means are shown as triangles connected by a dotted line. Averaged seasonal cycles of Gross Primary Productivity (GPP) and ecosystem respiration (R_{eco}) (b) and, of Photosynthetic Active Radiation (PAR) together with the age classes of Leaf Area Index (LAI) (c). In (d) the monthly mean precipitation from the TRMM dataset (1998-2019), the STILT-simulated averaged seasonal signal of CO_2 [ppm] evasion from rivers (see Table 3.2 to see input fluxes used in STILT) and the Equivalent Water Height anomalies from the Gravity Recovery and Climate Experiment (GRACE) are shown (all available at: https://grace.jpl.nasa.gov/data-analysis-tool/. Last access: February 02, 2021). The area over which the GRACE data were integrated is marked with a purple square in the small inset on the lower right of (d). The markers in (a) and (b) are shifted to improve visibility and all the error bars represent the monthly standard deviation. The shaded areas in the background highlight the wet (Feb-Jun) and dry (Jul-Nov) seasons. The dry and wet seasons are the climatological seasons calculated with the TRMM dataset described in Section 3.2.1.

From April to July EC-NEE exhibits an increasing source that can influence the increasing pattern in $\Delta CO_{2_{obs-bio}}$. The dry season decline in $\Delta CO_{2_{obs-bio}}$ can be partly attributed to a decrease in EC-NEE which is triggered mainly by a reduction in R_{eco} from May to August and a gradual increase in GPP after August (Figure 3.3b). The effect of atmospheric transport is also important here. For example, the height of the PBL is a variable that affects the measured CO_2 mole fractions at the tower. The PBL height tends to be deeper during the dry season (1300-1500 m) than in the wet season (1100-1200 m), which means that the volume in which CO_2 mole fractions are diluted is larger, causing more negative $\Delta CO_{2_{obs-bio}}$. This example illustrates how the seasonal effects of the footprint and the PBL height can influence $\Delta CO_{2_{obs-bio}}$. The observed phase differences indicate that $\Delta CO_{2_{obs-bio}}$ can decouple from the local EC-NEE in some months of the year, suggesting that the seasonality in $\Delta CO_{2_{obs-bio}}$ is controlled by overlapping effects of local and non-local drivers.

One of the most important non-local drivers of $\Delta CO_{2_{obs-bio}}$ is the heterogeneity of NEE across the seasonally-changing footprint area. The amplitude of the seasonal cycle of EC-NEE in Amazonia varies along the precipitation gradient (Saleska et al., 2009). Locations with a higher mean annual precipitation (MAP) ($>$2500 mm year^{-1}), like K34 (2.61° S, 60.21° W) have a smaller seasonal cycle amplitude, whereas drier sites (2000-2200 mm year^{-1}) further east in the Tapajós National Forest (K67 and K83) display a more pronounced seasonal cycle (Saleska et al., 2009). EC-NEE at ATTO (2.14° S, 58.99° W) shows interesting patterns as it falls between the range mentioned above, with a MAP of 2382 mm year^{-1} and a seasonal EC-NEE range of approximately 60 g C m^{-2} month^{-1} (600 kg C ha^{-1} month^{-1}). Thus, we observed a seasonal variability with a midyear source peak, different from the sustained net uptake throughout the year reported for K34 by Restrepo-Coupe et al. (2017). ATTO is located about 140 km northeast of K34: the sites are relatively close, yet exhibit different MAP and seasonal EC-NEE patterns. ATTO EC-NEE is more similar to that measured at the Tapajós National forest in having a dry season decline, reaching neutrality in September and October (Saleska et al., 2003; Goulden et al., 2004; Baker et al., 2008; Hayek et al., 2018), but it differs in that the wet season shows on average a weak source, which after March increases towards a seasonal peak in May. Interestingly, the ATTO EC-NEE seasonality has a similar phase to the Caxiuanã (CAX) site (Restrepo-Coupe et al., 2017). Following the classification in Saleska et al. (2009), the EC-NEE amplitude at ATTO falls close to the sites where R_{eco} is the most important factor.

From the $\Delta CO_{2_{obs-bio}}$ perspective, R_{eco} can be important from March to July, when EC-NEE and $\Delta CO_{2_{obs-bio}}$ are in phase. Further inspection of the local processes at ATTO indicates that R_{eco} correlates significantly with EC-NEE (r=0.55, p-value $<$ 0.01). Furthermore, river CO_2 evasion (Figure 3.3d) could also contribute to $\Delta CO_{2_{obs}}$, mainly from April to July, with a peak contribution of 1.7 ppm in May and June. Simulated aquatic CO_2 signals are in phase with water levels as shown by the Equivalent Water Height

anomalies. We consider this timing realistic, as CO_2 evasion from rivers and floodplains is enhanced at high water stages (Richey et al., 2002; Amaral et al., 2020), due to larger inundation areas and an increased water depth that leads to more respiration in the water column (Devol et al., 1995; Forsberg et al., 2017). Considering that the tower's STILT footprint during MJJ covers the main branch of the Amazon River (see Figure 3.1), we believe aquatic signals play an important role when interpreting the seasonal cycle of CO_2 measurements at ATTO.

GPP was found to be negatively correlated with EC-NEE but not significantly (r=-0.14, p-value=0.21). Therefore, the offset of photosynthesis by R_{eco} suggests that the first is less important for $\Delta CO_{2_{obs-bio}}$ at the local scale. Nevertheless, the local processes controlling GPP during the dry and wet seasons are worth highlighting here. The gradual rise in GPP during the dry season is driven by increasing light availability and a younger age distribution of leaves in the canopy (Figure 3.3c). Note that PAR increases simultaneously with a decline in the old class of leaf area index (LAI) and the increment of the mature and young LAI classes. Such leaf demography dynamics are similar to what Wu et al. (2016) showed for other sites in Amazonia, and consistent with the dry season green-up reported by several in-situ (Restrepo-Coupe et al., 2013; Lopes et al., 2016) and regional (Huete et al., 2006; Doughty et al., 2019) studies. Moreover, Wu et al. (2016) demonstrated that mature leaves are the most light-use efficient with the highest photosynthetic capacity (mol CO_2 mol^{-1} photon^{-1}) of all leaf age classes. Thus, the seasonal shift in LAI age classes produces a younger age composition of the canopy relative to the wet season, which on average has a higher photosynthetic capacity per leaf area (Wu et al., 2016; Albert et al., 2018). In addition, reduced GEP (interpreted here as GPP) for June and July was reported by Restrepo-Coupe et al. (2013) and Wu et al. (2016) for equatorial sites (e.g. Tapajós National Forest (K67), Cuieras Reserve (K34), and Caxiuana National Forest (CAX).

Drivers of inter-annual variability

Although our CO$_2$ time series is rather short for inferring inter-annual patterns, we present the response of $\Delta CO_{2_{obs}}$ and $\Delta CO_{2_{obs-bio}}$ to the 2015/2016 El Niño-induced drought (Figure 3.4a). Interestingly, the standardized anomalies of $\Delta CO_{2_{obs}}$ and $\Delta CO_{2_{obs-bio}}$ follow the same pattern, suggesting that the inter-annual variability is controlled by the vegetation signal and that contributions of rivers, fires, fossil fuels and ocean are negligible at this scale. For this reason, in the rest of this Section we refer to $\Delta CO_{2_{obs}}$ only, but the findings apply equally to $\Delta CO_{2_{obs-bio}}$.

The $>+1\sigma$ anomaly of $\Delta CO_{2_{obs}}$ in MJJ coincides with the onset of the El Niño, which started in June of 2015, with values above 1 according to the Multivariate El Niño Index (MEI) (Figure 3.4b). In the dry season of the same year (ASO), we observe a -1σ anomaly, illustrating a variable response of $\Delta CO_{2_{obs}}$ to El Niño in 2015. In contrast, in 2016 our observations reveal two $>+1.5\sigma$ anomalies, centered in the wet and dry seasons. Note that El Niño lasted until May in 2016, but the effects in $\Delta CO_{2_{obs}}$ seemed to persist well into the dry season of 2016.

It is interesting to note that the local EC-NEE (Figure 3.4a) anomaly is not always in phase with that of $\Delta CO_{2_{obs}}$. In 2015 the EC-NEE anomaly was in opposite sign to that of $\Delta CO_{2_{obs}}$ during MJJ and ASO, while in 2016 they followed similar patterns. Such differences in phase between EC-NEE and $\Delta CO_{2_{obs}}$ anomalies suggest that in 2015 the effects of El Niño at the EC-NEE scale were apparent only after ASO, whereas in the $\Delta CO_{2_{obs}}$ record it was already evident in MJJ. Therefore, the 2015 anomalies appear to be driven by a non-local (i.e. larger than the EC-NEE footprint) response to the El Niño. In contrast, the contribution to the positive anomalies in 2016 appears to be both at the local and non-local scales.

The variable response of the $\Delta CO_{2_{obs}}$ anomalies in 2015 are marked by an erratic behavior, showing opposing signs in MJJ (+) and ASO (-). The MJJ event is driven by an above average value in July, whereas that in ASO is pulled down by a negative value in September and October (not shown). Our eddy covariance data suggest that the $\Delta CO_{2_{obs}}$ positive anomaly in July can not be attributed to a local source of carbon, as the EC-NEE (see Figure 3.A5) for 2015 was within the seasonal variability of the 2014-2019 record. The negative anomaly in ASO, can not be explain by local factors either. A reduction in the observed CO$_2$ mole fractions due to a deeper boundary layer height, a 15% percent increase with respect to 2014 as shown by Carneiro & Fisch (2020), is likely but non-local factors are yet to be studied. Interestingly, the GPP reductions in 2015 reported in Koren et al. (2018) and van Schaik et al. (2018) for the region that overlaps with our MJJ footprint (i.e. Region B in that study) have an onset in October, failing to explain our July observation and indicating that the effect of the extreme heat and drought had a late onset at ATTO.
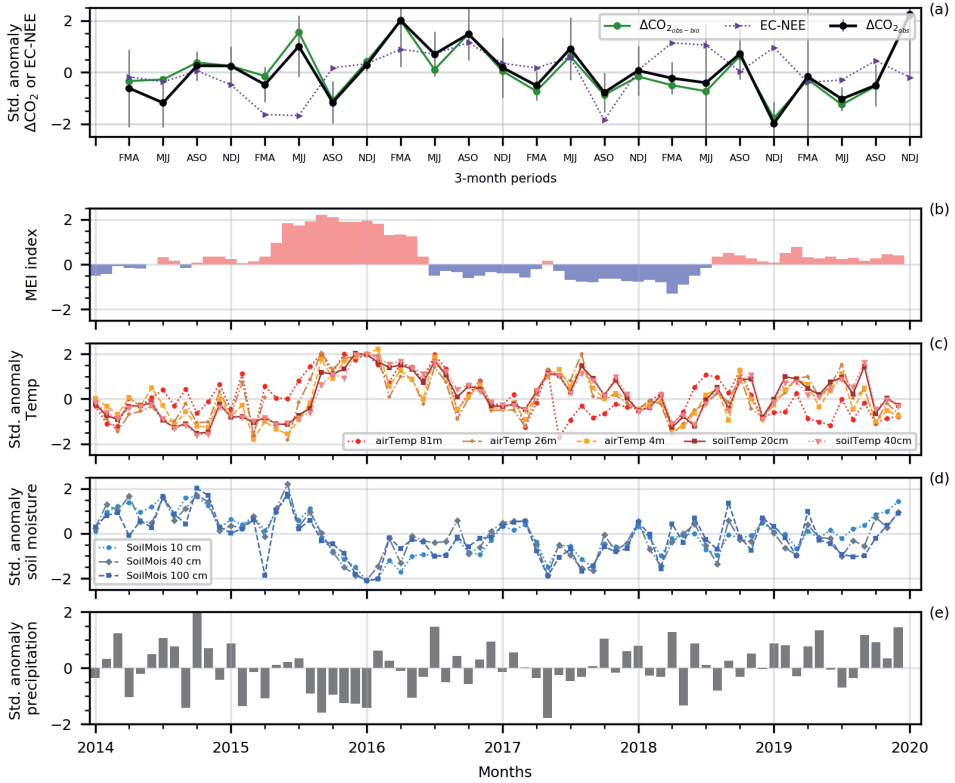
Figure 3.4: Standardized anomalies of $\Delta CO_{2_{obs-bio}}$, $\Delta CO_{2_{obs}}$ and EC-NEE (a) averaged over three-month periods, calculated against the 2014-2019 period, centered on the wet (FMA) and dry (ASO) seasons, with transition periods in between (MJJ and NDJ). The error bars denote the standard deviation for each season, calculated before aggregating to the seasonal mean. In (b) the bi-monthly Multivariate El Niño index shows the strength of the El Niño event as measured by five different variables and aggregated in one index (data obtained from: https://psl.noaa.gov/enso/mei/; accessed on June 10, 2020), with values higher than 0.5 corresponding to a strong El Niño event. In the last panels, we show monthly standardized anomalies of air temperature at 81, 26 and 4 m and soil temperature at 20 and 40 cm (c), soil moisture at 10, 40 and 100 cm in (d) and precipitation (e). Soil moisture, air and soil temperature were measured at the ATTO site. Precipitation is taken from the TRMM dataset (1998-2019).

The positive anomaly in $\Delta CO_{2_{obs}}$ during the dry season of 2016 has local and non-local contributions. Locally, a source of carbon in our EC-NEE record, driven by a higher than normal R$_{eco}$ (Figure 3.A5), can explain the $\Delta CO_{2_{obs}}$ 2016-ASO anomaly. Non-local drivers of this anomaly are attributed to a drought legacy effect (Kannenberg et al., 2020) that has been already characterized by Koren (2020) using atmospheric inverse modeling and remote sensing. Koren (2020) reported basin-wide positive anomalies in top-down-NEE and reductions in remote sensing proxies for GPP in the dry season of 2016. Persistent soil moisture depletion following the 2015/16 El Niño was put forward as a potential mechanism driving this legacy drought. A contributing factor to this 2016-dry-season anomaly, based on the results by Wu et al. (2016) and Gonçalves et al. (2020), is that drought in 2015 caused some trees (approximately 15%) to undergo an anomalous leaf flush in March of 2016 (see Figure 3.A6). This precocious flush altered the normal leaf age distribution over the following months, such that the abundance of photosynthetically efficient mature-stage leaves (2-6 months of age) was spread out over a longer period.

The meteorological effects of El Niño at local scale were measured later in 2015. Positive anomalies in air temperature within and above the canopy together with soil temperature (Figure 3.4c) reached values close to $+2\sigma$ from November of 2015 to February of 2016. The negative soil moisture anomalies in the last four months of 2015 were driven by the negative precipitation anomalies during the same time (Figure 3.4d,e). The soil moisture anomalies at 40 cm and 100 cm bounced back to values higher than -1σ in March 2016. However, even when precipitation returned to close-to-climatology values in February and March 2016, soil moisture at 10 cm depth did not fully recover until late 2016. This pattern shows a fast recovery in deep soil moisture compared to a persistent ($<$-1σ) soil moisture anomaly at 10 cm depth. The re-wetting of deeper layers, together with a still high soil temperature anomaly at 20 and 40 cm depth, could have reactivated heterotrophic respiration leading to above-average soil respiration rates during the wet season of 2016 (see Figure 3.A5).

The $\Delta CO_{2_{obs}}$ anomalies in the transition months of NDJ in 2018 and 2019 occurred in the absence of a large scale climate-driven phenomenon. Based on the EC-NEE response, it seems that both $\Delta CO_{2_{obs}}$ anomalies are due to non-local signals. During the 2018-NDJ event, all meteorological variables (air temperature, soil moisture and temperature, and precipitation) were within the 1σ range. To interpret the signals in 2019, it is worth mentioning two aspects. First, the 2019-NDJ average contains values only for November and December, as January data were not yet available at the time of writing. Second, the year 2019 was characterized by widespread fires driven by deforestation which began early in the year (Barlow et al., 2020). Thus, we suggest that the 2019-NDJ positive anomaly could have a contribution from fires, but the magnitude could be reduced when the January average is included.

3.3.2   STILT tagged tracer simulations

Simulated CO₂ and spatial distribution at seasonal scale

At the ATTO site, a clear seasonal variation of the footprint throughout the year (Figure 3.5a) can be observed, consistent with the large scale atmospheric circulation of the intertropical convergence zone (ITCZ) previously described in Andreae et al. (2012) and Pöhlker et al. (2019). The seasonal atmospheric circulation affects the mole fractions measured at ATTO by varying the areas of near- and far-field influence of the surface fluxes and also the origin of the background air masses. In general, during the wet season ATTO is located to the north of the ITCZ and is under the influence of the air coming from the Northern Hemisphere (NH), whereas during the dry season, the station is located south of the ITCZ, and thus the long range transport is from the Southern Hemisphere (SH) (Andreae et al., 2015). It is worth highlighting that during MJJ and ASO the main branch of the Amazon River is well covered by the 50th and 75th footprint percentiles.

The different NEE fluxes used as inputs in STILT show large spatial variability amongst them (Figure 3.5b-d). While CTE2020 and CT-SAM-Flask follow a similar spatial pattern, CT-SAM-OCO2 tends to predict a larger source of carbon to the atmosphere in MJJ. When comparing the bottom-up fluxes (Figure 3.5e-f) to those resulting from atmospheric inversions, it is clear that the former shows a stronger sink, which is particularly visible in the FLUXCOM data. The main differences between FLUXCOM and VPRM are the source regions in NDJ and ASO, more pronounced in FLUXCOM than in VPRM. Despite the aforementioned differences, in the core of the dry season (ASO) all products are consistent (with varying extent and magnitude) in the source regions in northeastern Brazil, in the states of Ceará, Pernambuco, Bahía, Piauí and Tocantins (see Figure 3.A7 for the names and locations of the northeastern states of Brazil).
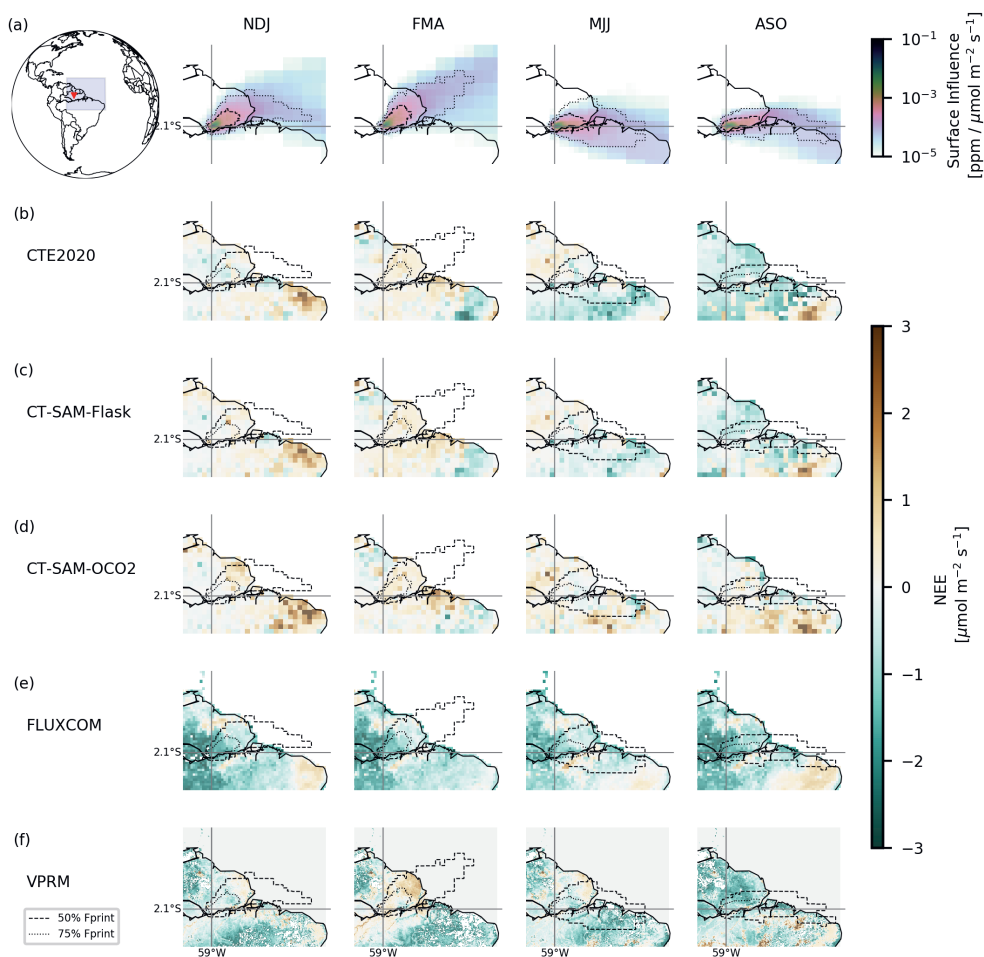
Figure 3.5: Seasonally-averaged concentration footprint (row a) for the inlet level of 80 m. These footprints were calculated with the output of hourly simulations of the STILT model covering the 2014-2019 time period. The first column in row (a) shows the regional context of the footprints and highlights the area shown in the rest of the panels. The ATTO site is indicated with a red marker. In the rest of the panels the location of the research site is indicated by the intersection of the parallel and meridian lines. NEE fluxes are shown in rows b to f.

We find that none of the simulations accurately capture the amplitude of $\Delta CO_{2_{obs}}$. Only in the case of FLUXCOM, does the shape of the seasonal cycle show a decline in the dry season and a wet-to-dry season increase similar to the pattern observerd at ATTO. The latter increase is also better predicted if the original product is augmented with additional fluvial fluxes (compare both panels in Figure 3.6). However, FLUXCOM-driven mole fractions predicted by our model are constantly lower than our measurements by 5 ppm, indicating a strong and persistent uptake of CO_2 (negative NEE) as shown in Figure 3.5. Such a strong sink was expected, as this product was previously found to have a too strong tropical carbon sink, due to a mixture of systematic biases in the eddy-covariance data used in upscaling, and the lack of site history effects on NEE (Jung et al., 2020). Simulations of $\Delta CO_{2_{sim}}$ based on VPRM, CTE2020, CT-SAM-Flask and CT-SAM-OCO2 fluxes show a very different seasonal cycle than $\Delta CO_{2_{obs}}$, showing an earlier and more rapid drop to a minimum in July. In terms of the amplitude of the seasonal cycle, VPRM predicts the largest with 5.94 ppm, followed by CTE2020 with 5.88 ppm, CT-SAM-OCO2 with 5.07 ppm, CT-SAM-Flask with 4.94 ppm and finally FLUXCOM with 3.21 ppm. The last two are the closest to the observed $\Delta CO_{2_{obs}}$ of 4.14 ppm.

The accuracy of the VPRM simulations was worse than expected considering that the model parameters were calibrated using eddy covariance measurements at several sites within Amazonia (Mahadevan et al., 2008). We find that the dry season increase in VPRM-$\Delta CO_{2_{sim}}$ could be triggered by increasing simulated R_{eco} associated with increasing temperature. VPRM represents R_{eco} as a linear function of temperature and does not include the effects of moisture (Mahadevan et al., 2008). Furthermore, the decrease in VPRM-$\Delta CO_{2_{sim}}$ from May to July, which anticipates that of $\Delta CO_{2_{obs}}$ by a month, could also be associated with the lack of moisture effects in R_{eco}. Note that the eddy covariance R_{eco} is higher than GPP from May to June in Figure 3.3b, suggesting an overall source of carbon to the atmosphere.

Simulated inter-annual variability and tracer contribution

In general, the observed inter-annual variability is not well captured by our STILT simulations (Figure 3.7a). In particular for the 2015 and 2016 anomalies associated with El Niño, the simulations show either an anticipation of the anomaly (i.e. 2015-NDJ) or output a signal with an opposite sign (i.e. 2016-ASO). Despite the spread between models in 2014-MJJ, 2015-MJJ and 2018-FMA, it is worth highlighting the general agreement between them, not only in 2015-NDJ and 2016-ASO but also in 2017-ASO, 2018-ASO, 2019-ASO and 2019-NDJ. The latter indicates that the disagreement between simulations is largest in the first part of the year, in which the influence of river CO_2 is predicted to be highest.

The influence of rivers, fires, fossil fuel emissions and ocean fluxes on the simulated CO_2 signal is very small compared to that of NEE (Figure 3.7b-e). Note that the simulated
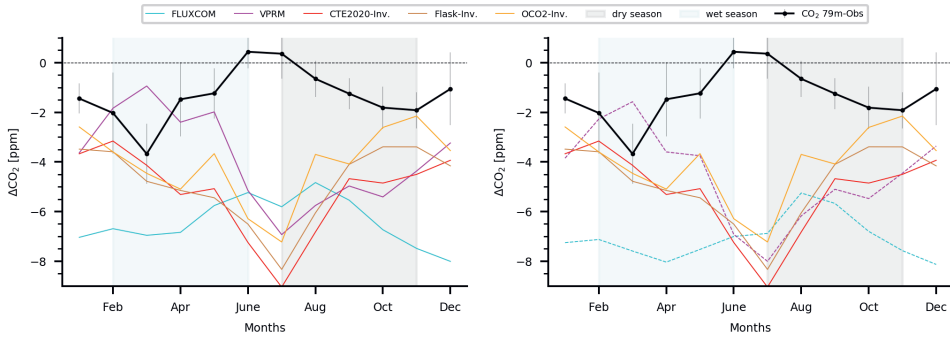
Figure 3.6: Mean seasonal cycle of the regional signal for each of the simulated ($\Delta CO_{2_{sim}}$) and observed ($\Delta CO_{2_{obs}}$) mole fractions of CO_2. On the left panel the simulations using bottom-up NEE fluxes (i.e. VPRM and FLUXCOM) include the river signals. On the right panel river signals are not included in the bottom-up NEE fluxes, shown with a dashed line. The error bar in the observations represents $\pm 1\ \sigma$. For the simulated and observed mole fractions we selected only daytime values (i.e. 13:00-17:00 LT) to ensure well-mixed conditions in the PBL. The dry and wet seasons in are the climatological seasons calculated with the TRMM dataset.

NEE contribution in general tends to show a sink of CO_2, mainly in the transition from wet to dry season, in contrast to $\Delta CO_{2_{obs}}$ and $\Delta CO_{2_{bio}}$. For the $\Delta CO_{2_{bio}}$ the signal from rivers, fires, fossil fuels and ocean was subtracted, which did not change the seasonal pattern when compared to $\Delta CO_{2_{obs}}$. Rivers contribute with 1 to 2 ppm depending on the month of the year. Note that the spatial resolution of the gridded flux for rivers is coarse (1° x 1°) and we have used a monthly climatology from Hastie et al. (2019) in STILT, thus the variable magnitude from year to year in the river tracer is mainly due to atmospheric transport. Fires and anthropogenic emissions (fossil fuels in equations 3.1, 3.2) add up to a contribution ranging from 0.2 to 0.4 ppm, concentrated in the dry season. The ocean is the least significant tracer component, contributing less than 0.1 ppm to the regional signal, reaching the highest values during NDJ. These simulations highlight the relevance of CO_2 evasion at the ATTO site.

When evaluating the model performance at a monthly scale, the CT-SAM-OCO2 simulation was the best, with an RMSE of 4.15 ppm. Note that the CT-SAM-OCO2 simulations were performed only for three years (i.e. 2015-2017). The VPRM and the CT-SAM-Flask followed with RMSE values of 4.21 ppm and 4.63 ppm respectively. CTE2020 and FLUX-COM had higher RMSE values with 4.96 ppm and 5.6 ppm. These RMSE scores are indicative of regional fluxes not covered by our footprints or the LBC, or from differences in vertical transport between the STILT model used for the footprints relative to the TM5 model (used in CarbonTracker).
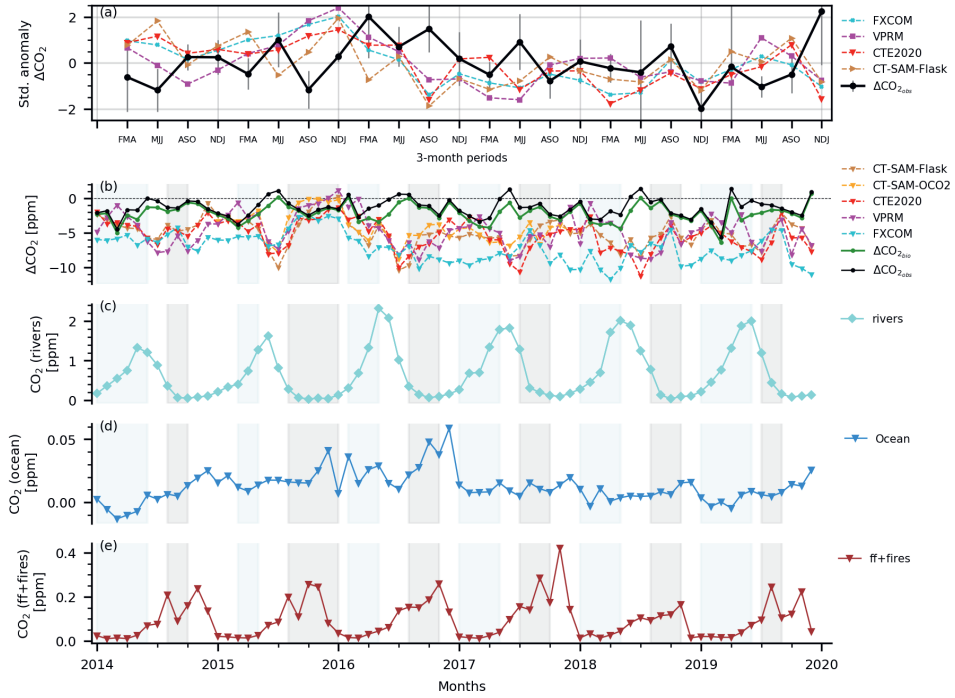
Figure 3.7: Standardized anomalies of $\Delta CO_{2_{obs}}$ and the simulated tracers in STILT (a) averaged over three-month periods, calculated against the 2014-2019 period and centered on the wet (FMA) and dry (ASO) seasons, with transition periods in between (MJJ and NDJ). The error bars denote the standard deviation for each season, calculated before aggregating to the seasonal mean. Thus, it shows the internal variation of each season for each year. Note that CT-SAM-OCO2 is not shown here since we did not have enough simulated years to calculate an anomaly. The climatological standard deviation used for the standardization is shown in Figure 3.A8. The monthly contribution of simulated NEE, $\Delta CO_{2_{obs}}$ and $\Delta CO_{2_{bio}}$ is shown in (b). $\Delta CO_{2_{bio}} = \Delta CO_{2_{obs}} - (river, ff, fires, ocean)$. In (c), (d) and (e), the contribution of rivers, oceans and fires and fossil fuels are shown. Note the different scales on the y-axis.

3.4   Discussion

3.4.1   Decomposing the $\Delta CO_{2_{obs}}$ signal

We showed that $\Delta CO_{2_{obs}}$ is controlled by local and non-local factors. The phase match/mismatch at seasonal and inter-annual scales between EC-NEE and $\Delta CO_{2_{obs}}$ was described as an indicator of the different spatial extents driving $\Delta CO_{2_{obs}}$. Amongst the local factors analyzed was EC-NEE, which was partitioned into GPP and R$_{eco}$ to better understand the underlying processes contributing to the local net flux. GPP and R$_{eco}$ presented a considerable seasonal variation, mainly characterized by a R$_{eco}$-dominated wet season and a late dry season increase in both GPP and R$_{eco}$. Seasonally, we found that EC-NEE was mainly controlled by R$_{eco}$. However, it is worth mentioning that when leaving 2015 and 2016 out of our analysis, we see a clear sink in the EC-NEE during the dry season. In contrast, focusing only on 2015 and 2016 we observe a suppression of GPP during the dry season and EC-NEE shows a sustained source as R$_{eco}$ is always larger than GPP. Therefore, seasonally we observed a larger role of R$_{eco}$ and a clear effect of the 2015/2016 El Niño in GPP, R$_{eco}$, EC-NEE and $\Delta CO_{2_{obs}}$ (see Figure 3.8).
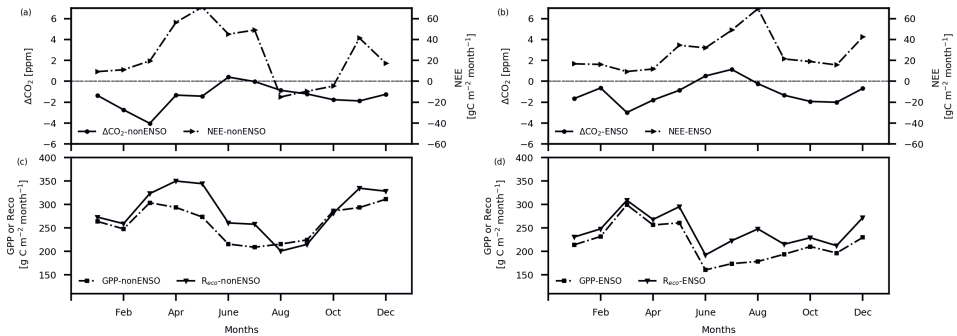
Figure 3.8: Regional CO$_2$ signal ($\Delta CO_{2_{obs}}$) and EC-NEE averaged over non-ENSO years (2014, 2017-2019) (a) and ENSO years 2015-2016 (b). In (c) and (d) the same time periods are shown but for GPP and R$_{eco}$.

At a more regional scale, the effects of the 2015/2016 El Niño-induced drought in Amazonia have been studied from multiple perspectives. The immediate effects of the drought (namely occurring in 2015 and 2016) caused reductions in GPP (Liu et al., 2017; van Schaik et al., 2018) (in line with our local measurements) and sun-induced fluorescence (SiF) (Koren et al., 2018; Castro et al., 2020). The study of Castro et al. (2020), which described the effect of the 2015/2016-El Niño event on SiF across the Amazon basin, sheds light on the variable response of vegetation to drought. At the regional scale, they found a widespread reduction in SiF, yet at the eco-region scale where ATTO is located, SiF reductions were comparatively less. However, Doughty et al. (2021) found positive

anomalies in SiF and GPP at the Amazon basin scale and at the grid cell in which ATTO is located. Therefore, the debate about the sign of the anomaly in 2015 remains open. The effects of the 2015/2016 El Niño drought caused long-term impacts on vegetation, Wigneron et al. (2020) found that the above-ground carbon stocks did not recover until 2017. Furthermore, top-down studies of previous droughts (Gatti et al., 2014; van der Laan-Luijkx et al., 2015) have shown that the Amazon carbon budget can turn from almost neutral in a wet year (i.e., 2011), into a source during drought (i.e., 2010). A reduction in biospheric uptake and an increase in CO_2 fire emissions were suggested as the main causes for the regional response in 2010, which was well captured by widespread aircraft measurements of CO_2 concentrations over the basin. Given these previous findings, local/non-local GPP reductions, long-term vegetation effects and fire emissions are factors that can in principle influence $\Delta CO_{2_{obs}}$, in addition to the role of R_{eco} and river signals, which were presented in our results. However, for the present study we found that even during the 2015/2016-El Niño the fire contribution to the local measurements was very small (see Figure 3.7), yet we do not rule out that this can be more important in the future, with a possible expansion of the agricultural frontier within the $\Delta CO_{2_{obs}}$ footprint.

The differential response of vegetation within the seasonally-changing footprint is an important non-local driver of $\Delta CO_{2_{obs}}$ that is worth discussing further. We have already mentioned the findings of Castro et al. (2020) in which they showed substantial variability of SiF at the eco-region scale. However, within the ATTO eco-region the SiF reductions were not as large as those regionally, which is in contrast to the effect of the 2015/2016-El Niño on GPP at ATTO, which showed a notable reduction in 2015 (see Figure 3.A5). This apparent discrepancy remains to be studied further, however some plausible hypotheses are a non-linear behavior between SiF and GPP caused by extreme heat and drought (Martini, D. 2021 personal communication) in 2015 or that the GPP reduction observed at ATTO was a local phenomenon within the eco-region used in Castro et al. (2020). Nevertheless, Doughty et al. (2021) showed a linear relationship of GPP and SiF at different spatial scales, so the discrepancy of our eddy tower GPP with both SiF studies remains to be studied further.

Now, shifting to a more seasonal perspective, sites at the Tapajós National Forest (K67 and K83) and Caxiuanã (CAX) show a dry-season increase in GPP, which is driven by leaf age and not by seasonal LAI (Wu et al., 2016). It is interesting that at ATTO we observe this dry-season GPP increase on the mean seasonality, yet the amplitude of EC-NEE is different at all sites, being larger at the Tapajós sites followed by ATTO, CAX and K34 (Saleska et al., 2009). At the sites with larger EC-NEE amplitude, the role of R_{eco} modulating the EC-NEE is more important, which in turn is determined by the annual average rainfall as shown by Saleska et al. (2009). A further example of regional heterogeneity is given by the study of Restrepo-Coupe et al. (2013), in which they showed that sites where the dry season is very long or the soil is shallow, GPP does not increase

during the dry season. This is the case for Rondônia, which has a long dry season similar to the Tapajós sites but with a shallow rocky soil, while Tapajós has deep soil which buffers the water available to plants (Nepstad et al., 2007).

The seasonal patterns of R_{eco} can be grouped into water-limited and oxygen-limited sites (Saleska et al., 2009). Water-limited sites, like the one in the Tapajós National forest (Saleska et al., 2003; Hutyra et al., 2007), exhibit dry season declines of R_{eco} as a result of an inhibited heterotrophic respiration due to a long dry season length that leads to the desiccation of decomposition sources near the surface (Saleska et al., 2003). The soil component of R_{eco} at oxygen-limited sites is inhibited with increasing soil moisture content, which is the case for K34 (Chambers et al., 2004). Our results suggest that the R_{eco} at ATTO follows an oxygen-limited regime with a MAP of 2383 mm year^{-1} despite having a relatively long dry season length (3 months, see Table 3.1). Note that when including 2015 and 2016 in our analysis, R_{eco} does not show an increase in October, being suppressed during the dry season (see Figure 3.8). Therefore, the response of R_{eco} to disturbance at ATTO is in contrast to what was reported by Davidson et al. (2004) after a rainfall exclusion experiment for another site located on clay-dominated soil, where no significant effect was found.

One of the novelties of our study is the use of results from the recently-developed model (ORCHILEAK) for aquatic CO_2 evasion in Amazonia (Hastie et al., 2019) as an input in our atmospheric transport simulations. We have shown that the seasonal peak of $\Delta CO_{2_{obs}}$ in June and July is influenced by a net carbon source driven by R_{eco} and the CO_2 evaded from rivers. The aquatic signal peaks in May and June (Figure 3.3), just when the $\Delta CO_{2_{obs}}$ footprint covers the main branch of the Amazon River, including its delta (see MJJ in Figure 3.1 and 3.5). Therefore, we suggest that the $\Delta CO_{2_{obs}}$ maximum in June has a larger contribution of CO_2 from rivers, while in July R_{eco} could be more relevant in the $\Delta CO_{2_{obs}}$. We furthermore highlight that by adding aquatic CO_2 signals to FLUXCOM-$\Delta CO_{2_{sim}}$: The shape of the seasonal cycle is closer to that of $\Delta CO_{2_{obs}}$, indicating that aquatic CO_2 evasion is important to correctly represent the seasonal cycle of CO_2 mole fractions at ATTO.

A full error propagation from the river flux fields to our simulated tracer is out of the scope of this study. However, we provide an estimate for the relative error of about 35% for the river flux fields, which scales linearly to our simulated river signals. This estimate was based on Hastie et al. (2019), specifically the annual CO_2 evasion of 746 (526-998) Tg C per year. It is important to note that this relative error has to be interpreted with caution, as our atmospheric transport model (STILT) has a higher spatial resolution and the footprints do not cover the entire basin as the ORCHILEAK model does. This model represents an important advance in coupling the terrestrial carbon cycle with the lateral forest-river continuum, though the additional sources of uncertainty can be highlighted here. In ORCHILEAK the carbon sources of the CO_2 degassed from aquatic surfaces are

attributed to: (1) dissolved organic carbon (DOC) and dissolved CO_2 transported laterally from the upland soil and (2) decomposition of submerged organic carbon and litter and respiration of submerged roots in wetlands and rivers (see Lauerwald et al. (2017) and Lauerwald et al. (2020)). Lateral transport from upland soil (1) is important for small streams (Johnson et al., 2006, 2007), which are lacking in ORCHILEAK. In addition, the lack of aquatic plants in ORCHILEAK introduces uncertainty in (2). Including small streams and aquatic plants in ORCHILEAK would enable the model to better simulate CO_2 evasion from aquatic habitats.

3.4.2 Fluxes are the major source of error in STILT simulations

Our study is the first to use the CO_2 ATTO record to independently evaluate optimized and non-optimized gridded NEE fluxes when transported in the atmosphere. From this evaluation we highlight two main important findings. The first is that none of the simulations, including the ones using optimized fluxes, accurately reproduce the seasonal cycle of the observed signal ($\Delta CO_{2_{obs}}$), which represents the regional flux and atmospheric transport influence. $\Delta CO_{2_{obs}}$ is almost always lower than the background inflow, indicating a sustained regional sink of CO_2. The second, is the importance of river CO_2 signals at ATTO when interpreting the CO_2 measurements and simulated biospheric signals. We showed that the phase of the seasonal cycle is better captured by FLUXCOM only when adding river signals (Figure 3.6), and that the amplitude of the seasonal cycle is overestimated by 0.8 ppm to 1.8 ppm (CT-SAM-Flask and VPRM).

We attribute the incapability of our system to accurately simulate $\Delta CO_{2_{obs}}$ mainly to errors in the input fluxes, which fail to capture the seasonal variability of NEE in the footprint area. Dynamic vegetation models are known to have difficulties simulating the seasonality of carbon fluxes in the equatorial (5°S to 5°N) band of Amazonia (Verbeeck et al., 2011; Restrepo-Coupe et al., 2017), but here we show that even when NEE of a process-based model (such as SiBCASA) is optimized with different data streams (using surface CO_2 observations CTE2020, additional aircraft profiles within the Amazonia CT-SAM-Flask and, satellite columns CT-SAM-OCO2), it does not capture the seasonality of $\Delta CO_{2_{obs}}$ sampled at ATTO. This finding is similar to that of Molina et al. (2015), in showing the difficulties of reproducing the seasonal cycle of NEE after an atmospheric inversion, but we further show the remaining challenges of a denser observational network, which could either be aircraft profiles (e.g., CT-SAM-Flask) within Amazonia or satellite columns (e.g., CT-SAM-OCO2). A still limited observational coverage, even with the aircraft network and the OCO2 columns, is perhaps one of the main remaining challenges.

The mismatch between the optimized fluxes and $\Delta CO_{2_{obs}}$ at inter-annual scale could be related to an incorrect seasonality in the prior NEE flux (i.e. NEE before optimization), but also to the frequency and spatial distribution of observations used in the assimilation. For CTE2020, CT-SAM-Flask and CT-SAM-OCO2 the same prior model is used (i.e. SiBCASA), but different data streams are assimilated. Tests indicate that the use of the same NEE prior leads to a similar shape of the seasonal cycle in the posterior NEE (not shown) and thus the $\Delta CO_{2_{sim}}$ in this study, regardless of the data assimilated for the optimization. Furthermore, the effects of temperature, soil moisture and precipitation anomalies in the underlying prior biosphere models (in particular for VPRM and SiB-CASA) could produce inaccurate vegetation NEE responses in terms of timing and/or sign. This could result in NEE fluxes with either an early too strong source (i.e. 2015-NDJ) or the opposite in sign in the same month possibly due to an enhanced uptake (i.e., 2016-ASO).

This study is the first time that the FLUXCOM NEE product has been evaluated using atmospheric transport to obtain CO_2 mole fractions at a particular site in the tropics. Interestingly, we found similar inter-annual patterns in $\Delta CO_{2_{sim}}$ to those using the optimized fluxes, but not with the observations. Jung et al. (2020) found a consistency in NEE anomalies between FLUXCOM and atmospheric inversions at global scales, and here we show that this finding holds at regional scales when using FLUXCOM in simulations of atmospheric CO_2. According to Jung et al. (2020), the reasons for the global consistency between FLUXCOM and atmospheric inversions are: 1. a spatial compensation of processes that are not well represented by the underlying model formulations and 2. the tendency of such models to be more sensitive to temperature signals, which are more important at larger spatial scales, as discussed in detail by Jung et al. (2017). Here we suggest that the spatial scale of our analysis can still suffer from the weaknesses listed above. In particular, note that the temperature sensitivity can be spotted by comparing Figures 3.4a and 3.7a; the bottom-up and top-down simulations converge in a 2σ anomaly in 2015-NDJ, coinciding with temperature anomalies of similar magnitude.

Inter-annual drought-induced impacts on vegetation in Amazonia can include: shifting carbon allocation from the canopy to fine roots following drought (Doughty et al., 2014), reduced growth due to water stress and warm temperatures (Clark et al., 2010), prioritizing growth at the expense of maintenance and defence (Doughty et al., 2015), and increased tree mortality (da Costa et al., 2010; Wang et al., 2012) together with reduced vegetation productivity (Feldpausch et al., 2016). In addition to the mechanisms listed above, the implementation of the different seasonal phenological stages (as shown in Figure 3.3 but also by Restrepo-Coupe et al. (2013), Lopes et al. (2016) and Wu et al. (2016)) needs to be improved in dynamic vegetation models as well as in process-based biosphere models, to produce more accurate NEE and thus $\Delta CO_{2_{sim}}$ estimates. Improving the sensitivity of tropical vegetation in dynamic vegetation models to water availability could also reduce the disagreement between top-down and bottom-up estimates for the global

carbon budget (Bastos et al., 2020).

Atmospheric transport uncertainties are also a source of errors in our simulations, mainly associated with the model's capability to resolve moist (deep) convection (Betts et al., 2009), vertical mixing within the boundary layer (Gerbig et al., 2008) and advection (i.e., wind speed and wind direction) correctly. The seasonality of convection in STILT shows more activity during the wet season (FMA) over the footprint area, consistent with the timing of convective events reported by Horel et al. (1989). Therefore, the probability of a particle being captured by an updraft or downdraft is higher during the wet season. We are aware that errors in representing deep convection could lead to a potential bias in the turnover time of the air between the mid and upper troposphere and the boundary layer. We acknowledge this limitation, but if present, such a bias is more likely to occur in the wet season. STILT is as good as the driving meteorological fields and their ability to capture convective events. Convection is a sub-grid process that can impact the ability of Eulerian models to reproduce tracer transport at the mesoscale in Amazonia (Beck et al., 2013) and it can also be triggered by small scale processes (Burleyson et al., 2016), which present difficulties for their representation in atmospheric transport models. Thus, using higher spatial resolution driving fields, such as ERA5 (C3S, 2017), is expected to improve the model's representation of convection, as shown specifically for Lagrangian models by Hoffmann et al. (2019). To reduce vertical mixing errors, we filter both the STILT simulations and the observations, so as to obtain only afternoon values (13:00-17:00 LT) (see in Figure 3.A4 the convergence of simulated and observed CO_2 in the afternoon).

Moreover, to evaluate advection errors at the receptor height (80 m), we compared local wind speed and direction measured at ATTO with the simulated quantities. We found a small bias in wind speed (-0.08 m s^{-1}) and a moderate bias in wind direction (-39 °). However, when evaluating directly the errors of the driving meteorological winds using three afternoon (14:00 LT) radiosondes at ATTO, we found that they decrease with height (Figure 3.A9). This indicates that as the particle trajectories reach higher elevations, the error tends to decrease; the particle height after 2 days of back trajectory was on average 1400 m. A study using a Lagrangian model to evaluate the role of the Amazon Basin moisture in the hydrological cycle (Drumond et al., 2014) supports the orientation of the footprints shown here. Drumond et al. (2014) show that moisture sources in Amazonia during the austral summer are coming from the tropical North Atlantic Ocean, which is in line with our footprints for NDJ and FMA. Overall, given these findings, we conclude that the errors in fluxes are much larger than those in transport.

3.5   Conclusions and outlook

In this study we presented and analysed the first six years of the CO$_2$ record from the Amazon Tall Tower Observatory. Using a Lagrangian atmospheric transport model we evaluated how well we could reproduce the observed CO$_2$ concentrations at ATTO. By combining atmospheric transport from STILT with a set of different NEE flux products, we found that the inversion results were not able to constrain the seasonal variability of $\Delta CO_{2_{obs}}$ in the footprint of the tower and very likely at the regional scale. It seems that the optimized products cannot adjust the prior seasonal cycle of NEE regardless of the data stream assimilated. Furthermore, we have presented evidence of the importance of river CO$_2$ evasion for getting the shape (but not the magnitude) of the seasonal cycle when using the FLUXCOM product, mainly capturing the increase in $\Delta CO_{2_{obs}}$ from May to July. We have further shown that the main controls of $\Delta CO_{2_{obs}}$ at seasonal and inter-annual scales result from the combined effect of local and non-local drivers, which can be inferred by the phase difference in EC-NEE and $\Delta CO_{2_{obs}}$.

This is not the first study to highlight the underlying processes that should be better represented in biosphere models, but it is the first evaluation of bottom-up and top-down NEE fluxes using an independent station with a long-term and continuous record in Amazonia. We therefore highlight the potential of the ATTO station, and the upcoming 325 m continuous record, as an independent validation site for atmospheric transport of CO$_2$ and for regional inversion estimates, which we are currently working on. Equally important are the seasonal patterns of carbon exchange, ecosystem respiration and leaf phenology that we have presented here, which add to the current body of literature (Saleska et al., 2003; von Randow et al., 2004; Hutyra et al., 2007; Baker et al., 2008; Restrepo-Coupe et al., 2013; Wu et al., 2016; Lopes et al., 2016) and provide in-situ information for constraining the heterogeneity of these processes in Amazonia. These findings are of utmost importance for regional carbon budget assessments, like the RECCAP2 initiative (`https://climate.esa.int/en/projects/reccap-2/`). By guiding the choice of prior fluxes to estimates with better NEE seasonality, improved posterior flux distributions and thus, regional carbon budgets, can be attained.

Appendix
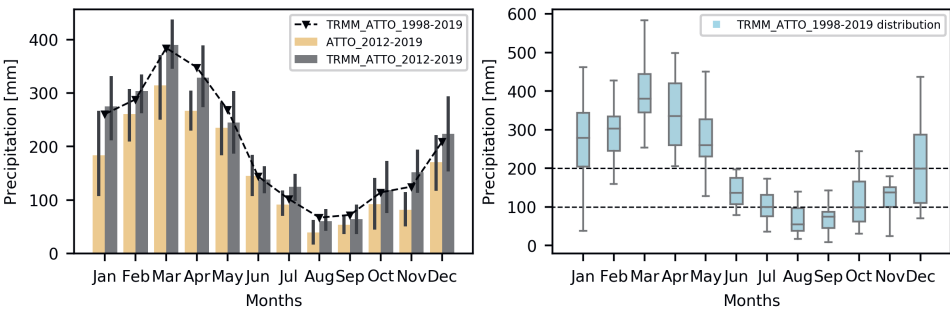
Figure 3.A1: On the left panel, the averaged seasonal cycle of precipitation at ATTO using the local measurements (2012-2019) and the TRMM record at ATTO for the same period. The climatological average for the 1998-2019 period was taken from TRMM. On the left panel, the seasonal distribution of precipitation from TRMM at the closest grid (2.125° S, 58.875°W) to ATTO (2.14°S, 58.99°W).

Table 3.A1: U* threshold percentiles [m s^{-1}] for each year at ATTO. Measurement height 81.65 m. The 50th percentile were used in this study.

Year	5th percentile	50th percentile	95th percentile
2014	0.033	0.074	0.120
2015	0.035	0.061	0.100
2016	0.060	0.105	0.164
2017	0.070	0.148	0.245
2018	0.063	0.117	0.184
2019	0.066	0.095	0.134

Table 3.A2: Comparison of different u* thresholds for different sites in Amazonia

Site-ID	Location	Biome Type	Canopy height (m)	Measurement period	EC measurement height (m)	U* threshold (m s^{-1})	Reference
K34	2.61°S/60.21°W	Tropical rainforest	35–40	14-Jun-99 to 30-Sep-06	53.1	0.2	Restrepo-Coupe et al. (2013)
K67	2.85°S/54.97°W	Tropical rainforest	35–40	2-Jan-02 to 23-Jan-06	57.8	0.266	Restrepo-Coupe et al. (2013)
K67	3.01°S/54.58°W	Sel. logged Tropical rainforest	35–40	29-Jun-00 to 12-Mar-04	64	0.24	Restrepo-Coupe et al. (2013)
CAX	1.72°S/51.53°W	Tropical rainforest	30–35	1-Jan-99 to 30-Jul-03	55.5	0.22	Restrepo-Coupe et al. (2013)
ATTO	2.14°S/58.99°W	Tropical rainforest	30–40	1-Jan-14 to 31-Dec-19	81.65	0.061-0.149	This study
ATTO	2.14°S/58.99°W	Tropical rainforest	30–40	1-Jan-14 to 31-Dec-18	46.46	0.178-0.203	This study
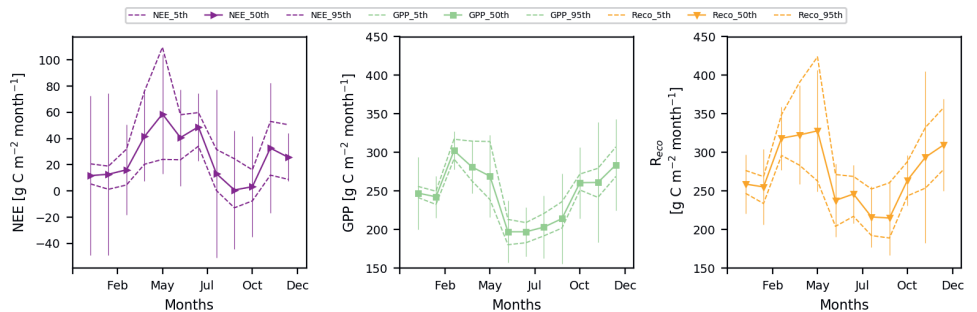
Figure 3.A2: Uncertainty range of the eddy-covariance derived NEE, GPP and R$_{eco}$ at seasonal scale. The error bars denote the standard deviation of each month across all years. Using the 5th and 95th percentiles the percentage of data remaining is 22.5% and 18.1%, respectively.
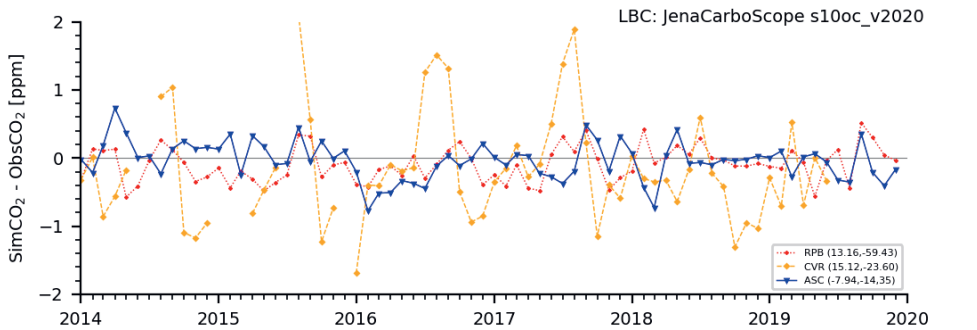
Figure 3.A3: Monthly bias of the Jena CarboScope optimized mole fractions at three background stations, Ascension Island (ASC), Ragged Point Barbados (RPB) and Cape Verde (CVR). Data from ASC and RPB were retrieved from: https://www.esrl.noaa.gov/gmd/dv/data/ and the CVR data can be accessed upon request to Martin Heimann (martin.heimann@bgc-jena.mpg.de).
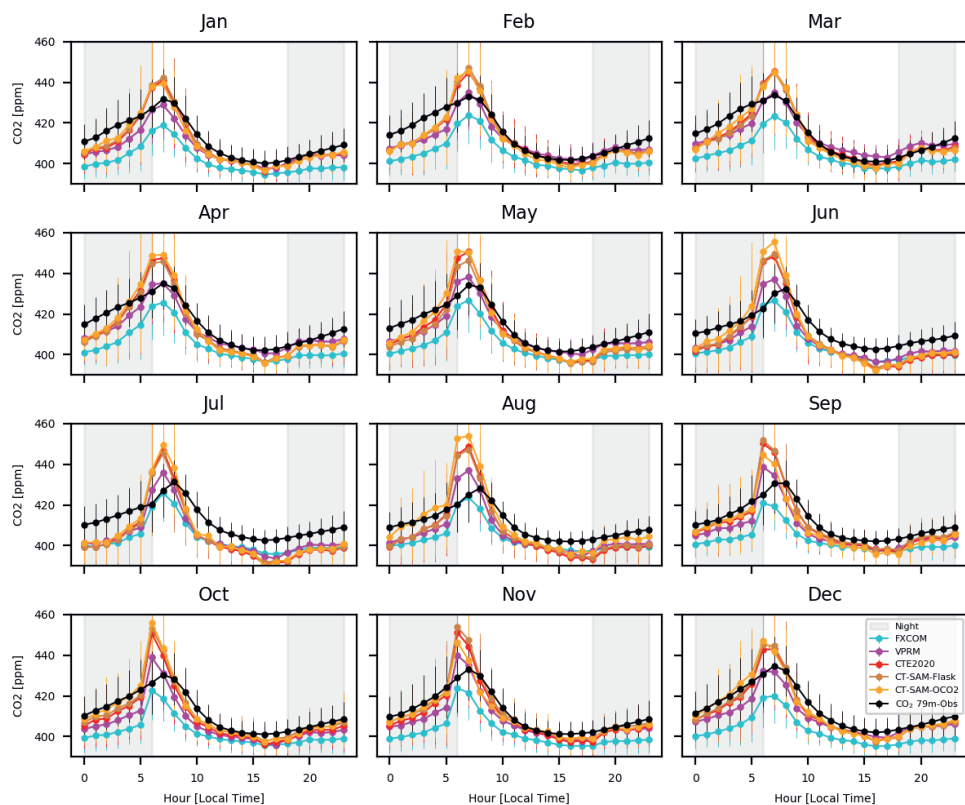
Figure 3.A4: Monthly averaged diurnal cycle of CO_2 mole fractions measured at ATTO and simulated with STILT using different input NEE fluxes. Note that the optimized fluxes (CTE2020, CT-SAM-Flask and CT-SAM-OCO2) were adjusted to represent the original diurnal variability of the prior SiBCASA model (as described in Methods, section 3.2.5).
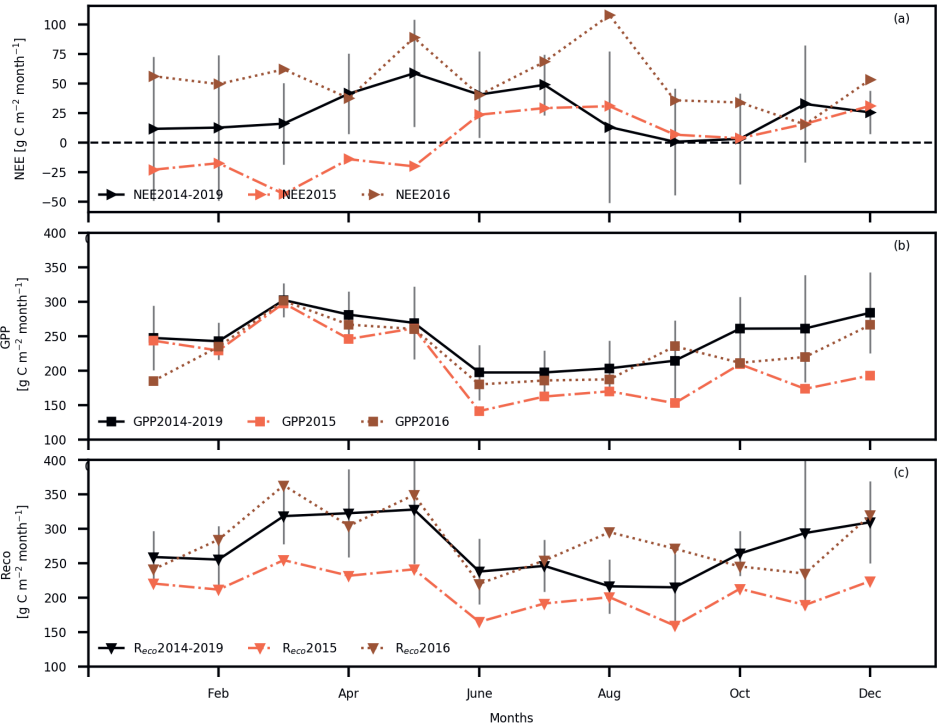
Figure 3.A5: NEE (a), GPP (b) and R$_{eco}$ (c) for the full measurement period 2014-2019 and the last El Niño years 2015 and 2016. The error bars show the monthly standard deviation for each month across all years.
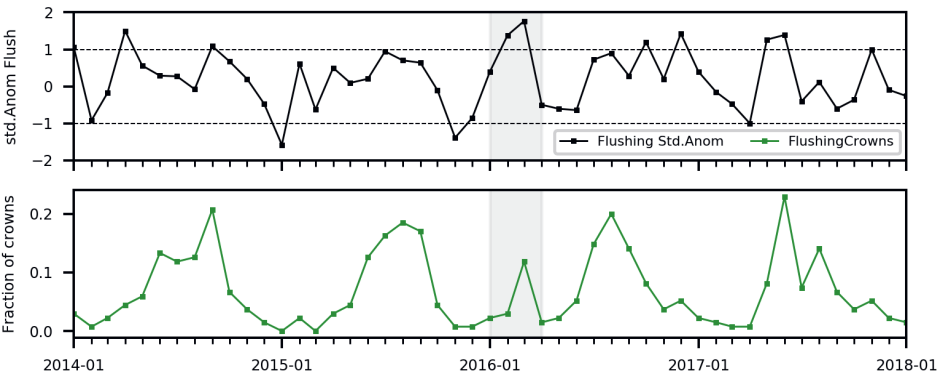
Figure 3.A6: Monthly flushing time series at ATTO (lower panel) and its standardized monthly anomaly (upper panel).
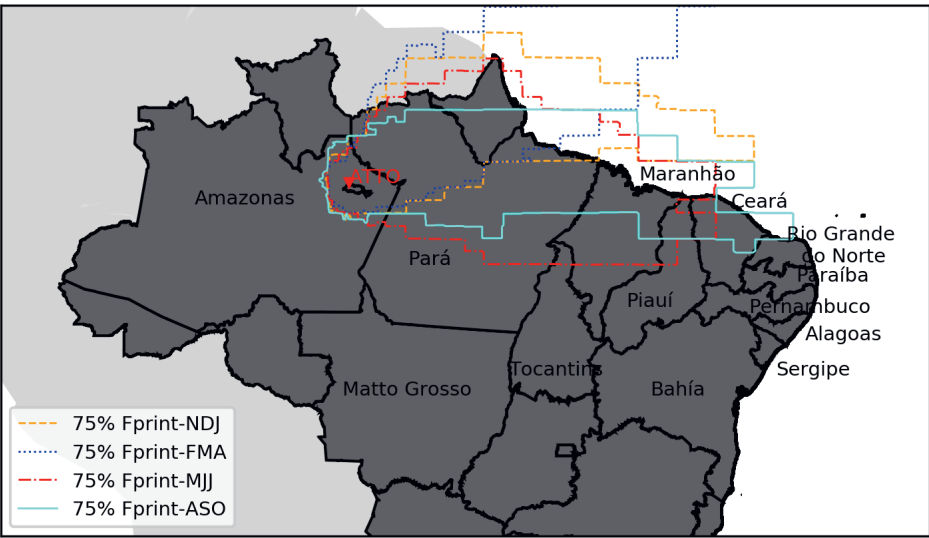
Figure 3.A7: Brazilian states overlayed with the 75th percentile footprint for each season.
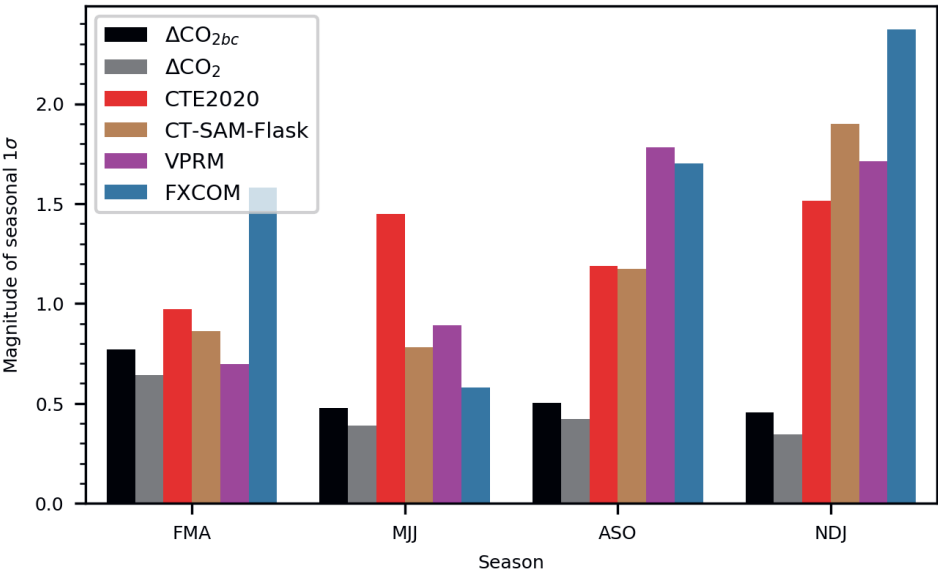
Figure 3.A8: Comparison of the standard deviation (1σ) magnitude used to produce the standardized anomalies in Figure 3.4 and 3.7. The "bc" denotes the bias correction done for the LBC.
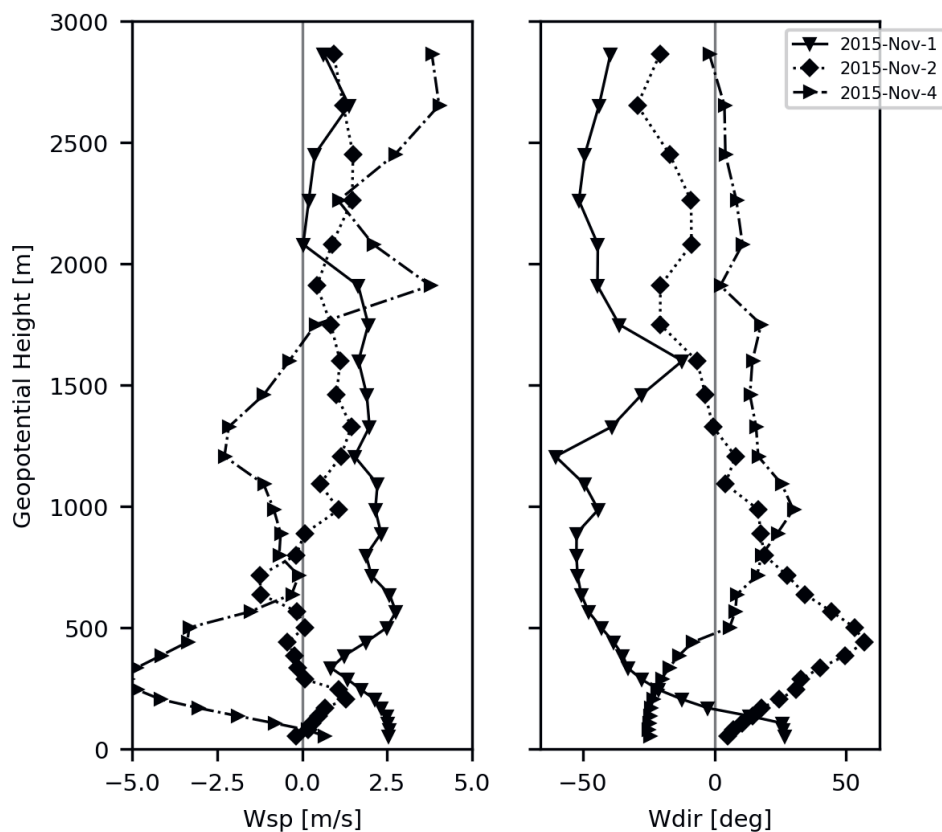
Figure 3.A9: Profiles of wind speed and wind direction bias for the ECMWF meteorological fields used in STILT and three radiosonde launches at ATTO. The vertical gray line is the zero bias reference line. The radiosondes at ATTO were collected in November 2015 during an Intensive Operational Period (IOP) by Rosa Santos. All launches were performed at 14:00 (local time).

Chapter 4

Net carbon exchange in tropical South America

*This chapter is to be submitted to *Global Biogeochemical Cycles*. Botía, S. and co-authors (2022), Constraining the net carbon exchange in Tropical South America.

Abstract

The contribution of vegetation to the South American carbon balance is critical for understanding the regional dynamics in net carbon exchange. Of particular interest is the role of the Amazon region as a sink or source of carbon to the atmosphere. Recent evidence indicates a weakening of the Amazon carbon sink, and when taking fires into account, the region represents a source of carbon to the atmosphere. In this study we use a regional atmospheric inversion system together with data from the Amazon Tall Tower Observatory (ATTO) and airborne profiles of CO_2, to constrain the Net Biome Exchange (NBE) in tropical South America. At the domain-wide scale we find that the atmospheric observations can constrain 64% of the land mass, with uncertainty reductions in most of the Amazon region, and the adjacent Cerrado and Caatinga biomes. At the continental scale, the optimized NBE results in a sink of -0.49 $\pm$ 0.1 PgC year^{-1} while the net carbon balance is a source of 0.11 $\pm$ 0.1 PgC year^{-1} for the years 2010-2018. Furthermore, we provide a region-specific analysis showing the effect of assimilating the Amazon Tall Tower Observatory CO_2 time series on the mean seasonal cycle of NBE for four areas within the Amazon, the Cerrado and the Caatinga. An emerging sink-source gradient between the Amazon region (sink) and integrated effect of the Cerrado and Caatinga (source) is found, but the source is located further east and outside the legal Amazon compared to recent work by Gatti et al (2021). We estimate an Amazon-wide NBE uptake of -0.35 $\pm$ 0.3 PgC year^{-1} for the period between 2010-2018. Our estimate agrees with others in an Amazon-wide negative NBE, yet there is considerable spread amongst top-down approaches for this region. Finally we highlight the areas with a limited constraint in our system and conclude that the observational network has to be further expanded for reducing the remaining uncertainty in top-down inverse approaches.

4.1   Introduction

Land ecosystems represent the largest carbon sink of atmospheric CO_2 (Friedlingstein et al., 2022), yet it is the most uncertain (Ballantyne et al., 2012) and variable (Le Quéré et al., 2018) component of the global carbon cycle. Several independent studies confirm that tropical land ecosystems drive most of the inter-annual variability (IAV) of the net land carbon flux (Bousquet et al., 2000; Jung et al., 2011; Peylin et al., 2013; Jung et al., 2017; Rödenbeck et al., 2018; Bastos et al., 2020), which in turn is tightly connected to the atmospheric CO_2 growth rate (Piao et al., 2020). In other words, the accumulation of CO_2 in the atmosphere depends to a large extent on the uptake and release of carbon taking place in tropical ecosystems. In these two aspects (uptake and release), South America plays a crucial role by hosting the Amazon rainforest, which covers one-third of the continent (Goulding et al., 2003).

The balance between uptake and release of carbon results in the Net Biome Exchange (NBE). Gross Primary Productivity (GPP) and Terrestrial Ecosystem Respiration (TER) are the main contributors to NBE, besides other small positive net fluxes. Studies using top-down approaches focused on the Amazon, have shown that the net balance between TER and GPP can turn into a source of carbon during drought years (Gatti et al., 2014; van der Laan-Luijkx et al., 2015; Alden et al., 2016). More recently, Gatti et al. (2021) suggested that the eastern part of the Amazon was on average a net source due to the effect of temperature and precipitation anomalies on vegetation. Furthermore, a bottom-up study in which plot level data was up-scaled to the Amazon region, Brienen et al. (2015) found a net sink of carbon over the last three decades, yet with a decreasing trend (Brienen et al., 2015; Hubau et al., 2020). Thus, multiple lines of evidence converge in an Amazon-wide vegetation carbon sink, yet large uncertainties remain (SPA, 2021) and the need to better understand spatial gradients becomes apparent. In this context, deforestation fires (van der Werf et al., 2010) and emissions from degradation (Assis et al., 2020), represent additional carbon sources, particularly important for the Amazon region (Aragão et al., 2018; Matricardi et al., 2020; Qin et al., 2021; Kruid et al., 2021). Since 2017, clear-cut deforestation has increased significantly in Brazil (Alencar et al., 2019; SEEG), not only releasing massive amounts of carbon (Assis et al., 2020) but also exposing larger areas of forest fragments to degradation (Matricardi et al., 2020). Such enormous threats to standing forest pose a challenging risk of gradually releasing the carbon stock of the Amazon, which amounts to 150-200 PgC (Saatchi et al., 2007; Malhi et al., 2009; Marques et al., 2017; Baccini et al., 2017).

Advancing our knowledge on the regional net carbon balance is essential for better understanding the processes controlling the vegetation-sink and emerging anthropogenic carbon sources. Changes in atmospheric CO_2 signals are linked to the net carbon balance, thus from an atmospheric perspective all underlying processes can potentially be constrained having reliable knowledge of the individual flux component.

However, this is not the case and disentangling individual sources and sinks is challenging using the atmospheric constraint. Top-down atmospheric inversions exploit the information embedded in measured CO_2 gradients of an observational network to constrain NBE fluxes, assuming that sources like fires and fossil fuels are well known. NBE estimates for tropical regions (Gurney et al., 2002; Rödenbeck et al., 2003; Peylin et al., 2013) and specifically for the Amazon region (Molina et al., 2015) have been conducted previously using global inversions, but lack of observations and errors in atmospheric transport led to large uncertainties (Gurney et al., 2002; Stephens et al., 2007; Peylin et al., 2013; Molina et al., 2015). Other inverse modeling efforts have used a relatively new data stream based on airborne CO_2 profiles (Gatti et al., 2014) to shed light on how fire influences the net carbon balance in specific years (2010-2011) (van der Laan-Luijkx et al., 2015) and the spatial differences of NBE in areas within the Amazon for 2010 to 2012 (Alden et al., 2016). At the time of these studies the data available permitted time-limited analyses, which provided insights primarily on the response to a drought year and normal/wet years. The longer dataset published by Gatti et al. (2021) enables to further examine inter-annual and seasonal signals using a similar top-down approach (Koren, 2020).

A recent finding using the decade-long airborne CO_2 measurements, points to an east-west gradient of the total carbon flux within the Amazon (Gatti et al., 2021). The eastern source is dominated by fires and a sign shift of NBE (from sink (-) to source (+)) in the arc of deforestation (Gatti et al., 2021). The west is reported as a close-to-neutral source with fires being less relevant and vegetation (NBE) very close to being neutral, yet showing a small uptake of CO_2. These findings underline the spatial dependence of fires and NBE in the Amazon carbon balance and raise the need for further understanding of such gradients using independent methods.

In this study, we use the CarboScope Regional (CSR) inversion system to assimilate the 2010-2018 airborne CO_2 profile record, and in addition data from measurements made at the Amazon Tall Tower Observatory (ATTO), the continuous and long-term CO_2 record (Botía et al., 2022). We build upon previous studies using the CSR system in Europe (Kountouris et al., 2018b,a), to explore its capability to constrain NBE fluxes at the continental scale over a larger domain, but with a sparser observational network. A sub-continental analysis with strong focus in the Amazon basin, but not limited to it, is performed to shed light on spatial gradients and seasonality of NBE. Furthermore, we evaluate the added value of having an in-situ site (ATTO) and also the appropriate prior error statistics to lay the foundation of the appropriate parameter settings in CSR for this specific regional domain. The latter serves not only as reference for future atmospheric inversions of other species, but also for contributing to the regional carbon balance assessment project (RECCAP2: `https://www.globalcarbonproject.org/reccap/overview.htm`) over the upcoming years.

4.2 Methods and Data

4.2.1 CarboScope Regional Inversion System

The inverse modeling approach of the CarboScope Regional Inversion System is described in detail by Rödenbeck (2005), so here we emphasize the fundamental concepts of the inversion and the two-step scheme linking the regional to a global scale inversion. The inversion system aims to minimize the cost function $J(x)$ (see equation 1), which consists of terms for model-data mismatch and prior information.

$$J(x) = (y - Hx)^T \boldsymbol{Q}_m^{-1}(y - Hx) + (x - x_p)^T \boldsymbol{Q}_p^{-1}(x - x_p) \qquad (4.1)$$

Where, y is a vector of size n containing the atmospheric observations for all sites and times (in ppm), x is the state vector (surface-atmosphere fluxes) of length m containing the unknowns which in theory are the surface fluxes. However, in this set up, the unknowns correspond to adjustable parameters that are used in additive corrections to the prior flux. H is the atmospheric transport operator (with Hx as the simulated mole fractions) of dimensions n x m that samples the m unknowns and provides the connection to y, in other words the sensitivity of each measurement to surface fluxes. The diagonal matrix Q_m (with dimensions n x n) weighs the mole fraction measurements considering measurement uncertainty, site-dependent representation errors and temporal error correlations that are implemented as a data density weighting (discussed in Section 4.2.2). The a priori term contains the prior flux field x_p and the covariance matrix Q_p, with prior flux uncertainties and spatial and temporal error correlation. The minimization of $J(x)$ is performed iteratively with respect to x using a conjugate gradient algorithm (Rödenbeck, 2005).

The CarboScope Regional (CSR) inversion system deploys a two-step scheme described in Rödenbeck et al. (2009) and Trusilova et al. (2010). Here we provide the relevant details of the regional system and of our set up. In the two-step scheme two types of atmospheric transport models with different spatial resolutions are used. In step 1, a global inversion using the CarboScope Global inversion system (Rödenbeck et al., 2003) is performed to obtain an optimized NBE flux field at a coarse global scale. Using this flux field and the TM3 atmospheric transport model (Heimann & Körner, 2003) at 4°x5° resolution driven by the NCEP reanalysis meteorological fields (Kalnay et al., 1996), simulated mole fractions increments for all sites are obtained. These "forward" runs represent an intermediate step and are done twice, see equation 2 (adapted from Rödenbeck et al. (2009)). The first one initializes TM3 at the coarse global scale and for the entire time period of the global inversion done in step 1. The second forward run is performed only for the regional domain (at coarse spatial resolution) and the desired period of interest (i.e. 2010-2018).

Both forward runs result in simulated mole fraction increments (Δc_{mod1} and Δc_{mod2}) to which an initial mole fraction (c_{ini}), corresponding to a well-mixed atmosphere, is added. The difference of the two runs corresponds to a far-field contribution from fluxes outside of the regional domain. All this together is subtracted from the measured mole fractions at the sites within the domain of interest. This difference represents a "remaining mole fraction" (Δc_{remain}), corresponding to signals from fluxes within the regional domain, as defined by Rödenbeck et al. (2009).

$$\Delta c_{remain} = c_{meas} - (\Delta c_{mod1} - \Delta c_{mod2} + c_{ini}) \tag{4.2}$$

In step 2, the regional inversion takes place using the high-resolution (0.25°x0.25°) model STILT (Lin et al., 2003) and using the Δc_{remain} as data vector. STILT is driven by the ECMWF-IFS short-term forecasts (following the contemporary IFS cycle development; for more info, see `https://www.ecmwf.int/en/publications/ifs-documentation`). In addition, a set of different prior fluxes (representing a prior ensemble) is used and the regional inversion is performed for each prior ensemble member individually. The set of priors are described in Section 4.2.3. The domain we have selected extends from 28.875ºS to 13.875ºN and from 83.875ºW to 34.125ºW, see Figure 4.1; we have limited our domain to 28.875ºS due to a lack of observational records further south. Our inversion set-up follows largely that of Kountouris et al. (2018a), but we use an isotropic exponential decay for the spatial error structure, mainly because in our domain unlike in mid-latitudes, the climatic gradients are similar in both latitude and longitude. We refer the reader to Table 4.1 and Section 4.2.4 for more on the rationale of this choice.

By prescribing a flux field as a fixed prior (i.e. not optimized), one accounts for that source/sink explicitly, otherwise that information will be implicitly contained in the optimized flux field, in this case NBE. To clarify the flux terms used in this work here we provide some definitions (see equations 4.3 and 4.5). Here NEP is the net ecosystem productivity, GPP is the gross primary productivity, and TER is terrestrial ecosystem respiration. When prescribing fluxes from fires ("Fires") and Fossil Fuels as fixed priors (as we do for all inversions), we account for these sources directly, therefore the inversion provides an optimized Net Biome Exchange (NBE). For the NBE we adopt the atmospheric approach in which a positive (+) is a source to the atmosphere and negative (-) a sink. As Fossil Fuels and Fires are prescribed in our set up, we obtain the net budget by adding these fluxes to the optimized NBE. In all inversions there is no prescription of River fluxes, therefore those signals are implicitly accounted for in the optimized NBE. To assess the effect of a potential net source of Rivers in our NBE, we made an additional experiment prescribing Rivers in one inversion (see Section 4.2.4).

$$NEP = TER - GPP \tag{4.3}$$

$$NBE = TER - GPP + Rivers \tag{4.4}$$

$$Fc, total = NBE + Fires + FossilFuels \tag{4.5}$$

4.2.2 Observational network

To further analyze the spatial distribution of NBE and the influence of our network's coverage, we have used the definition of sub-regions shown in Figure 4.1a. One of the criteria for the choice of these regional integration areas is that they should be independent from our observational network's coverage. With this, we avoid having contrasts between areas with better observational coverage than others. Thus, the selection of these areas follows to some extent a biome-like distribution (e.g. see the Caatinga and the Cerrado), but it does not represent individual biomes strictly elsewhere. The division within the Amazon serves to provide individual sub-regions dividing east-west but also north-south. In addition, we have also kept an individual sub-region for the main branch of the Amazon river. The location of the measurement sites is shown on Figure 4.1b together with their aggregated annual mean surface influence over 2010 to 2018. The coverage of the observational network in our regional domain concentrates in the areas within the Amazon but also in the northeast of Brazil. For the seasonal areas of influence for each individual site see Figure 4.A1.

In the global inversion (step 1) we have used the set of stations in the latest release of the CarboScope global system with nearly continuous coverage from 2010 onward (i.e. s10oc_v2021, see `http://www.bgc-jena.mpg.de/CarboScope/?ID=s10oc_v2021`, for details of stations and data providers.). To the default s10oc_v2021 station set, we added the ATTO CO_2 record (available at: `https://attodata.org/`), five sites within the Amazon region where airborne profiles (available at: `https://doi.pangaea.de/10.1594/PANGAEA.926834`) are collected (Gatti et al., 2021), and the weekly flask sampling record in Natal (NAT), a station in the northeastern part of Brazil (Dlugokencky et al., 2021). Therefore, the global inversion (step 1) is augmented with these sites (s10 + ATTO + NAT + Aircraft), and for the regional inversion (step 2) only the sites within our domain are used. The monthly time series at each site is shown in Figure 4.1c, indicating the data gaps and the evolution of the CO_2 over the last decade. Note that ATTO provides continuous data only since 2013 and there were major gaps in the aircraft network during 2015 and 2016. For the continuous data (ATTO) we use only daytime measurements (i.e. from 13:00 to 17:00 local time), to ensure we have measurements representative for the well-mixed boundary layer. Furthermore, the average number of aircraft profiles per month is two, see Figure 4.A2. For each measurement of each aircraft profile (full profile goes up to 4500 m), for the weekly flask measurements at NAT, and for every single data point at ATTO, we have simulated the surface influence using the STILT model.

Each measurement has an individual footprint which is used as the transport adjoint in the regional inversion. The STILT set-up follows that of Botía et al. (2022), but the spatial resolution used here is 0.25°x0.25°.

The model-data mismatch error (also called representation error) for the three types of sites is chosen to be 1.5 ppm for weekly time scales. We apply a data density weighting (e.g. hourly for ATTO), so the error will be inflated by $\sqrt{N_{hours/week}}$ (details see Kountouris et al. (2018a)). We have assumed the same representation error to the aircraft sites as well as to the ATTO site, resulting in equal constraint in the inversion. An aircraft profile (composed of several flasks) is scaled with $\sqrt{N_{flasks/profile}}$, similarly to ATTO observations having the weight of one weekly flask sample. This means that the continuous measurements, aircraft profiles and flasks are treated consistently in the inversion.

4.2.3   A-priori fluxes

For the regional inversion we use a set of five prior NEP flux models to create prior and posterior ensemble statistics. The first two are different versions of the Vegetation Photosynthesis and Respiration model (VPRM) (Mahadevan et al., 2008), a simple diagnostic model using MODIS imagery and fitted to eddy covariance data within the domain which provides NEP. One version corresponds to the default VPRM model, and for the second one we have filtered out the seasonal and inter-annual (VPRM_{FLAT}) variability. The motivation of this is to assess to what extent the CSR system depends on the prior to constrain the seasonal cycle and the inter-annual variations of the posterior NBE fluxes. The third prior ensemble member is the FLUXCOM product (Bodesheim et al., 2018), which up-scales site-level eddy covariance data to the globe using a random forest regression. Finally, we used two additional priors that consist of process-based models, the SiB4 (Haynes et al., 2019) and SiBCASA (Schaefer et al., 2008) models. The last three priors provide NEP as well, but for all we estimate a posterior NBE with the inversion. By having this set of priors we have a wide representation of the potential spatio-temporal dynamics of NBE over our domain.

The assumed regional prior uncertainty for the domain-wide and annually integrated flux is chosen to be consistent with the corresponding prior error for that region in the global CarboScope inversion (Kountouris et al., 2018a). Therefore, when spatially aggregating the (spatially and temporally correlated) prior error, regardless of the correlation length scale, it scales to the assumed prior uncertainty for the domain. We have made several experiments to test the effect of the prior error correlation length scale (i.e. different number of degrees of freedom) which we will discuss.
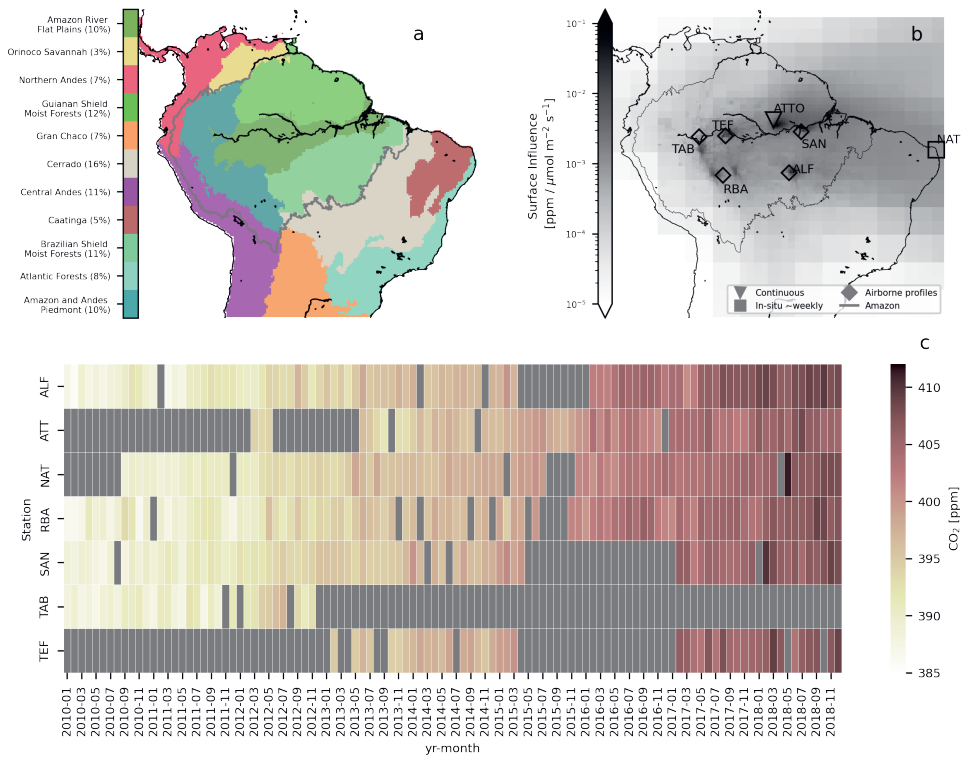
Figure 4.1: South American domain (from 13.875°N to 28.875°S and 83.875°W to 34.125°W) with a sub regional division adapted from EPA (2011) (a). A file with the regions created here can be provided per request (sbotia@bgc-jena.mpg.de). The percentages in the legend denote the area of the region relative to the full land area in the domain. The annual mean footprint, associated with the period where data are available is shown in b. The time series showing the monthly mean CO$_2$ mole fraction at each station or aircraft profile site is shown in c. The gaps are shown in grey and are due to logistical problems and/or instrument malfunction. The Amazon contour is based on Eva et al. (2005).

Furthermore, a non-optimized set of fluxes is used to account for important CO_2 sources that contribute to the integrated signal of CO_2 in the atmosphere within our domain. Ocean fluxes are based on (Rödenbeck et al., 2013) but specifically processed for our domain at higher (1°x1°) resolution. Following Steinbach et al. (2011), the EDGAR 4.3 inventory, sector and fuel-type specific and scaled at national level for each year based on the British Petroleum statistical review, is used to account for emissions related to burning of fossil fuels. The GFAS product (Kaiser et al., 2012) for fire emissions and the ORCHILEAK model (Hastie et al., 2019) to account for river out-gassing are also used.

4.2.4 Inversion experiments

Using the set of priors we made several experiments listed in Table 4.1. The reference inversion run consists on having VPRM as prior with a prior error correlation length scale of 200 km, an assumed prior uncertainty of 0.903 PgC and prescribed fire-CO_2 emissions from GFAS (Kaiser et al., 2012). Furthermore, using the other NEP priors we run individual inversions to produce a posterior NBE ensemble. This was performed using 200 km as correlation length scale, 0.903 PgC of assumed prior uncertainty, prescribed fires and the core station set (ATTO + NAT + Aircraft). To investigate the effect of a larger prior uncertainty we repeated the inversions above but doubling the prior uncertainty (see the *pu* ensemble on Table 4.1). Such increase gives more flexibility for the adjustments in the optimization. In addition, to assess the effect of a larger or smaller correlation length scale on the posterior NBE fluxes, we varied it from 66 to 800 km but using the same NEP prior (VPRM) (the *cl* ensemble on Table 4.1). To study the effect of assimilating the data from the ATTO site and the potential impact of the discontinuous record at TAB, we compared the posterior fluxes of a set of runs with and without those two sites (*st* ensemble on Table 4.1). Finally, to asses the effect of river out-gassing emissions on the posterior fluxes, we run an inversion using the reference inversion but with river outgassing prescribed, making the posterior fluxes estimated the NEP (equation 4.3) instead of NBE (equation 4.4). To facilitate referencing to each of these experiments in the results, we introduced a simple naming convention in Table 4.2.

The selection of a larger correlation length scale (200 km) in the reference inversion compared to other regional inversions (Munassar et al., 2021) is motivated by the following arguments. First, the sites in our observational record are stretched out over a large region, over which large swaths of forests have similar climatic characteristics in which we can assume that prior model errors (i.e., in VPRM) are correlated. Second, part of our atmospheric data are airborne profiles which are expected to integrate fluxes across larger scales. Therefore, the choice of 200 km is a trade-off between the need to reduce the number of degrees of freedom (given the expected homogeneity of evergreen forest around ATTO) and the desire to resolve flux corrections at smaller scales in the state vector.

Table 4.1: Inversion runs and ensemble experiments. Note that CO_2 fire emissions from GFAS were prescribed in all the inversions. The first row represents the reference inversion settings. The abbreviations *cl*, *pu* and *st* denote the ensemble of the correlation length, prior uncertainty and station set experiments, respectively.

ID	Prior flux and run name	Corr. Length Scale	Ass.Prior Uncer.	Rivers	Station Set
-	VPRM	200 km	0.903 PgC	No	Core*
	$VPRM_{flat}$	200 km	0.903 PgC	No	Core
	FLUXCOM	200 km	0.903 PgC	No	Core
	SiBCASA	200 km	0.903 PgC	No	Core
	SiB4	200 km	0.903 PgC	No	Core
cl	VPRM	800 km	0.903 PgC	No	Core
	VPRM	400 km	0.903 PgC	No	Core
	VPRM	200 km	0.903 PgC	No	Core
	VPRM	133 km	0.903 PgC	No	Core
	VPRM	66 km	0.903 PgC	No	Core
pu	VPRMx2	200 km	0.903 x 2 PgC	No	Core
	$VPRM_{flatx2}$	200 km	0.903 x 2 PgC	No	Core
	FLUXCOMx2	200 km	0.903 x 2 PgC	No	Core
	SiBCASAx2	200 km	0.903 x 2 PgC	No	Core
	SiB4x2	200 km	0.903 x 2 PgC	No	Core
st	VPRM	200 km	0.903 PgC	No	Core
	VPRMnoATT	200 km	0.903 PgC	No	CoreNoATTO
	VPRMnoTAB	200 km	0.903 PgC	No	CoreNoTAB
-	$VPRM_{riv}$	200 km	0.903 PgC	ORCHILEAK	Core

*Core station set refers to: NAT, RBA, ALF, SAN, ATTO, TAB, TEF.

4.2.5 Statistical metrics

To report our results we have adopted the following metrics. When referring to an *ensemble* we report the mean together with ($\pm$) the spread or the standard deviation across the ensemble as a metric of uncertainty for that estimate. Thus, the terms spread and standard deviation are used interchangeably. When referring to the inter-annual variability (IAV) of an ensemble, we report the standard deviation of the annual ensemble mean throughout the 9-year record of our inversion. Furthermore, when a single flux component (e.g. Fires, Fossil Fuels) or a single ensemble member is referred to, we report the mean together with the IAV calculated taking the standard deviation of the 9-year period of interest. The uncertainty calculated by the inversion system, what is often referred to as "bayesian" uncertainty, is used in the context of reporting uncertainty reduction at different spatial scales. This uncertainty primarily depends on the observation density and not on the selected prior, thus it was calculated using the reference inversion settings for all years. The naming convention on Table 4.2 will be used to refer to ensemble mean, spread and single ensemble members throughout the text.

Table 4.2: Naming convention for the inversion runs and experiments. Following equations 4.3 and 4.4 note that the prior fluxes are NEP and posterior NBE.

Run or ensemble	Prefix	middle identifier	Posfix	Example
Prior ensemble	pr	NEP	ens.mn* / ens.std*	prNEPens.mn
Posterior ensemble	pt	NBE	ens.mn / ens.std	ptNBEens.std
Prior ensemble member	pr	NEP used	-	prVPRM
Posterior ensemble member	pt	NBE used	-	ptVPRM
Experiment ensemble	cl/pu/st[+]	prNEP / ptNBE	ens.mn / ens.std	clptNBEens.std

[*]mn and std stand for mean and standard deviation. [+]See Table 1 for the description of these experiments.

4.3 Results

4.3.1 Continental analysis

Carbon budget and year-to-year variability

Continental scale posterior flux estimates using VPRM, VPRM$_{FLAT}$, SiB4 and SiBCASA converge to a similar annual mean flux of around -0.5 PgC year^{-1}, whereas the posterior flux estimates using FLUXCOM are lower by almost 2 PgC year^{-1} (Figure 4.2b). There is a large discrepancy in the magnitude among priors, from being almost neutral (e.g. SiB4) to a massive sink close to 5 PgC year^{-1} (e.g. FLUXCOM) (Figure 4.2a). FLUXCOM stands out as the outlier in these prior and posterior ensembles. Even increasing the prior uncertainty by a factor of 2 in FLUXCOM, results in a large posterior sink compared to the other posterior NBE fluxes. With the exception of SiB4, all priors are adjusted by introducing a smaller sink or even a weak source into the posterior (i.e. VPRM, VPRM$_{FLAT}$ and SiBCASA). We tested the robustness of these adjustments when either inverting for the total biospheric surface flux, or for the biosphere flux after river outgassing is added in the prior fluxes (Botía et al., 2022). In the latter case a stronger sink is indeed estimated (-0.2 PgC year^{-1}) for the vegetation component (NEP), resulting in a similar net balance (NBE) (not shown).

The inter-annual variability of NBE is strongly adjusted by the inversion. In the posterior ensemble the IAV is 0.2 PgC year^{-1}, while in the prior ensemble is 0.1 PgC year^{-1}. Before the inversion only VPRM and SIBCASA show some inter-annual changes. In contrast, the posterior flux estimates show more inter-annual variability for all ensemble members. Results from the inversion using the VPRM$_{FLAT}$ prior provide evidence that the inter-annual variability is added by the observational constraint. Note that this prior was filtered to not contain seasonal and inter-annual variability, and yet the posterior exhibits considerable adjustments relative to the prior. This demonstrates that the atmospheric data represents a good constraint for the inter-annual variability of the posterior NBE estimates. Nevertheless, we state that the magnitude of the yearly fluxes have a large variability among posterior ensemble members, certainly when considering FLUXCOM.
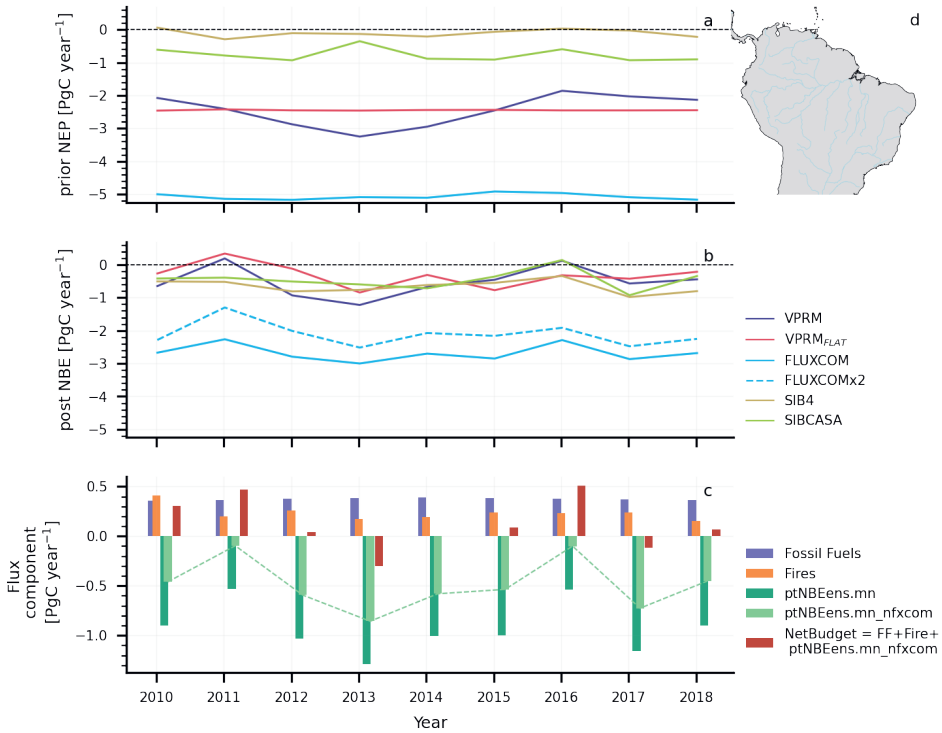
Figure 4.2: Annual NBE fluxes integrated over the continental domain for prior (a) and posterior (b). Individual flux components (e.g. Fires and Fossil Fuels) together with the posterior ensemble mean with (ptNBEens.mn) and without FLUXCOM (ptNBEens.mn_xFxcom) are shown on c. The net budget shown on c was calculated using ptNBEens.mn_xFxcom. The area for spatial integration is shown on d. Note that the y axis for c is different from a and b.

The net carbon budget was calculated by adding up fossil fuels, fires and the posterior NBE ensemble mean (ptNBEens.mn_nfxcom) (see equation 4.5). The difference of the posterior NBE ensemble mean with and without FLUXCOM is approximately 0.4 PgC. Including it would result in an unrealistically large NBE sink when compared to the other posterior ensemble members. For this reason, for the rest of this work all ensemble estimates are reported without FLUXCOM, when FLUXCOM is shown or included in an estimate, it will explicitly be stated.

The IAV of the net budget at continental scales is 0.2 PgC year^{-1} (similar to that of NBE) with an annual mean source of 0.11 ± 0.1 (Figure 4.2c). The variability of the net budget is controlled by the year-to-year changes of the posterior NBE in the ensemble mean. The inversion time span is rather short to infer any trend in the NBE sink and

we observe a large variability throughout the nine year period analyzed with a posterior NBE ensemble mean of -0.49 $\pm$ 0.1 PgC year^{-1}. Fires and fossil fuels have an annual mean contribution to the net budget of 0.6 PgC year^{-1} with an IAV of 0.06 PgC year^{-1} with minor year-to-year change. The variability of these flux components is mainly driven by fires with a mean annual emission of 0.2 $\pm$ 0.07 PgC year^{-1}, but fossil fuel emissions represent a larger source to the atmosphere. These flux components play an important role at continental scale contributing to increasing CO_2 mole fractions. The net budget presented here might be conservative (i.e. slightly low) as recent studies suggest that the GFAS fire emission estimates are biased low (Naus, 2021). In a year with high fire activity the bias can be a factor 2 higher. Thus, the latter shows that at this continental scale there are substantial uncertainties in the net budget mainly because of the challenges in constraining fire and vegetation components.

Constraint on seasonal amplitude and mean annual flux

An important finding at continental scale is that the annual mean NBE flux is better constrained than the amplitude of the mean seasonal cycle (see Figure 4.3a). The annual mean flux in the prior space ranged from -2.5 to -0.1 PgC year^{-1}, whereas after the inversion this is reduced to -0.7 to -0.3 PgC year^{-1}. In terms of the mean seasonal cycle amplitude (peak-to-peak) the numbers are from 10.4 to 0 PgC year^{-1} in the priors and 9.5 to 1.6 PgC year^{-1} in the posterior. However, despite the wide range in the amplitude, the shape of the seasonal cycle is similar amongst posterior estimates (see Figure 4.3b and c). Here, for both prVPRM and ptVPRM we observe the largest mean seasonal cycle amplitude. Overall, these findings suggest that the observational constraint adds information on the seasonal cycle patterns at the continental scale, but differences in the amplitude remain.

The mean seasonal cycle amplitude and the mean annual flux over 2010 to 2018, are reduced by 0.4 PgC year^{-1} and 0.1 PgC year^{-1} without assimilating ATTO (Figure 4.3). A similar response was found in the $VPRM_{FLAT}$ when excluding ATTO (not shown), demonstrating that assimilating data from this station results in an amplification of the seasonal cycle and a general weakening of the carbon uptake. As such, the effect of the ATTO-CO_2 record remains important even on the larger continental scale.
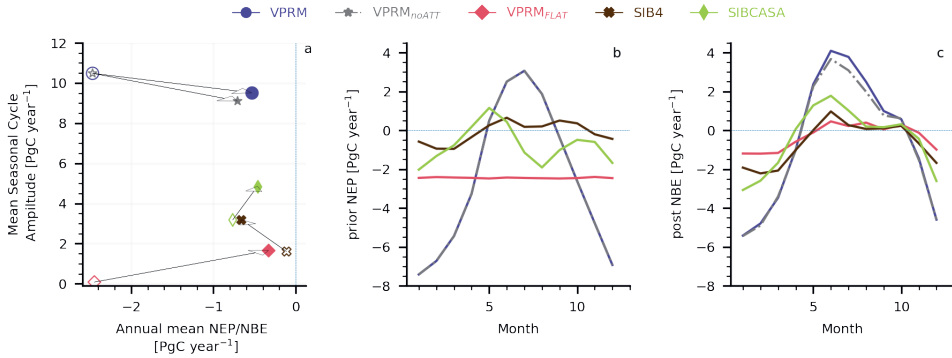
Figure 4.3: A comparison between the mean seasonal cycle amplitude (peak-to-peak) and the mean annual NEP for all priors (open symbols) and posterior NBE (filled symbols) ensemble members (a). We also display the mean seasonal cycle for priors (b) and posteriors (c).

Spatial patterns

Spatially the main adjustments are located in the eastern part of Brazil and north of the Amazon river delta (Figure 4.4b and 4.4c). The innovation (difference between posterior and prior fluxes) highlights such adjustments more clearly. The innovation in the eastern part is not driven by assimilating the NAT station data. This station is mainly receiving background signals and it is not affected by local dynamics (see Figure 4.A1), nevertheless the surface influence of all the other stations cover this part of the continent to different spatial extents. To further investigate the robustness of this innovation, we looked at the spatial patterns having different prior correlation length scales (see Figure 4.A3) and these adjustments appear regardless of the scale used. In addition, other inversions studies (van der Laan-Luijkx et al., 2017; Koren, 2020) report similar spatial patterns for the easternmost past of Brazil. In general, the priors are adjusted by the inversion either by introducing a weaker sink or a source throughout the averaging time period.

The central and northern part of the Andes mountain range together with the Orinoco Savannah are not constrained by the current observations and the spread remains large both in prior and posterior (Figure 4.4a and 4.4b). This large flux in both directions (+ and -) is introduced to the ensemble mean by the VPRM prior. Note that there is no innovation in these areas, which implies a reduced or even absent coverage of our observational network. Such reduced coverage will have an effect on the spread amongst posterior NBE ensembles members, as we will discuss in the next Section.
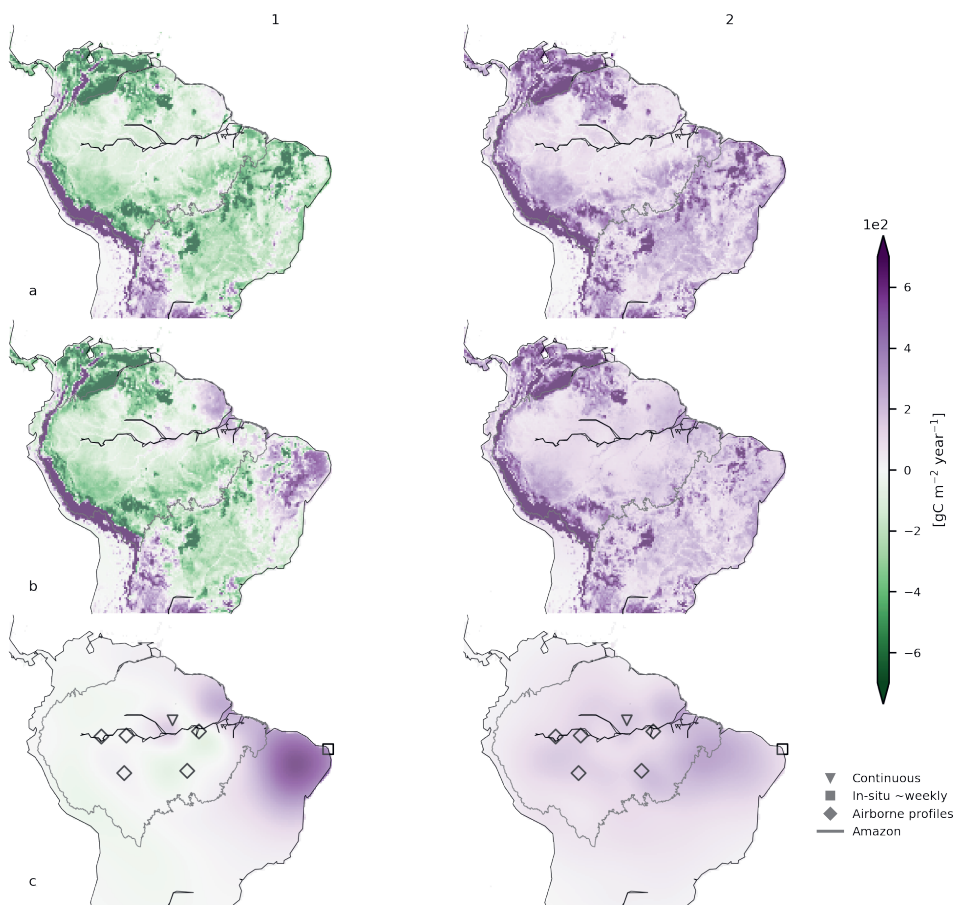
Figure 4.4: Spatial distribution of mean (1) and standard deviation (2) of the NEP prior (a) and posterior NBE (b) annual ensembles. Ensemble members include the reference case VPRM and the other flux priors: VPRM$_{FLAT}$, SiB4 and SiBCASA. The mean and standard deviation were calculated over 2010 to 2018. Row c shows the innovation, which is Posterior - Prior.

Uncertainties and ensemble spread

The reduction of the assumed prior uncertainty as determined by the posterior covariance using the reference inversion (ptVPRM) is 31%, from 0.9 to 0.6 PgC (Figure 4.5). Reducing the uncertainty depends mainly on the observational constraint, and as we have a sparse network this can increase by adding more observational sites. As a comparison, Munassar et al. (2021) achieved more than an 80% reduction using the CarboScope regional inversion (CSR) over Europe, but they assimilated the data from more than 40 stations for a smaller domain.

The standard deviation across the posterior ensemble decreases by 89% (down to 0.1 PgC, Figure 4.5) and it is smaller than the posterior uncertainty (0.6 PgC), which indicates a good convergence of the posterior NBE fluxes. The reduction in the ensemble spread (or standard deviation) when having FLUXCOM as a member is 49% and there is still a considerable spread among posterior fluxes, significantly larger than the posterior uncertainty. Moreover, doubling the prior uncertainty (ensemble *pu* on Table 4.1) results in a similar posterior ensemble spread (52%) (not shown). The large remaining spread in the posterior NBE ensemble indicates that increasing the prior uncertainty on each member by a factor of 2 does not result in a much larger ensemble spread reduction when having FLUXCOM as an ensemble member. These findings further support our decision to exclude FLUXCOM from the posterior NBE ensemble mean estimates.
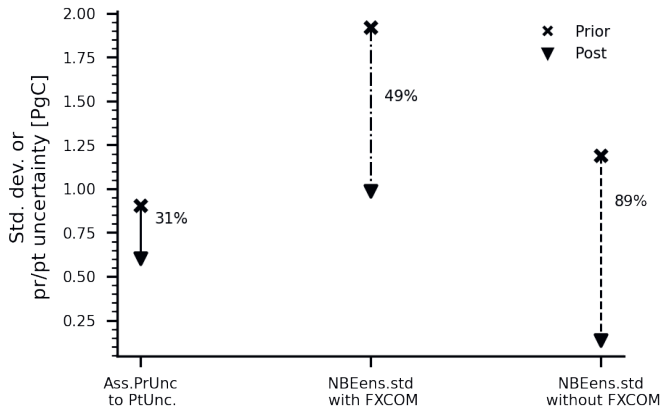
Figure 4.5: Reduction of the assumed prior uncertainty and resulting posterior uncertainty of the reference inversion (ptVPRM), together with the standard deviation reduction from prior to posterior ensembles under different scenarios. The *pu* denotes the ensemble run using twice the prior uncertainty. The other ensembles used the default settings, see Table 4.1.

To assess the variability associated with the choice of correlation length scale (ensemble *cl* on Table 4.1), we ran a set of inversions using a wide range of length scales but the same prior (VPRM). The posterior ensemble spread for this experiment is ± 0.27 PgC year^{-1}, which we take as a measure of how much out the posterior NBE ensemble mean can change by changing the correlation length scale. We also varied the assimilated data stream by excluding ATTO, NAT and TAB, in individual inversions (ensemble *st* on Table 4.1). At this spatial scale, the spread introduced by in- or excluding one of these stations is 0.08 PgC year^{-1} as determined by the standard deviation of the experiment *st* described in Table 4.1. Thus, the choice of correlation length scale has more impact on the posterior estimates than excluding ATTO, TAB or NAT in the set of sites from which data are assimilated.

Forward simulations of mole fractions

The bias (simulation - observation) at each site and the spread between models is strongly reduced by the inversion (Figure 4.6). The posterior fluxes used (ptVPRM, ptSIB4, ptSIBCASA and ptVPRM$_{FLAT}$) have 0.903 PgC and 200 km of prior uncertainty and correlation length scale. One aspect to highlight is the low bias for both process-based model priors, SiBCASA and SiB4. For all stations except ATTO, the bias is within ± 1 ppm for these prior models. The rest of the priors show a large spread in the bias ranging from -6 ppm (FLUXCOM at ATTO) to 0 ppm (FLUXCOM at SAN above 2000 m.a.s.l.). Therefore, we highlight the convergence at all stations using the posterior NBE after the large spread in the priors.

Forward simulations within the boundary layer (below 2 km, "low" aircraft samples, plus NAT and ATTO) show a larger spread between models for both prior and posterior. In the posterior runs the bias is reduced but the spread between models ranges from 0.09 ppm (TEF_low) to 0.4 ppm (NAT). The simulations above 2000 m.a.s.l. show smaller differences amongst models and in particular for the posterior mole fractions, the model biases are aligned with values within 0.04 ppm (TAB_high) to 0.08 ppm (TEF_high). Such vertical differences are driven by the decreasing effect of surface fluxes in the atmosphere. Measurements in the boundary layer simulations (< 2 km) are more influenced by the surface, whereas the simulations in the free troposphere are primarily influenced by background CO_2, which is well constrained in our set up.

In general, we see lower biases and a general convergence between models after optimizing the posterior fluxes. This better fit to the data indicates that the resulting posterior fluxes were significantly adjusted by the inversion system leading to a better match to the observations. The effect of these adjustments at a sub-continental scale will be discussed in the next Section.
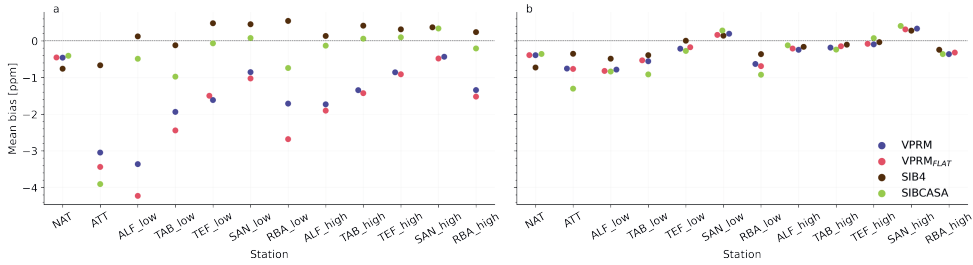
Figure 4.6: Mean bias of the simulated mole fractions at each site using prior (a) and posterior (b) fluxes. The low and high for the aircraft sites refer to the biases compared to measurements below (low) and above (high) 2000 m.a.s.l. The bias is calculated at each site at the time resolution of the observation without aggregating in time.

4.3.2 Sub-continental analysis

Region-specific observational constraint

We obtained a mean uncertainty reduction of 43% for the Amazon region, and for all the regions within it a reduction equals or above 20% (Figure 4.7). The Caatinga and Cerrado have a lower mean uncertainty reduction, with 27% and 24%, but larger than that for the 'Amazon and Andes Piedmont' (20%). The latter suggests that the innovation observed in Figure 4.4 for the easternmost part of Brazil is consistent with our observational constraint. And thus the posterior NBE fluxes in this region of Brazil are better constrained than those in the western part of the Amazon. The regions with a low or almost no uncertainty reduction highlight with more detail the limitations of our observational network. See for example the Central (5%) and Northern Andes (4%), the Orinoco Savannah (5%), the Gran Chaco (5%) and the Atlantic Forests (4%). All these regions are barely under the footprint of our observational network (Figure 4.A1). Given these findings, the rest of the analysis will be limited to the areas with an uncertainty reduction larger than or equal to 20%.
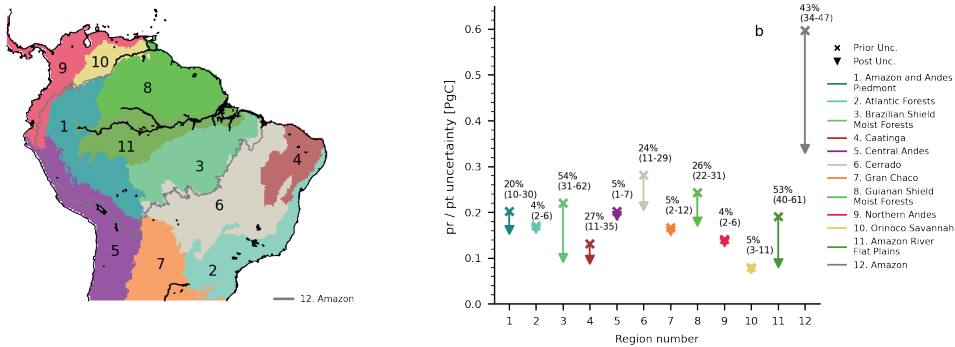
Figure 4.7: Areas for spatial integration of fluxes (a) and prior / posterior uncertainty for each of these areas (b). The percentages represent the mean uncertainty reduction over the period between 2010 and 2018, the values in brackets indicate the min-max range. For a complete time series for each region see Figure 4.A4.

Region-specific NBE and IAV

The areas within the Amazon basin exhibit interesting spatial differences (Figure 4.8a). The 'Amazon and Andes Piedmont' have the largest mean carbon uptake rate of the regions inside the Amazon with -296 gC m^{-2} year^{-1}. The Brazilian Shield moist forests follows with a mean rate of -206 gC m^{-2} year^{-1} and then the Guianan Shield Forest with a mean rate of -123 gC m^{-2} year^{-1}. The Amazon river flat plains represent the smallest sink of carbon within the Amazon, being very close to neutral in 2014.

These spatial gradients can change from one year to another and they depend partly on the continuity of the observations. Note that for 2010 to 2012, a period in which airborne profiles were still collected at TAB, the change from prior to posterior in the 'Amazon and Andes Piedmont' included a reduced magnitude of the NBE uptake. After 2012 this effect is reversed or there is even no change introduced by the inversion. After 2012, the TAB station was replaced by TEF, which is shifted 5 degrees more to the east and thus the footprint has reduced coverage of the western part of the Amazon. A simple test using only one NBE prior and excluding the observations at TAB shows that for two out of the three years we obtain an slightly enhanced sink (Figure 4.A5). Furthermore, the uncertainty reduction is higher from 2010 to 2012 than for the rest of the years (see Figure 4.A4). Therefore, it seems that the posterior NBE fluxes for the 'Amazon and Andes Piedmont' are better constrained from 2010 to 2012.

An important aspect to highlight is the small posterior ensemble spread for the Brazilian Shield Moist Forests (see Figure 4.8), together with a high mean uncertainty reduction of 54% (see Figure 4.7). This area, followed by the one covering the main branch of the Amazon river and the Guianan Shield Moist Forests, are better constrained throughout
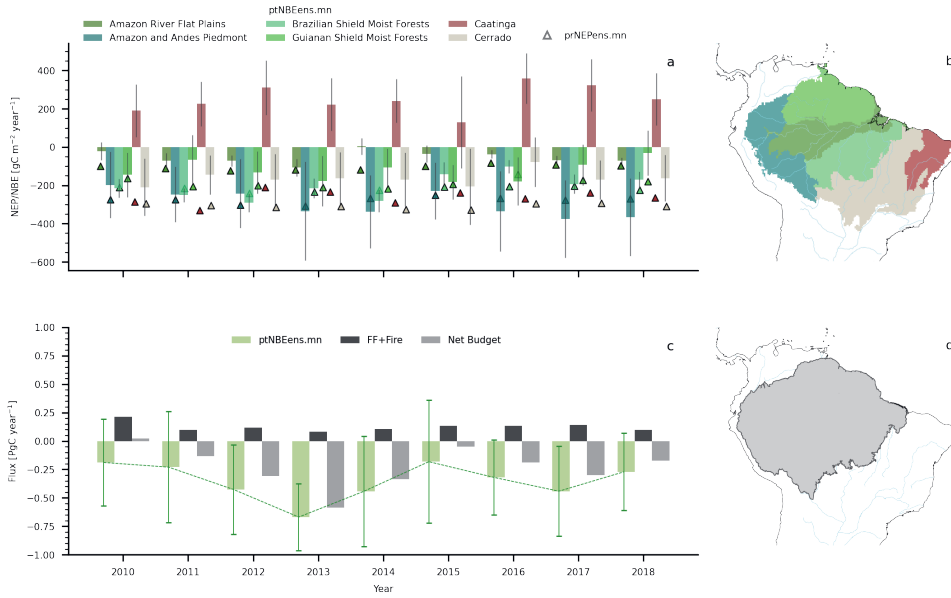
Figure 4.8: The posterior NBE ensemble mean (a) for the regions in (b). The error bars show the standard deviation of the ensemble for each specific region. The posterior NBE ensemble mean, fires + fossil fuels and the net budget (c) of the Amazon region (d).

the entire inversion period. This is reflected in a smaller ensemble spread and an uncertainty reduction larger than 20%. Therefore, any spatial gradients amongst those regions are expected to be more reliable. We observe that the Brazilian shield has a more negative NBE than the Guianan Shield, but this was reversed in 2015 and 2016, indicating that the 2015/2016 El Niño could have impacted the south of the Amazon more than the northern part. To infer a potential East-West gradient we focus on the period between 2010 and 2012 because of the reasons mentioned above. For these years it seems that there is a gradient between the Guianan shield (weaker sink) and the Amazon Andes Piedmont (stronger sink), yet this is not the case between the Amazon Andes Piedmont and the Brazilian shield. However, we state that the western part of the Amazon, even during 2010 and 2012 is not well constrained by our observational network, presenting the lowest uncertainty reduction (20%) for the areas within the Amazon. According to this we are more confident in the north-south gradients within the Amazon than a west-east differences.

The Cerrado and Caatinga regions show a consistent change from prior to posterior. The Cerrado has a reduced sink in the posterior ensemble mean (mean flux of -164 gC m^{-2} year^{-1}), and the Caatinga changes from being a sink to a strong source of carbon (mean source of 250 gC m^{-2} year^{-1}) in all the years. Such adjustments are in line with the

positive innovations shown in Figure 4.4 for these areas of the continent. These large adjustments indicate that the NEP priors used, in particular for these areas, simulate a very different carbon exchange as compared to the information we obtain from the atmospheric constraint. The combined effect of the Cerrado and Caatinga represents a mean source of carbon of 43 gC m^{-2} year^{-1}. Relative to the mean Amazonian carbon uptake (-48 gC m^{-2} year^{-1}) we present an emerging spatial gradient of carbon exchange extending from a semi-arid (source) ecosystem to tropical rainforest (sink). We will discuss this further in Section 4.4.

The inter-annual variability of NBE in the whole Amazon region is 0.15 PgC year^{-1} as given by the standard deviation of posterior ensemble mean shown in Figure 4.8c. Over the complete inversion period our posterior NBE ensemble estimate indicates that the Amazon vegetation was on average a sink of carbon of -0.35 ± 0.3 PgC year^{-1}. However, it is important to highlight that there is still a large variability amongst the posterior NBE ensemble members for each year. Our results show that only in 2010 the Amazon was a small net source of carbon. The others years show a highly variable but consistent net sink of carbon. Thus, the inter-annual variability of the net budget is controlled by NBE and to a lesser extent by Fires. For particular years, like 2015, the sign shift depends on the magnitude of the fire emissions. Even though NBE showed a reduced uptake, the net flux is still negative (this might be due to a possible underestimation of the fire emissions in that year). We stress that these estimates are preliminary as we acknowledge that our fire emission product (GFAS) is possibly biased low at least for CO emissions from fires as shown by Naus (2021). In addition, the posterior NBE ensemble has a large spread, which can vary from sink to source in a single year among posterior estimates. Therefore, the remaining variability in the posterior estimates at the Amazon scale represent a challenge to constrain the net budget.

Region-specific seasonality of NBE

Interestingly, the inversion introduces more variability relative to the prior, in the shape of the mean seasonal cycle amongst regions (Figure 4.9). In the prior, the peak of the seasonal cycle is May for the all regions within the Amazon except for the Brazilian Shield Moist Forest, where the peak coincides with that of the Cerrado and Caatinga in September (Figure 4.9a). After assimilating the atmospheric data, the peak (Figure 4.9b) for the Amazon region, the Guianan Shield Moist Forests and the Amazon River Flat Plains is shifted to June. For the Brazilian Shield Moist Forests, the peak is adjusted to January, whilst the change for the Cerrado and Caatinga was from September, to August and July respectively. The shift of one month for the Amazon region is not seen when excluding ATTO from the assimilation (Figure 4.9c). A further adjustment introduced by assimilating ATTO is the shape of the seasonal cycle of the Guianan Shield region, which shows a 5-month difference between the posterior with (June) and without ATTO (November). The effect of ATTO on the shape of the mean seasonal cycle is less evident

for the other regions, yet the mean flux is adjusted. From this we suggest the higher temporal resolution of the ATTO time series, introduces phase shifts and changes in the shape of the mean seasonal cycle of the posterior NBE estimates.
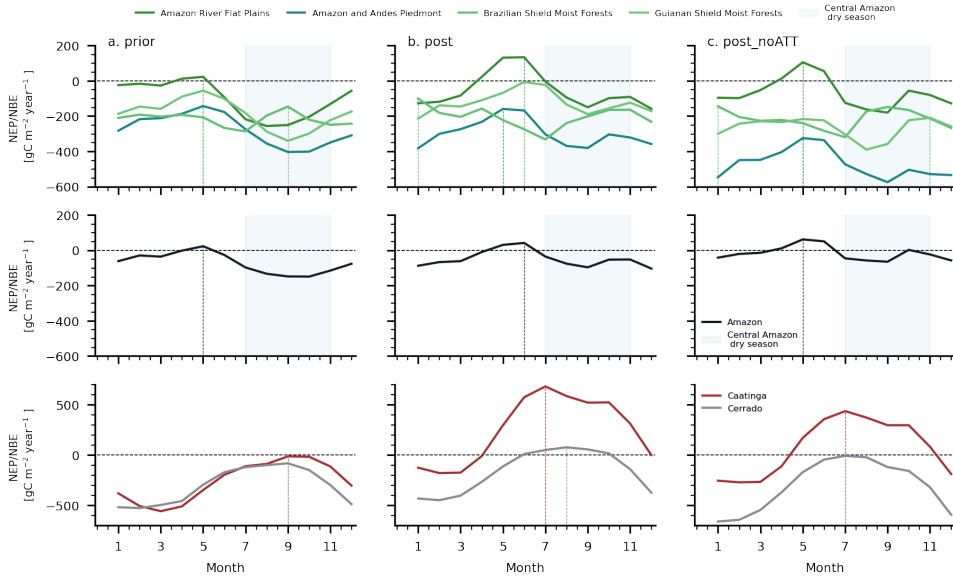
Figure 4.9: Mean seasonal cycle for the regions with an uncertainty reduction above 20%. The mean of the prior and posterior ensembles are shown in a and b. In c, the same as b is shown, but for an ensemble in which ATTO was not assimilated. Not that the y-axis has a different scale in the bottom row.

Our results show that the Amazon is a carbon sink during the dry season (for the central Amazon defined between July and October), but at the same time a large source is observed in the semi-arid ecosystems outside the Amazon. Note that the Amazon definition here (Eva et al., 2005) includes a part of the Central Andes. The north, west and central areas within the Amazon coincide with an enhanced uptake of NBE after June up until September in most cases. This contrasts the Cerrado and the Caatinga areas, both showing a source of carbon in this period. It is clear that the processes driving NBE, gross primary productivity and ecosystem respiration, are divergent in the Amazon and the areas outside of it, yet from the NBE is difficult to attribute a source or a sink to a specific process.

For the Amazon region, the ability to constrain both the annual mean flux and the mean seasonal cycle amplitude differs slightly (Figure 4.10a). The posterior mean flux range from -0.01 PgC year^{-1} (VPRM$_{FLAT}$) to -0.7 PgC year^{-1} (SiBCASA) and the amplitude from 0.5 PgC year^{-1} (VPRM$_{FLAT}$) to 1.8 PgC year^{-1} (VPRM$_{noATT}$). Furthermore, re-

garding the shape of the seasonal cycle we observe that to a large extent it is adjusted by the inversion but there seems to be a dependence on the shape of the prior (compare all priors to VPRM$_{FLAT}$ on Figure 4.10b,c). The convergence of the seasonal cycle shape in the posterior fluxes highlights the power of the observational constraint, but we also observe a slight dependence on the prior that can predetermine the posterior seasonal cycle dynamics.
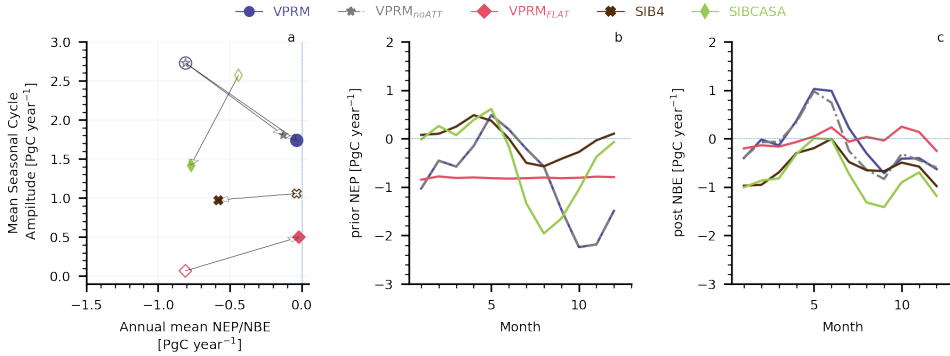
Figure 4.10: Comparison between the mean seasonal cycle amplitude (peak-to-peak) and the mean annual NEP for all priors (open symbols) and posterior NBE (filled symbols) ensemble members in the Amazon region (a). We also display the mean seasonal cycle for priors (b) and posteriors (c).

4.3.3   The added value of assimilating ATTO at local scale

Comparing the prior NEP and posterior NBE with independent in-situ Eddy Covariance Net Ecosystem Exchange (EC-NEE) measurements at ATTO shows the local effect of the inversion on the seasonal cycle (Figure 4.11-first row). EC-NEE results from the difference between GPP and Ecosystem Respiration, similar to NEP but at local scale. The EC-NEE footprint is of several kilometers while the NEP or NBE of the inversion represents a larger area of 0.25°x0.25° per grid cell, which is about 625 km^2. However, the comparison serves as an independent evaluation of the posterior NBE and an assessment of how well is the prior NEP simulated.

At ATTO there is a good agreement of all posterior ensemble members with the local eddy covariance measurements, but when excluding ATTO from the assimilated station set, this is not the case. When assimilating ATTO CO_2 mole fractions, there is a general agreement until September, after this month the eddy-covariance-NEE increases and this is not seen in the posterior estimates. In this comparison we have included FLUXCOM as we would like to highlight the adjustment of this prior NEP at this local scale, in which the shape and magnitude of the seasonal cycle was adjusted considerably. As we showed

before, at larger spatial scales FLUXCOM remains as an outlier, but the results at the local scale demonstrate that the inversion system has the ability to adjust a prior with a large bias at local scale.

We made a similar comparison but at a site where there is no atmospheric data and it is not covered by the surface influence of our observational network (Figure 4.11-second row). The site is located on the Orinoco Savannah with two years (2016-2017) of eddy covariance data available. Here we do not have any adjustment by the inversion, with an uncertainty reduction of 5% (see Figure 4.7), thus the posterior and prior are very similar. This exercise illustrates the power of the observational constraint at a site in which observations are assimilated, but it also highlights the need for more long-term mole fraction measurements in South America to better constrain NBE with inverse modeling.
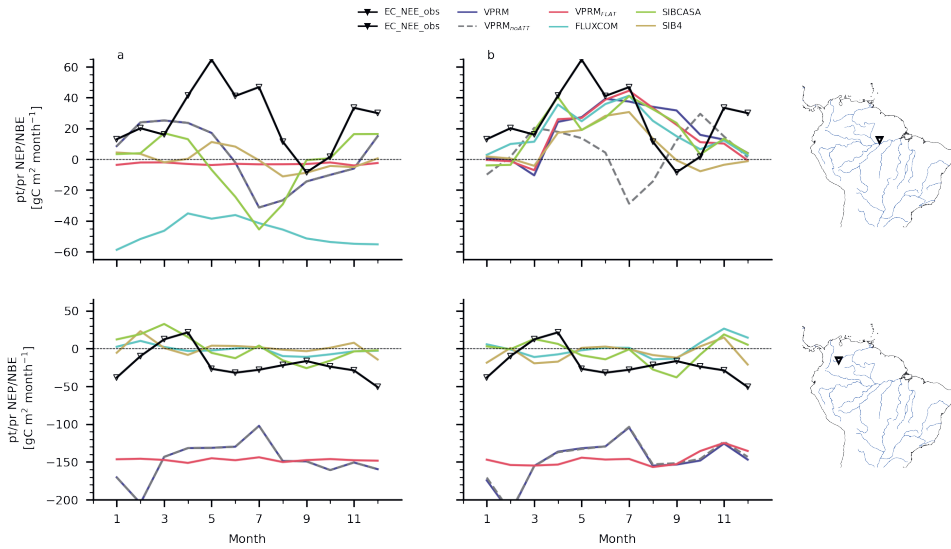
Figure 4.11: Mean seasonal cycle for the prior NEP (column a) and posterior NBE (column b) in the gridcell closest to ATTO (first row) and closest to a site in the Colombian Orinoco Savannah (second row) (Morales-Rincon et al., 2021). Prior NEP and posterior NBE are compared to independent EC-NEE measurements in both sites. Note that at each site the mean seasonal cycle was calculated for different periods as we were limited by the data availability at each location. At ATTO the seasonal average was over 2014 to 2018 and for the Orinoco site over 2016 to 2017.

4.4   Discussion

4.4.1   Comparison to Gatti et al., (2021)

This study is similar to Gatti et al. (2021) in the use of the aircraft profile network, but it differs in two important aspects: 1. we added an additional site (i.e. ATTO) and 2. obtained the regional fluxes using a regional atmospheric inversion. The method applied by Gatti et al. (2021) is a column budget technique, in which the difference between the measurements and a background concentration (calculated using back-trajectories), is associated with the travel time of air parcels from the coast to the measurement site. Here we focus on NBE for different spatial regions.

At the Amazon scale, our ensemble mean NBE estimates tend to show a slightly larger sink (mean sink of -0.13 gC m^{-2} day^{-1}) than those of Gatti et al. (2021) (mean sink of -0.05 gC m^{-2} day^{-1}), but for most of the years Gatti et al. (2021) estimates are within the spread of our posterior ensemble (see Figure 4.12). There is particularly a good agreement in 2010, 2011 and 2017 and 2018, but for 2013 and 2016 their estimate is outside our posterior ensemble spread (1-σ). Even though both estimates show a comparable magnitude, a small difference for individual years (e.g. 2016) could imply a sink-source discrepancy that is important when assessing the role of the vegetation at this spatial scale. Furthermore, the year-to-year variability seems to be more pronounced in our study than in Gatti et al. (2021). Such a difference, mainly in 2012 and 2013, is difficult to explain having in mind the agreement seen in other years and also having similar observational data (we added ATTO). However, it is plausible that in our approach the discontinuity of TAB can create an artifact in 2013 causing a large sink, as we already showed previously. Gatti et al. (2021) merged the surface influence areas of TAB and TEF into one site and proceeded with a joined analysis.

Is the Gatti et al. (2021) east (neutral)-west (sink) difference in the Amazonian NBE confirmed in this work? The answer is no, we do not see directly the same pattern within Amazonia. Instead in this study the inversion yields a large source in the semi-arid areas in the northeast of Brazil, dominated by the Caatinga, setting up an east-west NBE gradient that is not *within* the legal Amazon though. Within the Amazon, in both the East and Central regions, our estimates are far from Gatti et al. (2021). Compared to Gatti et al. (2021) (-0.08 gC m^{-2} day^{-1}) our estimate for the Central Amazon is a stronger sink (-0.33 gC m^{-2} day^{-1}), while for the East Amazon region we find -0.23 gC m^{-2} day^{-1} versus 0.04 gC m^{-2} day^{-1} reported by Gatti et al. (2021). For the western and northern part from 2010 to 2012, but also in 2015 we found on average a source of carbon (from 0.19 to 0.64 gC m^{-2} day^{-1}) with large variability, whereas Gatti et al. (2021) finds a small sink ranging from -0.16 to -0.01 gC m^{-2} day^{-1}. Interestingly, from 2013 onwards (except 2015) the agreement between our estimates and Gatti et al. (2021) are better than the comparison of the East and Central parts.
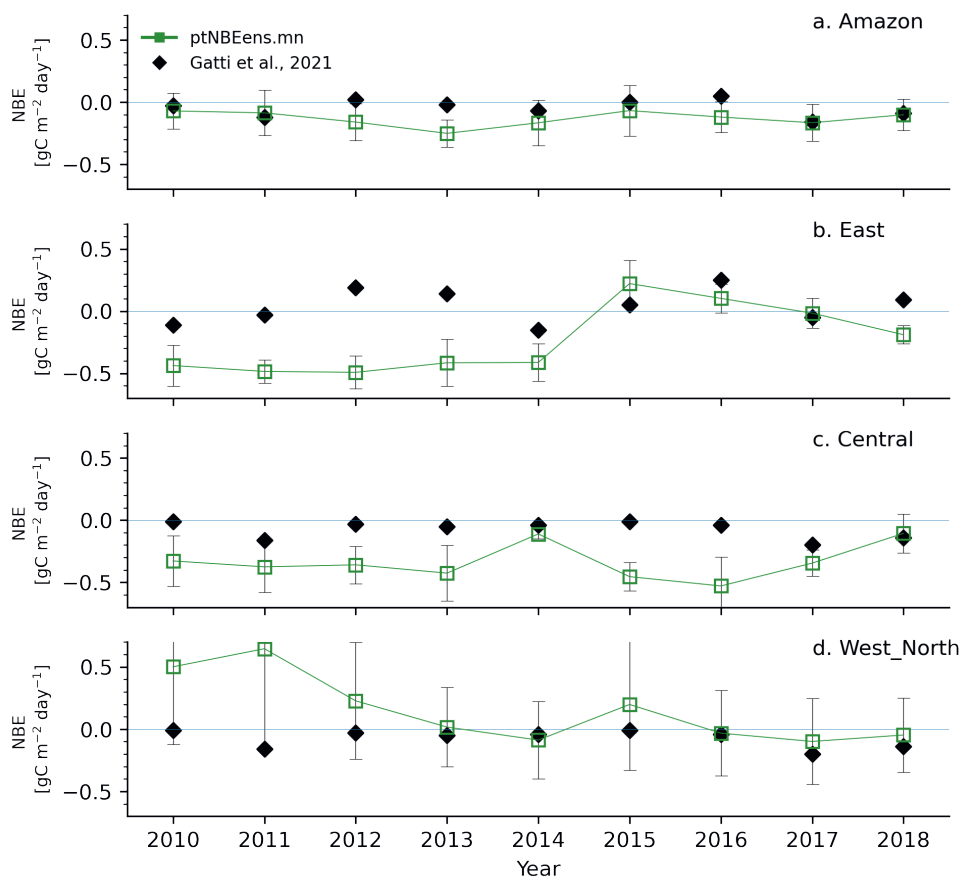
Figure 4.12: Comparison between the posterior ensemble mean NBE fluxes of this study, with those reported by Gatti et al. (2021) in their Extended Data Figure 6, panels b, c and d correspond to the regions 1, 2 and 3. Here we show mean NBE fluxes for the same regions as in Gatti et al. (2021). Our posterior ensemble mean does not contain FLUXCOM.

A possible source of discrepancy between this study and Gatti et al. (2021), could be the spatial attribution of the eastern source. Gatti et al. (2021) attribute the eastern positive fluxes, obtained using the column budget technique, to the region of influence of the SAN and ALF sites (Region 1 in Extended Data Figure 6a in Gatti et al. (2021)) which strongly covers the eastern Amazon. In our study a similar source is needed to match the atmospheric profile data, but it is placed further east in the Caatinga, and outside the legal Amazon bounds. Such a solution is possible in our system with individual (though correlated) grid points that can be assigned extra flux, but it is not possible in the setup of Gatti et al. (2021), where a mean flux rate is assigned to the full footprint covered by the observations. Thus, the degrees of freedom to place sources/sinks in specific biomes further upwind are not present. While recognizing such spatial differences between the studies, we nevertheless conclude that the east (neutral) to west (sink) gradient within Amazonia that Gatti et al. (2021) reports is not seen in our posterior estimates. Therefore, it is likely that the atmospheric signal of a carbon source that is unmistakably in the data, but attributed to different spatial regions by the different methodologies. Understanding this discrepancy, and determining the location of the eastern Brazilian CO_2 source should have highest priority in further work.

The spatially integrated NBE for the Amazon basin estimated in this study, suggests a larger sink when compared to other top-down studies (Table 4.3). For the same period of interest (2010-2018) and using a similar data constraint but different methodologies, our estimate (-0.35 $\pm$ 0.3 PgC year^{-1}) is -0.23 PgC year^{-1}, a stronger sink compared to that of Gatti et al. (2021) (-0.12 $\pm$ 0.4 PgC year^{-1}). However, the uncertainty ranges of both estimates overlap. For a positive ENSO year (2010) and the one after (2011), Gatti et al. (2014) and van der Laan-Luijkx et al. (2015) estimated a carbon uptake of -0.15 $\pm$ 0.1 PgC year^{-1} and -0.27 $\pm$ 0.4 PgC year^{-1}, both very close when considering the uncertainty range. Our estimates for those two years are closer to van der Laan-Luijkx et al. (2015) with -0.20 $\pm$ 0.4 PgC year^{-1}. For the period of 2010-2012 we obtain a mean sink of -0.30 $\pm$ 0.3 PgC year^{-1}, while Alden et al. (2016) reported -0.14 $\pm$ 0.3 $\pm$, which is closer to Gatti et al. (2021). Note that most of these estimates have a large uncertainty. Therefore, studies converge on a mean carbon sink for the Amazon, but the magnitude of it is still highly uncertain.

Part of this uncertainty can be associated with the fire emission magnitude. The Gatti et al. (2021) approach with the column budget technique solves for the total flux with respect to a background signal linked to each of the aircraft profiles. Using an observation-based $CO:CO_2$ relationship they obtained the contribution of fires and subtract that from the total. Here, we use the GFAS fire emission product, which as we acknowledged before is likely biased-low, thus our prescribed fire has a lower contribution to the observed mole fractions, yet the signal not included in the prescribed fires are implicitly captured by the atmospheric constraint and thus contained in the optimized NBE. Quantifying this signal remains challenging. Studies like van der Laan-Luijkx et al. (2015); Koren (2020);

Table 4.3: Benchmark of NBE for the Amazon region based on top-down approaches, taken from Science Panel for the Amazon Report. The mean in this study corresponds to the posterior ensemble mean, the uncertainty to the standard deviation of the 8-yr mean of each ensemble member and the inter-annual variability (IAV) to the standard deviation across the annual posterior ensemble mean. Units in PgC year^{-1}.

	Period	NBE	Uncertainty	IAV
This study	2010-2018	-0.35	$\pm$ 0.3	$\pm$ 0.1
This study	2010-2011	-0.20	$\pm$ 0.4	
This study	2010-2012	-0.30	$\pm$ 0.3	
Gatti et al. (2021)	2010-2018	-0.12	$\pm$ 0.4	
Gatti et al. (2014)	2010-2011	-0.15	$\pm$ 0.1	
Alden et al. (2016)	2010-2012	-0.14	$\pm$ 0.3	
van der Laan-Luijkx et al. (2015)	2010-2011	-0.27	$\pm$ 0.4	

Naus (2021), show that a further optimization of Fires in a bayesian set up, can have an important impact on the magnitude of the derived fire-CO signal, which can be translated to a fire-CO$_2$ signal and thus impact the net budget on the regional scale.

4.4.2   Linking NBE to processes at seasonal scale

Understanding if either GPP or TER drive the seasonal dynamics of NBE is challenging. Tower-based eddy covariance studies are spatially limited, but previous studies showed that the seasonal amplitude of NEE was negatively correlated with Mean Annual Precipitation (MAP) (Saleska et al., 2009). In that work, they defined sites in which eddy covariance-NEE was either dominated by photosynthesis (large NEE amplitude with less MAP) or respiration (small NEE amplitude with more MAP). At the ATTO site with a MAP of 2300 mm year^{-1} respiration was suggested to dominate the seasonality of eddy-NEE, exceeding GPP during the wet season and increasing in synchrony with GPP during the dry season in non-ENSO years (Botía et al., 2022). Using a regional inversion system for 2010-2012, Alden et al. (2016), did not find a consistent seasonality in NBE, yet temperature and precipitation anomalies were correlated with NBE in the central and eastern parts of the Amazon.

In top-down approaches a further partitioning of NBE needs to be performed using GPP proxies (Liu et al., 2017) like Sun-induced Fluorescence (SiF), which has been found to have contrasting responses during anomalous years. Koren et al. (2018) and Castro et al. (2020) found SiF reductions during 2015 and 2016, while Doughty et al. (2021) reported positive anomalies in SiF at the Amazon scale. Plant phenology (i.e. the temporal patterns of recurrent biological events, such as leaf flush and senescence, stem or root growth and flowering (SPA, 2021)) has been suggested as an important factor in both

TER and GPP. A higher photosynthetic capacity, due to a younger leaf age distribution in the upper canopy was found to control GPP in the central part of Amazon (Wu et al., 2016; Lopes et al., 2016), with GPP increases during the dry season (Restrepo-Coupe et al., 2013). Such dry season increase is not simulated by dynamic vegetation models (Restrepo-Coupe et al., 2017), making it difficult to simulate photosynthetic uptake in central Amazon. Furthermore, soil respiration was associated to the phenology of leaf and fine root dynamics (Keller et al., 2004a; Girardin et al., 2016), but with varied seasonal responses across sites (Saleska et al., 2009).

In this study, we showed that the inversion introduces more variability in the mean seasonal cycle (MSC) of NBE with respect to the prior (Figure 4.9), resulting in interesting differences for the regions within the Amazon. It seems that TER exceeds GPP only in the Amazon river flat plains, where we observe a clear source of carbon in May and June. For the north (Guianan Shield Moist Forests) and west (Amazon and Andes piedmont) a consistent sink is found, exhibiting a decreasing NBE during the dry season (defined from July to October) after a peak in June or May. For these regions, GPP potentially exceeds TER leading to a sink of carbon. The southern Amazon (Brazilian Shield Moist Forests), which has been more affected by deforestation and climate stressors (Gatti et al., 2021) shows a different seasonality peaking in January with a minimum in July. Given these findings we hypothesize that the role of GPP in the shape of the MSC dominates over TER, as on average we observe a negative NBE. However, more research has to be done to confirm this.

4.4.3   Prior uncertainty and correlation length scale

The assumed prior uncertainty and the prior correlation length scale are two important parameters that limit the information gain in the atmospheric inversion. The set of priors that we used have large differences in flux magnitude (see Figure 4.2), larger than the assumed prior uncertainty. The convergence of the posterior NBE estimates was acceptable for VPRM, $VPRM_{FLAT}$, SIB4 and SIBCASA, but FLUXCOM remained as an outlier even after doubling the assumed prior uncertainty. Also when going to scales smaller than the full domain, for example by looking at the NBE aggregated for the Amazon (region 12 of Figure 4.7), there is still not full convergence of the posterior ensemble (Figure. 4.13). On the other hand, local fluxes are fully constrained by the inversion irrespective of the prior, as can be seen from the comparison to eddy covariance measurements (Section 4.3.3). Therefore, with the assumed prior uncertainty (the reference of 0.903 PgC) at local scale (where data is assimilated) the inversion system is flexible enough to adjust all priors, but at larger scales this is not the case.

A diagnostic to evaluate the assumed prior uncertainty is the reduced $\chi_r^2 = 2\frac{J_{min}}{n}$ (Rödenbeck et al., 2003), in which the cost function at the minimum is divided by the effective number of observations. With this measure, we evaluated the goodness of fit for each
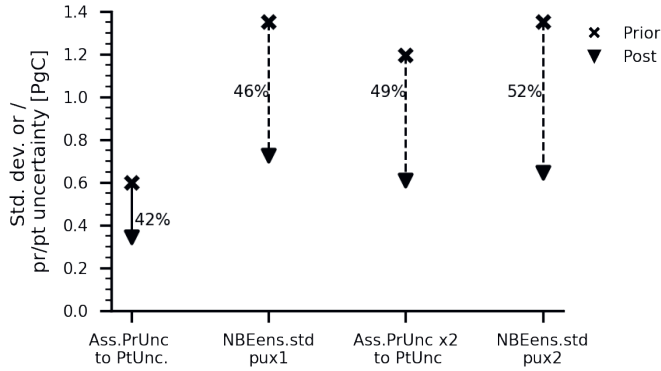
Figure 4.13: Comparison of uncertainty reduction and ensemble spread for the Amazon region. We compare the reference inversion (pu1x) and one with twice the assumed prior uncertainty (pu2x). Note that here FLUXCOM is included to further discuss the implications of doubling the assumed prior uncertainty.

ensemble member using the default prior uncertainty, as well as doubling it (Table 4.4). For both cases the χ_r^2 is larger than 3, but increasing the prior uncertainty results in only slightly lower χ_r^2 values. The reason for this is likely related to the fact that most of the region is still under-sampled. This also indicates that the model-data mismatch term might be the one dominating the large χ_r^2 values.

Increasing the assumed model-data mismatch error of 1.5 ppm (time scales of a week) by a factor two to 3 ppm is expected to change χ_r^2 to values closer to one. On the other hand, the balance in the cost function between the model-data mismatch term and the prior information term decides on location of the minimum, and this balance would not be changed when increasing both uncertainty terms by a factor of two. In other words, we believe that although the χ_r^2 values indicate that model-data mismatch errors might be underestimated, the resulting posterior estimates are not strongly affected.

Table 4.4: χ_r^2 for the reference inversion settings and the experiments doubling the prior uncertainty.

Ensemble member	χ_r^2 (PU=0.903 PgC)	χ_r^2 (PU=0.903 x 2 PgC)
VPRM	5.4	4.4
VPRM$_{FLAT}$	5.3	4.3
FLUXCOM	5.4	4.4
SIB4	3.7	3.1
SIBCASA	8.8	7.3

*PU stands for prior uncertainty

4.5 Conclusions

In this study we have used the ATTO CO_2 record together with a network of aircraft profiles in the CarboScope regional inversion system to estimate carbon fluxes in South America. We have made a continental scale analysis, highlighting that there is a better agreement in the annual mean NBE of the posterior ensemble estimates than in the mean seasonal cycle amplitude. We found that the inter-annual variability of the net carbon budget is dominated by NBE, but fossil fuels and fires are important sources leading to a mean net source of 0.11 ± 0.1 PgC year^{-1} at the continental scale. However, at this scale we found that the observational network is limited to adjust priors with large biases, exhibiting one of the main limitations of inverse modeling top-down approaches.

A region-specific analysis of NBE showed that the spatial coverage of the data constraint used in this study has limitations to reduce the uncertainty in the western and southern parts of our domain. These regions, in which the uncertainty reduction was 5% or lower, include the Central and Northern Andes, the Orinoco Savannah, the Gran Chaco and the Atlantic Forests, adding up to 36% relative to the total area of our domain. The other regions include the areas within the Amazon basin, the Cerrado and Caatinga on the eastern part of our domain. These represent the remaining 64% of the land mass, in which we obtained uncertainty reductions above 20%. For the regions having a larger uncertainty reduction, we found interesting spatial gradients. Those within the Amazon were on average a sink of carbon. Comparing the northern (Guianan Shield moist forest) and southern (Brazilian Shield moist forest) parts of the Amazon, we found a stronger sink in the south. This was reversed during 2015 and 2016, suggesting that the impact of the 2015/2016 El Niño could have been stronger in the south of the Amazon. When comparing these two regions with the western part of the Amazon, there are larger differences between the north (Guianan Shield moist forest) and west ('Amazon and Andes piedmont'), than those found between the south (Brazilian Shield Moist Forest) and west. Interestingly, the Caatinga and Cerrado were on average a source of carbon, thus an emerging sink-source gradient between the Amazon and these eastern regions was found.

The effects of assimilating the ATTO CO_2 record on the seasonality of NBE, were evaluated at regional and local scale. For the regions with a large uncertainty reduction assimilating ATTO resulted in a phase shift of the mean seasonal cycle, suggesting an important observational constraint at this time scale. Locally, we found good agreement between eddy-covariance-NEE and all posterior ensemble members. The latter shows the potential of such a site in constraining NEP priors with large difference, but at larger spatial scales this is not the case and challenges remain.

We estimated an Amazonian carbon uptake of -0.35 ± 0.3 PgC year^{-1} for the period between 2010-2018. This estimate indicates a stronger carbon sink, compared to other top-down estimates (see Table 4.3) for the same period of time. In general, a benchmark

comparison to other top-down methods agree on estimating a sink of carbon, yet the uncertainty of this estimate remains large. To reduce such uncertainty using inverse top-down approaches for a region like the Amazon, we still need a better observational coverage, mainly in the western part close to the Andes foothills. Future work using the CSR system will focus on interpreting the posterior NBE, in light of climatic variables like precipitation and temperature, mainly to disentangle the individual contribution of GPP and TER to NBE.

Appendix
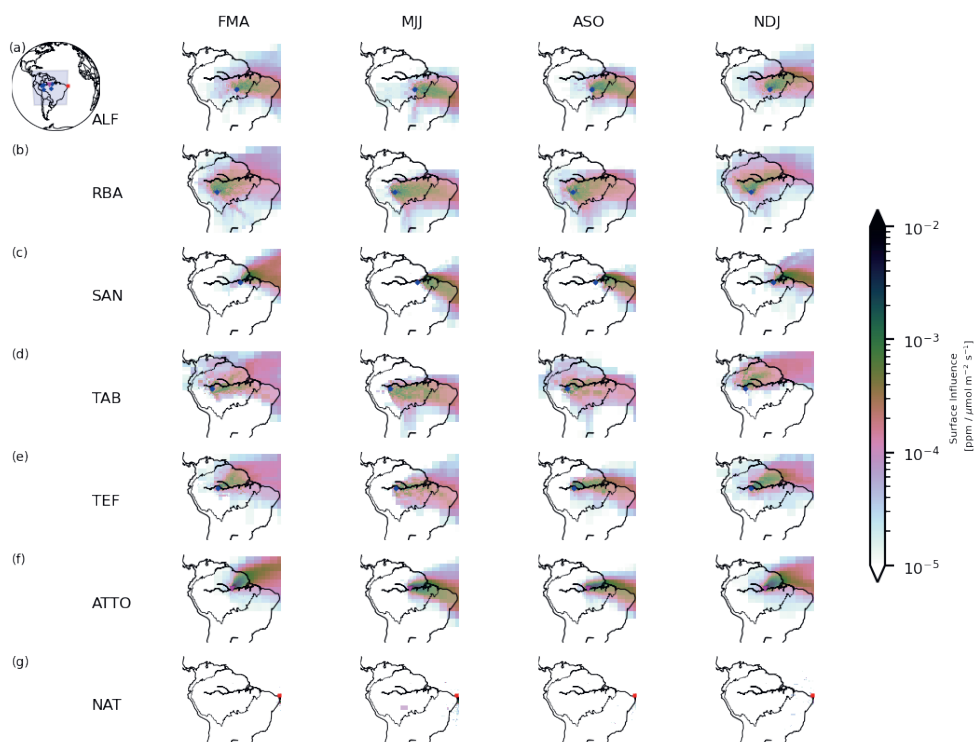
Figure 4.A1: Seasonal surface influence for each station used in the inversion. The averaging period for each station corresponds to the period of data availability, which is site-specific.
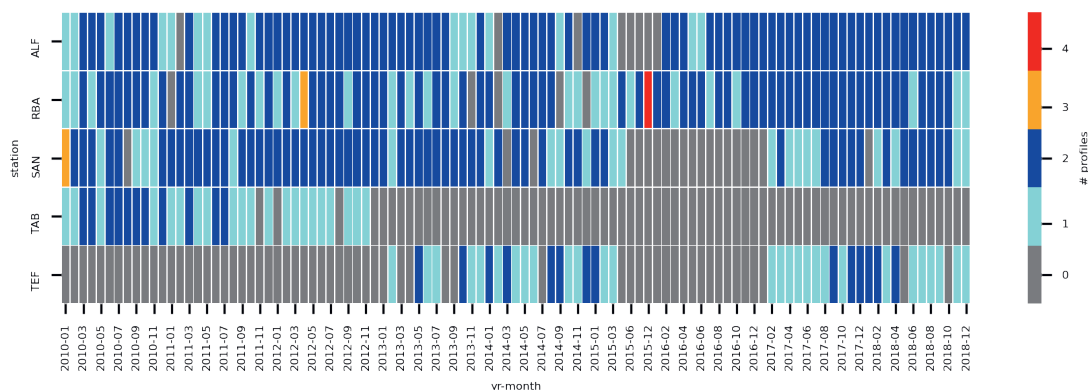
Figure 4.A2: Number of aircraft profiles per month over the period of interest in the inversion. An aircraft profile goes up until 4500 m.a.s.l and on average collects samples at 14 heights.
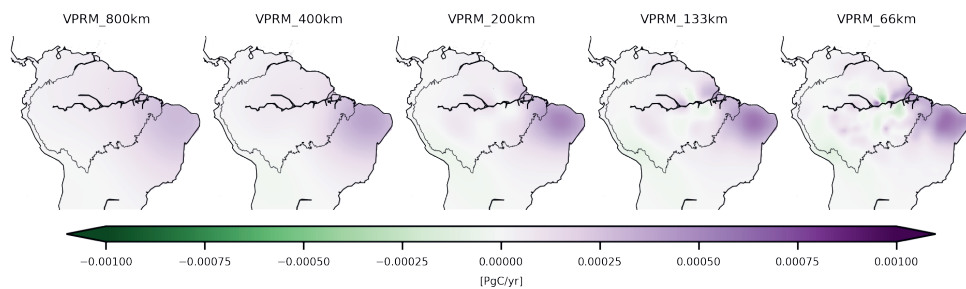
Figure 4.A3: NBE Innovation (Posterior - Prior) for experiments using different correlation length scales, but the same prior (VPRM).
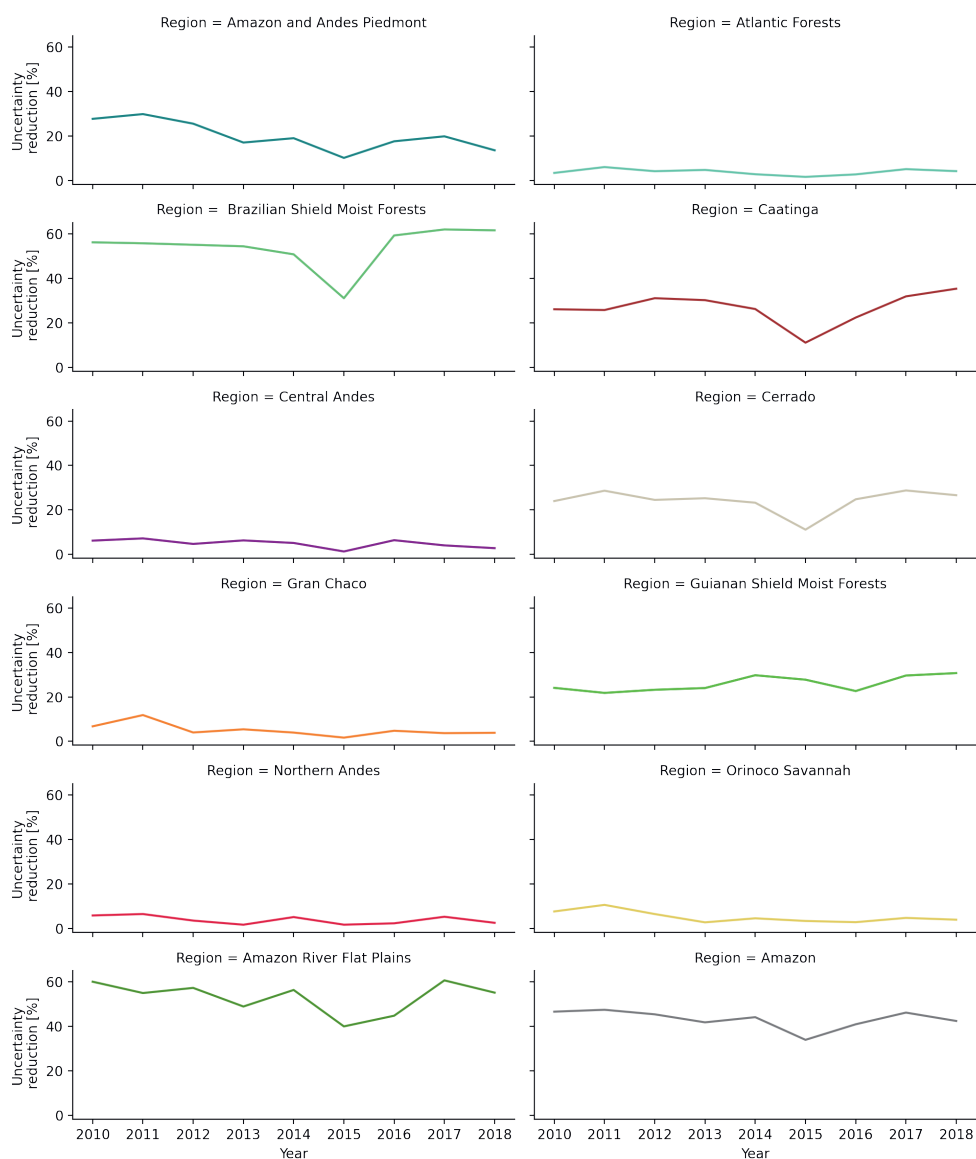
Figure 4.A4: Prior to posterior uncertainty reduction throughout the complete inversion period (2010-2018).
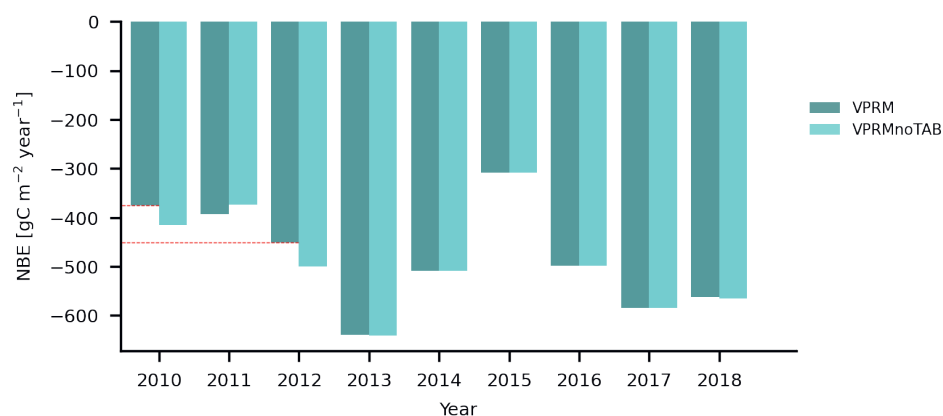
Figure 4.A5: Annual posterior fluxes using the same NEP prior (VPRM) but using different set of data assimilated. For the VPRM run the core set was used, for VPRMnoTAB we left TAB out. Note that TAB was active from 2010 to 2012, so those are the years that in which not assimilating it will show an effect. The red lines highlight the years in which the VPRM is lower than the VPRMnoTAB.

Note on correlation scale and prior uncertainty

The effect of a larger prior uncertainty on the posterior estimates can be on average 0.4 PgC higher (less uptake) than the reference case (Figure 4.A6a). Note that for each prior flux the effect is of similar magnitude throughout the years, except for SiB4. Having large differences here indicate that the prior can be further adjusted to fit the observational constraint. However, assuming a large prior uncertainty implies a reduction of the weight given by the prior information used (i.e. the biosphere models). This can be appropriate for a region like the Amazon, in which there are still big challenges to reproduce photo-synthetic uptake using biosphere models (Restrepo-Coupe et al., 2013), which can impact NBE. This challenge is similar for other approaches (Jung et al., 2020) but for estimating NEP in the tropics. In a Bayesian set-up, like ours, theoretically the choice of the prior uncertainty values should not be done after performing the inversion, yet in practice such assumption is difficult to fulfill as we eventually can learn from a first-guess optimization. Therefore, we recommend to perform an initial check of the priors and their magnitudes before inversion, and with this make the selection of the prior uncertainty. In a subsequent study, we will perform more experiments on this.

The prior error correlation length scale determines the degrees of freedom in the inversion. Having a larger scale results in fewer degrees of freedom and a more spatially-smoothed innovation. On the contrary, a smaller scale results in more degrees of freedom and a more locally-induced innovation. The selection of a 200 km scale for our reference inversion, as we stated earlier, is based on the scale of the influence of the aircraft network, but also on the scale at which we expect errors are correlated in the prior models. An experiment with other scales (Figure 4.A6), shows that below 200 km there is not so much change in the posterior estimates. But when the scale is larger, the posterior estimate can be as much as $1 \, \text{PgC year}^{-1}$ higher relative to the smaller scales. However, the adjustments obtained with a larger scale could be unrealistic knowing that our observational constraint have spatial limitations. Other studies have selected their prior error structure using data-driven methodologies (Kountouris et al., 2018b) or estimating it together with the posterior fluxes using a geostatistical approach (Michalak, 2004). For this study, after evaluating several scales we decided to use 200 km to have a compromise between enhanced local adjustments and unrealistic large distribution of the inversion-adjustments.
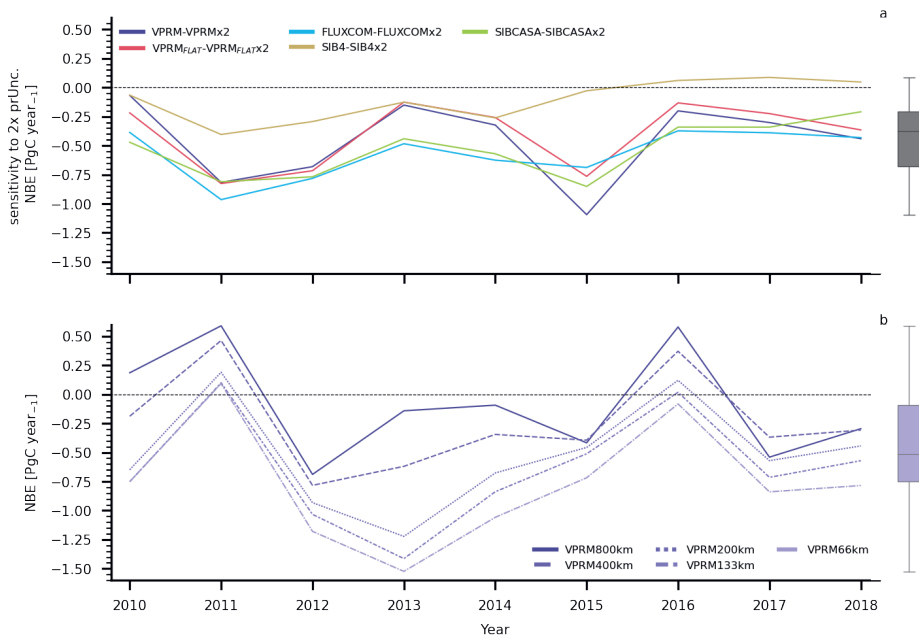
Figure 4.A6: The difference between annual and spatially aggregated posterior fluxes with 0.903 PgC and 0.903x2 PgC of prior uncertainty using different prior fluxes (a). On b, using VPRM as prior, a set of posterior fluxes is shown but varying the prior correlation length scale.

Chapter 5

Discussion and outlook

5.1   Discussion

In this work we have analyzed a unique observational record for methane and carbon dioxide in the Amazon region. We performed an observational analysis in Chapter 2 to study nighttime methane signals at ATTO. Carbon dioxide was studied by using an atmospheric transport model (Chapter 3) together with a Bayesian flux estimation system (Chapter 4). Our findings cover different spatio-temporal scales. The nighttime study for methane has site-specific implications at seasonal scale, while for carbon dioxide the seasonal and inter-annual variability was analyzed using the ATTO data and also using the inversion system with a regional perspective. In this last Chapter we discuss the role of atmospheric transport in using and interpreting atmospheric observations, the seasonality of greenhouses gases at regional scale and the spatial gradients found for Net Biome Exchange (NBE) uptake using the inversion system. These topics serve to examine how this work helps shape future research directions not only at ATTO but also at the Amazon-wide scale.

5.1.1   The role of atmospheric transport in interpreting atmospheric observations

Long-term atmospheric measurements are useful to understand underlying ecosystem processes, in particular at a site like ATTO where anthropogenic emissions are negligible. However, the interpretation of mole fraction measurements requires understanding of atmospheric transport, which can be characterized locally using micro-meteorology measurements or using atmospheric transport models for a more regional perspective. Each method has different shortcomings which impact our ability to understand the measured signals. Here we discuss these limitations having in mind future studies and ideas to overcome them.

In Chapter 2, using more than five years of continuous data we described the seasonal patterns and atmospheric conditions of a nighttime methane enhancement at the top of the 80 m tower. These events were mentioned by Andreae et al. (2015) with no additional description but highlighting their unexpected nature: strong methane enhancements at the uppermost level of the 80 m tower with no connection to the surface. Analyzing more years of data, we found that these events are more frequent during the dry season (July, August and September), when the amplitude of the average diurnal cycle was found to be four times larger than that of the wet season, driven by the nighttime enhancement. Although this would at first sight suggest stronger dry season CH_4 sources, we found that these signals are associated with a seasonal shift in wind direction that brings air from a potential source located southeast of the site. The nights when these events occurred were characterised by having stronger radiative cooling, low friction velocity, and a strong thermal inversion above the canopy. Under these stable atmospheric conditions, turbulent motions are caused by wind shear and are very weak. This case study demonstrates that

long-term measurements are useful to diagnose seasonal patterns, but the interpretation and source attribution depends on atmospheric transport.

Considering that atmospheric stability is not well resolved by mesoscale models (Sandu et al., 2013), we provided a thorough description of the atmospheric conditions and provide hypotheses for the source attribution of these CH_4 enhancements. We have in this process ruled out other potential sources like biomass burning and the Amazon river floodplains, while suggesting the Uatumã river as the likely source. However, there are a number of limitations to this approach. A previous study at ATTO (Oliveira et al., 2018), showed that some nights the nocturnal boundary layer height can be below the 80 m inlet. In this case, the CH_4 measured would be from the residual layer, associated with previous daytime dynamics and not linked to CH_4 emitted during that night. Characterizing the nocturnal PBL height from the perspective of the nighttime CH_4 signals is crucial for better understanding such nighttime events. Furthermore, the confirmation of the Uatumã river as the methane source is difficult only relying on the observations at ATTO. One would require a higher resolution modeling effort (i.e. Large Eddy Simulations (LES)) to study the atmospheric transport mechanism and CH_4 flux measurements at the river to confirm this source. Yet another helpful source of information is the isotopic signature of $\delta 13C\text{-}CH_4$ of the sources around ATTO. With the newly installed analyzer (Picarro Inc. Model G2201-i) providing continuous $\delta 13C\text{-}CH_4$, an attempt to characterize the source of the nighttime enhancement can also be done.

In Chapter 3 we have explored what we can learn from the atmospheric CO_2 record at a larger spatial scale. We used an atmospheric transport model to obtain the contribution of the background CO_2 to the measured CO_2 mole fractions at ATTO. By subtracting the contribution of the background CO_2 we were able to study the regional signal of CO_2, which is driven by sources and sinks within the footprint of the tower. We found that the regional signal had a marked seasonal cycle ($\sim$4 ppm amplitude), that when confronted to local CO_2 flux measurements from eddy covariance, showed phase differences indicating a decoupling between local and non-local (i.e. larger than the eddy covariance footprint) drivers of the regional CO_2. In other words, as the atmospheric record integrates signals from a larger footprint, it contains information not only linked to local processes but also from further away. An example of this was the response of the regional signal to the 2015/2016 El Niño. Our analysis suggests that the effect of the drought at ATTO, as inferred from the anomalies of the eddy covariance CO_2 flux, had a late onset beginning in the wet season in 2016, while the CO_2 regional signal shows positive anomalies already in 2015. The physiological reasons for such decoupling need to be studied further, but it demonstrates that the atmospheric record has a large potential for process understanding at multiple spatial scales. However, atmospheric transport plays a fundamental role in this process understanding, because it connects the upwind surface fluxes to the measured signals at ATTO. In addition, transport is crucial for estimating the background CO_2 to obtain the regional signals. In Chapter 3 we have concluded that errors in biosphere

fluxes are larger than those in atmospheric transport when simulating CO_2 mole fractions at ATTO, but we believe that a more thorough quantification of transport errors can still be done, primarily a characterization of the uncertainties in mixing height estimates from the STILT model at ATTO, and how these compare to uncertainties in other transport models.

Lastly, Chapters 2 and 3 demonstrate that the power of long-term atmospheric observations relies on the understanding of seasonal and inter-annual patterns that can be linked to ecosystem processes. However, challenges in simulating atmospheric transport and biosphere CO_2 exchange need to be overcome to improve our interpretation of the atmospheric signals. For example, regional estimates of net CO_2 exchange obtained with top-down methods (inversions or column budgeting techniques), should be constantly evaluated and compared with bottom-up estimates to reduce the spread between methods and the overall uncertainty of the multiple estimates. The RECCAP2 effort is a good example in this direction, but the lack of a continental observational network undermines the ability to target specific areas which complicates regional budgets. Furthermore, improving the ability to simulate nighttime transport would enable us to use nighttime measurements (note that in Chapter 4 we only use daytime measurements) and independently estimate ecosystem respiration, and directly estimate the nighttime methane source, all constrained with atmospheric data.

5.1.2   Drivers of seasonal GHG variability in the Amazon

Throughout this thesis, we have put a strong focus on the seasonal patterns observed in the atmospheric data and here we attempt to discuss more generally the main drivers at regional scale for both species, CH_4 and CO_2.

CO_2 Seasonality

The seasonal changes in atmospheric CO_2 in the Amazon region are mainly controlled by the net biome exchange (NBE). In Chapter 4, we showed the seasonal cycle of NBE for the whole Amazon region, and for four regions within it: The Amazon and Andes Piedmont (west), the Amazon River Flat plains, the Brazilian Shield Moist forest (southeast), and the Guianan Shield Moist forest (north-northeast). At the basin-wide scale we observe a small carbon source during May and June followed by an uptake of carbon from July to March. When zooming into the regions, the western part, the Amazon river and the Guianan Shield Moist forests have a similar seasonality with a clear uptake having an onset in July. The Brazilian Shield Moist forests displays a different seasonal cycle with a decreasing NBE from the peak in January and reaching a minimum in July (maximal carbon uptake). To what extent GPP or TER are driving the posterior NBE in each of these regions is one of the key questions to be answered in a next study, but information from Chapter 3 can already shed light on these processes at ATTO. In Chapter 3, using

the local eddy covariance flux we found that respiration controlled the seasonal variations in net ecosystem exchange. In Chapter 4, when looking at the closest grid cell to ATTO, the seasonality of the posterior NBE ensemble mean was very close to that of the local eddy covariance. From this we can speculate that in sites similar to ATTO, variability in respiration dominates the net carbon flux and thus atmospheric CO_2.

Saleska et al. (2009) found a negative relationship between mean annual precipitation (MAP) and the amplitude (peak-to-peak) of the mean seasonal cycle of NEE at different eddy covariance sites in South America but mainly within the Amazon. From this relationship, they defined sites where NEE is dominated by either photosynthesis (larger NEE amplitude and less MAP) or respiration (more MAP and smaller NEE amplitude). Looking further into this relationship but using our posterior NBE ensemble mean and precipitation of the Tropical Rainfall Measuring Mission (TRMM, Huffman et al. (2016)), we found a similar correlation to that of Saleska et al. (2009) at the same eddy covariance sites they used in their study (see Figure 5.1). Although the correlation is not significant for this small selection of sites (driven mainly by the BAN site, without it p<0.1), it calls for more research in this direction to associate the posterior NBE with environmental drivers. Exploring this relationship at the domain-wide scale should be part of a future study using the posterior NBE results from the regional inversion.
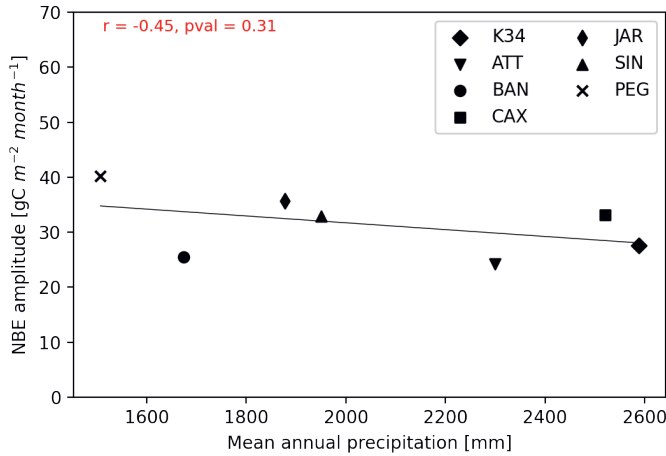
Figure 5.1: Mean annual precipitation from TRMM (Huffman et al., 2016) and the seasonal amplitude of the posterior NBE ensemble mean. The sites are the same as in Saleska et al. (2009) but we have added ATTO.

The dry season decline of NBE for the western and northern regions together with the Amazon river area can also be part of a future study. Whether such decline is driven by an increase in GPP or a reduction in TER remains to be seen. But in Chapter 3 we

showed that at ATTO, the eddy covariance data for non-El Niño years show an increase of respiration and GPP during the dry season. In the beginning of the dry season, GPP exceeds respiration leading to a sink of carbon, while later in the season respiration exceeds GPP, resulting in a source of carbon. Respiration has been linked to seasonal changes in fine root production and leaf flushing (Girardin et al., 2016; Raich, 2017), but also to the lagged response of deep and shallow soil CO_2 production to soil drying rates (Davidson et al., 2004). Relative to respiration, there have been more studies looking into the seasonality of photosynthesis in the Amazon, as we discuss next.

The GPP pattern observed at ATTO is in line with Restrepo-Coupe et al. (2013) and Guan et al. (2015), in which a dry season increase was reported. In contrast, Lee et al. (2013) found a higher GPP in the wet season than the dry season and they concluded that stomatal conductance decreases with increasing vapor pressure deficit leading to a decline in GPP. This hypothesis is contradicted by Green et al. (2020), who found a positive response of photosynthesis to increased vapor pressure deficit in the wettest regions in the Amazon during the dry season. The GPP increase during the dry season has been associated with a canopy green-up described in optical remote sensing studies (Huete et al., 2006; Myneni et al., 2007). These studies were challenged by Morton et al. (2014) stating that the observed green-up results from artefacts in the remote sensing sensor geometry. So far there seems to be more studies supporting an increase in dry season leaf production. Brando et al. (2010) showed an increase in leaf production during the 2005 drought and Wu et al. (2016) showed that leaf production in the dry season lead to a younger leaf age distribution in the canopy and thus more efficient capture of carbon dioxide per light photon. Furthermore, using field data to analyze the net productivity of trees and allocation of carbon to leaves, Girardin et al. (2016) found that Amazon forests maximize leaf production in the dry season. Thus partitioning the inversion-derived NBE into TER and GPP is an interesting path to follow. The evidence showing an increasing GPP in the dry season has to be placed in the NBE context, because the dry season decline in NBE could be driven by a large TER flux that can exceed GPP, like at ATTO in the late dry season. Therefore, efforts towards partitioning NBE will likely provide better understanding of the main controls of atmospheric CO_2 regionally.

CH$_4$ Seasonality

The seasonal variability of atmospheric CH_4 in the Amazon is mainly driven by wetland emissions according to Basso et al. (2021). In that study, using aircraft profiles they showed that there are marked regional differences in CH_4 fluxes within the Amazon. The northeast region close to Santarém and the Amazon river delta had the largest CH_4 fluxes with a bimodal seasonality, peaking at the start of the wet and dry seasons. More to the northwest, fluxes were high but with almost no seasonality and in southern sites the seasonality had similar amplitude with lower flux magnitudes. Basso et al. (2021) also showed that the relative contribution of fire-CH_4 emissions to the total CH_4 mole

fractions is higher in the southern sites than in the northern ones. Agricultural activities, mainly livestock via enteric fermentation, is another relevant non-fire methane source in the southern part of the Amazon (Basso et al., 2021). However, the seasonality of these activities are not well described and need further study.

The patterns described in Chapter 2 reveal a pronounced seasonal cycle of the nighttime methane signals at ATTO. Although site-specific, these findings can provide a way forward linking the atmospheric signals to CH_4 production processes in the Uatumã river. One of the questions to be answered is: how much does the upstream damming of the river increase the methane flux? It is difficult to answer this question without a long-term record of fluxes on the river, but a comparison with other rivers might shed light on this question. Current efforts are centered in characterizing the CH_4 fluxes of Uatumã river, so in the future this comparison can be made.

Further work looking at the entire methane record at ATTO (not only nighttime) should be performed to add regional scale conclusions associated with the ATTO footprint. This effort was partially done by Botia et al. (2020), applying a similar approach to that of Chapter 3, using forward simulations with different wetland flux products and evaluating the simulated CH_4 mole fractions at ATTO. For the ATTO footprint, the observed regional signal (measurements - background) had a distinct peak in the transition from wet to dry seasons (June and July), whereas the simulated regional CH_4 signal reaches the seasonal peak one month earlier. The latter suggests that we need to further evaluate the errors in current wetland emission models (i.e. WetCHARTs (Bloom et al., 2017) and the WETCHIMP intercomparison (Melton et al., 2013)) and those in transport, but already from the observations at ATTO we see that the highest mole fractions occur in a period of receding water levels just before the onset of the dry season.

An interesting point of convergence between the ATTO signals (Botia et al., 2020) and the aircraft profiles (Basso et al., 2021) is the emergent importance of the ascending and receding water level phases as observed by atmospheric mole fraction measurements. Basso et al. (2021) states that the bimodal seasonality of wetland emissions in the northeast close to Santarém need to be better explained. For the ATTO record, we found a similar behavior pointing to larger emissions just after the wet season. Some of the potential explanations for this are the following: A lower water level results in lower hydrostatic pressure, making the ebullition (bubbles) pathway more effective (Sawakuchi et al., 2014). In addition, the peak after the wet season can be explained by a longer CH_4 production time in sediments over the wet season which can then be emitted at lower water stages (Barbosa et al., 2020).

It is clear that wetlands and flooded forests play an important role in the Amazon as the largest source of CH_4. However, upland valleys can also represent small CH_4 sources that could be relevant when extrapolated regionally. The upland valleys were mentioned in Chapter 2 as potential sources of the nighttime methane signals together with the

Uatumã river. Based on this indication, air samples and soil fluxes were measured in a short field-campaign around the ATTO site in 2019. The flux measurements suggested a consistent source of CH_4 in the upland valley (not shown, personal communication Hella van Asperen, 2019). Moreover, from few discrete air samples (flasks) we obtained the isotopic signature of CH_4 at the valley and also at different locations ($\delta^{13}C$ and δ^2H, see Figure 5.2). In general, we see a strong biogenic source falling mainly in the wetland category and difficult to differentiate, yet there are some interesting details. The isotopic composition of an airborne sample taken during the BARCA campaign (Beck et al., 2012) confirms the biogenic source of methane in the Amazonian troposphere, though the heavier signature in $\delta^{13}C$ is because the air mass has undergone mixing with the tropospheric background, which is heavier than that produced biogenically. When looking closer to the sources around ATTO (tower, river and valley), the range in $\delta^{13}C$ values could serve as a potential indicator to differentiate within biogenic sources. The river and valley seem to be more depleted (more negative) than the signatures measured at the Tower, but the T79m_s2 signature shows that these signals could be identified. Moreover, the signature from the "valley", which shows a heavier δ^2H, can also serve to characterize specific sources for a potential attribution. Having a thorough characterization of the isotopic signature of biogenic sources could help interpreting seasonal signals in the continuous $\delta^{13}C\text{-}CH_4$ record recently installed at ATTO.

However, more samples need to be taken to improve the characterization around ATTO. This research path together with the higher emissions at low water stages mentioned previously are promising ways forward, that are currently ongoing progress. This can add valuable information for the methane scientific community in terms of isotopic signature of natural sources, to better understand the role of wetlands and the Amazon in the current atmospheric growth rate of CH_4.

Rivers

In Chapter 2, we suggested that the Uatumã river is likely the source of the nighttime CH_4 signals at ATTO. In Chapter 3, we found that including river outgassing as a flux component in forward simulations of CO_2 mole fractions improved the shape of the seasonal cycle when compared to observations. Following this finding, in Chapter 4, we made experiments to assess the impact of prescribing rivers in the atmospheric inversions of net biome exchange. The river fluxes in Chapter 3 and 4 were taken from the recently developed ORCHILEAK model. This model couples the terrestrial carbon component with the lateral export of carbon and the water-surface outgassing of CO_2. For more details on the model limitations we refer the reader to Chapter 3 and for the model description to Lauerwald et al. (2017) and Hastie et al. (2019). Even though rivers were not a central subject of study in this thesis, they emerged as an important component for interpreting the ATTO measurements. Therefore, here we revisit the role of rivers and other aquatic habitats in the seasonal variability of CH_4 and CO_2 in the Amazon.
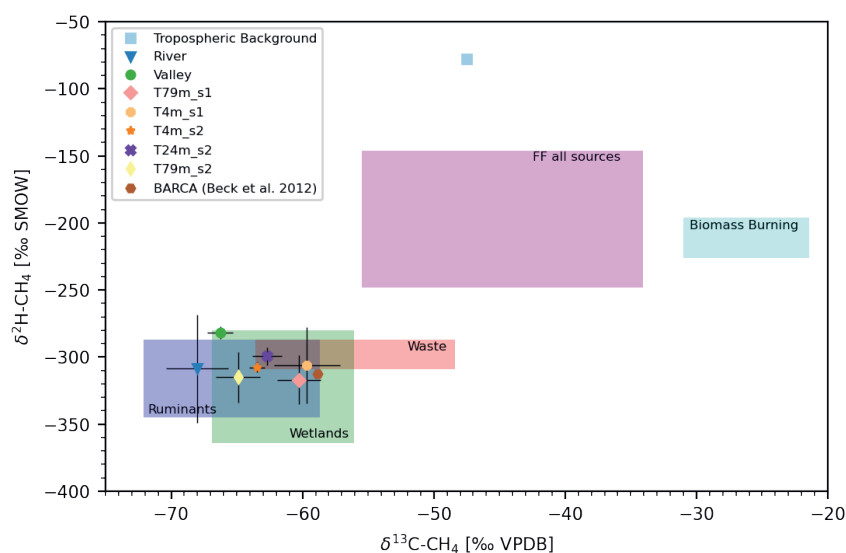
Figure 5.2: Isotopic composition of CH_4 in the samples collected at ATTO in 2019. The samples with the ”_s2” postfix were collected by another PhD student as part of her own project but during the same dry season in 2019. The shaded areas indicate the range reported for know sources (Sherwood et al., 2017), the FF stands for Fossil Fuel.

The processes producing emissions of CH_4 or CO_2 in aquatic habitats like flooded forests and rivers are very different, but from an atmospheric perspective, the net flux is what contributes to having a source or sink of the species of interest in these environments. Aquatic vegetation and algae play a role in the uptake and release of CO_2 (Melack et al., 2009; Melack, 2016), while decomposition of organic material in rivers and flooded forest sediments results in CO_2 and CH_4 production (Melack et al., 2009; Melack, 2016). The lateral export of dissolved organic carbon (DOC) and particulate organic carbon (POC) from upland terra-firme forest to the aquatic habitats contributes to a lesser extent to the outgassed CO_2. Therefore, net fluxes of CO_2 depend on the primary productivity and respiration of aquatic vegetation and the CO_2 from decomposition processes (Engle et al., 2008). A recent synthesis based on previous research and flux measurements in aquatic habitats in the Amazon, suggested that rivers were in balance (neither sinks or sources or CO_2) (SPA, 2021), but considerable uncertainties remain in estimating the basin-wide totals of net fluxes and aquatic net primary productivity. A modeling study by Hastie et al. (2019) included river outgassing as a source to the atmosphere when calculating the net carbon balance of the Amazon. Assuming that rivers are a source of carbon to the atmosphere, as we implicitly did by using the ORCHILEAK model (Hastie et al., 2019),

and in light of our results from Chapter 3, we believe that the seasonality of river CO_2 emissions are important for interpreting the ATTO CO_2 measurements. Furthermore, our results from Chapter 4 showed that when including the potential river source the biosphere becomes a slightly larger sink, something that was not considered by previous top-down studies (Gatti et al., 2014; van der Laan-Luijkx et al., 2015; Alden et al., 2016; Gatti et al., 2021).

For CH_4, the role of rivers and aquatic habitats is more clear as we mentioned earlier. In the absence of a strong uptake flux, the anaerobic methane source is dominant. Our findings from Chapter 2 fit in a broader context associated with the impacts of the Balbina dam located upstream of the Uatumã river, on the hydrology and ecology of the flooded forests along this river. These impacts can lead to enhanced CH_4 production, as we suggested in Chapter 2 based on two main reasons. The first is that the Uatumã river has enhanced CH_4 concentrations downstream of the Balbina dam. Part of the methane produced in the dam leaks to the river after the turbine intake (Kemenes et al., 2007). Kemenes et al. (2007) also showed that the concentrations in the Uatumã can be 3 orders of magnitude higher than other similar rivers (Richey et al., 1988). The second reason is associated with an enhanced carbon input for anaerobic decomposition coming from the dead stands of flooded forest. The damming of the river changed the flooding pulse downstream, causing large tree mortality over the last three decades (Resende et al., 2019). However, even though we found a clear seasonal pattern for the nighttime signals, this is a site-specific finding that serves as a reference when considering possible impacts when damming another river in a similar habitat.

5.1.3   Amazon and beyond: the Cerrado and Caatinga in perspective

In Chapter 4 we have shown that the inversion adjusts prior CO_2 fluxes significantly, leading to a source of carbon in the northeast of Brazil in the posterior NBE. The Cerrado and Caatinga biomes were on average a sink of carbon in the prior ensemble mean (Chapter 4), meaning that the biosphere models used in this study simulate on average a sink of carbon for these regions. Note however that such sinks in the biosphere models results only from spin-up, increased warming, or CO_2 fertilization and are not at all driven by local knowledge or empirical observations on the vegetation carbon balance (Fawcett et al., 2022). The adjustments after the inversion resulted in a weak sink for the Cerrado and a consistent source over the years for the Caatinga. We showed that this result is robust against changing the spatial error structure in the inversion settings, but it is in contrast to what Gatti et al. (2021) found. They suggested that vegetation of the southeast of the Amazon was loosing the capacity to capture carbon, reporting on average a positive NBE for the years 2010 to 2018, thus locating a net source of carbon within the Amazon in the southeast regions. In that study, they limited their analyses to the legal Amazon domain but used the same aircraft data as we use in our study. In Chapter 4, we have discussed the potential reasons for the difference of our results with those of Gatti et al. (2021), so

here we discuss our findings in the context of other research and pose a hypothesis that could explain the carbon source in the semiarid regions northeast of Brazil.

The Cerrado and Caatinga biomes cover approximately 35% of the Brazilian land mass (Beuchle et al., 2015) and are characterized by a savannah-type ecosystem (Cerrado) (Sano et al., 2007) and seasonally dry tropical forest (Caatinga) (Prado, 2003). Both biomes have a marked seasonality in precipitation, with mean annual precipitation of less than 750 mm year^{-1} in the Caatinga (Prado, 2003; Leal et al., 2005), and from 800 to 2000 mm year^{-1} in the Cerrado (Ratter et al., 1997). Studies focusing on ecosystem functioning conducted in both biomes using eddy covariance measurements, have shown that these ecosystems have similar seasonal patterns in net ecosystem exchange. In general, with the onset of the rainy season higher carbon uptake is observed over converted pasture and also over natural vegetation (Miranda et al., 1997; Varella et al., 2004; Santos et al., 2004; Silva et al., 2017; Mendes et al., 2020; Alves et al., 2021). Studies focusing on soil CO_2 emissions comparing converted pasture and both natural ecosystems, Caatinga (Ribeiro et al., 2016) and Cerrado (Varella et al., 2004), found no significant differences in magnitude between the pasture and the natural ecosystem. Both coincided in higher CO_2 emissions at the onset of the rainy season (Varella et al., 2004; Ribeiro et al., 2016). The findings of (Ribeiro et al., 2016) are in line with Mendes et al. (2020), where they observed an increase in ecosystem respiration with the onset of the rainy season, but offset by GPP. Integrated over time, these ecosystems in their natural form or converted to pasture seemed to be carbon sinks when no disturbance is taken into account (Santos et al., 2004; Bustamante et al., 2012; Silva et al., 2017; Mendes et al., 2020; Alves et al., 2021).

However, these biomes have suffered considerable natural vegetation loss due to the expansion of the agricultural frontier. Beuchle et al. (2015), found that over the period between 1990 and 2010, both biomes had a continued net loss of natural vegetation. More recently, most of the agricultural expansion in the Cerrado has been concentrated in a region called MATOPIBA, which refers to portions of the Maranhão, Tocantins, Piauí and Baia states (Spera et al., 2016). Drought periods in the Caatinga can extend over years (Leal et al., 2005), making agricultural activities more difficult to sustain, yet considerable pasture conversion for extensive livestock has changed the Caatinga lanscape (Leal et al., 2005). Such anthropogenic pressure starting in deforestation and resulting in pasture or cropland conversion leads to fire CO_2 emissions (van der Werf et al., 2010, 2017). The Cerrado biome was found to have higher fire CO_2 emissions than the Caatinga, with an increasing trend over the last years (da Silva Junior et al., 2020). Moreover, the annual fire regime fluctuates between naturally-occurring low-intensity fires at the end of the wet season ignited by lighting, and anthropogenic high-intensity fires at the end of dry season (Ramos-Neto & Pivello, 2000).

Frequent fires can lead to aboveground biomass reduction changing the ecosystem from a sink to a source of carbon (de Azevedo et al., 2020). Moreover, Bustamante et al. (2012) found that a large portion of the CO_2 emissions from pasture management (i.e. burning practices) in Brazil are originated in the Cerrado. Over the period of 2003 to 2013, changes in vegetation stocks due to cropland conversion in the Cerrado and specifically in the MATOPIBA region, contributed with 33% of the forest carbon emissions (Noojipady et al., 2017). Note that the latter does not take into account fire and decomposition sources.

Given these studies, carbon emissions in these two biomes, but primarily in the Cerrado, can be grouped in two categories. The first one being associated directly with fires (either from deforestation or pasture management), and the second arising from degradation after conversion of natural vegetation to pastures or croplands. The emissions in the second category are associated with changes in carbon stocks, decomposition, and sink to source shifts due to climate change (Bustamante et al., 2012). Having this in mind, we hypothesize that the carbon source in the semi-arid ecosystems of the Cerrado and Caatinga given by the inversion (Chapter 4) is likely due to agricultural expansion in the Cerrado, mainly from the second category mentioned above. On top, their possibility for secondary forest regrowth is compromised. This contrasts the Amazon biome which is highly resilient (Poorter et al., 2021) and has shown a relatively fast recovery in aboveground biomass by secondary forest growth (Poorter et al., 2016). This would make the carbon source we find in this thesis not only large, but likely also to influence the regional carbon balance for decades to come. Hence, the hypothesis of the Cerrado and Caatinga source, driven by carbon stock changes and fires, should be part of a future study in which additional ways (to those in Chapter 4) of testing the robustness of the inversion results are explored. For example, not only testing different spatial error correlation length scales, but also testing the assumption of isotropic (same in both latitude and longitude) exponential decay of the spatial error structure.

5.1.4 Outlook

Besides the potential ways forward we have implicitly suggested in the previous topics, additional research paths arising from this thesis are briefly mentioned here. In this thesis we have mainly used the uppermost inlet of the 80-m tower, but future work should focus on interpreting the vertical gradients of the long-term GHG record and also from the newly installed data streams. Calculating fluxes with the gradient method, not only on the 80-m tower but also using the FTIR profile measurements on the 325-m Tall Tower is an interesting path to follow. Using the 80-m tower profiles, Shujiro Komiya at MPI-BGC has shown interesting results, confirming at local scale the large carbon uptake in 2017 that we also observe in Chapter 4 regionally. This work has to be expanded for the measurements at the Tall Tower. In addition, the newly installed G2201-i Picarro, providing δ^{13}C-CO_2/CH_4, can also provide insights on the isotopic fluxes of both CO_2 and

CH_4. With δ^{13}C-CO_2 the potential of having an additional method for partitioning of the net CO_2 flux into GPP and Respiration seems promising (Wehr et al., 2016). In addition, the stable isotopes of CH_4 can inform us about the nighttime source of the enhancements studied in Chapter 2, while the 325 m profile can finally provide an upper level (> 80 m) constraint to better describe the nighttime CH_4 dynamics from the perspective of the residual layer and nocturnal boundary layer.

Another tracer that can be used together with greenhouse gases is Radon (^{222}Rn). A radon monitor was installed in 2018 at 80 m on the Tall Tower and the system has been running since then. With already more than three years of data, some of the possible studies using this tracer are the following. ^{222}Rn can serve to better constrain vertical mixing in the atmospheric transport model STILT, which can lead to improved simulations of trace gases at ATTO. In addition, by using the Radon Tracer Method one could attempt estimating upwind fluxes of a specific tracer. A master student in Wageningen University (supervised jointly by Santiago Botía and Ingrid Luijkx) has shown that by combining the ^{222}Rn record with eddy covariance and the CO_2 mole fractions one can estimate reasonable ^{222}Rn fluxes during nighttime at ATTO. This ^{222}Rn flux can then be used to estimate regional scale CH_4 fluxes using the Radon Tracer Method (Levin et al., 1999), but considering the limitations that this methods entails (Levin et al., 2021).

In addition to these observational-based studies using the current and newly available data streams at ATTO, a future effort should focus on setting up the regional inversion system for CH_4. Part of this work has been done in Chapter 4 for CO_2, so extending the application of the CarboScope regional system to CH_4 over the Amazon domain is feasible in the future. An important aspect to analyze is the inclusion of satellite data in the regional inversions. Assimilating XCO_2 and XCH_4 in combination with in-situ (ATTO) and flask profiles (aircraft data) could provide a better spatial coverage that can help reduce the uncertainty in places not yet constrained by the current atmospheric network. Some of the issues to overcome in such an effort are associated with weighting the data based on their model-data mismatch error which has a temporal correlation. Moreover, satellite-derived columns could be biased towards dry season retrievals, which are less affected by clouds. Nevertheless, recent efforts using satellite data (Tunnicliffe et al., 2020; Saunois et al., 2020; Wilson et al., 2021) show consistent results for the Amazon region, yet improvements in several aspects are needed. Some of this issues are, discrepancies between only-satellite driven and surface-only inversions, how chemical transport models deal with the atmospheric distribution of the OH radical, and the source/sink attribution in the posterior fluxes (Saunois et al., 2020).

Shifting to CO_2, an interesting future line of research can focus on interpreting the spatial gradients of NBE reported on Chapter 4, but also on partitioning the NBE signal in GPP and Respiration. An possibility for partitioning NBE using the inversion system, is to use the newly installed profile measurements at the Tall Tower (325 m) and assimilate partial

columns during night. Regarding the spatial gradients of NBE, as they can vary regionally the processes driving them are expected to be different but in principle should be prone to be constrained from atmospheric signals. It has been shown that secondary forests due to their rapid growth have higher net carbon sequestration rates (Poorter et al., 2016; Requena Suarez et al., 2019). Their potential for carbon sequestration in the Amazon region has been highlighted by Chazdon et al. (2016) and Heinrich et al. (2021). Moreover, Brienen et al. (2015) suggested an increasing trend in tree mortality, while Esquivel-Muelbert et al. (2020) showed the spatial distribution of mortality rates in the Amazon with the southeast having greater rates on average. Another processes that can have an impact on CO_2 emissions is forest degradation (Assis et al., 2020). If tree mortality is the dominant control of the spatial distribution of aboveground biomass (Johnson et al., 2016) and forest degradation is larger than previously thought (Matricardi et al., 2020), with both having increasing trends (Brienen et al., 2015; Matricardi et al., 2020), there should be a detectable signal in the atmosphere. These processes, should be captured by changes in atmospheric CO_2 mole fractions and thus in surface fluxes. However, the actual sparse observational coverage and the temporal resolution (i.e. aircraft data) undermines this capability. Therefore, a promising way forward is to develop methods and observational networks targeted to understand and quantify their magnitude and spatial distribution by atmospheric changes in CO_2 and using atmospheric inversions.

References

Acevedo, O. C., Mahrt, L., Puhales, F. S., Costa, F. D., Medeiros, L. E., & Degrazia, G. A. (2016). Contrasting structures between the decoupled and coupled states of the stable boundary layer: Stable Boundary Layer Coupling. *Quarterly Journal of the Royal Meteorological Society*, *142*, 693–702. doi:doi: 10.1002/qj.2693.

Acevedo, O. C., Maroneze, R., Costa, F. D., Puhales, F. S., Degrazia, G. A., Martins, L. G. N., Oliveira, P. E. S., & Mortarini, L. (2019). The Nocturnal Boundary Layer transition from Weakly to Very Stable. Part 1. Observations. *Quaterly Journal of the Royal Meteorological Society*, . doi:doi: 10.1002/qj.3642.

Acevedo, O. C., Moraes, O. L. L., Degrazia, G. A., & Medeiros, L. E. (2006). Intermittency and the Exchange of Scalars in the Nocturnal Surface Layer. *Boundary-Layer Meteorology*, *119*, 41–55. doi:doi: 10.1007/s10546-005-9019-3.

Akagi, S. K., Yokelson, R. J., Wiedinmyer, C., Alvarado, M. J., Reid, J. S., Karl, T., Crounse, J. D., & Wennberg, P. O. (2011). Emission factors for open and domestic biomass burning for use in atmospheric models. *Atmospheric Chemistry and Physics*, *11*, 4039–4072. doi:doi: 10.5194/acp-11-4039-2011.

Albert, L. P. et al. (2018). Age-dependent leaf physiology and consequences for crown-scale carbon uptake during the dry season in an Amazon evergreen forest. *New Phytologist*, *219*, 870–884. doi:doi: https://doi.org/10.1111/nph.15056.

Alden, C. B. et al. (2016). Regional atmospheric CO_2 inversion reveals seasonal and geographic differences in Amazon net biome exchange. *Global Change Biology*, *22*, 3427–3443. doi:doi: 10.1111/gcb.13305.

Aleixo, I., Norris, D., Hemerik, L., Barbosa, A., Prata, E., Costa, F., & Poorter, L. (2019). Amazonian rainforest tree mortality driven by climate and functional traits. *Nature Climate Change*, *9*, 384–388. doi:doi: 10.1038/s41558-019-0458-0.

Alencar, A., Moutinho, P., Arruda, V., Balzani, C., & Ribeiro, J. (2019). *Amazon Burning: Locating the fires*. Technical Report, . Available at: https://ipam.org.br/wp-content/uploads/2019/09/AmazonBurning_LocatingTheFires.pdf.

Alves, J. D. N., Ribeiro, A., Rody, Y. P., Loos, R. A., & Hall, K. B. (2021). Carbon uptake and water vapor exchange in a pasture site in the Brazilian Cerrado. *Journal

of Hydrology, *594*, 125943. doi:doi: 10.1016/j.jhydrol.2020.125943.

Amaral, J. H. F., Melack, J. M., Barbosa, P. M., MacIntyre, S., Kasper, D., Cortés, A., Silva, T. S. F., Nunes de Sousa, R., & Forsberg, B. R. (2020). Carbon Dioxide Fluxes to the Atmosphere From Waters Within Flooded Forests in the Amazon Basin. *Journal of Geophysical Research: Biogeosciences*, *125*. doi:doi: 10.1029/2019JG005293.

Andreae, M. O. (2001). The Biosphere: Pilot or Passenger on Spaceship Earth? In *Contributions to Global Change Research* (pp. p59–66).

Andreae, M. O. (2019). Emission of trace gases and aerosols from biomass burning – an updated assessment. *Atmospheric Chemistry and Physics*, *19*, 8523–8546. doi:doi: 10.5194/acp-19-8523-2019.

Andreae, M. O. et al. (2015). The Amazon Tall Tower Observatory (ATTO): overview of pilot measurements on ecosystem ecology, meteorology, trace gases, and aerosols. *Atmospheric Chemistry and Physics*, *15*, 10723–10776. doi:doi: 10.5194/acp-15-10723-2015.

Andreae, M. O., Artaxo, P., Beck, V., Bela, M., Freitas, S., Gerbig, C., Longo, K., Munger, J. W., Wiedemann, K. T., & Wofsy, S. C. (2012). Carbon monoxide and related trace gases and aerosols over the Amazon Basin during the wet and dry seasons. *Atmospheric Chemistry and Physics*, *12*, 6041–6065. doi:doi: 10.5194/acp-12-6041-2012.

Andreae, M. O., & Merlet, P. (2001). Emission of trace gases and aerosols from biomass burning. *Global Biogeochemical Cycles*, *15*, 955–966. doi:doi: 10.1029/2000GB001382.

Andrews, A. E. et al. (2014). CO_2, CO, and CH_4 measurements from tall towers in the NOAA Earth System Research Laboratory's Global Greenhouse Gas Reference Network: instrumentation, uncertainty analysis, and recommendations for future high-accuracy greenhouse gas monitoring efforts. *Atmospheric Measurement Techniques*, *7*, 647–687. doi:doi: 10.5194/amt-7-647-2014. Publisher: Copernicus GmbH.

Aragão, L. E. O. C. et al. (2018). 21st Century drought-related fires counteract the decline of Amazon deforestation carbon emissions. *Nature Communications*, *9*, 1–12. doi:doi: 10.1038/s41467-017-02771-y.

Araújo, A. C. d., Kruijt, B., Nobre, A. D., Dolman, A. J., Waterloo, M. J., Moors, E. J., & Souza, J. S. d. (2008). Nocturnal accumulation of CO2 underneath a tropical forest canopy along a topographical gradient. *Ecological Applications*, *18*, 1406–1419. doi:doi: 10.1890/06-0982.1.

Archer, D., Eby, M., Brovkin, V., Ridgwell, A., Cao, L., Mikolajewicz, U., Caldeira, K., Matsumoto, K., Munhoven, G., Montenegro, A., & Tokos, K. (2009). Atmospheric Lifetime of Fossil Fuel Carbon Dioxide. *Annual Review of Earth and Planetary Sciences*, *37*, 117–134. doi:doi: 10.1146/annurev.earth.031208.100206.

Arrhenius, S., & Holden, E. S. (1897). ON THE INFLUENCE OF CARBONIC ACID

IN THE AIR UPON THE TEMPERATURE OF THE EARTH. *Publications of the Astronomical Society of the Pacific*, *9*, 14–24.

van Asperen, H., Alves-Oliveira, J. R., Warneke, T., Forsberg, B., de Araújo, A. C., & Notholt, J. (2021). The role of termite CH_4 emissions on the ecosystem scale: a case study in the Amazon rainforest. *Biogeosciences*, *18*, 2609–2625. doi:doi: 10.5194/bg-18-2609-2021. Publisher: Copernicus GmbH.

Assahira, C., Piedade, M. T. F., Trumbore, S. E., Wittmann, F., Cintra, B. B. L., Batista, E. S., Resende, A. F. d., & Schöngart, J. (2017). Tree mortality of a flood-adapted species in response of hydrographic changes caused by an Amazonian river dam. *Forest Ecology and Management*, *396*, 113–123. doi:doi: 10.1016/j.foreco.2017.04.016.

Assis, T. O., Aguiar, A. P. D. d., Randow, C. v., Gomes, D. M. d. P., Kury, J. N., Ometto, J. P. H. B., & Nobre, C. A. (2020). CO2 emissions from forest degradation in Brazilian Amazon. *Environmental Research Letters*, *15*, 104035. doi:doi: 10.1088/1748-9326/ab9cfc. Publisher: IOP Publishing.

de Azevedo, G. B., Rezende, A. V., de Oliveira Sousa Azevedo, G. T., Miguel, E. P., de Gois Aquino, F., Bruzinga, J. S. C., de Oliveira, L. S. C., Pereira, R. S., & Teodoro, P. E. (2020). Woody biomass accumulation in a Cerrado of Central Brazil monitored for 27 years after the implementation of silvicultural systems. *Forest Ecology and Management*, *455*, 117718. doi:doi: 10.1016/j.foreco.2019.117718.

Baccini, A., Goetz, S. J., Walker, W. S., Laporte, N. T., Sun, M., Sulla-Menashe, D., Hackler, J., Beck, P. S. A., Dubayah, R., Friedl, M. A., Samanta, S., & Houghton, R. A. (2012). Estimated carbon dioxide emissions from tropical deforestation improved by carbon-density maps. *Nature Climate Change*, *2*, 182–185. doi:doi: 10.1038/nclimate1354. Number: 3 Publisher: Nature Publishing Group.

Baccini, A., Walker, W., Carvalho, L., Farina, M., Sulla-Menashe, D., & Houghton, R. A. (2017). Tropical forests are a net carbon source based on aboveground measurements of gain and loss. *Science*, *358*, 230–234. doi:doi: 10.1126/science.aam5962.

Baker, I. T., Prihodko, L., Denning, A. S., Goulden, M., Miller, S., & Rocha, H. R. d. (2008). Seasonal drought stress in the Amazon: Reconciling models and observations. *Journal of Geophysical Research: Biogeosciences*, *113*. doi:doi: https://doi.org/10.1029/2007JG000644.

Baker, J. C. A., & Spracklen, D. V. (2019). Climate Benefits of Intact Amazon Forests and the Biophysical Consequences of Disturbance. *Frontiers in Forests and Global Change*, *2*. doi:doi: 10.3389/ffgc.2019.00047. Publisher: Frontiers.

Bakwin, P. S., Tans, P. P., Hurst, D. F., & Zhao, C. (1998). Measurements of carbon dioxide on very tall towers: results of the NOAA/CMDL program. *Tellus B: Chemical and Physical Meteorology*, *50*, 401–415. doi:doi: 10.3402/tellusb.v50i5.16216.

Ballantyne, A. P., Alden, C. B., Miller, J. B., Tans, P. P., & White, J. W. C. (2012).

Increase in observed net carbon dioxide uptake by land and oceans during the past 50 years. *Nature*, *488*, 70–72. doi:doi: 10.1038/nature11299.

Barbosa, P. M., Melack, J. M., Amaral, J. H. F., MacIntyre, S., Kasper, D., Cortés, A., Farjalla, V. F., & Forsberg, B. R. (2020). Dissolved methane concentrations and fluxes to the atmosphere from a tropical floodplain lake. *Biogeochemistry*, *148*, 129–151. doi:doi: 10.1007/s10533-020-00650-1.

Barichivich, J., Gloor, E., Peylin, P., Brienen, R. J. W., Schöngart, J., Espinoza, J. C., & Pattnayak, K. C. (2018). Recent intensification of Amazon flooding extremes driven by strengthened Walker circulation. *Science Advances*, *4*, eaat8785. doi:doi: 10.1126/sciadv.aat8785.

Barlow, J., Berenguer, E., Carmenta, R., & França, F. (2020). Clarifying Amazonia's burning crisis. *Global Change Biology*, *26*, 319–321. doi:doi: 10.1111/gcb.14872.

Bartlett, K. B., Crill Patrick M., Sebacher Daniel I., Harriss Robert C., Wilson John O., & Melack John M. (1988). Methane flux from the central Amazonian floodplain. *Journal of Geophysical Research: Atmospheres*, *93*, 1571–1582. doi:doi: 10.1029/JD093iD02p01571.

Basso, L. S. et al. (2021). Amazon methane budget derived from multi-year airborne observations highlights regional variations in emissions. *Communications Earth & Environment*, *2*, 1–13. doi:doi: 10.1038/s43247-021-00314-4.

Bastos, A. et al. (2020). Sources of Uncertainty in Regional and Global Terrestrial CO_2 Exchange Estimates. *Global Biogeochemical Cycles*, *34*. doi:doi: 10.1029/2019GB006393.

Basu, S., Baker, D. F., Chevallier, F., Patra, P. K., Liu, J., & Miller, J. B. (2018). The impact of transport model differences on CO_2 surface flux estimates from OCO-2 retrievals of column average CO_2. *Atmospheric Chemistry and Physics*, *18*, 7189–7215. doi:doi: https://doi.org/10.5194/acp-18-7189-2018. Publisher: Copernicus GmbH.

Beck, V. et al. (2012). Methane airborne measurements and comparison to global models during BARCA. *Journal of Geophysical Research: Atmospheres*, *117*. doi:doi: 10.1029/2011JD017345.

Beck, V., Gerbig, C., Koch, T., Bela, M. M., Longo, K. M., Freitas, S. R., Kaplan, J. O., Prigent, C., Bergamaschi, P., & Heimann, M. (2013). WRF-Chem simulations in the Amazon region during wet and dry season transitions: evaluation of methane models and wetland inundation maps. *Atmospheric Chemistry and Physics*, *13*, 7961–7982. doi:doi: 10.5194/acp-13-7961-2013.

Beer, C. et al. (2010). Terrestrial Gross Carbon Dioxide Uptake: Global Distribution and Covariation with Climate. *Science*, *329*, 834–838. doi:doi: 10.1126/science.1184984.

Bergamaschi, P., Frankenberg, C., Meirink, J. F., Krol, M., Villani, M. G., Houweling,

S., Dentener, F., Dlugokencky, E. J., Miller, J. B., Gatti, L. V., Engel, A., & Levin, I. (2009). Inverse modeling of global and regional CH4 emissions using SCIAMACHY satellite retrievals. *Journal of Geophysical Research*, *114*. doi:doi: 10.1029/2009JD01 2287.

Betts, A. K., Fisch, G., von Randow, C., Silva Dias, M. A. F., Cohen, J. C. P., da Silva, R., & Fitzjarrald, D. R. (2009). The Amazonian boundary layer and mesoscale circulations. In M. Keller, M. Bustamante, J. Gash, & P. Silva Dias (Eds.), *Geophysical Monograph Series* (pp. 163–181). Washington, D. C.: American Geophysical Union volume 186. doi:doi: 10.1029/2008GM000725.

Beuchle, R., Grecchi, R. C., Shimabukuro, Y. E., Seliger, R., Eva, H. D., Sano, E., & Achard, F. (2015). Land cover changes in the Brazilian Cerrado and Caatinga biomes from 1990 to 2010 based on a systematic remote sensing sampling approach. *Applied Geography*, *58*, 116–127. doi:doi: 10.1016/j.apgeog.2015.01.017.

Bloom, A. A., Bowman, K. W., Lee, M., Turner, A. J., Schroeder, R., Worden, J. R., Weidner, R., McDonald, K. C., & Jacob, D. J. (2017). A global wetland methane emissions and uncertainty dataset for atmospheric chemical transport models (WetCHARTs version 1.0). *Geoscientific Model Development*, *10*, 2141–2156. doi:doi: 10.5194/gmd-10-2141-2017.

Bloom, A. A., Palmer, P. I., Fraser, A., & Reay, D. S. (2012). Seasonal variability of tropical wetland CH4 emissions: the role of the methanogen-available carbon pool. *Biogeosciences*, *9*, 2821–2830. doi:doi: 10.5194/bg-9-2821-2012.

Bodesheim, P., Jung, M., Gans, F., Mahecha, M. D., & Reichstein, M. (2018). Upscaled diurnal cycles of land–atmosphere fluxes: a new global half-hourly data product. *Earth System Science Data*, *10*, 1327–1365. doi:doi: https://doi.org/10.5194/essd-10-1327-2 018. Publisher: Copernicus GmbH.

Borchert, R., Calle, Z., Strahler, A. H., Baertschi, A., Magill, R. E., Broadhead, J. S., Kamau, J., Njoroge, J., & Muthuri, C. (2015). Insolation and photoperiodic control of tree development near the equator. *New Phytologist*, *205*, 7–13. doi:doi: 10.1111/nph. 12981.

Botia, S., Galkowski, M., Marshall, J., Koch, T., Lavric, J. V., Walter, D., Komiya, S., Fisch, G., Peters, W., Andreae, M. O., Heimann, M., & Gerbig, C. (2020). Six years of atmospheric CO2, CH4 and CO at the Amazon Tall Tower Observatory: a new opportunity to study processes on seasonal and inter-annual scales, . *2020*, GC009–0013. Conference Name: AGU Fall Meeting Abstracts ADS Bibcode: 2020AGUFMGC0090013B.

Botía, S. et al. (2020). Understanding nighttime methane signals at the Amazon Tall Tower Observatory (ATTO). *Atmospheric Chemistry and Physics*, *20*, 6583–6606. doi:doi: https://doi.org/10.5194/acp-20-6583-2020. Publisher: Copernicus GmbH.

Botía, S. et al. (2022). The CO2 record at the Amazon Tall Tower Observatory: A new

opportunity to study processes on seasonal and inter-annual scales. *Global Change Biology*, *28*, 588–611. doi:doi: 10.1111/gcb.15905.

Bousquet, P., Peylin, P., Ciais, P., Le Quéré, C., Friedlingstein, P., & Tans, P. P. (2000). Regional Changes in Carbon Dioxide Fluxes of Land and Oceans Since 1980. *Science*, *290*, 1342–1346. doi:doi: 10.1126/science.290.5495.1342. Publisher: American Association for the Advancement of Science.

Brando, P. M., Goetz, S. J., Baccini, A., Nepstad, D. C., Beck, P. S. A., & Christman, M. C. (2010). Seasonal and interannual variability of climate and vegetation indices across the Amazon. *Proceedings of the National Academy of Sciences*, *107*, 14685–14690. doi:doi: 10.1073/pnas.0908741107.

Bridgham, S. D., Cadillo-Quiroz, H., Keller, J. K., & Zhuang, Q. (2013). Methane emissions from wetlands: biogeochemical, microbial, and modeling perspectives from local to global scales. *Global Change Biology*, *19*, 1325–1346. doi:doi: 10.1111/gcb.12131.

Brienen, R. J. W. et al. (2015). Long-term decline of the Amazon carbon sink. *Nature*, *519*, 344–348. doi:doi: 10.1038/nature14283.

Burleyson, C. D., Feng, Z., Hagos, S. M., Fast, J., Machado, L. A. T., & Martin, S. T. (2016). Spatial Variability of the Background Diurnal Cycle of Deep Convection around the GoAmazon2014/5 Field Campaign Sites. *Journal of Applied Meteorology and Climatology*, *55*, 1579–1598. doi:doi: 10.1175/JAMC-D-15-0229.1.

Bustamante, M. M. C., Nardoto, G. B., Pinto, A. S., Resende, J. C. F., Takahashi, F. S. C., & Vieira, L. C. G. (2012). Potential impacts of climate change on biogeochemical functioning of Cerrado ecosystems. *Brazilian Journal of Biology*, *72*, 655–671. doi:doi: 10.1590/S1519-69842012000400005.

C3S (2017). ERA5: Fifth generation of ECMWF atmospheric reanalyses of the global climate.

Canadell, J. G. et al. (2021). Global Carbon and other Biogeochemical Cycles and Feedbacks. In *Climate Change 2021: The Physical Science Basis. Contribution of Working Group I to the Sixth Assessment Report of the Intergovernmental Panel on Climate Change [Masson-Delmotte, V., P. Zhai, A. Pirani, S.L. Connors, C. Péan, S. Berger, N. Caud, Y. Chen, L. Goldfarb, M.I. Gomis, M. Huang, K. Leitzell, E. Lonnoy, J.B.R. Matthews, T.K. Maycock, T. Waterfield, O. Yelekçi, R. Yu, and B. Zhou (eds.)]* (p. 144). Cambridge, United Kingdom and New York, NY, USA.: Cambridge University Press.

Carmo, J. B. d., Keller, M., Dias, J. D., Camargo, P. B. d., & Crill, P. (2006). A source of methane from upland forests in the Brazilian Amazon. *Geophysical Research Letters*, *33*. doi:doi: 10.1029/2005GL025436.

Carneiro, R. G. (2018). *Erosão da Camada Limite Noturna e suas Implicações no Crescimento da Camada Limite Convectiva na Região Central da Amazônia (Experimento*

GoAmazon 2014/5). Ph.D. thesis Instituto Nacional de Pesquisas Espaciais (INPE).

Carneiro, R. G., & Fisch, G. (2020). Observational analysis of the daily cycle of the planetary boundary layer in the central Amazon during a non-El Niño year and El Niño year (GoAmazon project 2014/5). *Atmospheric Chemistry and Physics*, *20*, 5547–5558. doi:doi: https://doi.org/10.5194/acp-20-5547-2020. Publisher: Copernicus GmbH.

Carslaw, D. C., & Ropkins, K. (2012). openair — An R package for air quality data analysis. *Environmental Modelling & Software*, *27-28*, 52–61. doi:doi: 10.1016/j.envsoft.2011.09.008.

Carslaw, K. S., Boucher, O., Spracklen, D. V., Mann, G. W., Rae, J. G. L., Woodward, S., & Kulmala, M. (2010). A review of natural aerosol interactions and feedbacks within the Earth system. *Atmospheric Chemistry and Physics*, *10*, 1701–1737. doi:doi: 10.5194/acp-10-1701-2010.

Carvalhais, N. et al. (2014). Global covariation of carbon turnover times with climate in terrestrial ecosystems. *Nature*, *514*, 213–217. doi:doi: 10.1038/nature13731.

Castro, A. O., Chen, J., Zang, C. S., Shekhar, A., Jimenez, J. C., Bhattacharjee, S., Kindu, M., Morales, V. H., & Rammig, A. (2020). OCO-2 Solar-Induced Chlorophyll Fluorescence Variability across Ecoregions of the Amazon Basin and the Extreme Drought Effects of El Niño (2015–2016). *Remote Sensing*, *12*, 1202. doi:doi: 10.3390/rs12071202. Number: 7 Publisher: Multidisciplinary Digital Publishing Institute.

Cava, D., Giostra, U., Siqueira, M., & Katul, G. (2004). Organised Motion and Radiative Perturbations in the Nocturnal Canopy Sublayer above an Even-Aged Pine Forest. *Boundary-Layer Meteorology*, *112*, 129–157. doi:doi: 10.1023/B:BOUN.0000020160.28184.a0.

Chambers, J. Q., Tribuzy, E. S., Toledo, L. C., Crispim, B. F., Higuchi, N., Santos, J. d., Araújo, A. C., Kruijt, B., Nobre, A. D., & Trumbore, S. E. (2004). Respiration from a Tropical Forest Ecosystem: Partitioning of Sources and Low Carbon Use Efficiency. *Ecological Applications*, *14*, 72–88. doi:doi: 10.1890/01-6012.

Chazdon, R. L. et al. (2016). Carbon sequestration potential of second-growth forest regeneration in the Latin American tropics. *Science Advances*, *2*, e1501639. doi:doi: 10.1126/sciadv.1501639.

Chen, X. et al. (2020). Novel Representation of Leaf Phenology Improves Simulation of Amazonian Evergreen Forest Photosynthesis in a Land Surface Model. *Journal of Advances in Modeling Earth Systems*, *12*. doi:doi: https://doi.org/10.1029/2018MS001565.

Ciais, P. et al. (2013). Carbon and Other Biogeochemical Cycles. In: Climate Change 2013: The Physical Science Basis. Contribution of Working Group I to the Fifth Assessment Report of the Intergovernmental Panel on Climate Change [Stocker, T.F., D.

Qin, G.-K. Plattner, M. Tignor, S.K. Allen, J. Boschung, A. Nauels, Y. Xia, V. Bex and P.M. Midgley (eds.)]. In *IPCC AR5 Report*. Cambridge University Press, Cambridge, United Kingdom and New York, NY, USA.

Clark, D. B., Clark, D. A., & Oberbauer, S. F. (2010). Annual wood production in a tropical rain forest in NE Costa Rica linked to climatic variation but not to increasing CO2. *Global Change Biology*, *16*, 747–759. doi:doi: https://doi.org/10.1111/j.1365-2486.2009.02004.x.

da Costa, A. C. L. et al. (2010). Effect of 7 yr of experimental drought on vegetation dynamics and biomass storage of an eastern Amazonian rainforest. *New Phytologist*, *187*, 579–591. doi:doi: 10.1111/j.1469-8137.2010.03309.x.

Covey, K. R., & Megonigal, J. P. (2019). Methane production and emissions in trees and forests. *New Phytologist*, *222*, 35–51. doi:doi: 10.1111/nph.15624.

Crowell, S. et al. (2019). The 2015–2016 carbon cycle as seen from OCO-2 and the global in situ network. *Atmospheric Chemistry and Physics*, *19*, 9797–9831. doi:doi: https://doi.org/10.5194/acp-19-9797-2019. Publisher: Copernicus GmbH.

Davidson, E. A. et al. (2012). The Amazon basin in transition. *Nature*, *481*, 321–328. doi:doi: 10.1038/nature10717.

Davidson, E. A., & Artaxo, P. (2004). Globally significant changes in biological processes of the Amazon Basin: results of the Large-scale Biosphere–Atmosphere Experiment. *Global Change Biology*, *10*, 519–529. doi:doi: 10.1111/j.1529-8817.2003.00779.x.

Davidson, E. A., Ishida, F. Y., & Nepstad, D. C. (2004). Effects of an experimental drought on soil emissions of carbon dioxide, methane, nitrous oxide, and nitric oxide in a moist tropical forest. *Global Change Biology*, *10*, 718–730. doi:doi: https://doi.org/10.1111/j.1365-2486.2004.00762.x.

De Oliveira, A. P., & Fitzjarrald, D. R. (1994). The Amazon river breeze and the local boundary layer: II. Linear analysis and modelling. *Boundary-Layer Meteorology*, *67*, 75–96. doi:doi: 10.1007/BF00705508.

Devol, A. H., Forsberg, B. R., Richey, J. E., & Pimentel, T. P. (1995). Seasonal variation in chemical distributions in the Amazon (Solimões) River: A multiyear time series. *Global Biogeochemical Cycles*, *9*, 307–328. doi:doi: 10.1029/95GB01145.

Devol, A. H., Richey, J. E., Forsberg, B. R., & Martinelli, L. A. (1990). Seasonal dynamics in methane emissions from the Amazon river floodplain to the troposphere, . (pp. 16417–16426).

Dias-Junior, C. Q., Sá, L. D., Marques Filho, E. P., Santana, R. A., Mauder, M., & Manzi, A. O. (2017). Turbulence regimes in the stable boundary layer above and within the Amazon forest. *Agricultural and Forest Meteorology*, *233*, 122–132. doi:doi: 10.1016/j.agrformet.2016.11.001.

Dias-Júnior, C. Q. et al. (2019). Is There a Classical Inertial Sublayer Over the Amazon Forest? *Geophysical Research Letters*, *46*, 5614–5622. doi:doi: 10.1029/2019GL083237.

Dlugokencky, E. (2019). NOAA/GML, Trends in atmospheric methane.

Dlugokencky, E. (2020). NOAA/GML, Trends in atmospheric methane.

Dlugokencky, E., Mund, J., Crotwell, A., Crotwell, M., & Thoning, K. (2021). Atmospheric Carbon Dioxide Dry Air Mole Fractions from the NOAA GML Carbon Cycle Cooperative Global Air Sampling Network (1968-2020). Version: 2021-07-30.

Dlugokencky, E., & Tans, P. (2021). NOAA/GML, Trends in atmospheric carbon dioxide.

Dlugokencky E., Nisbet Euan G., Fisher Rebecca, & Lowry David (2011). Global atmospheric methane: budget, changes and dangers. *Philosophical Transactions of the Royal Society A: Mathematical, Physical and Engineering Sciences*, *369*, 2058–2072. doi:doi: 10.1098/rsta.2010.0341.

Doughty, C. E. et al. (2014). Allocation trade-offs dominate the response of tropical forest growth to seasonal and interannual drought. *Ecology*, *95*, 2192–2201. doi:doi: https://doi.org/10.1890/13-1507.1.

Doughty, C. E. et al. (2015). Drought impact on forest carbon dynamics and fluxes in Amazonia. *Nature*, *519*, 78–82. doi:doi: 10.1038/nature14213.

Doughty, R., Köhler, P., Frankenberg, C., Magney, T. S., Xiao, X., Qin, Y., Wu, X., & Moore, B. (2019). TROPOMI reveals dry-season increase of solar-induced chlorophyll fluorescence in the Amazon forest. *Proceedings of the National Academy of Sciences*, *116*, 22393–22398. doi:doi: 10.1073/pnas.1908157116.

Doughty, R., Xiao, X., Qin, Y., Wu, X., Zhang, Y., & Moore, B. (2021). Small anomalies in dry-season greenness and chlorophyll fluorescence for Amazon moist tropical forests during El Niño and La Niña. *Remote Sensing of Environment*, *253*, 112196. doi:doi: 10.1016/j.rse.2020.112196.

Draxler, R., & Hess, G. (1998). An overview of the HYSPLIT_4 modelling system for trajectories. *Aust. Meteorol. Mag.*, *47*.

Drumond, A., Marengo, J., Ambrizzi, T., Nieto, R., Moreira, L., & Gimeno, L. (2014). The role of the Amazon Basin moisture in the atmospheric branch of the hydrological cycle: a Lagrangian analysis. *Hydrology and Earth System Sciences*, *18*, 2577–2598. doi:doi: 10.5194/hess-18-2577-2014.

Dutaur, L., & Verchot, L. V. (2007). A global inventory of the soil CH4 sink. *Global Biogeochemical Cycles*, *21*. doi:doi: 10.1029/2006GB002734.

Dörr, H., Katruff, L., & Levin, I. (1993). Soil texture parameterization of the methane uptake in aerated soils. *Chemosphere*, *26*, 697–713. doi:doi: 10.1016/0045-6535(93)90454-D.

Engle, D. L., Melack, J. M., Doyle, R. D., & Fisher, T. R. (2008). High rates of net primary production and turnover of floating grasses on the Amazon floodplain: implications for aquatic respiration and regional CO2 flux. *Global Change Biology*, *14*, 369–381. doi:doi: https://doi.org/10.1111/j.1365-2486.2007.01481.x.

Enting, I. G. (2002). *Inverse Problems in Atmospheric Constituent Transport*. Cambridge Atmospheric and Space Science Series. Cambridge: Cambridge University Press. doi:doi: 10.1017/CBO9780511535741.

EPA (2011). Level III Ecoregions of Central and South America. US Environmental Protection Agency.

Espinoza, J.-C., Marengo, J. A., Schongart, J., & Jimenez, J. C. (2022). The new historical flood of 2021 in the Amazon River compared to major floods of the 21st century: Atmospheric features in the context of the intensification of floods. *Weather and Climate Extremes*, *35*, 100406. doi:doi: 10.1016/j.wace.2021.100406.

Esquivel-Muelbert, A. et al. (2020). Tree mode of death and mortality risk factors across Amazon forests. *Nature Communications*, *11*, 5515. doi:doi: 10.1038/s41467-020-189 96-3.

Etminan, M., Myhre, G., Highwood, E. J., & Shine, K. P. (2016). Radiative forcing of carbon dioxide, methane, and nitrous oxide: A significant revision of the methane radiative forcing. *Geophysical Research Letters*, *43*, 12,614–12,623. doi:doi: 10.1002/2016GL071930.

Eva, H. et al. (2005). *A proposal for defining the geographical boundaries of Amazonia; synthesis of the results from an expert consultation workshop organized by the European Commission in collaboration with the Amazon Cooperation Treaty Organization - JRC Ispra, 7-8 June 2005*.

Fawcett, D. et al. (2022). Assessing Model Predictions of Carbon Dynamics in Global Drylands. *Frontiers in Environmental Science*, *10*.

Feldpausch, T. R. et al. (2012). Tree height integrated into pantropical forest biomass estimates. *Biogeosciences*, *9*, 3381–3403. doi:doi: 10.5194/bg-9-3381-2012.

Feldpausch, T. R. et al. (2016). Amazon forest response to repeated droughts. *Global Biogeochemical Cycles*, *30*, 964–982. doi:doi: 10.1002/2015GB005133.

Fisch, G., Tota, J., Machado, L. A. T., Silva Dias, M. A. F., da F. Lyra, R. F., Nobre, C. A., Dolman, A. J., & Gash, J. H. C. (2004). The convective boundary layer over pasture and forest in Amazonia. *Theoretical and Applied Climatology*, *78*. doi:doi: 10.1007/s00704-004-0043-x.

Fitzjarrald, D. R., & Moore, K. E. (1990). Mechanisms of nocturnal exchange between the rain forest and the atmosphere. *Journal of Geophysical Research*, *95*, 16839. doi:doi: 10.1029/JD095iD10p16839.

Fleischer, K. et al. (2019). Amazon forest response to CO 2 fertilization dependent on plant phosphorus acquisition. *Nature Geoscience*, *12*, 736–741. doi:doi: 10.1038/s415 61-019-0404-9. Number: 9 Publisher: Nature Publishing Group.

Forsberg, B. R., Melack, J. M., Richey, J. E., & Pimentel, T. P. (2017). Regional and seasonal variability in planktonic photosynthesis and planktonic community respiration in Amazon floodplain lakes. *Hydrobiologia*, *800*, 187–206. doi:doi: 10.1007/s10750-017 -3222-3.

Friedlingstein, P. et al. (2022). Global Carbon Budget 2021. *Earth System Science Data*, *14*, 1917–2005. doi:doi: 10.5194/essd-14-1917-2022. Publisher: Copernicus GmbH.

Friedlingstein, P. et al. (2020). Global Carbon Budget 2020. *Earth System Science Data*, *12*, 3269–3340. doi:doi: https://doi.org/10.5194/essd-12-3269-2020. Publisher: Copernicus GmbH.

Fu, R., Yin, L., Li, W., Arias, P. A., Dickinson, R. E., Huang, L., Chakraborty, S., Fernandes, K., Liebmann, B., Fisher, R., & Myneni, R. B. (2013). Increased dry-season length over southern Amazonia in recent decades and its implication for future climate projection. *Proceedings of the National Academy of Sciences*, *110*, 18110–18115. doi:doi: 10.1073/pnas.1302584110.

Garcia, M. N., Ferreira, M. J., Ivanov, V., dos Santos, V. A. H. F., Ceron, J. V., Guedes, A. V., Saleska, S. R., & Oliveira, R. S. (2021). Importance of hydraulic strategy trade-offs in structuring response of canopy trees to extreme drought in central Amazon. *Oecologia*, *197*, 13–24. doi:doi: 10.1007/s00442-021-04924-9.

Gash, J., Nobre, J. M., Roberts, J. M., & Victoria, R. L. (1996). Amazonian deforestation and climate. *Journal of Tropical Ecology*, *12*, 778–778. doi:doi: 10.1017/S02664674000 10026.

Gatti, L. V. et al. (2021). Amazonia as a carbon source linked to deforestation and climate change. *Nature*, *595*, 388–393. doi:doi: 10.1038/s41586-021-03629-6.

Gatti, L. V. et al. (2014). Drought sensitivity of Amazonian carbon balance revealed by atmospheric measurements. *Nature*, *506*, 76–80. doi:doi: 10.1038/nature12957.

Gaubert, B. et al. (2019). Global atmospheric CO_2 inverse models converging on neutral tropical land exchange, but disagreeing on fossil fuel and atmospheric growth rate. *Biogeosciences*, *16*, 117–134. doi:doi: https://doi.org/10.5194/bg-16-117-2019. Publisher: Copernicus GmbH.

Gerbig, C., Dolman, A. J., & Heimann, M. (2009). On observational and modelling strategies targeted at regional carbon exchange over continents. *Biogeosciences*, *6*, 1949–1959. doi:doi: https://doi.org/10.5194/bg-6-1949-2009. Publisher: Copernicus GmbH.

Gerbig, C., Körner, S., & Lin, J. C. (2008). Vertical mixing in atmospheric tracer transport

models: error characterization and propagation. *Atmospheric Chemistry and Physics*, *8*, 591–602. doi:doi: https://doi.org/10.5194/acp-8-591-2008. Publisher: Copernicus GmbH.

Gerbig, C., Lin, J. C., Wofsy, S. C., Daube, B. C., Andrews, A. E., Stephens, B. B., Bakwin, P. S., & Grainger, C. A. (2003). Toward constraining regional-scale fluxes of CO2 with atmospheric observations over a continent: 2. Analysis of COBRA data using a receptor-oriented framework. *Journal of Geophysical Research: Atmospheres*, *108*. doi:doi: 10.1029/2003JD003770.

Girardin, C. A. J., Malhi, Y., Doughty, C. E., Metcalfe, D. B., Meir, P., del Aguila-Pasquel, J., Araujo-Murakami, A., da Costa, A. C. L., Silva-Espejo, J. E., Farfán Amézquita, F., & Rowland, L. (2016). Seasonal trends of Amazonian rainforest phenology, net primary productivity, and carbon allocation. *Global Biogeochemical Cycles*, *30*, 700–715. doi:doi: 10.1002/2015GB005270. _eprint: https://onlinelibrary.wiley.com/doi/pdf/10.1002/2015GB005270.

Gloor, M., Bakwin, P., Hurst, D., Lock, L., Draxler, R., & Tans, P. (2001). What is the concentration footprint of a tall tower? *Journal of Geophysical Research: Atmospheres*, *106*, 17831–17840. doi:doi: 10.1029/2001JD900021.

Gloor, M., Barichivich, J., Ziv, G., Brienen, R., Schöngart, J., Peylin, P., Ladvocat Cintra, B. B., Feldpausch, T., Phillips, O., & Baker, J. (2015). Recent Amazon climate as background for possible ongoing and future changes of Amazon humid forests: AMAZON CLIMATE AND TROPICAL FORESTS. *Global Biogeochemical Cycles*, *29*, 1384–1399. doi:doi: 10.1002/2014GB005080.

Gloor, M., Fan, S.-M., Pacala, S., & Sarmiento, J. (2000). Optimal sampling of the atmosphere for purpose of inverse modeling: A model study. *Global Biogeochemical Cycles*, *14*, 407–428. doi:doi: 10.1029/1999GB900052.

Gloor, M. et al. (2012). The carbon balance of South America: a review of the status, decadal trends and main determinants. *Biogeosciences*, *9*, 5407–5430. doi:doi: 10.5194/bg-9-5407-2012.

de Gonçalves, L. G. G. et al. (2013). Overview of the Large-Scale Biosphere–Atmosphere Experiment in Amazonia Data Model Intercomparison Project (LBA-DMIP). *Agricultural and Forest Meteorology*, *182-183*, 111–127. doi:doi: 10.1016/j.agrformet.2013.04.030.

Gonçalves, N. B., Lopes, A. P., Dalagnol, R., Wu, J., Pinho, D. M., & Nelson, B. W. (2020). Both near-surface and satellite remote sensing confirm drought legacy effect on tropical forest leaf phenology after 2015/2016 ENSO drought. *Remote Sensing of Environment*, *237*, 111489. doi:doi: 10.1016/j.rse.2019.111489.

Goulden, M. L., Miller, S. D., & Rocha, H. R. d. (2006). Nocturnal cold air drainage and pooling in a tropical forest. *Journal of Geophysical Research: Atmospheres*, *111*.

doi:doi: 10.1029/2005JD006037.

Goulden, M. L., Miller, S. D., Rocha, H. R. d., Menton, M. C., Freitas, H. C. d., Figueira, A. M. e. S., & Sousa, C. A. D. d. (2004). Diel and Seasonal Patterns of Tropical Forest Co2 Exchange. *Ecological Applications*, *14*, 42–54. doi:doi: 10.1890/02-6008.

Goulding, M., Barthem, R., & Ferreira, E. (2003). The Smithsonian atlas of the Amazon, .

Gouveia, N. A., Gherardi, D. F. M., & Aragão, L. E. O. C. (2019). The Role of the Amazon River Plume on the Intensification of the Hydrological Cycle. *Geophysical Research Letters*, *46*, 12221–12229. doi:doi: 10.1029/2019GL084302.

Green, J. K., Berry, J., Ciais, P., Zhang, Y., & Gentine, P. (2020). Amazon rainforest photosynthesis increases in response to atmospheric dryness. *Science Advances*, *6*. doi:doi: 10.1126/sciadv.abb7232.

Griffith, D. W. T., Deutscher, N. M., Caldow, C., Kettlewell, G., Riggenbach, M., & Hammer, S. (2012). A Fourier transform infrared trace gas and isotope analyser for atmospheric applications. *Atmospheric Measurement Techniques*, *5*, 2481–2498. doi:doi: 10.5194/amt-5-2481-2012. Publisher: Copernicus GmbH.

Guan, K. et al. (2015). Photosynthetic seasonality of global tropical forests constrained by hydroclimate. *Nature Geoscience*, *8*, 284–289. doi:doi: 10.1038/ngeo2382.

Gurney, K. R. et al. (2002). Towards robust regional estimates of CO 2 sources and sinks using atmospheric transport models. *Nature*, *415*, 626–630. doi:doi: 10.1038/415626a. Number: 6872 Publisher: Nature Publishing Group.

Harriss, R. C. et al. (1990). The Amazon Boundary Layer Experiment: Wet season 1987. *Journal of Geophysical Research: Atmospheres*, *95*, 16721–16736. doi:doi: 10.1029/JD 095iD10p16721.

Harriss, R. C., Wofsy, S. C., Garstang, M., Browell, E. V., Molion, L. C. B., McNeal, R. J., Hoell Jr., J. M., Bendura, R. J., Beck, S. M., Navarro, R. L., Riley, J. T., & Snell, R. L. (1988). The Amazon Boundary Layer Experiment (ABLE 2A): dry season 1985. *Journal of Geophysical Research: Atmospheres*, *93*, 1351–1360. doi:doi: 10.1029/JD093iD02p01351.

Hastie, A., Lauerwald, R., Ciais, P., & Regnier, P. (2019). Aquatic carbon fluxes dampen the overall variation of net ecosystem productivity in the Amazon basin: An analysis of the interannual variability in the boundless carbon cycle. *Global Change Biology*, *25*, 2094–2111. doi:doi: https://doi.org/10.1111/gcb.14620.

Hayek, M. N. et al. (2018). Carbon exchange in an Amazon forest: from hours to years. *Biogeosciences*, *15*, 4833–4848. doi:doi: 10.5194/bg-15-4833-2018.

Haynes, K. D., Baker, I. T., Denning, A. S., Stöckli, R., Schaefer, K., Lokupitiya, E. Y., & Haynes, J. M. (2019). Representing Grasslands Using Dynamic Prognostic Phenology

Based on Biological Growth Stages: 1. Implementation in the Simple Biosphere Model (SiB4). *Journal of Advances in Modeling Earth Systems*, *11*, 4423–4439. doi:doi: 10.1029/2018MS001540.

Heimann, M., & Körner, S. (2003). *The global atmospheric tracer model TM3*. Technical Report Tech. Rep. 5., MPI-BGC Jena (Germany).

Heinrich, V. H. A. et al. (2021). Large carbon sink potential of secondary forests in the Brazilian Amazon to mitigate climate change. *Nature Communications*, *12*, 1785. doi:doi: 10.1038/s41467-021-22050-1. Number: 1 Publisher: Nature Publishing Group.

Hess, L. L., Melack, J. M., Affonso, A. G., Barbosa, C., Gastil-Buhl, M., & Novo, E. M. L. M. (2015). Wetlands of the Lowland Amazon Basin: Extent, Vegetative Cover, and Dual-season Inundated Area as Mapped with JERS-1 Synthetic Aperture Radar. *Wetlands*, *35*, 745–756. doi:doi: 10.1007/s13157-015-0666-y.

Hoffmann, L., Günther, G., Li, D., Stein, O., Wu, X., Griessbach, S., Heng, Y., Konopka, P., Müller, R., Vogel, B., & Wright, J. S. (2019). From ERA-Interim to ERA5: the considerable impact of ECMWF's next-generation reanalysis on Lagrangian transport simulations. *Atmospheric Chemistry and Physics*, *19*, 3097–3124. doi:doi: 10.5194/acp-19-3097-2019.

Horel, J. D., Hahmann, A. N., & Geisler, J. E. (1989). An investigation of the Annual Cycle of Convective Activity over the Tropical Americas. *Journal of Climate*, *2*, 1388–1403. doi:doi: 10.1175/1520-0442(1989)002⟨1388:AIOTAC⟩2.0.CO;2. Publisher: American Meteorological Society Section: Journal of Climate.

Howarth, R. W. (2019). Ideas and perspectives: is shale gas a major driver of recent increase in global atmospheric methane? *Biogeosciences*, *16*, 3033–3046. doi:doi: https://doi.org/10.5194/bg-16-3033-2019.

Hu, L. et al. (2019). Enhanced North American carbon uptake associated with El Niño. *Science Advances*, *5*, eaaw0076. doi:doi: 10.1126/sciadv.aaw0076.

Hubau, W. et al. (2020). Asynchronous carbon sink saturation in African and Amazonian tropical forests. *Nature*, *579*, 80–87. doi:doi: 10.1038/s41586-020-2035-0.

Huete, A., Didan, K., Shimabukuro, Y., Ratana, P., Saleska, S., Hutyra, L., Yang, W., Nemani, R., & Myneni, R. (2006). Amazon green-up with sunlight in dry season. *Geophysical Research Letters - GEOPHYS RES LETT*, *33*. doi:doi: 10.1029/2005GL025583.

Huffman, C., Bolvin, D., Nelkin, E., & Adler, R. (2016). TRMM (TMPA) Precipitation L3 1 day 0.25 degree x 0.25 degree V7. Edited by Andrey Savtchenko, Goddard Earth Sciences Data and Information Services Center (GES DISC), Accessed: January 10, 2021. DOI: 10.5067/TRMM/TMPA/DAY/7.

Hutyra, L. R., Munger, J. W., Saleska, S. R., Gottlieb, E., Daube, B. C., Dunn, A. L.,

Amaral, D. F., Camargo, P. B. d., & Wofsy, S. C. (2007). Seasonal controls on the exchange of carbon and water in an Amazonian rain forest. *Journal of Geophysical Research: Biogeosciences*, *112*. doi:doi: https://doi.org/10.1029/2006JG000365.

Högström, U. (1990). Analysis of Turbulence Structure in the Surface Layer with a Modified Similarity Formulation for Near Neutral Conditions. *Journal of the atmospheric sciences*, *47*, 1949–1972.

Jackson, R. (2020). Eunice Foote, John Tyndall and a question of priority. *Notes and Records: the Royal Society Journal of the History of Science*, *74*, 105–118. doi:doi: 10.1098/rsnr.2018.0066. Publisher: Royal Society.

Jackson, R. B., Saunois, M., Bousquet, P., Canadell, J. G., Poulter, B., Stavert, A. R., Bergamaschi, P., Niwa, Y., Segers, A., & Tsuruta, A. (2020). Increasing anthropogenic methane emissions arise equally from agricultural and fossil fuel sources. *Environmental Research Letters*, *15*, 071002. doi:doi: 10.1088/1748-9326/ab9ed2.

Janssens-Maenhout, G. et al. (2017). EDGAR v4.3.2 Global Atlas of the three major GreenhouseGas Emissions for the period 1970–2012. . doi:doi: 10.5194/essd-2017-79.

Johnson, M. O. et al. (2016). Variation in stem mortality rates determines patterns of above-ground biomass in Amazonian forests: implications for dynamic global vegetation models. *Global Change Biology*, *22*, 3996–4013. doi:doi: 10.1111/gcb.13315. _eprint: https://onlinelibrary.wiley.com/doi/pdf/10.1111/gcb.13315.

Johnson, M. S., Lehmann, J., Couto, E. G., Filho, J. P. N., & Riha, S. J. (2006). DOC and DIC in Flowpaths of Amazonian Headwater Catchments with Hydrologically Contrasting Soils. *Biogeochemistry*, *81*, 45–57. doi:doi: 10.1007/s10533-006-9029-3.

Johnson, M. S., Weiler, M., Couto, E. G., Riha, S. J., & Lehmann, J. (2007). Storm pulses of dissolved CO2 in a forested headwater Amazonian stream explored using hydrograph separation. *Water Resources Research*, *43*. doi:doi: https://doi.org/10.1029/2007WR006359.

Joos, F., & Spahni, R. (2008). Rates of change in natural and anthropogenic radiative forcing over the past 20,000 years. *Proceedings of the National Academy of Sciences*, *105*, 1425–1430. doi:doi: 10.1073/pnas.0707386105.

Jung, M., Henkel, K., Herold, M., & Churkina, G. (2006). Exploiting synergies of global land cover products for carbon cycle modeling. *Remote Sensing of Environment*, *101*, 534–553. doi:doi: 10.1016/j.rse.2006.01.020.

Jung, M. et al. (2011). Global patterns of land-atmosphere fluxes of carbon dioxide, latent heat, and sensible heat derived from eddy covariance, satellite, and meteorological observations. *Journal of Geophysical Research: Biogeosciences*, *116*. doi:doi: 10.1029/2010JG001566. Publisher: John Wiley & Sons, Ltd.

Jung, M. et al. (2017). Compensatory water effects link yearly global land CO 2 sink

changes to temperature. *Nature*, *541*, 516–520. doi:doi: 10.1038/nature20780.

Jung, M. et al. (2020). Scaling carbon fluxes from eddy covariance sites to globe: synthesis and evaluation of the FLUXCOM approach. *Biogeosciences*, *17*, 1343–1365. doi:doi: https://doi.org/10.5194/bg-17-1343-2020. Publisher: Copernicus GmbH.

Junk, W. J., Piedade, M. T. F., Schöngart, J., Cohn-Haft, M., Adeney, J. M., & Wittmann, F. (2011). A Classification of Major Naturally-Occurring Amazonian Lowland Wetlands. *Wetlands*, *31*, 623–640. doi:doi: 10.1007/s13157-011-0190-7.

Kaiser, J. W., Heil, A., Andreae, M. O., Benedetti, A., Chubarova, N., Jones, L., Morcrette, J.-J., Razinger, M., Schultz, M. G., Suttie, M., & van der Werf, G. R. (2012). Biomass burning emissions estimated with a global fire assimilation system based on observed fire radiative power. *Biogeosciences*, *9*, 527–554. doi:doi: 10.5194/bg-9-527-2012.

Kalnay, E. et al. (1996). The NCEP/NCAR 40-Year Reanalysis Project. *Bulletin of the American Meteorological Society*, *77*, 437–472.

Kannenberg, S. A., Schwalm, C. R., & Anderegg, W. R. L. (2020). Ghosts of the past: how drought legacy effects shape forest functioning and carbon cycling. *Ecology Letters*, *23*, 891–901. doi:doi: https://doi.org/10.1111/ele.13485.

Kaplan, J. O. (2002). Wetlands at the Last Glacial Maximum: Distribution and methane emissions. *Geophysical Research Letters*, *29*, 3–1–3–4. doi:doi: 10.1029/2001GL013366.

Karipot, A., Leclerc, M. Y., Zhang, G., Lewin, K. F., Nagy, J., Hendrey, G. R., & Starr, G. (2008). Influence of nocturnal low-level jet on turbulence structure and CO2 flux measurements over a forest canopy. *Journal of Geophysical Research: Atmospheres*, *113*. doi:doi: 10.1029/2007JD009149.

Keeling, C. D., Bacastow, R. B., Bainbridge, A. E., Ekdahl Jr., C. A., Guenther, P. R., Waterman, L. S., & Chin, J. F. S. (1976). Atmospheric carbon dioxide variations at Mauna Loa Observatory, Hawaii. *Tellus*, *28*, 538–551. doi:doi: 10.1111/j.2153-3490.1976.tb00701.x.

Keenan, T. F., Migliavacca, M., Papale, D., Baldocchi, D., Reichstein, M., Torn, M., & Wutzler, T. (2019). Widespread inhibition of daytime ecosystem respiration. *Nature Ecology & Evolution*, *3*, 407–415. doi:doi: 10.1038/s41559-019-0809-2.

Keller, M. et al. (2004a). ECOLOGICAL RESEARCH IN THE LARGE-SCALE BIOSPHERE–ATMOSPHERE EXPERIMENT IN AMAZONIA: EARLY RESULTS. *Ecological Applications, 14(4) Supplement, pp. S3–S16*, .

Keller, M., Silva-Dias, M. A., Nepstad, D. C., & Silva-Andreae, M. O. (2004b). The large-scale biosphere-atmosphere experiment in Amazonia: Analyzing regional land use change effects. In R. S. DeFries, G. P. Asner, & R. A. Houghton (Eds.), *Geophysical Monograph Series* (pp. 321–334). Washington, D. C.: American Geophysical Union volume 153. doi:doi: 10.1029/153GM24.

Kemenes, A., Forsberg, B. R., & Melack, J. M. (2007). Methane release below a tropical hydroelectric dam. *Geophysical Research Letters*, *34*. doi:doi: 10.1029/2007GL029479.

Khanna, J., Medvigy, D., Fueglistaler, S., & Walko, R. (2017). Regional dry-season climate changes due to three decades of Amazonian deforestation. *Nature Climate Change*, *7*, 200–204. doi:doi: 10.1038/nclimate3226.

Kirschke, S. et al. (2013). Three decades of global methane sources and sinks. *Nature Geoscience*, *6*, 813–823. doi:doi: 10.1038/ngeo1955.

Klein, V. P., & Piedade, M. T. F. (2019). Orchidaceae occurring in white-sand ecosystems of the Uatumã Sustainable Development Reserve in Central Amazon. *Phytotaxa*, *419*, 113–148. doi:doi: 10.11646/phytotaxa.419.2.1.

Kondo, M. et al. (2020). State of the science in reconciling top-down and bottom-up approaches for terrestrial CO_2 budget. *Global Change Biology*, *26*, 1068–1084. doi:doi: 10.1111/gcb.14917.

Koren, G. (2020). *Constraining the exchange of carbon dioxide over the Amazon: New insights from stable isotopes, remote sensing and inverse modeling.*. Ph.D. thesis Wageningen Univeristy.

Koren, G., van Schaik, E., Araújo, A. C., Boersma, K. F., Gärtner, A., Killaars, L., Kooreman, M. L., Kruijt, B., van der Laan-Luijkx, I. T., von Randow, C., Smith, N. E., & Peters, W. (2018). Widespread reduction in sun-induced fluorescence from the Amazon during the 2015/2016 El Niño. *Philosophical Transactions of the Royal Society B: Biological Sciences*, *373*, 20170408. doi:doi: 10.1098/rstb.2017.0408.

Kountouris, P., Gerbig, C., Rödenbeck, C., Karstens, U., Koch, T. F., & Heimann, M. (2018a). Atmospheric CO_2 inversions on the mesoscale using data-driven prior uncertainties: quantification of the European terrestrial CO_2 fluxes. *Atmospheric Chemistry and Physics*, *18*, 3047–3064. doi:doi: https://doi.org/10.5194/acp-18-3047-2018. Publisher: Copernicus GmbH.

Kountouris, P., Gerbig, C., Rödenbeck, C., Karstens, U., Koch, T. F., & Heimann, M. (2018b). Technical Note: Atmospheric CO_2 inversions on the mesoscale using data-driven prior uncertainties: methodology and system evaluation. *Atmospheric Chemistry and Physics*, *18*, 3027–3045. doi:doi: 10.5194/acp-18-3027-2018. Publisher: Copernicus GmbH.

Krol, M., Houweling, S., Bregman, B., & Bergamaschi, P. (2005). The two-way nested global chemistry-transport zoom model TM5: algorithm and applications. *Atmos. Chem. Phys.*, (p. 16).

Kruid, S., Macedo, M. N., Gorelik, S. R., Walker, W., Moutinho, P., Brando, P. M., Castanho, A., Alencar, A., Baccini, A., & Coe, M. T. (2021). Beyond Deforestation: Carbon Emissions From Land Grabbing and Forest Degradation in the Brazilian Amazon. *Frontiers in Forests and Global Change*, *4*.

van der Laan-Luijkx, I. T. et al. (2015). Response of the Amazon carbon balance to the 2010 drought derived with CarbonTracker South America. *Global Biogeochemical Cycles*, *29*, 1092–1108. doi:doi: 10.1002/2014GB005082.

van der Laan-Luijkx, I. T. et al. (2017). The CarbonTracker Data Assimilation Shell (CTDAS) v1.0: implementation and global carbon balance 2001–2015. *Geoscientific Model Development*, *10*, 2785–2800. doi:doi: 10.5194/gmd-10-2785-2017.

Lasslop, G., Reichstein, M., Papale, D., Richardson, A. D., Arneth, A., Barr, A., Stoy, P., & Wohlfahrt, G. (2010). Separation of net ecosystem exchange into assimilation and respiration using a light response curve approach: critical issues and global evaluation. *Global Change Biology*, *16*, 187–208. doi:doi: https://doi.org/10.1111/j.1365-2486.2009.02041.x.

Lauerwald, R., Regnier, P., Camino-Serrano, M., Guenet, B., Guimberteau, M., Ducharne, A., Polcher, J., & Ciais, P. (2017). ORCHILEAK (revision 3875): a new model branch to simulate carbon transfers along the terrestrial–aquatic continuum of the Amazon basin. *Geoscientific Model Development*, *10*, 3821–3859. doi:doi: https://doi.org/10.5194/gmd-10-3821-2017. Publisher: Copernicus GmbH.

Lauerwald, R., Regnier, P., Guenet, B., Friedlingstein, P., & Ciais, P. (2020). How Simulations of the Land Carbon Sink Are Biased by Ignoring Fluvial Carbon Transfers: A Case Study for the Amazon Basin. *One Earth*, *3*, 226–236. doi:doi: 10.1016/j.oneear.2020.07.009. Publisher: Elsevier.

Le Quéré, C. et al. (2018). Global Carbon Budget 2018. *Earth System Science Data*, *10*, 2141–2194. doi:doi: 10.5194/essd-10-2141-2018.

Leal, I. R., Da Silva, J. M. C., Tabarelli, M., & Lacher Jr., T. E. (2005). Changing the Course of Biodiversity Conservation in the Caatinga of Northeastern Brazil. *Conservation Biology*, *19*, 701–706. doi:doi: 10.1111/j.1523-1739.2005.00703.x.

Lee, J.-E., Frankenberg, C., van der Tol, C., Berry, J. A., Guanter, L., Boyce, C. K., Fisher, J. B., Morrow, E., Worden, J. R., Asefi, S., Badgley, G., & Saatchi, S. (2013). Forest productivity and water stress in Amazonia: observations from GOSAT chlorophyll fluorescence. *Proceedings of the Royal Society B: Biological Sciences*, *280*, 20130171. doi:doi: 10.1098/rspb.2013.0171.

Levin, I., Glatzel-Mattheier, H., Marik, T., Cuntz, M., Schmidt, M., & Worthy, D. E. (1999). Verification of German methane emission inventories and their recent changes based on atmospheric observations. *Journal of Geophysical Research: Atmospheres*, *104*, 3447–3456. doi:doi: 10.1029/1998JD100064.

Levin, I. et al. (2020). A dedicated flask sampling strategy developed for Integrated Carbon Observation System (ICOS) stations based on CO_2 and CO measurements and Stochastic Time-Inverted Lagrangian Transport (STILT) footprint modelling. *Atmospheric Chemistry and Physics*, *20*, 11161–11180. doi:doi: 10.5194/acp-20-11161-2020.

Levin, I., Karstens, U., Hammer, S., DellaColetta, J., Maier, F., & Gachkivskyi, M. (2021). Limitations of the radon tracer method (RTM) to estimate regional greenhouse gas (GHG) emissions – a case study for methane in Heidelberg. *Atmospheric Chemistry and Physics*, *21*, 17907–17926. doi:doi: 10.5194/acp-21-17907-2021.

Lin, J. C., Gerbig, C., Wofsy, S. C., Andrews, A. E., Daube, B., Davis, K., & Grainger, C. A. (2003). A near-field tool for simulating the upstream influence of atmospheric observations: The Stochastic Time-Inverted Lagrangian Transport (STILT) model. *Journal of Geophysical Research*, *108*, ACH 2–1–ACH 2–17. doi:doi: 10.1029/2002JD003161.

Liu, J. et al. (2017). Contrasting carbon cycle responses of the tropical continents to the 2015–2016 El Niño. *Science*, *358*. doi:doi: 10.1126/science.aam5690.

Lopes, A. P., Nelson, B. W., Wu, J., Graça, P. M. L. d. A., Tavares, J. V., Prohaska, N., Martins, G. A., & Saleska, S. R. (2016). Leaf flush drives dry season green-up of the Central Amazon. *Remote Sensing of Environment*, *182*, 90–98. doi:doi: 10.1016/j.rse.2016.05.009.

Lovejoy, T. E., & Nobre, C. (2018). Amazon Tipping Point. *Science Advances*, *4*, eaat2340. doi:doi: 10.1126/sciadv.aat2340. Publisher: American Association for the Advancement of Science.

Mahadevan, P., Wofsy, S. C., Matross, D. M., Xiao, X., Dunn, A. L., Lin, J. C., Gerbig, C., Munger, J. W., Chow, V. Y., & Gottlieb, E. W. (2008). A satellite-based biosphere parameterization for net ecosystem CO_2 exchange: Vegetation Photosynthesis and Respiration Model (VPRM). *Global Biogeochemical Cycles*, *22*. doi:doi: 10.1029/2006GB002735.

Mahrt, L. (1999). Stratified Atmospheric Boundary Layers. *Boundary-Layer Meteorology*, *90*, 375–396. doi:doi: 10.1023/A:1001765727956.

Mahrt, L. (2009). Characteristics of Submeso Winds in the Stable Boundary Layer. *Boundary-Layer Meteorology*, *130*, 1–14. doi:doi: 10.1007/s10546-008-9336-4.

Malhi, Y. et al. (2015). The linkages between photosynthesis, productivity, growth and biomass in lowland Amazonian forests. *Global Change Biology*, *21*, 2283–2295. doi:doi: 10.1111/gcb.12859.

Malhi, Y., Rowland, L., Aragão, L. E. O. C., & Fisher, R. A. (2018). New insights into the variability of the tropical land carbon cycle from the El Niño of 2015/2016. *Philosophical Transactions of the Royal Society B: Biological Sciences*, *373*, 20170298. doi:doi: 10.1098/rstb.2017.0298. Publisher: Royal Society.

Malhi, Y., Saatchi, S., Girardin, C., & AragãO, L. E. O. C. (2009). The Production, Storage, and Flow of Carbon in Amazonian Forests. In *Amazonia and Global Change* (pp. 355–372). American Geophysical Union (AGU).

Malhi, Y. et al. (2006). The regional variation of aboveground live biomass in old-growth Amazonian forests. *Global Change Biology*, *12*, 1107–1138. doi:doi: 10.1111/j.1365-2 486.2006.01120.x.

Marengo, J. A., & Espinoza, J. C. (2016). Extreme seasonal droughts and floods in Amazonia: causes, trends and impacts. *International Journal of Climatology*, *36*, 1033–1050. doi:doi: 10.1002/joc.4420.

Marht, L., Thomas, C., Richardson, S., Seaman, N., Stauffer, D., & Zeeman, M. (2013). Non-stationary Generation of Weak Turbulence for Very Stable and Weak-Wind Conditions. *Boundary Layer Meteorology*, (pp. 179–199). doi:doi: 10.1007/s10546-012-9782-x.

Marques, J. D. d. O., Luizão, F. J., Teixeira, W. G., Nogueira, E. M., Fearnside, P. M., & Sarrazin, M. (2017). Soil Carbon Stocks under Amazonian Forest: Distribution in the Soil Fractions and Vulnerability to Emission. *Open Journal of Forestry*, *7*, 121–142. doi:doi: 10.4236/ojf.2017.72008.

Martin, S. T. et al. (2016). Introduction: Observations and Modeling of the Green Ocean Amazon (GoAmazon2014/5). *Atmospheric Chemistry and Physics*, *16*, 4785–4797. doi:doi: 10.5194/acp-16-4785-2016.

Martinson, G. O., Werner, F. A., Scherber, C., Conrad, R., Corre, M. D., Flessa, H., Wolf, K., Klose, M., Gradstein, S. R., & Veldkamp, E. (2010). Methane emissions from tank bromeliads in neotropical forests. *Nature Geoscience*, *3*, 766–769. doi:doi: 10.1038/ngeo980.

Matricardi, E. A. T., Skole, D. L., Costa, O. B., Pedlowski, M. A., Samek, J. H., & Miguel, E. P. (2020). Long-term forest degradation surpasses deforestation in the Brazilian Amazon. *Science*, *369*, 1378–1382. doi:doi: 10.1126/science.abb3021. Publisher: American Association for the Advancement of Science.

Mauder, M., & Foken, T. (2004). Documentation and Instruction Manual of the Eddy Covariance Software Package TK2.

Melack, J. M. (2016). Aquatic Ecosystems. In L. Nagy, B. R. Forsberg, & P. Artaxo (Eds.), *Interactions Between Biosphere, Atmosphere and Human Land Use in the Amazon Basin* Ecological Studies (pp. 119–148). Berlin, Heidelberg: Springer.

Melack, J. M., Basso, L. S., Fleischmann, A. S., Botía, S., Guo, M., Zhou, W., Barbosa, P. M., Amaral, J. H., & MacIntyre, S. (2022). Challenges Regionalizing Methane Emissions Using Aquatic Environments in the Amazon Basin as Examples. *Frontiers in Environmental Science*, *10*.

Melack, J. M., & Hess, L. L. (2010). Remote Sensing of the Distribution and Extent of Wetlands in the Amazon Basin, in Amazonian Floodplain Forests: Ecophysiology, Biodiversity and Sustainable Management. volume 210. (Junk, w. j., piedade, m. t. f., wittmann, f., schöngart, j., and parolin ed.).

Melack, J. M., Hess, L. L., Gastil, M., Forsberg, B. R., Hamilton, S. K., Lima, I. B., & Novo, E. M. (2004). Regionalization of methane emissions in the Amazon Basin with microwave remote sensing. *Global Change Biology*, *10*, 530–544. doi:doi: 10.1111/j.1365-2486.2004.00763.x.

Melack, J. M., Novo, E. M. L. M., Forsberg, B. R., Piedade, M. T. F., & Maurice, L. (2009). Floodplain Ecosystem Processes. In *Amazonia and Global Change* (pp. 525–541). American Geophysical Union (AGU).

Melton, J. R. et al. (2013). Present state of global wetland extent and wetland methane modelling: conclusions from a model inter-comparison project (WETCHIMP). *Biogeosciences*, *10*, 753–788. doi:doi: 10.5194/bg-10-753-2013.

Mendes, K. R. et al. (2020). Seasonal variation in net ecosystem CO2 exchange of a Brazilian seasonally dry tropical forest. *Scientific Reports*, *10*, 9454. doi:doi: 10.1038/s41598-020-66415-w.

Michalak, A. M. (2004). A geostatistical approach to surface flux estimation of atmospheric trace gases. *Journal of Geophysical Research*, *109*, D14109. doi:doi: 10.1029/2003JD004422.

Miller, J. B., Gatti, L. V., d'Amelio, M. T. S., Crotwell, A. M., Dlugokencky, E. J., Bakwin, P., Artaxo, P., & Tans, P. P. (2007). Airborne measurements indicate large methane emissions from the eastern Amazon basin. *Geophysical Research Letters*, *34*. doi:doi: 10.1029/2006GL029213.

Miranda, A. C., Miranda, H. S., Lloyd, J., Grace, J., Francey, R. J., Mcintyre, J. A., Meir, P., Riggan, P., Lockwood, R., & Brass, J. (1997). Fluxes of carbon, water and energy over Brazilian cerrado: an analysis using eddy covariance and stable isotopes. *Plant, Cell & Environment*, *20*, 315–328. doi:doi: 10.1046/j.1365-3040.1997.d01-80.x.

Mitchard, E. T. A. (2018). The tropical forest carbon cycle and climate change. *Nature*, *559*, 527–534. doi:doi: 10.1038/s41586-018-0300-2.

Molina, L. et al. (2015). On the ability of a global atmospheric inversion to constrain variations of CO2 fluxes over Amazonia. *Atmospheric Chemistry and Physics*, *15*, 8423–8438. doi:doi: 10.5194/acp-15-8423-2015.

Morales-Rincon, L. A., Hernandez, A. J., Rodriguez-Hernandez, N. S., & Jimenez, R. (2021). Carbon Exchange and Accumulation in an Orinoco High Plains Native Savanna Ecosystem as Measured by Eddy Covariance. *Frontiers in Environmental Science*, *9*.

Morton, D. C., Nagol, J., Carabajal, C. C., Rosette, J., Palace, M., Cook, B. D., Vermote, E. F., Harding, D. J., & North, P. R. J. (2014). Amazon forests maintain consistent canopy structure and greenness during the dry season. *Nature*, *506*, 221–224. doi:doi: 10.1038/nature13006.

Munassar, S., Rödenbeck, C., Koch, T., Totsche, K. U., Gałkowski, M., Walther, S., &

Gerbig, C. (2021). NEE estimates 2006–2019 over Europe from a pre-operational ensemble-inversion system. *Atmospheric Chemistry and Physics Discussions*, (pp. 1– 28). doi:doi: 10.5194/acp-2021-873. Publisher: Copernicus GmbH.

Myhre, G. et al. (2013). Anthropogenic and Natural Radiative Forcing. In *Climate Change 2013: The Physical Science Basis. Contribution of Working Group I to the Fifth Assessment Report of the Intergovernmental Panel on Climate Change* (p. 82). Cambridge, United Kingdom and New York, NY, USA.: Cambridge University Press.

Myneni, R. B. et al. (2007). Large seasonal swings in leaf area of Amazon rainforests. *Proceedings of the National Academy of Sciences*, *104*, 4820–4823. doi:doi: 10.1073/pn as.0611338104.

NASA-JPL (2013). NASA Shuttle Radar Topography Mission Global 1 arc second [Data set]. NASA EOSDIS Land Processes DAAC.

Naus, S. (2021). *Improving estimates of the atmospheric oxidative capacity and Amazon fire emissions*. Ph.D. thesis Wageningen Univeristy.

Nehrkorn, T., Eluszkiewicz, J., Wofsy, S. C., Lin, J. C., Gerbig, C., Longo, M., & Freitas, S. (2010). Coupled weather research and forecasting–stochastic time-inverted lagrangian transport (WRF–STILT) model. *Meteorology and Atmospheric Physics*, *107*, 51–64. doi:doi: 10.1007/s00703-010-0068-x.

Nepstad, D. C., Tohver, I. M., Ray, D., Moutinho, P., & Cardinot, G. (2007). Mortality of Large Trees and Lianas Following Experimental Drought in an Amazon Forest. *Ecology*, *88*, 2259–2269. doi:doi: 10.1890/06-1046.1.

Nisbet, E. G. et al. (2016). Rising atmospheric methane: 2007-2014 growth and isotopic shift. *Global Biogeochemical Cycles*, *30*, 1356–1370. doi:doi: 10.1002/2016GB005406.

Noojipady, P., Morton, C. D., Macedo, N. M., Victoria, C. D., Huang, C., Gibbs, K. H., & Bolfe, L. E. (2017). Forest carbon emissions from cropland expansion in the Brazilian Cerrado biome. *Environmental Research Letters*, *12*, 025004. doi:doi: 10.1088/1748-9 326/aa5986. Publisher: IOP Publishing.

Oliveira, P. E. S., Acevedo, O. C., Sörgel, M., Tsokankunku, A., Wolff, S., Araújo, A. C., Souza, R. A. F., Sá, M. O., Manzi, A. O., & Andreae, M. O. (2018). Nighttime wind and scalar variability within and above an Amazonian canopy. *Atmospheric Chemistry and Physics*, *18*, 3083–3099. doi:doi: 10.5194/acp-18-3083-2018.

Pangala, S. R. et al. (2017). Large emissions from floodplain trees close the Amazon methane budget. *Nature*, . doi:doi: 10.1038/nature24639.

Pangala, S. R., Gowing, D. J., Hornibrook, E. R. C., & Gauci, V. (2014). Controls on methane emissions from Alnus glutinosa saplings. *The New Phytologist*, *201*, 887–896. doi:doi: 10.1111/nph.12561.

Papale, D., Reichstein, M., Aubinet, M., Canfora, E., Bernhofer, C., Kutsch, W., Long-

doz, B., Rambal, S., Valentini, R., Vesala, T., & Yakir, D. (2006). Towards a standardized processing of Net Ecosystem Exchange measured with eddy covariance technique: algorithms and uncertainty estimation. *Biogeosciences*, *3*, 571–583. doi:doi: 10.5194/bg-3-571-2006.

Peters, W. et al. (2007). An atmospheric perspective on North American carbon dioxide exchange: CarbonTracker. *Proceedings of the National Academy of Sciences*, *104*, 18925–18930. doi:doi: 10.1073/pnas.0708986104.

Peters, W., Miller, J. B., Whitaker, J., Denning, A. S., Hirsch, A., Krol, M. C., Zupanski, D., Bruhwiler, L., & Tans, P. P. (2005). An ensemble data assimilation system to estimate CO_2 surface fluxes from atmospheric trace gas observations. *Journal of Geophysical Research*, *110*. doi:doi: 10.1029/2005JD006157.

Peylin, P. et al. (2013). Global atmospheric carbon budget: results from an ensemble of atmospheric CO_2 inversions. *Biogeosciences*, *10*, 6699–6720. doi:doi: https://doi.org/10.5194/bg-10-6699-2013. Publisher: Copernicus GmbH.

Pfannerstill, E. Y. et al. (2018). Total OH Reactivity Changes Over the Amazon Rainforest During an El Niño Event. *Frontiers in Forests and Global Change*, *1*. doi:doi: 10.3389/ffgc.2018.00012.

Phillips, O. L. et al. (2009). Drought Sensitivity of the Amazon Rainforest. *Science*, *323*, 1344–1347. doi:doi: 10.1126/science.1164033.

Piao, S., Wang, X., Wang, K., Li, X., Bastos, A., Canadell, J. G., Ciais, P., Friedlingstein, P., & Sitch, S. (2020). Interannual variation of terrestrial carbon cycle: Issues and perspectives. *Global Change Biology*, *26*, 300–318. doi:doi: 10.1111/gcb.14884. _eprint: https://onlinelibrary.wiley.com/doi/pdf/10.1111/gcb.14884.

Poorter, L. et al. (2016). Biomass resilience of Neotropical secondary forests. *Nature*, *530*, 211–214. doi:doi: 10.1038/nature16512. Number: 7589 Publisher: Nature Publishing Group.

Poorter, L. et al. (2021). Multidimensional tropical forest recovery. *Science*, *374*, 1370–1376. doi:doi: 10.1126/science.abh3629.

Prado, D. (2003). As caatingas da América do Sul. In *Ecologia e Biogeografía da Caatinga* (pp. 3–73). Universidade Federal de Pernambuco. (Inara leal, marcelo tabarelli, j.m.c. silva ed.).

Prather, M. J., Holmes, C. D., & Hsu, J. (2012). Reactive greenhouse gas scenarios: Systematic exploration of uncertainties and the role of atmospheric chemistry. *Geophysical Research Letters*, *39*. doi:doi: 10.1029/2012GL051440.

Pöhlker, C. et al. (2019). Land cover and its transformation in the backward trajectory footprint region of the Amazon Tall Tower Observatory. *Atmospheric Chemistry and Physics*, *19*, 8425–8470. doi:doi: 10.5194/acp-19-8425-2019.

Qin, Y. et al. (2021). Carbon loss from forest degradation exceeds that from deforestation in the Brazilian Amazon. *Nature Climate Change*, *11*, 442–448. doi:doi: 10.1038/s415 58-021-01026-5.

Querino, C. A. S., Smeets, C. J. P. P., Vigano, I., Holzinger, R., Moura, V., Gatti, L. V., Martinewski, A., Manzi, A. O., de Araújo, A. C., & Röckmann, T. (2011). Methane flux, vertical gradient and mixing ratio measurements in a tropical forest. *Atmospheric Chemistry and Physics*, *11*, 7943–7953. doi:doi: 10.5194/acp-11-7943-2011.

Quesada, C. A. et al. (2012). Basin-wide variations in Amazon forest structure and function are mediated by both soils and climate. *Biogeosciences*, *9*, 2203–2246. doi:doi: 10.5194/bg-9-2203-2012. Publisher: Copernicus GmbH.

Raich, J. W. (2017). Temporal Variability of Soil Respiration in Experimental Tree Plantations in Lowland Costa Rica. *Forests*, *8*, 40. doi:doi: 10.3390/f8020040.

Ramos-Neto, M. B., & Pivello, V. R. (2000). Lightning Fires in a Brazilian Savanna National Park: Rethinking Management Strategies. *Environmental Management*, *26*, 675–684. doi:doi: 10.1007/s002670010124.

von Randow, C., Manzi, A. O., Kruijt, B., de Oliveira, P. J., Zanchi, F. B., Silva, R. L., Hodnett, M. G., Gash, J. H. C., Elbers, J. A., Waterloo, M. J., Cardoso, F. L., & Kabat, P. (2004). Comparative measurements and seasonal variations in energy and carbon exchange over forest and pasture in South West Amazonia. *Theoretical and Applied Climatology*, *78*, 5–26. doi:doi: 10.1007/s00704-004-0041-z.

von Randow, C. et al. (2013). Inter-annual variability of carbon and water fluxes in Amazonian forest, Cerrado and pasture sites, as simulated by terrestrial biosphere models. *Agricultural and Forest Meteorology*, *182-183*, 145–155. doi:doi: 10.1016/j.ag rformet.2013.05.015.

Ratter, J. A., Ribeiro, J. F., & Bridgewater, S. (1997). The Brazilian cerrado vegetation and threats to its biodiversity. *Annals of Botany (United Kingdom)*, .

Reichstein, M. et al. (2005). On the separation of net ecosystem exchange into assimilation and ecosystem respiration: review and improved algorithm. *Global Change Biology*, *11*, 1424–1439. doi:doi: https://doi.org/10.1111/j.1365-2486.2005.001002.x.

Requena Suarez, D. et al. (2019). Estimating aboveground net biomass change for tropical and subtropical forests: Refinement of IPCC default rates using forest plot data. *Global Change Biology*, *25*, 3609–3624. doi:doi: 10.1111/gcb.14767.

Resende, A. F. d., Schöngart, J., Streher, A. S., Ferreira-Ferreira, J., Piedade, M. T. F., & Silva, T. S. F. (2019). Massive tree mortality from flood pulse disturbances in Amazonian floodplain forests: The collateral effects of hydropower production. *Science of The Total Environment*, *659*, 587–598. doi:doi: 10.1016/j.scitotenv.2018.12.208.

Restrepo-Coupe, N. et al. (2013). What drives the seasonality of photosynthesis across

the Amazon basin? A cross-site analysis of eddy flux tower measurements from the Brasil flux network. *Agricultural and Forest Meteorology*, *182-183*, 128–144. doi:doi: 10.1016/j.agrformet.2013.04.031.

Restrepo-Coupe, N. et al. (2017). Do dynamic global vegetation models capture the seasonality of carbon fluxes in the Amazon basin? A data-model intercomparison. *Global Change Biology*, *23*, 191–208. doi:doi: https://doi.org/10.1111/gcb.13442.

Ribeiro, K., Sousa-Neto, E. R. d., Carvalho, J. A. d., Sousa Lima, J. R. d., Menezes, R. S. C., Duarte-Neto, P. J., da Silva Guerra, G., & Ometto, J. P. H. B. (2016). Land cover changes and greenhouse gas emissions in two different soil covers in the Brazilian Caatinga. *Science of The Total Environment*, *571*, 1048–1057. doi:doi: 10.1016/j.scit otenv.2016.07.095.

Richey, J. E., Devol, A. H., Wofsy, S. C., Victoria, R., & Riberio, M. N. G. (1988). Biogenic gases and the oxidation and reduction of carbon in Amazon River and floodplain waters: Amazon dissolved gases. *Limnology and Oceanography*, *33*, 551–561. doi:doi: 10.4319/ lo.1988.33.4.0551.

Richey, J. E., Krusche, A. V., Johnson, M. S., da Cunha, H. B., & Ballester, M. V. (2009). The role of rivers in the regional carbon balance. In J. Gash, M. Keller, & P. Silva-Dias (Eds.), *Amazonia and Global Change* (pp. 489–504). volume 186.

Richey, J. E., Melack, J. M., Aufdenkampe, A. K., Ballester, V. M., & Hess, L. L. (2002). Outgassing from Amazonian rivers and wetlands as a large tropical source of atmospheric CO2. *Nature*, *416*, 617–620. doi:doi: 10.1038/416617a.

Rigby, M. et al. (2017). Role of atmospheric oxidation in recent methane growth. *Proceedings of the National Academy of Sciences*, *114*, 5373–5377. doi:doi: 10.1073/pnas .1616426114.

Ringeval, B., Houweling, S., van Bodegom, P. M., Spahni, R., van Beek, R., Joos, F., & Röckmann, T. (2014). Methane emissions from floodplains in the Amazon Basin: challenges in developing a process-based model for global applications. *Biogeosciences*, *11*, 1519–1558. doi:doi: 10.5194/bg-11-1519-2014.

Rödenbeck, C. (2005). *Estimating CO2 sources and sinks from atmospheric mixing ratio measurements using a global inversion of atmospheric transport*. Technical Report, Max Planck Institute for Biogeochemistry. URL: `http://www.bgc-jena.mpg.de/~christi an.roedenbeck/INVERSION/HOWTO/`.

Rödenbeck, C., Gerbig, C., Trusilova, K., & Heimann, M. (2009). A two-step scheme for high-resolution regional atmospheric trace gas inversions based on independent models. *Atmos. Chem. Phys.*, (p. 12).

Rödenbeck, C., Houweling, S., Gloor, M., & Heimann, M. (2003). CO2 flux history 1982–2001 inferred from atmospheric data using a global inversion of atmospheric transport. *Atmos. Chem. Phys.*, (p. 46).

Rödenbeck, C., Keeling, R. F., Bakker, D. C. E., Metzl, N., Olsen, A., Sabine, C., & Heimann, M. (2013). Global surface-ocean p^{co_2} and sea–air CO_2 flux variability from an observation-driven ocean mixed-layer scheme. *Ocean Science*, *9*, 193–216. doi:doi: 10.5194/os-9-193-2013. Publisher: Copernicus GmbH.

Rödenbeck, C., Zaehle, S., Keeling, R., & Heimann, M. (2018). History of El Niño impacts on the global carbon cycle 1957–2017: a quantification from atmospheric CO_2 data. *Philosophical Transactions of the Royal Society B: Biological Sciences*, *373*, 20170303. doi:doi: 10.1098/rstb.2017.0303.

Saatchi, S. S., Houghton, R. A., Alvalá, R. C. D. S., Soares, J. V., & Yu, Y. (2007). Distribution of aboveground live biomass in the Amazon basin. *Global Change Biology*, *13*, 816–837. doi:doi: https://doi.org/10.1111/j.1365-2486.2007.01323.x.

Salati, E., & Vose, P. B. (1984). Amazon Basin: A System in Equilibrium. *Science*, *225*, 129–138. doi:doi: 10.1126/science.225.4658.129.

Saleska, S., Rocha, H. R. d., Kruijt, B., & Nobre, A. D. (2009). Changes in Amazonian forest biomass, dynamics, and composition, 1980–2002. In M. Keller, M. Bustamante, J. Gash, & P. Silva Dias (Eds.), *Geophysical Monograph Series* (pp. 373–387). Washington, D. C.: American Geophysical Union volume 186. doi:doi: 10.1029/2008GM000739.

Saleska, S. R. et al. (2003). Carbon in Amazon Forests: Unexpected Seasonal Fluxes and Disturbance-Induced Losses. *Science*, *302*, 1554–1557. doi:doi: 10.1126/science.109116 5.

Sanderson, M. G. (1996). Biomass of termites and their emissions of methane and carbon dioxide: A global database. *Global Biogeochemical Cycles*, *10*, 543–557. doi:doi: 10.1 029/96GB01893.

Sandu, I., Beljaars, A., Bechtold, P., Mauritsen, T., & Balsamo, G. (2013). Why is it so difficult to represent stably stratified conditions in numerical weather prediction (NWP) models? *Journal of Advances in Modeling Earth Systems*, *5*, 117–133. doi:doi: 10.1002/jame.20013.

Sano, E. E., Rosa, R., Brito, J. L. S., & Ferreira, L. G. (2007). *Mapeamento de Cobertura Vegetal do Bioma Cerrado: estratégias e resultados*. Technical Report, EMBRAPA.

Santos, A. J., Quesada, C. A., Da Silva, G. T., Maia, J. F., Miranda, H. S., Carlos Miranda, A., & Lloyd, J. (2004). High rates of net ecosystem carbon assimilation by Brachiara pasture in the Brazilian Cerrado. *Global Change Biology*, *10*, 877–885. doi:doi: 10.1111/j.1529-8817.2003.00777.x.

Saturno, J. et al. (2018). Black and brown carbon over central Amazonia: long-term aerosol measurements at the ATTO site. *Atmospheric Chemistry and Physics*, *18*, 12817–12843. doi:doi: 10.5194/acp-18-12817-2018.

Saunois, M. et al. (2016). The global methane budget 2000–2012. *Earth System Science*

Data, *8*, 697–751. doi:doi: 10.5194/essd-8-697-2016.

Saunois, M. et al. (2017). Variability and quasi-decadal changes in the methane budget over the period 2000–2012. *Atmospheric Chemistry and Physics*, *17*, 11135–11161. doi:doi: 10.5194/acp-17-11135-2017. Publisher: Copernicus GmbH.

Saunois, M. et al. (2020). The Global Methane Budget 2000–2017. *Earth System Science Data*, *12*, 1561–1623. doi:doi: 10.5194/essd-12-1561-2020. Publisher: Copernicus GmbH.

Sawakuchi, H. O., Bastviken, D., Sawakuchi, A. O., Krusche, A. V., Ballester, M. V. R., & Richey, J. E. (2014). Methane emissions from Amazonian Rivers and their contribution to the global methane budget. *Global Change Biology*, *20*, 2829–2840. doi:doi: 10.1111/gcb.12646.

Schaefer, H. et al. (2016). A 21st-century shift from fossil-fuel to biogenic methane emissions indicated by 13CH4. *Science*, *352*, 80–84. doi:doi: 10.1126/science.aad2705.

Schaefer, K., Collatz, G. J., Tans, P., Denning, A. S., Baker, I., Berry, J., Prihodko, L., Suits, N., & Philpott, A. (2008). Combined Simple Biosphere/Carnegie-Ames-Stanford Approach terrestrial carbon cycle model. *Journal of Geophysical Research*, *113*. doi:doi: 10.1029/2007JG000603.

van Schaik, E., Killaars, L., Smith, N. E., Koren, G., van Beek, L. P. H., Peters, W., & van der Laan-Luijkx, I. T. (2018). Changes in surface hydrology, soil moisture and gross primary production in the Amazon during the 2015/2016 El Niño. *Philosophical Transactions of the Royal Society B: Biological Sciences*, *373*, 20180084. doi:doi: 10.1098/rstb.2018.0084.

Schjønning, P., McBride, R., Keller, T., & Obour, P. (2017). Predicting soil particle density from clay and soil organic matter contents. *Geoderma*, *286*, 83–87. doi:doi: 10.1016/j.geoderma.2016.10.020.

Schuh, A. E., Denning, A. S., Corbin, K. D., Baker, I. T., Uliasz, M., Parazoo, N., Andrews, A. E., & Worthy, D. E. J. (2010). A regional high-resolution carbon flux inversion of North America for 2004. *Biogeosciences*, *7*, 1625–1644. doi:doi: https://doi.org/10.5194/bg-7-1625-2010. Publisher: Copernicus GmbH.

SEEG (). Total Emissions | SEEG - System Gas Emissions Estimation. Available at: https://plataforma.seeg.eco.br/total_emission#.

Sherwood, O. A., Schwietzke, S., Arling, V. A., & Etiope, G. (2017). Global Inventory of Gas Geochemistry Data from Fossil Fuel, Microbial and Burning Sources, version 2017. *Earth System Science Data*, *9*, 639–656. doi:doi: 10.5194/essd-9-639-2017.

Shiga, Y. P., Michalak, A. M., Fang, Y., Schaefer, K., Andrews, A. E., Huntzinger, D. H., Schwalm, C. R., Thoning, K., & Wei, Y. (2018). Forests dominate the interannual variability of the North American carbon sink. *Environmental Research Letters*, *13*,

084015. doi:doi: 10.1088/1748-9326/aad505. Publisher: IOP Publishing.

Silva, P. F. d., Lima, J. R. d. S., Antonino, A. C. D., Souza, R., Souza, E. S. d., Silva, J. R. I., & Alves, E. M. (2017). Seasonal patterns of carbon dioxide, water and energy fluxes over the Caatinga and grassland in the semi-arid region of Brazil. *Journal of Arid Environments*, *147*, 71–82. doi:doi: 10.1016/j.jaridenv.2017.09.003.

da Silva Junior, C. A., Teodoro, P. E., Delgado, R. C., Teodoro, L. P. R., Lima, M., de Andréa Pantaleão, A., Baio, F. H. R., de Azevedo, G. B., de Oliveira Sousa Azevedo, G. T., Capristo-Silva, G. F., Arvor, D., & Facco, C. U. (2020). Persistent fire foci in all biomes undermine the Paris Agreement in Brazil. *Scientific Reports*, *10*, 16246. doi:doi: 10.1038/s41598-020-72571-w.

Sitch, S. et al. (2015). Recent trends and drivers of regional sources and sinks of carbon dioxide. *Biogeosciences*, *12*, 653–679. doi:doi: https://doi.org/10.5194/bg-12-653-2015. Publisher: Copernicus GmbH.

SPA (2021). *Amazon Assessment Report 2021*. Technical Report, UN Sustainable Development Solutions Network (SDSN). URL: `https://www.theamazonwewant.org/amazon-assessment-report-2021/` science Panel for the Amazon.

Spera, S. A., Galford, G. L., Coe, M. T., Macedo, M. N., & Mustard, J. F. (2016). Land-use change affects water recycling in Brazil's last agricultural frontier. *Global Change Biology*, *22*, 3405–3413. doi:doi: 10.1111/gcb.13298.

Steeneveld, G. J., Holtslag, A. A. M., Nappo, C. J., van de Wiel, B. J. H., & Mahrt, L. (2008). Exploring the Possible Role of Small-Scale Terrain Drag on Stable Boundary Layers over Land. *Journal of Applied Meteorology and Climatology*, *47*, 2518–2530. doi:doi: 10.1175/2008JAMC1816.1.

Steinbach, J., Gerbig, C., Rödenbeck, C., Karstens, U., Minejima, C., & Mukai, H. (2011). The CO_2 release and Oxygen uptake from Fossil Fuel Emission Estimate (COFFEE) dataset: effects from varying oxidative ratios. *Atmospheric Chemistry and Physics*, *11*, 6855–6870. doi:doi: 10.5194/acp-11-6855-2011. Publisher: Copernicus GmbH.

Stephens, B. B. et al. (2007). Weak Northern and Strong Tropical Land Carbon Uptake from Vertical Profiles of Atmospheric CO2. *Science*, *316*, 1732–1735. doi:doi: 10.1126/science.1137004.

Stohl, A. (1998). Computation, accuracy and applications of trajectories—A review and bibliography. *Atmospheric Environment*, *32*, 947–966. doi:doi: 10.1016/S1352-2310(97)00457-3.

Stohl, A., & Wotawa, G. (1995). A method for computing single trajectories representing boundary layer transport. *Atmospheric Environment*, *29*, 3235–3238. doi:doi: 10.1016/1352-2310(95)00259-2.

Stull, R. B. (1988). *An introduction to Boundary Layer Mateorology*. Kluwer Academic

Publishers.

Sun, J., Desjardins, R., Mahrt, L., & MacPherson, I. (1998). Transport of carbon dioxide, water vapor, and ozone by turbulence and local circulations. *Journal of Geophysical Research: Atmospheres*, *103*, 25873–25885. doi:doi: 10.1029/98JD02439.

Sun, J., Mahrt, L., Banta, R. M., & Pichugina, Y. L. (2012). Turbulence Regimes and Turbulence Intermittency in the Stable Boundary Layer during CASES-99. *Journal of the Atmospheric Sciences*, *69*, 338–351. doi:doi: 10.1175/JAS-D-11-082.1.

Thompson, R. L. et al. (2016). Top–down assessment of the Asian carbon budget since the mid 1990s. *Nature Communications*, *7*, 10724. doi:doi: 10.1038/ncomms10724. Number: 1 Publisher: Nature Publishing Group.

Tiedtke, M. (1989). A Comprehensive Mass Flux Scheme for Cumulus Parameterization in Large-Scale Models. *Monthly Weather Review*, *117*, 1779–1800. doi:doi: 10.1175/1520-0493(1989)117⟨1779:ACMFSF⟩2.0.CO;2. Publisher: American Meteorological Society.

Trusilova, K., Rödenbeck, C., Gerbig, C., & Heimann, M. (2010). Technical Note: A new coupled system for global-to-regional downscaling of CO2 concentration estimation. *Atmos. Chem. Phys.*, (p. 9).

Tunnicliffe, R. L. et al. (2020). Quantifying sources of Brazil's CH_4 emissions between 2010 and 2018 from satellite data. *Atmospheric Chemistry and Physics*, *20*, 13041–13067. doi:doi: 10.5194/acp-20-13041-2020.

Turner, A. J., Frankenberg, C., & Kort, E. A. (2019). Interpreting contemporary trends in atmospheric methane. *Proceedings of the National Academy of Sciences*, *116*, 2805–2813. doi:doi: 10.1073/pnas.1814297116.

Turner, A. J., Frankenberg, C., Wennberg, P. O., & Jacob, D. J. (2017). Ambiguity in the causes for decadal trends in atmospheric methane and hydroxyl. *Proceedings of the National Academy of Sciences*, *114*, 5367–5372. doi:doi: 10.1073/pnas.1616020114.

Tóta, J., Fitzjarrald, D. R., Staebler, R. M., Sakai, R. K., Moraes, O. M. M., Acevedo, O. C., Wofsy, S. C., & Manzi, A. O. (2008). Amazon rain forest subcanopy flow and the carbon budget: Santarém LBA-ECO site. *Journal of Geophysical Research: Biogeosciences*, *113*. doi:doi: 10.1029/2007JG000597.

Tóta, J., Roy Fitzjarrald, D., & da Silva Dias, M. A. F. (2012). Amazon Rainforest Exchange of Carbon and Subcanopy Air Flow: Manaus LBA Site—A Complex Terrain Condition. *The Scientific World Journal*, *2012*, 1–19. doi:doi: 10.1100/2012/165067.

Vale, R., Santana, R., Gomes, A. C., & Tóta, J. (2018). Increased nocturnal CO2 concentration during breeze circulation events in a tropical reservoir. *Ambiente e Agua - An Interdisciplinary Journal of Applied Science*, *13*, 1. doi:doi: 10.4136/ambi-agua.2186.

Varella, R. F., Bustamante, M. M. C., Pinto, A. S., Kisselle, K. W., Santos, R. V., Burke,

R. A., Zepp, R. G., & Viana, L. T. (2004). Soil Fluxes of Co2, Co, No, and N2o from an Old Pasture and from Native Savanna in Brazil. *Ecological Applications*, *14*, 221–231. doi:doi: 10.1890/01-6014.

Verbeeck, H., Peylin, P., Bacour, C., Bonal, D., Steppe, K., & Ciais, P. (2011). Seasonal patterns of CO_2 fluxes in Amazon forests: Fusion of eddy covariance data and the ORCHIDEE model. *Journal of Geophysical Research*, *116*, G02018. doi:doi: 10.1029/2010JG001544.

Verchot, L. V., Davidson, E. A., Cattânio, J. H., & Ackerman, I. L. (2000). Land-Use Change and Biogeochemical Controls of Methane Fluxes in Soils of Eastern Amazonia. *Ecosystems*, *3*, 41–56. doi:doi: 10.1007/s100210000009.

Vickers, D., & Mahrt, L. (1997). Quality Control and Flux Sampling Problems for Tower and Aircraft Data. *Journal of Atmospheric and Oceanic Technology*, *14*, 512–526. doi:doi: 10.1175/1520-0426(1997)014⟨0512:QCAFSP⟩2.0.CO;2.

Wang, W., Peng, C., Kneeshaw, D., Larocque, G., & Luo, Z.-B. (2012). Drought-induced tree mortality: Ecological consequences, causes, and modeling. *Environmental Reviews*, *20*, 109–121. doi:doi: 10.1139/a2012-004.

Webb, A. J. et al. (2016). CH4 concentrations over the Amazon from GOSAT consistent with in situ vertical profile data. *Journal of Geophysical Research: Atmospheres*, *121*, 11,006–11,020. doi:doi: 10.1002/2016JD025263.

Wehr, R., Munger, J. W., McManus, J. B., Nelson, D. D., Zahniser, M. S., Davidson, E. A., Wofsy, S. C., & Saleska, S. R. (2016). Seasonality of temperate forest photosynthesis and daytime respiration. *Nature*, *534*, 680–683. doi:doi: 10.1038/nature17966. Number: 7609 Publisher: Nature Publishing Group.

Welch, B., Gauci, V., & Sayer, E. J. (2019). Tree stem bases are sources of CH_4 and N_2O in a tropical forest on upland soil during the dry to wet season transition. *Global Change Biology*, *25*, 361–372. doi:doi: 10.1111/gcb.14498.

van der Werf, G. R., Randerson, J. T., Giglio, L., Collatz, G. J., Mu, M., Kasibhatla, P. S., Morton, D. C., DeFries, R. S., Jin, Y., & van Leeuwen, T. T. (2010). Global fire emissions and the contribution of deforestation, savanna, forest, agricultural, and peat fires (1997–2009). *Atmos. Chem. Phys.*, *10*, 11707–11735. doi:doi: 10.5194/acp-10-11707-2010.

van der Werf, G. R., Randerson, J. T., Giglio, L., van Leeuwen, T. T., Chen, Y., Rogers, B. M., Mu, M., van Marle, M. J. E., Morton, D. C., Collatz, G. J., Yokelson, R. J., & Kasibhatla, P. S. (2017). Global fire emissions estimates during 1997–2016. *Earth System Science Data*, *9*, 697–720. doi:doi: 10.5194/essd-9-697-2017.

Wiegner, M., & Geiß, A. (2012). Aerosol profiling with the Jenoptik ceilometer CHM15kx. *Atmospheric Measurement Techniques*, *5*, 1953–1964. doi:doi: 10.5194/amt-5-1953-2012.

Wigneron, J.-P., Fan, L., Ciais, P., Bastos, A., Brandt, M., Chave, J., Saatchi, S., Baccini, A., & Fensholt, R. (2020). Tropical forests did not recover from the strong 2015–2016 El Niño event. *Science Advances*, *6*. doi:doi: 10.1126/sciadv.aay4603.

Wilson, C., Chipperfield, M. P., Gloor, M., Parker, R. J., Boesch, H., McNorton, J., Gatti, L. V., Miller, J. B., Basso, L. S., & Monks, S. A. (2021). Large and increasing methane emissions from eastern Amazonia derived from satellite data, 2010–2018. *Atmospheric Chemistry and Physics*, *21*, 10643–10669. doi:doi: 10.5194/acp-21-10643-2021.

Wilson, C., Gloor, M., Gatti, L. V., Miller, J. B., Monks, S. A., McNorton, J., Bloom, A. A., Basso, L. S., & Chipperfield, M. P. (2016). Contribution of regional sources to atmospheric methane over the Amazon Basin in 2010 and 2011. *Global Biogeochemical Cycles*, *30*, 400–420. doi:doi: 10.1002/2015GB005300.

Winderlich, J., Chen, H., Gerbig, C., Seifert, T., Kolle, O., Lavrič, J. V., Kaiser, C., Höfer, A., & Heimann, M. (2010). Continuous low-maintenance $CO_2/CH_4/H_2O$ measurements at the Zotino Tall Tower Observatory (ZOTTO) in Central Siberia. *Atmospheric Measurement Techniques*, *3*, 1113–1128. doi:doi: 10.5194/amt-3-1113-2010.

Winderlich, J., Gerbig, C., Kolle, O., & Heimann, M. (2014). Inferences from CO_2 and CH_4 concentration profiles at the Zotino Tall Tower Observatory (ZOTTO) on regional summertime ecosystem fluxes. *Biogeosciences*, *11*, 2055–2068. doi:doi: https://doi.org/10.5194/bg-11-2055-2014. Publisher: Copernicus GmbH.

Wu, J. et al. (2016). Leaf development and demography explain photosynthetic seasonality in Amazon evergreen forests. *Science*, *351*, 972–976. doi:doi: 10.1126/science.aad5068.

Wutzler, T., Lucas-Moffat, A., Migliavacca, M., Knauer, J., Sickel, K., Šigut, L., Menzer, O., & Reichstein, M. (2018). Basic and extensible post-processing of eddy covariance flux data with REddyProc. *Biogeosciences*, *15*, 5015–5030. doi:doi: https://doi.org/10.5194/bg-15-5015-2018. Publisher: Copernicus GmbH.

Zeri, M., & Sá, L. D. A. (2011). Horizontal and Vertical Turbulent Fluxes Forced by a Gravity Wave Event in the Nocturnal Atmospheric Surface Layer Over the Amazon Forest. *Boundary-Layer Meteorology*, *138*, 413–431. doi:doi: 10.1007/s10546-010-9563-3.

About the author

Time gradually defines a person's vital needs. Physical activities where endurance and mental control are equally necessary, have long been some of my essential needs. This is why I ran a marathon, cycle long distances and whenever is possible climb up mountains. I decided to follow an academic pathway driven by a vital need to understand our environment. Just after I finished my bachelor in Environmental Engineering, I was not sure about the specific topic I wanted to follow, but I was leaning to learn more about the Earth System. This certainty came about while doing a semester program (www.sea.edu) in which we sailed from New Zealand to Tahiti doing ocean related research. My project was about the carbon (DIC) transport by different water masses from the southern ocean to lower latitudes. This great experience was my first contact with carbon cycle research.

From the ocean to the forest. With its cultural and biological diversity the Amazon rainforest had always been an intriguing and inspiring place for me, but had never really studied it seriously. I started doing Amazon-related research in 2016 looking at the "Effect of fire emissions on the carbon cycle of the Amazon for 2010-2015" in my Master Thesis in Wageningen University, in The Netherlands. After finishing the master's degree in Environmental Sciences, I moved to Jena in Germany and started a Ph.D. in 2018 at the MPI-BGC. During this time, I have studied methane and carbon dioxide at ATTO from an atmospheric perspective, which means that by looking at the atmospheric changes of these two gases (methane and carbon dioxide) I tried to interpret how the forest responds to different drivers at various spatial and temporal scales.

After these long years of Ph.D., I think that a full understanding of the complexities of Nature is impossible, but this impossibility is what triggers new scientific questions which will eventually lead to great developments and breakthroughs. Science is about endurance and resisting, but also about the flexibility of changing our minds and methods. This constant questioning of theories and practices is what makes the scientific method special and successful. But science is not the only way to gain and accumulate knowledge, is just an additional one that adds to other traditional ways of understanding our environment. I hope I can continue in this pathway always with these ideas in mind.

Peer-reviewed journal publications

Botía, S., Gerbig, C., Marshall, J., Lavric, J. V., Walter, D., Pöhlker, C., Holanda, B., Fisch, G., de Araújo, A. C., Sá, M. O., Teixeira, P. R., Resende, A. F., Dias-Junior, C. Q., van Asperen, H., Oliveira, P. S., Stefanello, M., and Acevedo, O. C.: Understanding nighttime methane signals at the Amazon Tall Tower Observatory (ATTO), Atmos. Chem. Phys., 20, 6583–6606, https://doi.org/10.5194/acp-20-6583-2020, 2020.

Botía, S., Komiya, S., Marshall, J., Koch, T., Gałkowski, M., Lavric, J., Gomes-Alves, E., Walter, D., Fisch, G., Pinho, D. M., Nelson, B. W., Martins, G., Luijkx, I. T., Koren, G., Florentie, L., Carioca de Araújo, A., Sá, M., Andreae, M. O., Heimann, M., Peters, W., Gerbig, C.: The CO_2 record at the Amazon Tall Tower Observatory: A new opportunity to study processes on seasonal and inter-annual scales. Global Change Biology, 28, 588–611. https://doi.org/10.1111/gcb.15905, 2022.

van der Woude, A. M., de Kok, R., Smith, N., Luijkx, I. T., **Botía, S.**, Karstens, U., Kooijmans, L. M. J., Koren, G., Meijer, H., Steeneveld, G.-J., Storm, I., Super, I., Scheeren, B. A., Vermeulen, A., and Peters, W.: Near real-time CO2 fluxes from CarbonTracker Europe for high resolution atmospheric modeling, Earth Syst. Sci. Data Discuss. [preprint], https://doi.org/10.5194/essd-2022-175, in review, 2022.

Dias-Junior, C, Q., Gomes, R. C., Fisch, G., D'Oliveira. F.A., Sörgel, M., **Botía, S.**, Machado, L. A., Wolff, S., dos Santos, R. M., and Pöhlker, C.: Intercomparison of planetary boundary layer height retrievals using ERA5 reanalysis over Central Amazonia. Remote Sensing, in review, 2022.

Melack, J.M., Basso, L.S., Fleischmann, A.S., **Botía, S.**, Guo, M., Zhou, W., Barbosa, P.M., Amaral, J.H.F., and MacIntyre, S.: Challenges Regionalizing Methane Emissions Using Aquatic Environments in the Amazon Basin as Examples. Front. Environ. Sci. 10:866082. doi: 10.3389/fenvs.2022.866082, 2022.

Bezerra, V. L., Dias-Júnior, C. Q., Vale, R. S., Santana, R. A., **Botía, S.**, Manzi, A. O., Cohen, J. C. P., Martins, H. S., Chamecki, M., and Fuentes, J. D.: Near-Surface Atmospheric Turbulence in the Presence of a Squall Line above a Forested and Deforested Region in the Central Amazon. Atmosphere, 12(4), 461. https://doi.org/10.3390/atmos12040461, 2021.

Corrêa, P. B., Dias-Júnior, C. Q., Cava, D., Sörgel, M., **Botía, S.**, Acevedo, O., Oliveira, P. Manzi, A., Machado, L. A., Martins, H., Tsokankunku, A., Araújo, A. C., Lavric, J., Walter, D., Mortarini, L.: A case study of a gravity wave induced by Amazon forest orography and low level jet generation. Agricultural and Forest Meteorology, 307, 108457. 2021.

Netlands Research School for the
Socio-Economic and Natural Sciences of the Environment

D I P L O M A

for specialised PhD training

The Netherlands research school for the
Socio-Economic and Natural Sciences of the Environment
(SENSE) declares that

Santiago Botía Bocanegra

born on 15th October 1988 in Bogotá, Colombia

has successfully fulfilled all requirements of the
educational PhD programme of SENSE.

Wageningen, 30th September 2022

Chair of the SENSE board

Prof. dr. Martin Wassen

The SENSE Director

Prof. Philipp Pattberg

K O N I N K L I J K E   N E D E R L A N D S E
A K A D E M I E   V A N   W E T E N S C H A P P E N

The SENSE Research School declares that **Santiago Botía Bocanegra** has successfully fulfilled all requirements of the educational PhD programme of SENSE with a work load of 45.3 EC, including the following activities:

SENSE PhD Courses

o   Research in context activity: 'Organizing a two day workshop bringing together the latest research relevant to RECCAP2 (Regional Carbon Cycle Assessment and Processes (2020)

Other PhD and Advanced MSc Courses

o   Atmosphere and Ocean, IMPRS-Jena (2018)
o   Rules for good scientific practice, IMPRS-Jena (2018)
o   Coding courses online Datacamp, Online (2018)
o   Thermodynamics of Earth System Processes, IMPRS-Jena (2018)
o   Earth observation techniques, IMPRS-Jena (2018)
o   Earth System Modeling workshop, MPI-Meteorology (2018)
o   Terrestrial Biosphere, IMPRS-Jena (2020)
o   Biogeochemical Cycles in the Earth System, IMPRS-Jena (2020)
o   Applied statistics and data analysis: Part 1. Basics, IMPRS-Jena (2020)
o   Applied statistics and data analysis: Part 2. Advanced, IMPRS-Jena (2020)
o   Reviewing a paper manuscript, Wageningen Graduate Schools (2020)

External training at a foreign research institute

o   Research stays, INPE/INPA, Brazil (2018-2019)
o   Research stays at ATTOMPI/INPA, Brazil (2019-2021)

Management and Didactic Skills Training

o   PhD representative of the Biogeochemical Signals Department in Jena(2019)
o   Organizer of the Earth System PhD Conference in Jena (2019)
o   Supervising MSc student with thesis 2022)
o   Course assistant in the MSc course 'Earth System Modeling' (2021)

Oral Presentations

o   *Tracking Nighttime Methane Signals at the Amazon Tall Tower Observatory*. AGU, 10-14 December 2018, Washington, United States of America
o   *The rhythm of atmospheric signals at ATTO*. Berlin Science Week, 3 November2021, Berlin, Germany
o   *Methane signals at ATTO*. Heidelberg University, 13-14 June, 2019, Heidelberg, Germany
o   *Atmospheric transport of greenhouse gases at ATTO*. Munich Technical University, WRF model workshop, 7-8, May 2019, Munich, Germany

SENSE coordinator PhD education

Dr. ir. Peter Vermeulen

2022